Transition Metal Sulfide Derived Nanocomposites for Oxygen Reduction Reaction and Water Splitting Applications

Thesis Submitted to AcSIR

For the Award of the Degree of

DOCTOR OF PHILOSOPHY

In

Chemical Sciences

By

Mr. Rajith Illathvalappil

Registration Number: 10CC17J26035

Under the guidance of

Dr. Sreekumar Kurungot

CSIR-National Chemical Laboratory

Pune-411008, India

April 2020

CERTIFICATE

This is to certify that the work incorporated in this Ph.D. thesis entitled **"Transition Metal Sulfide Derived Nanocomposites for Oxygen Reduction Reaction and Water Splitting Applications"** submitted by Mr. Rajith Illathvalappil to Academy of Scientific and Innovative Research (AcSIR) in fulfillment of the requirements for the award of the Degree of Doctor of Philosophy, embodies original research work under my guidance. I further certify that this work has not been submitted to any other University or Institution in part or full for the award of any degree or diploma. Research materials obtained from other sources has been duly acknowledged in the thesis. Any text, illustration, table etc., used in the thesis from other sources, have been duly cited and acknowledged.

It is also certified that this work done by the student, under my supervision, is plagiarism free.

Rajith Illathvalappil
(Student)

Dr. Sreekumar Kurungot
(Supervisor)

DECLARATION

I, hereby declare that all the experiments in thesis entitled **"Transition Metal Sulfide Derived Nanocomposites for Oxygen Reduction Reaction and Water Splitting Applications"** submitted for the degree of Doctor of Philosophy in Chemical Sciences to the Academy of Scientific and Innovative Research (AcSIR) have been carried out by me at the Physical and Materials Chemistry Division, CSIR-National Chemical Laboratory, Pune-411008, India, under the supervision of **Dr. Sreekumar Kurungot**. This work is original and has not been submitted to any other University or Institution in part or full for the award of any degree or diploma.

Mr. Rajith Illathvalappil

Physical and Materials Chemistry Division,

CSIR- National Chemical Laboratory

Pune-411008, India.

Date: 14-04-2020

Acknowledgement

At this moment of my doctorate life, I wish to take this opportunity to give my vote of thanks to those who are directly or indirectly helped and encouraged me to achieve at this level. I feel that words are not sufficient to express my gratitude to all of these eminent people.

First of all, I would like to thank my research guide Dr. Sreekumar Kurungot for his valuable guidance and constant support. He trained me to manage multiple research activities by giving important responsibilities. His time management and dedication to completing the various projects in a short-duration is inspiring. He provided me the entire freedom to work in the lab and gave me the opportunity to associate with various research groups within and outside CSIR-NCL for the collaboration works. Because of this, I have been benefited from a large number of publications. The incredible work and progress made in the fuel cell project under his leadership in notable. I'm grateful to him for involving me in every part of the fuel cell system development and the interactions with the industry partner. I have learned many things during those periods and the valuable advice provided by him resolved many clogs and helped to speed-up my works. The work presentation, monthly meeting and weekly literature presentations molded me to develop as an independent researcher with clarity in the scientific background. The trust he kept on me for managing the various purchase-related activities in the lab is appreciable.

I am thankful to Prof. Ashwini K. Nangia (Director, CSIR-NCL) and Dr. Sourav Pal (Former Director, CSIR-NCL) for providing the opportunity to work in this esteemed laboratory and to make use of the facilities of this laboratory. I am grateful to Dr. P. A joy, Chair of Physical and Materials Chemistry Division, for providing the infrastructures in the division.

I am grateful to my doctoral advisory committee (DAC) members, Dr. Girish R. Desale, Dr. R. Nandini Devi and Dr. Santosh K. Jha for their valuable suggestions, comments and fruitful discussions during the DAC meetings. The suggestions and discussions have helped me to improve the quality of the work.

I would like to thank student academic office (SAO) staff, Chairman Dr. B. L. V Prasad, former Chairman Dr. Mysore Shashidhar, AcSIR Coordinator Dr. Mahesh J. Kulkarni, Mr. Purushothaman, Mr. P. V Iyer, Mrs. Purnima Khole, Ms. Komal, Mrs. Vaishali, Mrs. Poornima and Mr. Santosh, for timely processing my Ph.D. related documents.

My senior Dr. Sreekuttan M. Unni needs a special mention. He taught me the different electrochemical characterization techniques and their analysis. The suggestions and support provided by him at the beginning of my research life are remarkable.

I would like to thank Dr. Ahish K. Lele, Dr. Ulhas K. Kharul, Dr. Neelima Bulakh, Dr. Harshawardhan Pol, Mr. Vivek Borkar and Mr. Swapnil Aherrao for the valuable support in the fuel cell project-related activities.

I would like to thank Mr. Gholap, Dr. Selvaraj, Dr. Vinod, Mr. Shriniwas Deo, Mrs. Rupali, Mr. Venkitesh, Mr. Thushar, Mrs. Sheethal, and Mr. Ketan for the valuable help in the characterization of various samples and effective scientific discussions.

Thanks to Mrs. Sunita Barve and Mr. Gati K. Nayak for the effective library facilities for accessing the various journals and the support provided in the plagiarism checking.

My special gratitude to my seniors Dr. Sreekuttan M. Unni, Dr. Vishal M. Dhavale, Dr. Bihag Anothumakkool, Dr. Harshitha Barike and Dr. Palaniselvam Thangavelu for their mentoring and care during my initial days in CSIR-NCL.

My special thanks to Dr. Nandini Devi and her students Dr. Leena George and Priyanka Walko, Dr. Suresh Bhat and his student Fayis K. P, Dr. Santosh Babu and his student Ranjeesh K. C, Dr. R. Vaidhyanathan (IISER-Pune) and his students Shyamapanda Nandi and Debanjan, Dr. U. S Hareesh (CSIR-NIIST) and his students Shijina, Minju and Vaishnapriya, Dr. Sujith Ghosh (IISER-Pune) and his student Bipilab, Dr. Avinash S. Kumbhar (Savitribai Phule Pune University) and his student Sakharam for the fruitful collaboration work.

I would like to thank my former teachers in the School of Chemical Sciences, Kannur University, Dr. K. R. Haridas and Dr. S. Sudheesh for their constant encouragement during my academic and research life.

My special thanks to Siddheshwar N. Bhange, Pranav K. G, Vidyanand V, Roby Soni, Santosh K. Singh, Varchaswal Kashyap, Nadeema Ayasha, Meena Ghosh, Dr. Gourav Singla, Sachin Kumar, Narugopal Manna, Ajmal P, Dr. Raji V, Dr. Silpa N, Swati Dilwale, Geeta Kharabe, Maria Kurian, Dr. Vrushali and Dr. Debasee Das for their affection, support and joyful environment in the lab.

I would like to thank Sachin Gaikwad, Pritish, Ruhi, Harikrishnan, Dheeraj, Abdul, Mahesh, Sachin Patil and Aniket for the joyful association in the fuel cell project.

I would like to thank Ms. Reshma, Ms. Arya, Ms. Athira, Ms. Muskan, Ms. Jesna and Ms. Salva, the project interns who worked with me during their project internship in our lab.

My sincere thanks to Sanoop, Pranav, Vidyanand, Shibin, Ranjeesh, Sarath Ramdas, Taha, Sudheesh, Sreekuttan, Vijayadas, Arun Torris, Rajesh, Bipin Lal and Reji for providing enjoyable moments during my stay in Pune.

I would like to thank NCL friends Vipin, Shabeeb, Fayis, Rashid, Santosh, Abdul Khayum, Anumon, Vedikuyil, Munaveer, Ashwathi, Betsy, Prabhu, Ashwini, Kiran, Manuraj, Lavanya, Amrutha and Immanuel for their care and support.

Finally, I find no words to express my gratitude to my father Raveendran and mother Shyamala for their constant support, love and care that have helped me to achieve at this level. I'm thankful to my brother Rajeesh, sister Ambika, sister-in-law Athira and Eva for their affection and support. I thank all of my family members for their encouragement and support provided in my life.

Though, many have not been mentioned here, but their support and affection are with me.

List of Abbreviations

Abbreviation	Expansion
AEM	Anion Exchange Membrane
AEMFC	Anion Exchange Membrane Fuel Cell
ADT	Accelerated Durability Test
BET	Brunauer-Emmet-Teller
CA	Chronoamperometry
CE	Counter Electrode
CO	Carbon Monoxide
CV	Cyclic Voltammetry
EDAX	Energy Dispersive X-ray Analysis
ECSA	Electron Microscopy for Chemical Analysis
ECSA	Electrochemical Active Surface Area
GO	Graphene Oxide
GC	Glassy Carbon
HOR	Hydrogen Oxidation Reaction
HR-TEM	High Resolution Transmission Electron Microscopy
K-L	Koutecky-Levich
LSV	Linear Sweep Voltammetry
MEA	Membrane Electrode Assembly
MCFC	Molten Carbonate Fuel Cell

MOF	Metal Organic Framework
NGr	Nitrogen-doped Graphene
NPM	Non-Precious Metal
OCV	Open Circuit Voltage
OER	Oxygen Evolution Reaction
ORR	Oxygen Reduction Reaction
PAFC	Phosphoric Acid Fuel Cell
PBI	Polybenzimidazole
PEM	Polymer Electrolyte membrane
PEMFC	Polymer Electrolyte membrane Fuel Cell
RE	Reference Electrode
rGO	Reduced Graphene Oxide
RHE	Reversible Hydrogen Electrode
RDE	Rotating Disk Electrode
RRDE	Rotating Ring Disc Electrode
SAED	Selected Area Electron Diffraction
SEM	Scanning Electron Microscopy
SOFC	Solid Oxide Fuel Cell
TEM	Transmission Electron Microscopy
TMS	Transition Metal Sulfide
TMO	Transition Metal Oxide
TPB	Triple Phase Boundary

WE	Working Electrode
XRD	X-ray Diffraction
XPS	X-ray Photoelectron Spectroscopy

Table of Contents

Chapter 2

Chapter 3

Chapter 4

Chapter 5

Chapter 6

Preface

The increasing global energy crisis along with the depletion of non-renewable energy sources and their environmental impacts of global warming and greenhouse effects impose the society to explore sustainable clean energy cost-effectively. The unexpected change in the earth's climate is related to the greenhouse effect, and to tackle those serious issues, it is essential to reduce or avoid the use of fossil fuel-based energy sources. The energy production from solar, wind and tidal based renewable energy sources is projected to be increasing. However, the intermittency and geometrical dependence limit the extensive energy production from these renewable sources. Therefore, the viable conversion of chemical energy into electrical energy is receiving enormous importance for fulfilling the increasing energy demand. In this regard, the production of energy from hydrogen (H_2) can have paramount benefits in terms of efficiency and sustainability.

Looking into the hydrogen economy, the steam reforming of natural gas, coal gasification, *etc*., adopted currently for the H_2 production release CO and CO_2 and, thus, are not carbon neutral in nature. Therefore, these methods are not feasible for the green production of H_2. Hence, a sustainable and efficient method should be followed for the generation of H_2. The production of H_2 from the water gives a tremendous platform for fuel production in a viable method. The electrolysis of water produces H_2 in a carbon-neutral way and plays an important role in the sustainable production of H_2. Along with the sustainable production of H_2, the development of proper technology for converting the chemical energy of H_2 into useful energy is an important area of the research. The polymer electrolyte membrane fuel cells (PEMFCs) can convert the chemical energy stored in the fuels, mainly H_2, into the electric energy with zero-emission of greenhouse gases. Moreover, PEMFCs are highly fascinating among other varieties of fuel cells due to their high efficiency and low operating temperature for the conversion of H_2 into electrical energy. Hence, PEMFCs can be widely employed as a promising clean power technology for stationary as well as portable applications. As a result, PEMFCs have become a prime focus of the research community over the years. However, the slow kinetics of oxygen reduction reaction (ORR) at the cathode is a major bottleneck for achieving higher efficiency. To address the slow kinetics of oxygen reduction, noble metal-based catalyst like Pt/C is widely used to facilitate the ORR in PEMFCs. This would increase the cost of the system and, ultimately acts as the bottleneck for the wide commercialization of this green technology.

The water electrolysis involves hydrogen evolution reaction (HER) at the cathode and oxygen evolution reaction (OER) at the anode. Due to the involvement of the transfer of four electrons and the coupled reactions for the formation of O_2, OER is comparatively sluggish than HER. Hence, the conversion between H_2O and O_2, known as the oxygen electrochemistry, thus plays an important role in the technology for making H_2 from water. Therefore, electrocatalysts are essential to reduce the overpotential and accelerate the reactions for the production of H_2 through the water electrolysis. There are numerous materials such as RuO_2 and IrO_2 that have been explored as catalysts for aiding OER. However, the limiting factors like high cost, short durability, and insufficiency in the availability of these materials form the bottleneck for the large-scale production of a cost-effective and long-lasting OER catalyst. This ultimately affects the bulk-scale production of H_2 through the water electrolysis.

In order to tackle the problems associated with the wide commercialization of fuel cells and water electrolysers, the rational design of an efficient and durable catalyst is an urgent requirement. To develop a cost-effective and efficient catalyst for ORR and OER, extensive research has been focused on the non-noble metal-based catalysts. Recently, transition metal sulfide (TMS) derived nanocomposites have emerged as a suitable catalyst for fuel cells, solar cells, water splitting, electrochemical sensors, supercapacitors, and batteries. Excellent stability and improved activity of metal sulfide have spurred the exploration of TMS derived electrocatalysts for the fuel cells and water splitting applications. In view of this, the present dissertation is intended to developd the TMS derived nanocomposites for facilitating the reactions in PEMFCs and water electrolysers. The supported metal sulfides of Mo, Co, and Ni on various conducting substrates are synthesized through the environmentally friendly hydrothermal methods. To improve the active center density and subsequently the catalytic activity of the produced transition metal sulfides, various strategies have been adopted during the synthesis. The electrical conductivity, porosity, and morphology of the nanocomposites were tuned carefully to achieve the better catalytic activity of the prepared materials. Overall, a systematic strategy has been adopted in each case to achieve improved activity and thereby reducing the overpotential of the synthesized materials in comparison with the *state-of-the-art* catalysts. The outcome of the individual chapters are highlighted below;

Chapter 1 provides an overview of the global energy scenario and the importance of the hydrogen economy. The fundamental reactions of PEMFCs and water electrolyzers are described in this chapter. The chapter also covers the mechanism of ORR and OER. The working principle of different kinds of fuel cells and water electrolyser is discussed in detail.

The significance of electrocatalysts for improving the performance of PEMFCs and the water electrolysers is explained with appropriate literature reports. The significance of the development of cost-effective and efficient transition metal sulfide (TMS) based catalysts for facilitating ORR and OER is also covered in this chapter. The scope and objectives of the thesis are stated at the end of Chapter 1.

Chapter 2 deals with the development of layer separated dispersion of molybdenum sulfide (MoS_2) on reduced graphene oxide (rGO) mediated by cobalt hydroxide through a hydrothermal process ($Co(OH)_2$-MoS_2/rGO). The developed material is used for facilitating the ORR. $Co(OH)_2$-MoS_2/rGO displays an oxygen reduction onset potential of 0.86 V and a half-wave potential ($E_{1/2}$) of 0.74 V *vs*. RHE in 0.1 M KOH solution, which are much higher than that of the corresponding values (0.71 and 0.35 V, respectively) displayed by the as-synthesized pristine MoS_2 (P-MoS_2) under the identical experimental conditions. The Tafel slope corresponding to oxygen reduction for $Co(OH)_2$-MoS_2/rGO is estimated to be 63 mV/decade compared to 68 mV/decade displayed by the *state-of-the-art* Pt/C catalyst. The calculated number of electron transfer during oxygen reduction for $Co(OH)_2$-MoS_2/rGO is in the range of 3.2-3.4 in the potential range of 0.70 to 0.10 V, which again stands out as a valid evidence on the much favourable mode of oxygen reduction accomplished by the system compared to its pristine counterpart. Overall, the study demonstrates a viable strategy of tackling the inherent limitations, such as low electrical conductivity and limited access to the active sites, faced by the layered structures like MoS_2 to position them among the group of potential Pt-free electrocatalysts for ORR.

Chapter 3 illustrates the synthesis of an efficient and durable catalyst for electrochemical ORR which is active both in the alkaline and acidic conditions by dispersing few-layer graphitic carbon coated Co_9S_8 nanoparticles on the nitrogen-doped carbon (NVC-G) support (Co_9S_8/NVC-G). The hydrothermal route followed by heat-treatment in an inert atmosphere lead to the formation of Co_9S_8/NVC-G. The few-layer graphitic carbon formed on the surface of Co_9S_8 nanoparticles is assisting to accomplish their small size and it also prevents agglomeration of the nanoparticles. Co_9S_8/NVC-G displays nearly 70 mV overpotential compared to the *state-of-the-art* Pt/C in 0.1 M KOH solution. The half-wave potential ($E_{1/2}$) difference of the present system is nearly 75 mV with the commercial Pt/C. Co_9S_8/NVC-G displays promising ORR activity in the acidic conditions as well with nearly 140 mV overpotential compared to its Pt/C counterpart. The system shows about 170 mV lower $E_{1/2}$ value with Pt/C. The system displays good stability both in acidic and basic conditions

compared to the Pt/C system. Finally, testing of a single cell of a PEMFC was performed by employing Co_9S_8/NVC-G as the cathode catalyst and Nafion-212 as the proton exchange membrane. The system displays a maximum power density of 245 mW cm^{-2} in H_2-O_2 and 115 mW cm^{-2} in H_2-air feeding conditions.

Chapter 4 discloses the development of an efficient electrocatalyst for OER by adopting a strategy wherein layered assembly of NiO and MoO_3 could be dispersed on Vulcan carbon support to simultaneously maintain exposure of the synergistically activated sites and electrical conductivity of the matrix. The hydrothermal process played a key role in establishing the coexisting few-layer assembly of NiO and MoO_3 on Vulcan carbon, which involved conversion of preformed MoS_2 sheets to MoO_3 and concomitant growth of $Ni(OH)_2$ layer prior to its conversion to NiO during the subsequent heat treatment process (NiO@MoO_3/VC). The NiO sheets have exposed edges and they are instrumental in enhancing the OER activity of NiO@MoO_3/VC. The overpotential of NiO@MoO_3/VC for achieving the 10 mA cm^{-2} current density is 280 mV, which is an improved value over 292 mV obtained in the case of the *state-of-the-art* RuO_2 catalyst. NiO@MoO_3/VC also demonstrates outstanding stability for 15 h in 1 M KOH solution at 1.51 V *vs.* RHE. Finally, the overall water splitting was performed in 1 M KOH solution by employing NiO@MoO_3/VC as the anode catalyst and Pt/C as the cathode catalyst. The system requires a potential of 1.59 V to reach the current density of 10 mA cm^{-2}, replaces the RuO_2 from the anode of the electrolyser with the home-made catalyst.

Chapter 5 discusses the synthesis of highly efficient Co_9S_8-Ni_3S_2 based hierarchical nanoflower arrays on nickel foam (NF) through the one-pot hydrothermal method (Co_9S_8-Ni_3S_2/NF) for overall water splitting applications. The nanoflower arrays are self-supported on the NF without any binder, possessing the required porosity and structural characteristics. The obtained Co_9S_8-Ni_3S_2/NF is displaying high hydrogen evolution reaction (HER) as well as oxygen evolution reaction (OER) activities in 1 M KOH solution. The overpotentials exhibited by this system at 25 mA cm^{-2} are nearly 277 and 102 mV for HER and OER, respectively in 1 M KOH solution. Subsequently, the overall water splitting was performed in 1 M KOH solution by employing Co_9S_8-Ni_3S_2/NF as both the anode and cathode electrodes, where the system required only 1.49, 1.60 and 1.69 V to deliver the current densities of 10, 25, and 50 mA cm^{-2}, respectively. Comparison of the activity of Co_9S_8-Ni_3S_2/NF with the *state-of-the-art* Pt/C and RuO_2 coated on NF displays an enhanced performance for Co_9S_8-Ni_3S_2/NF both in the half-cell as well as in the full cell, emphasizing the significance of the present work.

Chapter 6 Summarize the important observations and outcomes of each working chapter of the thesis. A brief introduction to the importance of the hydrogen economy and the significance of electrocatalysts for sustainable energy production is incorporated. The strategy adopted for developing efficient ORR and OER catalysts is discussed. A concise discussion of the improvement achieved in the electrochemical activity of the synthesized materials is mentioned. The future scope of the thesis work and the fundamental research and advancement required for the wide commercialization of fuel cells and water electrolyser are stated in this chapter.

Chapter-1

An Overview of the Hydrogen Economy and Development of Electrocatalysts for Oxygen Reduction Reaction and Water Splitting Applications

The present chapter comprises a brief discussion on the current global energy scenario, hydrogen economy, its importance, and development of electrocatalysts for sustainable energy systems. To reduce the adverse environmental impacts of fossil fuel-based energy sources and pave the transition towards sustainability, exploring green energy resources and technologies is of significant importance. The low carbon emitting energy sources are crucial to mitigate global warming and the associated environmental challenges. In the current scenario, polymer electrolyte membrane fuel cells (PEMFCs) and water electrolysers are widely considered as the major clean energy technologies that can alleviate the challenges associated with energy, environment and sustainability. The oxygen electrochemistry plays an important role in the development of PEMFCs and water electrolysers. However, the sluggish kinetics of oxygen reduction reaction (ORR) and oxygen evolution reaction (OER) act as the major challenge and bottleneck restricting the widespread application of these devices. Therefore, the development of low-cost ORR and OER electrocatalysts is of utmost significance towards the commercialization of these sustainable clean energy systems. In view of this, a concise literature survey on the current status of the precious metal and non-precious metal-based electrocatalysts for ORR and OER is carried out. The scope and objectives of the thesis are included at the end of this chapter.

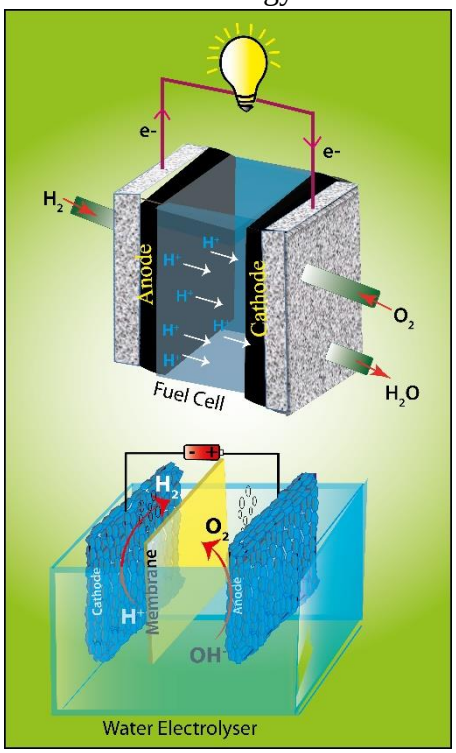

1.1 Introduction

The increasing global population and energy requirements deplete the non-renewable energy sources rapidly. Recent studies indicate that the energy requirement will be increased by 30% from the year 2020 to 2040.[1] Currently, more than 85% of the total energy production is accounted from the non-renewable energy sources like oil (33%), coal (30%), and natural gas (24%) (**Figure 1.1**). Renewable energy sources are accounted for only 2% of the global energy production. The combustion of fossil fuel-based energy sources emits CO_2, SO_2, NO_2, *etc*., into the atmosphere. This would lead to "global warming" and "greenhouse effect".[2] The global phenomenon of abrupt climate change is related to the greenhouse effect, and to tackle these serious issues, it is essential to reduce or avoid the use of fossil fuel-based energy sources.[3] Therefore, the carbon emission-free power sources are receiving worldwide attention due to their eco-friendly and environmental benignity.[4] The energy production from solar, wind and tidal based renewable energy sources is projected to be increasing. However, the intermittency and geometrical dependence limit the extensive energy production from these renewable sources. Therefore, the viable conversion of chemical energy into electrical energy is receiving huge importance for fulfilling the increasing energy demand.[5] In this regard, the production of energy from hydrogen (H_2) can have paramount benefits in terms of efficiency and sustainability.[6] Compared to the fossil fuel-based energy sources, H_2 is having high specific energy (142 MJ/kg). It is vital for employment as an alternate fuel since it can massively contribute towards carbon-neutrality.[7] The 'Hydrogen Economy' is vital in this circumstance because the sustainable H_2 generation and its employment for energy production require substantial attention and advancement in terms of science and technology.[8]

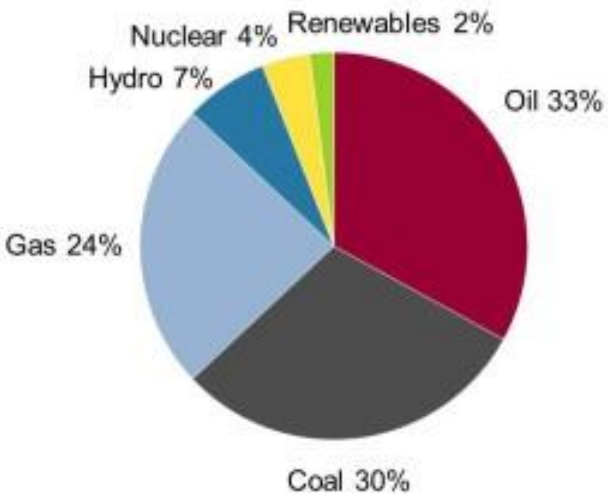

Figure 1.1. *Global energy production by various energy sources.* (*Courtesy: https://hms-ag.com/energy-coal-market-2/primary-energy-coal/).*

1.2 Hydrogen Economy

Hydrogen economy deals with the use of H_2 as a fuel with low carbon emission, mainly in the transportation and stationary applications.[9] At present, around 70 million tonnes of H_2 per year in its pure form is required for various applications. Currently, the major part (98%) of the H_2 is produced from the steam reforming of natural gases. The process is highly energy-intensive and carried out at nearly 1000 °C and 10-40 bar pressure. The process entails almost 2% of the total global energy requirement. Besides, CO_2 generated during the steam reforming process is contributing to the greenhouse effect to a greater extent and emits about 830 million tonnes of CO_2 per year in the atmosphere. Further, the process entirely depends on the fossil fuel for the production of H_2 and overshadows the benefits attainable from the clean nature of H_2. Therefore, these methods are not feasible for the green production of H_2. Hence, sustainable and cost-effective methods should be adopted for the H_2 generation. The electrolysis of water is a perfect method for the production of H_2[10]. The water electrolysis produces H_2 in a carbon-neutral way and plays an essential role in the sustainable production of H_2.[11] For the production of 1 kg of H_2 through water electrolysis, 9 litre of water is required. This would also generate 8 kg of O_2, and the process is free from greenhouse gas emission.[12] However, only 2% of the global H_2 is currently produced from water electrolysis. The production cost per kilogram of H_2 through the steam reforming process is 2-3 $, and through water electrolysis, is 10-23 $.[13] The high production cost, along with the lack of highly efficient catalysts, limits the large-scale production of H_2 through water electrolysis.[14] Hence, the cost-effective production of H_2 through water electrolysis is highly desirable.

Along with the sustainable production of H_2, the development of suitable technology for converting the chemical energy of H_2 into useful energy is an essential area of research. PEMFCs are most important in this direction because of the efficient conversion of chemical energy into electrical energy.[15] PEMFCs convert the chemical energy stored in the fuels, mainly H_2, into the electric energy with zero-emission of greenhouse gases.[16] The plot of energy density against the power density of different energy storage and conversion devices is called the Ragone plot and is shown in **Figure 1.2**. The Ragone plot indicates that the PEMFCs possess high energy density compared to other energy devices like capacitors, batteries, and supercapacitors. The high energy density of an electrochemical device is very important to provide the power output for a longer duration. Hence, PEMFCs can be widely employed as a promising clean power technology for stationary as well as portable applications.[17] As a result,

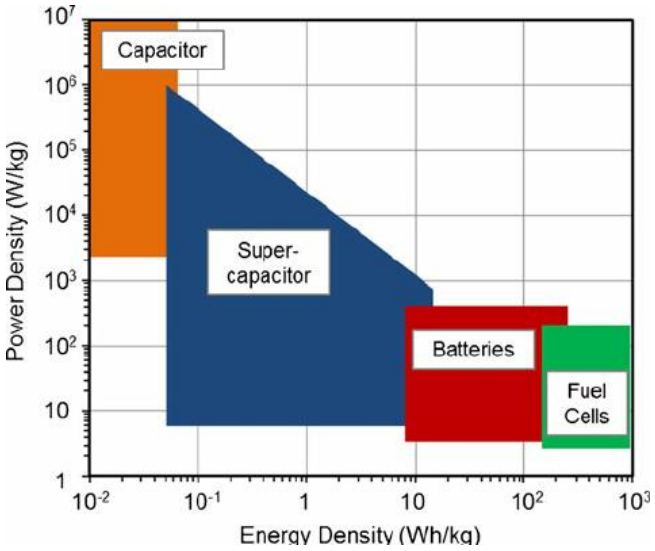

Figure 1.2. *Ragone plot of the different energy storage and conversion devices, indicating the energy density against power density.*[18] *(Reprinted with permission from* ***Springer Nature; License Number: 4765350455824****).*

PEMFCs have become a prime focus of the research community over the years. However, the slow kinetics of oxygen reduction reaction (ORR) at the cathode of a PEMFCs is a major bottleneck for achieving higher efficiency.[19-21] In order to address this intricacy, noble metal-based catalyst like Pt/C is widely used to facilitate the ORR in PEMFCs. Due to this, about 50% of the PEMFCs cost is arising from the catalyst part.[22] Apart from the high cost, the scarcity, poor durability and low methanol tolerance of Pt restricts its extensive application.[23-24] This would ultimately hinder the broad commercialization of this highly efficient green technology, which should be addressed in the ongoing research activities.

On the other hand, the water electrolysis involves the hydrogen evolution reaction (HER) at the cathode and the oxygen evolution reaction (OER) at the anode. Due to the involvement of four electrons and the coupled reactions for the formation of O_2, OER is comparatively sluggish than HER.[25] [26] Hence, the conversion between H_2O and O_2, which is known as the oxygen electrochemistry plays a vital role in the technology for making H_2 from water. This demands the development of efficient electrocatalysts with low overpotentials to accelerate the production of H_2 by water electrolysis. The precious-metal-based catalysts like IrO_2/RuO_2 are employed at the anode for facilitating the OER during water electrolysis.[27-28] However, the scarcity in the availability, high cost and poor durability of Ir and Ru based OER catalysts limit their application.[29] This eventually affects the large-scale production of H_2 through the water electrolysis.

To tackle the problems associated with the commercialization of PEMFCs and water electrolyser, the rational design of an efficient and durable catalyst is an urgent requirement.[30] To develop a cost-effective and efficient catalyst for ORR and OER, extensive research works have been focused on various nanomaterials. Several nanomaterial-based catalysts have been developed for aiding the ORR and OER. The alloys of precious metals, non-precious metal-based nanomaterials, and metal-free electrocatalysts are various classes of catalysts employed.[28, 31-32] Considering the activity, cost and stability, developing the non-precious metal-based catalysts for ORR and OER is receiving significant attention. The non-precious metal-based catalysts include metal oxides, nitrides, sulfides, phosphides *etc*., supported on conducting substrates.[33-35] The poor stability of several non-precious metal-based catalysts in both acidic and alkaline conditions restricts their practical implementation in PEMFCs and water electrolysers.[36-37] In this regard, transition metal sulfide (TMS) derived nanocomposites have emerged as a suitable catalyst for PEMFCs, solar cells, water splitting, electrochemical sensors, supercapacitors, and batteries.[38-41] Excellent stability and fascinating activity of metal sulfide have spurred the exploration of TMS derived nanomaterials for the PEMFCs and water splitting applications.[42-44] The metal sulfides possess high electrical conductivity due to the narrow bandgap present in the material. This would improve electrochemical performance by maintaining the proper electronic conductivity in the system. Therefore, the development of metal sulfide derived ORR catalysts is crucial for replacing the Pt-based cathode in the PEMFCs.[45] Similarly, the metal sulfide derived catalysts are important in water electrolyser application to improve the activity and avoid the use of precious metal-based catalysts like RuO_2/IrO_2 in the anode.[10]

In view of the above discussions, the present dissertation deals with the development of TMS derived nanocomposites for facilitating the reactions in PEMFCs and water electrolyser applications. The supported metal sulfides of Mo, Co, and Ni on various conducting substrates are developed by facile synthesis methods. To improve the active centre density and subsequently the catalytic activity of the produced TMS-based catalysts, various strategies have been adopted during the synthesis. The electrical conductivity, porosity, and morphology of the nanocomposites were tuned carefully to achieve the better catalytic activity of the prepared materials. Overall, a systematic strategy has been carried out to achieve improved activity and thereby reducing the overpotential of the synthesized materials in comparison with the *state-of-the-art* catalysts. The enhancement achieved in the catalytic activity is correlated with the structural modifications of the developed catalysts.

Fuel Cells and Water Electrolyser

As discussed above, PEMFCs and water electrolyser can alleviate the energy challenges and environmental problems in the context of current global scenario. For this, the extensive attention and advancement in electrocatalyst development is a vital factor. Since the material developed as part of this dissertation is applicable for the PEMFCs and water electrolysers, a brief discussion on the classification and fundamental characteristics of these technologies is included in the following section. The discussion starts with fuel cells followed by the water electrolysers.

1.3 Fuel Cells

Fuel cells are electrochemical energy conversion devices in which chemical energy stored in the fuel is converted into electrical energy without any combustion of the fuels. The fuel cell is comprised of two electrodes separated with an electrolyte. At the anode, the oxidation of fuel produces protons and electrons. The electrons will travel towards the cathode through an external circuit. At the cathode, the reduction of oxidant takes place. The typical fuels are H_2 or small molecules like methanol, ethanol, formic acid *etc*., and the oxidant is air or O_2. Depending upon the electrolyte employed to separate the electrodes, fuel cells are classified into different types. The operating conditions of the fuel cells largely depend on the nature of

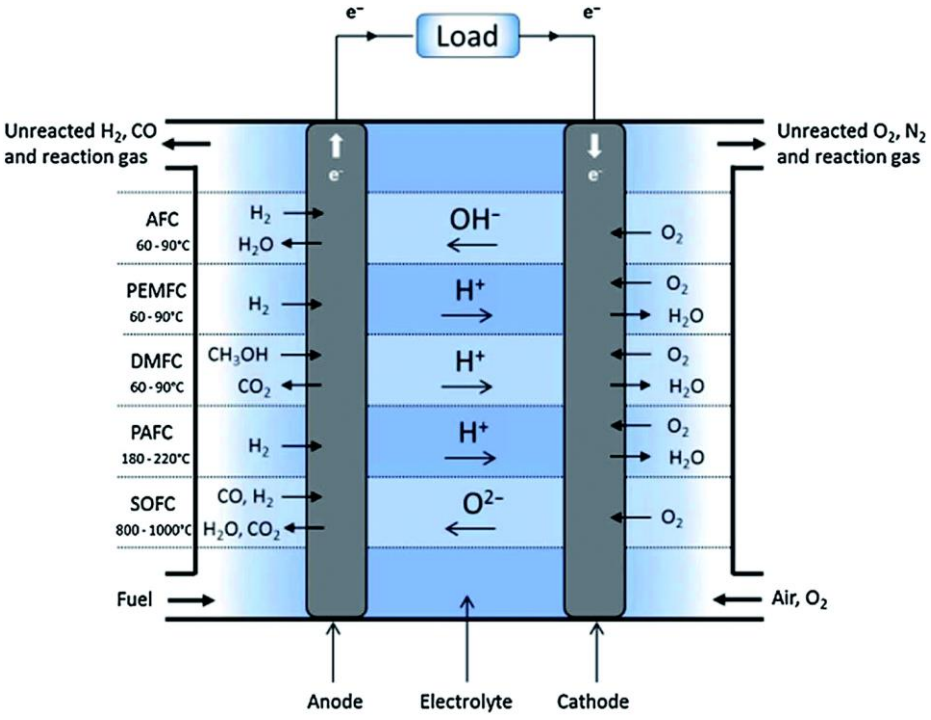

Figure 1.3. *Schematic overview of the different types of fuel cells.*[46] *(Reprinted with permission from* ***Elsevier; License Number: 4774150459782****).*

the separator employed. **Figure 1.3** illustrates the types of fuel cells, and the following section discusses the different types of fuel cells;

1.3.1 Phosphoric Acid Fuel Cell (PAFC)

In PAFCs, the liquid phosphoric acid is used as the electrolyte to transfer the protons from anode to cathode. The phosphoric acid is saturated within silicon carbide. The operating temperature of PAFC is 150-200 °C, and Pt-based catalyst is being employed on the electrodes for facilitating the reactions. The excess heat energy generated during the cell operation can further utilized through the co-generation method. The use of liquid electrolyte can corrode the device components. Besides, the evaporation of the acid may also take place and affect the performance during the course of operation and storage. The electrode reactions taking place in a PAFC are given below:

Anode: $2H_2 \longrightarrow 4H^+ + 4e^-$

Cathode: $O_2 + 4H^+ + 4e^- \longrightarrow 2H_2O$

Overall cell reaction: $2H_2 + O_2 \longrightarrow 2H_2O$

Generally, PAFCs are used for stationary applications.

1.3.2 Solid Oxide Fuel Cell (SOFC)

In SOFCs, solid oxide ceramic membrane (yttria-stabilized zirconia, YSZ) is used to transport the ions. In principle, the oxide ion (O_2^-) produced on the cathode after the reduction of oxygen is transported towards the anode through the ceramic membrane. At the anode, O_2^- ions reacts with protons to form water. The operating temperature of SOFC is much higher (800-1000 °C). Due to this, SOFCs are not suitable for mobile applications. The reactions in a SOFC are illustrated as below:

Anode: $2H_2 + 2O_2^- \longrightarrow 2H_2O + 4e^-$

Cathode: $O_2 + 4e^- \longrightarrow 2O^{2-}$

Overall cell reaction: $2H_2 + O_2 \longrightarrow 2H_2O$

The efficiency of SOFCs can be improved by utilizing the waste heat from the system.

1.3.3 Molten Carbonate Fuel Cell (MCFC)

In MCFC, the molten carbonate salt is used as the electrolyte to conduct the carbonate ions (CO_3^{2-}). Similar to SOFC, the operating temperature of MCFC is also higher and is above 600 °C. In MCFC, the use of a reformer is not required on the anode for producing the H_2. At

elevated temperature, H_2 is produced from the hydrocarbons at the anode. The as-produced H_2 is reacted with the carbonate ions from the electrolyte and produces water, CO_2 and electrons. At the cathode, oxygen reacts with CO_2 from the anode and the electrons coming through the external circuit would lead to the formation of carbonate ions. This would replenish the electrolyte and balance the cell reaction. The reactions in an MCFC are given below:

Anode: $CO_3^{2-} + H_2 \longrightarrow H_2O + CO_2 + 2e^-$

Cathode: $CO_2 + ½\ O_2 + 2e^- \longrightarrow CO_3^{2-}$

Overall cell reaction: $H_2 + ½\ O_2 \longrightarrow H_2O$

Due to the high operating temperature, the MCFC is having a high start-up time. This restricts their use in mobile applications and is suitable mostly in the stationary requirements. The cell life of MCFC is affecting the carbonate electrolyte, which corrodes the anode and cathode.

1.3.4 Polymer Electrolyte Membrane Fuel Cells

In polymer electrolyte membrane fuel cells, the anode and cathode are separated with a solid polymer electrolyte membrane and is capable of transporting only the ions and not the electrons. According to the type of membrane used, the polymer electrolyte membrane fuel cells can be classified into proton exchange membrane fuel cells (PEMFCs) and anion exchange membrane fuel cells (AEMFCs). In PEMFCs, the membrane conducts protons and in AEMFCs, hydroxyl ions transport occurs through the membrane. The H_2 or liquid fuels like methanol, ethanol *etc*., can be used as fuel. Due to the advancement in the proton exchange membranes (PEM), the PEMFCs are getting wide attention compared to AEMFCs. The membranes like Nafion and acid doped polybenzimidazole (PBI) are well-known PEM and possessing the conductivity in the order of 10^{-1} S cm^{-1} or above and are currently employed in the fuel cell systems. The Nafion membrane-based PEMFCs are operated at a relatively lower temperature (< 100 °C) with proper humidification in the system. The PBI membrane-based PEMFCs are usually operated above 150 °C, and the system does not require any humidification during the operation. The primary components of a polymer electrolyte membrane fuel cell are electrodes, membrane, current collector, gaskets, sub-gaskets, and bipolar plates. The performance of the polymer electrolyte membrane fuel cells largely depends on the efficiency of the cathode catalyst. The membrane electrode assembly (MEA) is known as the heart of the fuel cell since the efficiency of the fuel cell is majorly determined by the reaction kinetics at the electrodes and the ionic conductivity of the membrane. The major cost

of the fuel cell is arising from the cathode (**Figure 1.4**), where Pt-based catalyst is employed to facilitate ORR.[47]

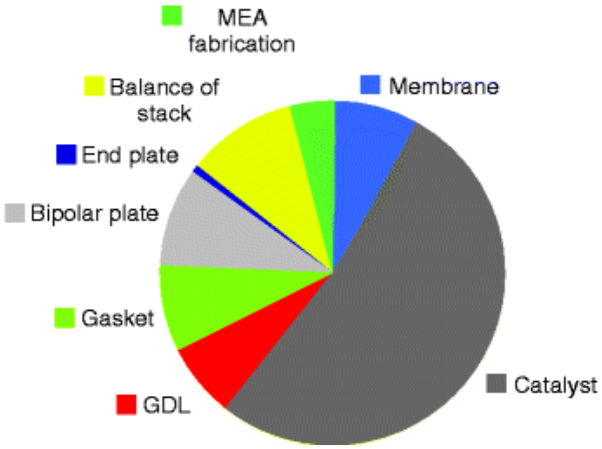

***Figure 1.4**. Pie-chart representing the cost analysis of the PEMFC stack.[48] (Reprinted with the permission from **Springer Nature; License Number: 4800321357896)**.*

1.3.4a Principle of PEMFCs

The PEMFCs consist of two electrodes, namely anode and cathode separated with a proton exchange membrane. Fuel oxidation occurs at the anode and produces protons and electrons. The protons move towards the cathode through the membrane. The electrons travel through the external circuit as electricity and enter into the cathode. In the cathode, reduction of oxygen occurs by combining with the incoming protons from the anode and electrons from the external circuit and finally produces water as the by-product. Graphite/metal plate with flow-field

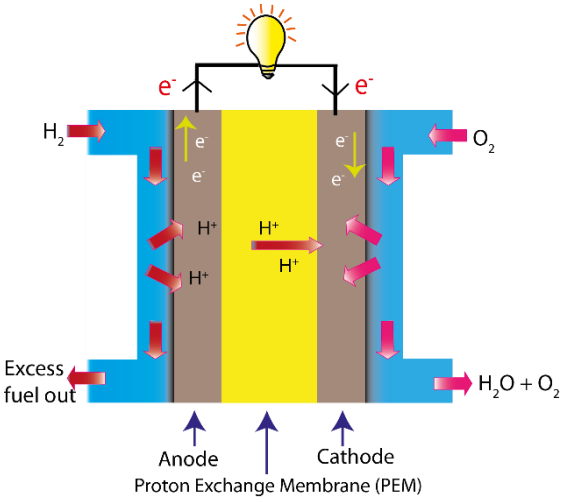

***Figure 1.5.** Schematic illustration of the working principle of proton exchange membrane fuel cell (PEMFC).*

patterns are used to supply the reactant gases to the respective electrodes through the diffusion layer. The unreacted gases and the water by-products are removed through the outlets. **Figure 1.5** represents the working principle of PEMFC.

The electrode reactions in PEMFCs are represented as below [49]:

Anode: $2H_2 \longrightarrow 4H^+ + 4e^-$ $E° = 0.0$ V

Cathode: $O_2 + 4H^+ + 4e^- \longrightarrow 2H_2O$ $E° = 1.23$ V

Overall cell reaction: $2H_2 + O_2 \longrightarrow 2H_2O$ $E° = 1.23$ V

1.3.4b Principle of AEMFCs

In AEMFC, the electrodes are separated with an anion exchange membrane (AEM). At the cathode, hydroxide ions are formed during the reduction of O_2. The OH^- ions are transported towards the anode through the AEM. At the anode, the OH- ions combine with H^+ ions to form water, the by-product of the reaction. The electrons produced during the oxidation of H_2 at the anode travel through the external circuit and reaches the cathode and participate in the ORR process. The working principle of AEMFC is presented in **Figure 1.6**.

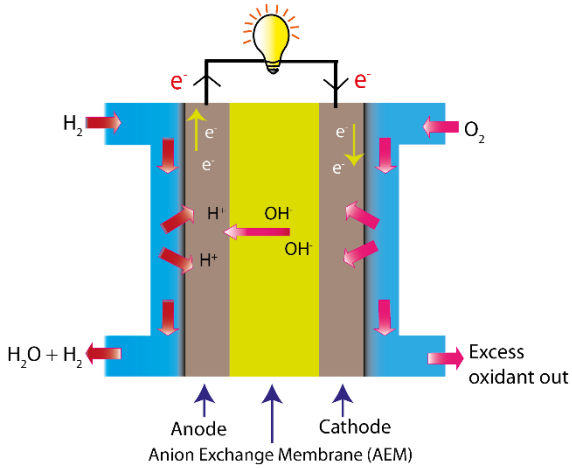

Figure 1.6. *Schematic illustration of the working principle of anion exchange membrane fuel cell (AEMFC).*

The electrode reactions in AEMFCs are represented as below [50]:

Anode: $2H_2 + 4OH^- \longrightarrow 4H_2O + 4e^-$ $E° = -0.83$ V

Cathode: $O_2 + 2H_2O + 4e^- \longrightarrow 4OH^-$ $E° = 0.40$ V

Overall cell reaction: $2H_2 + O_2 \longrightarrow 2H_2O$ $E° = 1.23$ V

The ORR kinetics is much faster in alkaline medium and, AEMFC provides the feasibility of using noble metal-free catalysts for delivering higher efficiency. However, the ionic conductivity and stability of the available AEM do not meet the commercial target. Therefore, the development of AEMFC is in the infancy stage compared to the already matured PEMFC technology.

1.3.5 Current-Potential Characteristics of the Fuel Cells

The theoretical open-circuit voltage (OCV) of polymer electrolyte membrane fuel cell is 1.23 V. However, due to the overpotential associated with the electrode reactions, the practical OCV is less than 1.23 V. The loss in the voltage would affect the efficiency of the fuel cells. The electrical efficiency (ε) of the fuel cell depends on the Gibbs free energy change (ΔG) and enthalpy change (ΔH) according to the following relation:

$$\varepsilon = \frac{\Delta G}{\Delta H} = \frac{-2FE^{\circ}}{\Delta H}$$

where, F is the Faradays constant, and E° is the standard cell potential. The theoretical efficiency of a fuel cell is ~83%; however, the practical efficiency is limited between 40-60%.[49] The reduction in efficiency is attributed to the voltage losses occurring during the cell operation. This is due to the overpotential associated with the reactions, contact resistance present in the cell, membrane resistance, *etc*. In fuel cells, the voltage drop occurs with the current dragging from the cell. This is due to the three different types of polarizations occurring

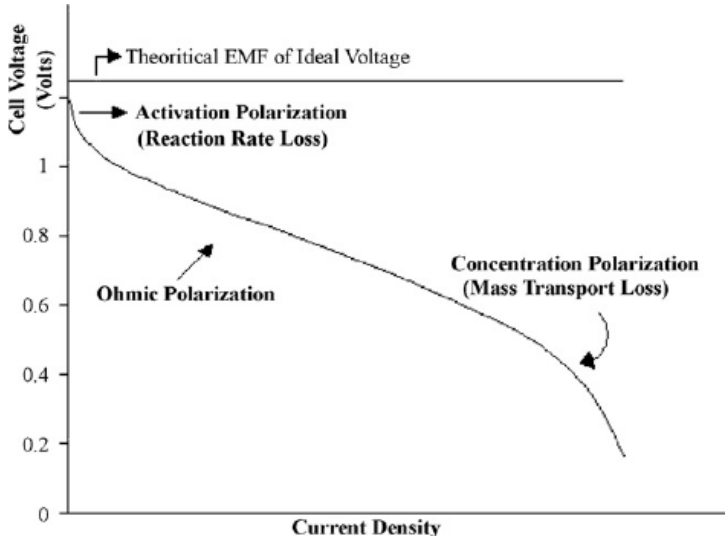

Figure 1.7. *A typical current-voltage response of a fuel cell.*[51] *(Reprinted with permission from* ***Elsevier; License Number: 4798231395076****).*

in the MEA named activation, ohmic, and mass-transport polarizations (**Figure 1.7**). The activation polarization is originating from the electrocatalysts, and the overpotential associated with the reactions greatly determines the voltage loss. The ORR kinetics is sluggish compared to HOR. Because of this, the activation polarization is mainly contributed from the cathode side, where the ORR is taking place. The reason for the ohmic loss is attributed to the occurrence of various types of internal resistance contributions in the cell. This includes the resistance arising from the membrane, which is used to separate the electrodes, contact issues with the components of the cell, resistance within the electrode due to the presence of electronically insulating components such as binder and other additives. The third polarization loss is due to the mass transport limitations on the active centers. This is mainly arising because of the limited transport of the fuel and oxidant on the catalyst surface than the required rate. The main reason behind these are the presence of excess binders that can block the active centers and reduce the diffusion of the gases reactant to the active sites. Also, the produced water present on the surface of the catalyst can reduce the oxygen diffusion towards the active centers. To improve the accessible catalytic centers of the reactant gases in fuel cells, tuning the 'triple-phase-boundary' (TPB) is important. TPB is formed by the combination of catalyst, ionomer, and reactant gases. **Figure. 1.8** illustrates the schematic representation of TPB. For

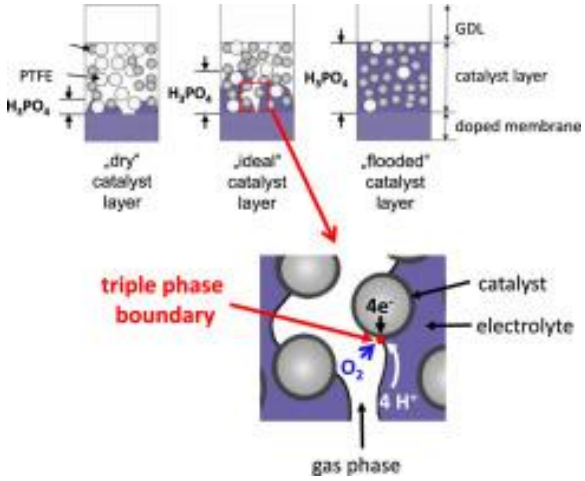

Figure 1.8. *Schematic representation of the triple-phase-boundary (TPB) in a fuel cell.*[52] *(Reprinted with permission from* ***Elsevier; License Number: 4798331336237****).*

achieving a batter fuel cell performance, the effective formation of TPB is a crucial requirement. Because, the transport of electrons through the catalyst, ionic transport through the ionomer, and transport of reactant gases are necessary to complete the reactions at the respective electrodes. Usually, the catalyst ink is prepared by dispersing the catalysts and ionomer in a particular solvent (example isopropyl alcohol) with the desired ratio. This would

achieve a proper contact of ionomer with the catalyst and further effective formation of TPB. The catalyst-ionomer ink is applied on a gas diffusion layer (GDL) using either conventional brush coating, spray coating, bar coating, or screen-printing methods. These methods can help in achieving the gas diffusion electrode (GDE) with a specific loading of the catalyst.

1.3.6 Polymer Electrolyte Membrane

The perfluoro-sulfonic acid (PFSA) polymer membranes known as Nafion® is usually employed as the polymeric separator in low-temperature PEMFCs. **Figure 1.9** represents the chemical structure of Nafion®. The proton transfer would occur in the membrane through either

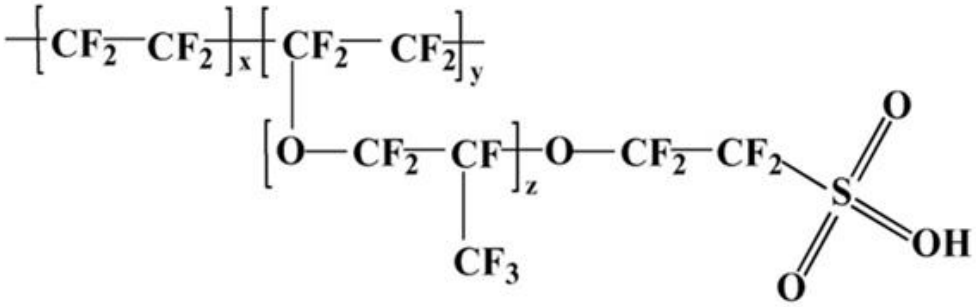

Figure 1.9. *Representation of the chemical structure of the Nafion membrane (Courtesy: Wikipedia.com).*

the 'Grotthuss mechanism' or 'Vehicle mechanism'. **Figure 1.10** represents the schematic of the Grotthuss and vehicle mechanism. The Grotthuss mechanism involves the transfer of the proton between the hydronium ions through hydrogen bonding. However, the vehicle mechanism involves the complete migration of the hydronium ions. Therefore, ionic

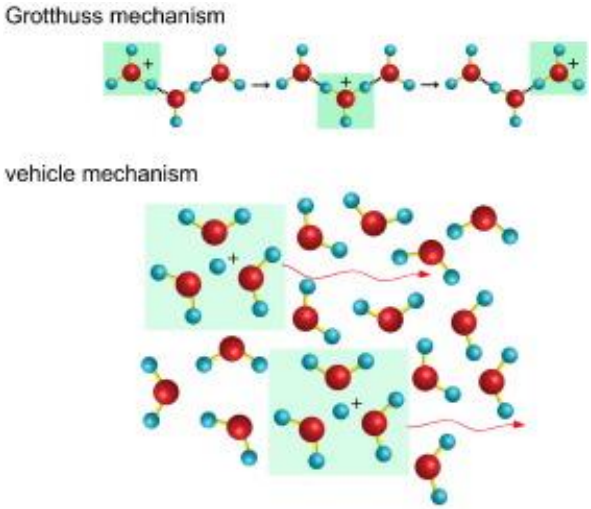

Figure 1.10. *Schematic representation of the proton conduction mechanism.*[53] *(Reprinted with permission from* ***Elsevier; License Number: 4800930529097****).*

conductivity through the vehicle type mechanism is slow compared to the Grotthuss type mechanism. For obtaining higher ionic conductivity, the Grotthuss mechanism is preferred in membranes. For the transport of protons, the Nafion® membrane requires humidification. Because of this, the operating temperature of Nafion® membrane-based fuel cell is below 100 °C.

1.3.7 Importance of Polymer Electrolyte Membrane Fuel Cells

The PEMFCs are characterised by their high thermodynamic efficiency compared to internal combustion engines (ICEs). Due to the absence of movable parts, the operation of PEMFCs is noise-free and is much reliable than conventional ICEs. The energy density of PEMFCs is much higher than many other power systems and the emission of greenhouse gases is absent. The by-product formed during the working of PEMFCs is only water. Hence, PEMFCs are green technologies with incredible applications in stationary and portable applications. However, the sluggish oxygen reduction reaction (ORR) on the PEMFC cathode restricts the wide exploration. Hence, the development of a highly efficient catalyst for facilitating ORR is crucial for the development of PEMFCs. The platinum supported carbon (Pt/C) is being employed on the cathode of PEMFCs for assisting ORR. However, the limiting factors like high cost, low availability, and poor stability associated with Pt/C restrict the wide commercialization of PEMFCs cost-effectively.[54] Hence, developing ORR catalysts with low-cost material with performance comparable to that of Pt is a challenging task. The use of facile synthesis strategies would enhance the significance of the developed catalyst.

1.3.8 Electrocatalysts for Polymer Electrolyte Membrane Fuel Cells

In order to facilitate the reactions in fuel cells, electrocatalysts are indeed essential. The HOR on the anode of the fuel cell is facile compared to the cathodic ORR. Breaking of the O=O bond requires higher energy (498 kJ/mol) compared to break the single bond in H_2 (432 kJ/mol).[49] ORR involves the O_2 bond breaking coupled with the transfer of four protons and electrons. This insight the reason for the kinetically sluggish nature of ORR.

1.3.8a Oxygen Reduction Reaction (ORR)

ORR is an important reaction in energy conversion devices like fuel cells and metal-air batteries. ORR is the cathodic process in PEMFC/AEMFC and, majorly affects and controls the efficiency of the system. Hence, the fuel cell efficiency is mainly depending on the catalytic activity of the ORR catalysts. The development of efficient catalysts for facilitating the ORR is important in the wide commercialization of fuel cells and to produce sustainable energy. The

Pt-based catalyst like Pt/C is the best material for aiding ORR. Looking in to the mechanism of ORR, it proceeds through two different pathways; i) four-electron pathway, which produces H_2O during the reduction of O_2 and, ii) the two-electron pathway produces H_2O_2 from O_2.[3] The four-electron transfer pathway is preferred for fuel cells because the H_2O_2 produced during the two-electron pathway oxidizes the membrane and the carbon support during the fuel cell operation. This would ultimately reduce the performance and efficiency of the fuel cell. The two pathways of ORR in the acidic and alkaline medium can be represented as below:

Acidic media:

Four-electron pathway

$$O_2 + 4H^+ + 4e^- \longrightarrow 2H_2O \quad (E° = 1.23\ V) \quad (1)$$

Two-electron pathway

$$O_2 + 2H^+ + 2e^- \longrightarrow H_2O_2 \quad (E° = 0.695\ V) \quad (2)$$

$$H_2O_2 + 2H^+ + 2e^- \longrightarrow 2H_2O \quad (E° = 1.76\ V) \quad (3)$$

The alternate decomposition of the H_2O_2 produced in (2) leads to the formation of H_2O and O_2 as follows:

$$2H_2O_2 \longrightarrow 2H_2O + O_2 \quad (4)$$

Alkaline media:

Four-electron pathway

$$O_2 + 2H_2O + 4e^- \longrightarrow 4OH^- \quad (E° = 0.401\ V) \quad (5)$$

Two-electron pathway

$$O_2 + H_2O + 2e^- \longrightarrow HO_2^- + OH^- \quad (E° = -0.065\ V) \quad (6)$$

$$HO_2^- + H_2O + 2e^- \longrightarrow 3OH^- \quad (E° = 0.867\ V) \quad (7)$$

The alternate decomposition of the HO_2^- produced in (6) leads to the formation of OH^- and O_2 as follows:

$$2HO_2^- \longrightarrow 2OH^- + O_2 \quad (8)$$

The ORR on Pt usually proceeds *via* a $4e^-$ process due to the presence of increased d-band vacancy in Pt, which increases the metal-O_2 interaction and subsequently weakens the bond in O_2. Also, the interatomic distance in Pt is favourable for the adsorption of O_2.[32]

1.3.8b Mechanism of ORR

The four-electron and two-electron process usually proceed through either associative or

dissociative mechanism. In the "associative mechanism", molecular O_2 is adsorbed on the active centre and direct transfer of proton/electron occurs leading to the formation of OOH, which further breaks into O and OH. In the "dissociative mechanism", splitting of the O-O bond in O_2 occurs before the transfer of proton/electron followed by the formation of OH and then finally H_2O. The mechanism on the Pt surface can be represented as follows:

1.3.8b (i) Associative mechanism

$$Pt + O_2 \longrightarrow Pt\text{-}O_{2\,ads} \quad (9)$$

$$Pt\text{-}O_{2\,ads} + H^+ + e^- \longrightarrow Pt\text{-}O_2H_{\,ads} \quad (10)$$

$$Pt\text{-}O_2H_{ads} + H^+ + e \longrightarrow H_2O + Pt\text{-}O_{\,ads} \quad (11)$$

$$Pt\text{-}O_{\,ads} + H^+ + e^- \longrightarrow Pt\text{-}OH_{\,ads} \quad (12)$$

$$Pt\text{-}OH_{\,ads} + H^+ + e^- \longrightarrow Pt + H_2O \quad (13)$$

1.3.8b (ii) Dissociative mechanism

$$Pt + {}_{1/2}O_2 \longrightarrow Pt\text{-}O_{\,ads} \quad (14)$$

$$Pt\text{-}O_{\,ads} + H^+ + e^- \longrightarrow Pt\text{-}OH_{\,ads} \quad (15)$$

$$Pt\text{-}OH_{\,ads} + H^+ + e^- \longrightarrow Pt + H_2O \quad (16)$$

Due to the complexity associated in ORR, the exact mechanism is not completely understood till now.

The Volcano plot reflects the Sabatier's principle and explains the electronic structure and intrinsic surface adsorption energies of a catalyst with its catalytic performance. Sabatier's principle says that the reaction intermediates neither bind too strongly nor too weekly to the catalyst surface. Accordingly, the oxygen adsorption strength should not be too strong with the substrate, and it should not be too weak also.[55] Because, the strong interaction of the oxygen with the catalyst substrate creates difficulty in leaving the intermediates from the surface. This would block the catalyst surface from the approach of the reactants and further its conversion into the product. A weak interaction of the reactants with the substrates leads to the slow kinetics in the conversion of the reactant into the product. Therefore, to obtain faster kinetics, the reactants should interact with the substrate moderately, and the formed products should leave from the substrate surface without any difficulty. Hence, from **Figure 1.11**, it can be clear that the adsorption energy of oxygen with the Pt surface is having intermediate energy, and it

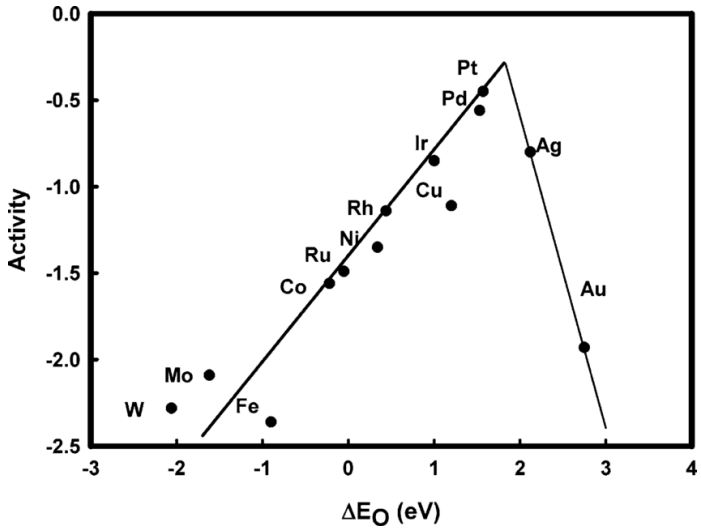

***Figure 1.11**. Volcano plot indicating the oxygen reduction activity as a function of oxygen binding energy.[55] (Reprinted with permission, Copyright © 2004, **American Chemical Society**).*

would favour the faster reduction on the surface of Pt. Therefore, Pt supported on carbon (Pt/C) is widely employed to facilitate ORR. However, the dissolution, poisoning, and coalescence of Pt nanoparticle in Pt/C would reduce the surface area and electrocatalytic activity during the long-term operation and further decrease the efficiency of the fuel cell.[47] To address the issues about stability and cost-effectiveness of Pt/C, numerous Pt-based alloy catalysts with controlled architecture have been investigated for the ORR application. This includes the alloys of Pt with Ni, Co, Fe, Cu *etc*., with different stoichiometric ratios. The alloys of Pt with low-cost transition metals would improve the catalytic activity and reduce the Pt loading. This would reduce the overall cost of the catalyst. Apart from the Pt-based catalysts, several Pt-free catalysts are also developed for aiding the ORR. Therefore, the research has been enduring to produce several catalysts with favourable conditions for the conversion of O_2 into H_2O. The following section gives a brief discussion on the development of ORR catalysts.

1.3.9 Precious-metal based ORR catalyst:

a) Pt-alloy with transition metals

Various Pt alloys have been developed with low-cost transition metals to improve the ORR activity and further address the issues of Pt-based catalysts. The electronic structure of the Pt is altering with suitable transition metal (TM) by lowering the d-band center of Pt, and this affects the adsorption of O_2.[56] Also, the shortening of Pt-Pt interatomic distance due to the presence of TM in the alloy favours the adsorption of O_2 and subsequently facilitates the

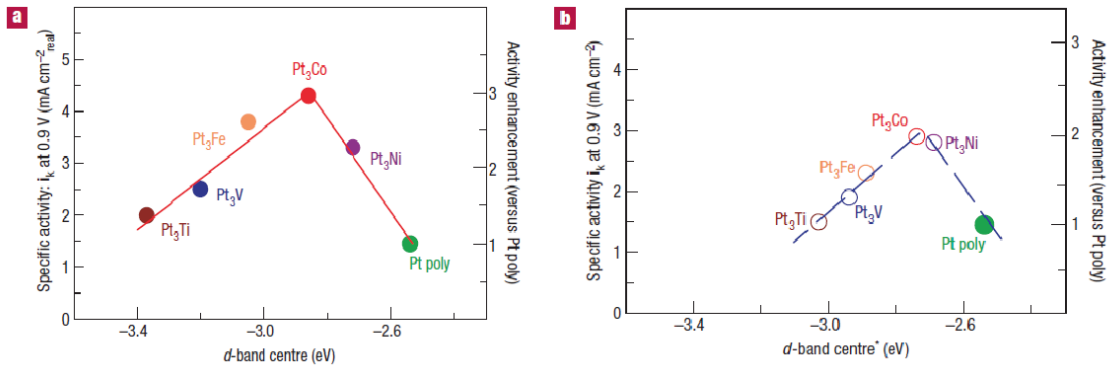

***Figure 1.12**. Relationship between the d-band center and experimentally measured specific activity of various Pt alloy catalysts in 0.1 M $HClO_4$ solution at 333K: (a) Pt-skin and (b) Pt-skeleton surface.[57] (Reprinted with permission from **Springer Nature; License Number: 4803991389940)**.*

ORR.[32] Stamenkovic *et al*. studied the specific activity of various Pt_3M (M= Fe, Co, Ni, V and Ti) alloys with the d-band center.[57] According to the study, the ORR activity on Pt, Pt skeleton, and Pt skin surfaces following the order Pt < Pt skeleton < Pt skin. Among the studied alloys by Stamenkovic *et al*., the Pt_3Co skin morphology is exhibiting the improved activity and is about 2-3 times higher than of Pt (**Figure 1.12a-b**). The study indicates that for obtaining a better ORR catalyst, the adsorption energies of the intermediates species on the Pt surface should counterbalance the surface coverage of the blocking oxygenated species. The dependence of ORR activity on the morphology of Pt alloy is studied by Chen *et al*.[58] The

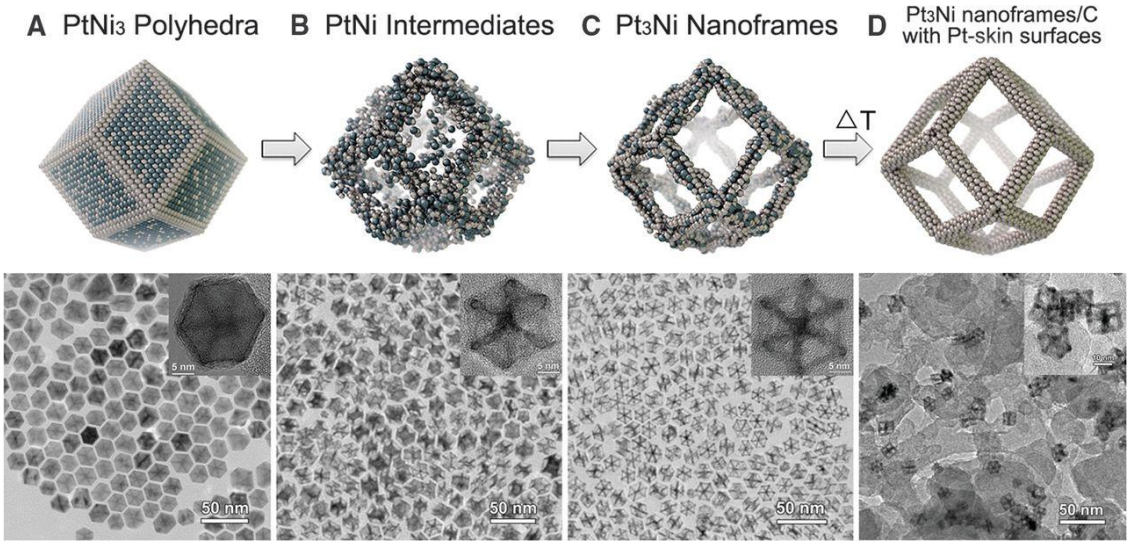

***Figure 1.13**. Schematic representation of the structural evolution of Pt_3Ni nanoframes from $PtNi_3$ polyhedra along with the corresponding TEM images.[58] Reprinted with permission from **The American Association for the Advancement of Science; License Number: 4804070610055)**.*

Pt_3Ni nanoframes is produced from the interior leaching of $PtNi_3$ polyhedra by dispersing in the non-polar solvents like hexane and chloroform at ambient conditions. The three-dimensional morphology of Pt_3Ni with the interior cavity provides easy access for O_2 on the Pt surface and enhances the ORR activity (**Figure 1.13**). The Pt(111)- skin layer structure in Pt_3Ni enables nearly 22-fold improvement in the specific activity and a 36-fold improvement in the mass activity than Pt/C. Even though the material is exhibiting higher activity in the half cell study, the performance in a real system is missing. Also, the bulk scale production of the material with uniform morphology and maintaining the activity is a challenge.

b) Core-shell morphology with transition metals

The leaching of TM from Pt alloy during the operation in the acidic conditions is the major problem of the ORR catalysts. To tackle this issue, covering the TM with a thin coating of Pt and achieving the core-shell structure is attractive. In the core-shell model, the low-cost TM is present as the core and a thin coating of Pt is present as the shell (TM_{core} @ Pt_{shell}). This not only increases the material stability but also reduces the amount of Pt in the catalyst. The thickness of the Pt shell influence the ORR activity and, increasing the thickness of the shell reduces the intrinsic activity of the catalyst.[59] Due to this, suitable synthesis methods are essential to produce the core-shell model. **Figure 1.14** represents the various synthesis

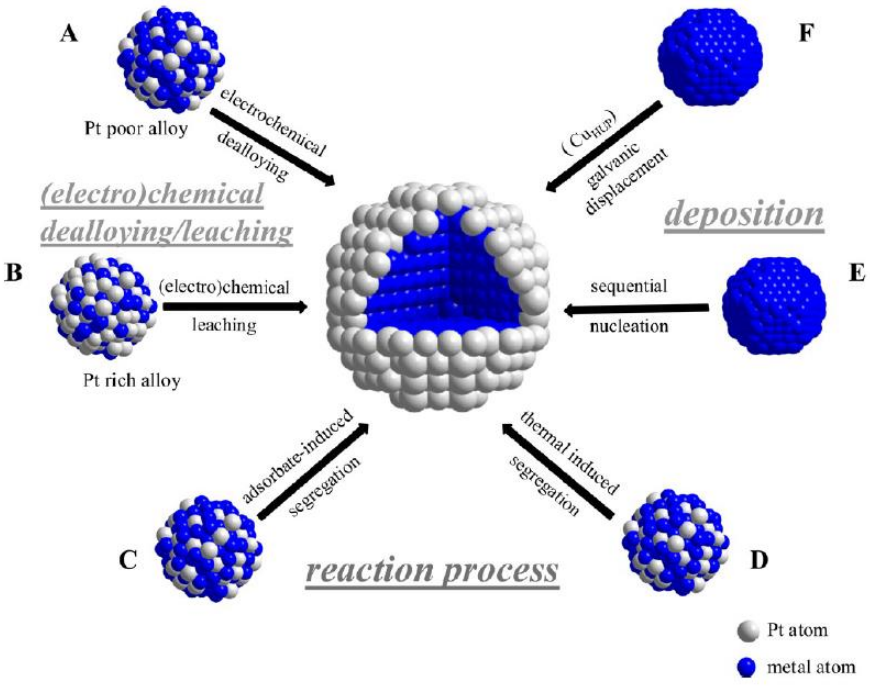

***Figure 1.14**. Schematic representation of the various synthesis methods for the core-shell morphology.[59] (Reprinted with permission, Copyright © 2013, **American Chemical Society**).*

strategies adopted for the development of the core-shell structure. The electrochemical dealloying, underpotential deposition (UPD) followed by galvanic displacement, high-temperature annealing, electrochemical leaching *etc*., are the important routes of core-shell synthesis. Kuttiyiel *et. al* developed the PtNiN core-shell structure with NiN as the core and Pt as the shell (**Figure 1.15**).[60] The PtNiN is synthesized by the chemical reduction followed by sequential annealing in the N_2 and the NH_3 atmosphere at ambient pressure. The Ni nitride tunes the electronic structure of the Pt shell and favours the ORR. The use of Ni nitride core increases the catalytic activity and stability of PtNiN/C. The mass and specific activities of PtNiN/C is 4.5 and 6.5-fold higher than of Pt/C. This indicates the benefit attained from the core-shell structure.

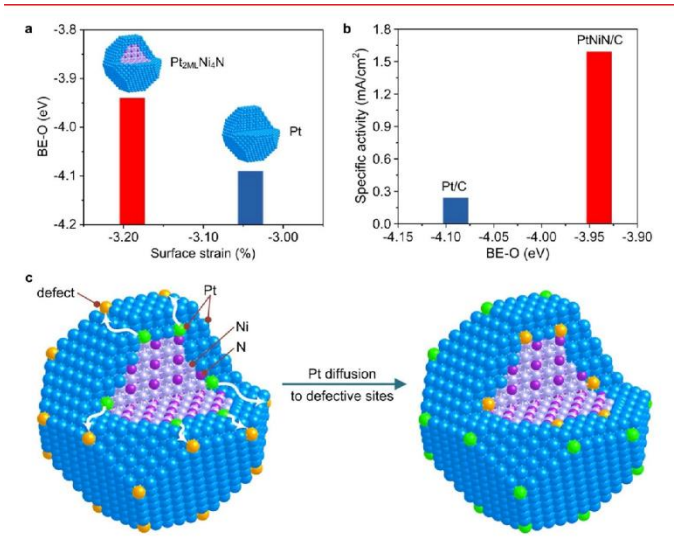

Figure 1.15*. (a) Surface strain vs. binding energy comparison of Pt and PtNiN core-shell, (b) specific activity vs. binding energy of Pt/C and PtNiN/C and (c) schematic representation of the formation of core-shell structure.*[60] *(Reprinted with permission, Copyright © 2012,* ***American Chemical Society****).*

1.3.10 Non-precious-metal based ORR catalyst:

The development of non-precious-metal (NPM) based catalysts with high ORR activity and stability has attracted a major focus due to the possibility of reducing the catalyst cost significantly. The NPM-based catalysts include metal oxide, carbide, sulfide, nitride *etc*., supported on various carbon supports.[61-64] Recently, the Fe-N-C based systems are getting importance for ORR. Wang *et al*. developed Fe-N-C catalyst by the heat-treatment of Fe-doped graphitic carbon nitride (Fe-g-C_3N_4@C) and applied for ORR (**Figure 1.16**).[65] The catalyst displays a half-wave ($E_{1/2}$) potential of 0.75 V *vs*. RHE in 0.1 M $HClO_4$ solution. The system

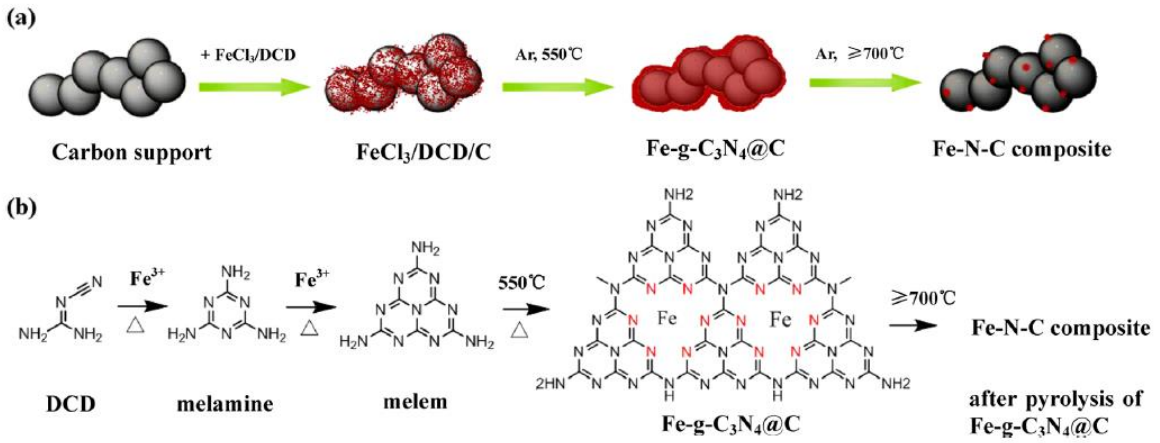

Figure 1.16. *Illustration of the synthesis of Fe-g-C_3N_4@C and Fe-N-C.*[65] *(Reprinted with permission, Copyright © 2014,* ***American Chemical Society****).*

exhibits better stability with only 12 mV negative shift in the $E_{1/2}$ value. Wu *et al*. synthesized S-doped Fe-N-C system by the pyrolysis of metal-organic-framework (MOF).[66] The system shows an $E_{1/2}$ value of 0.82 V *vs*. RHE in 0.1 M H_2SO_4 solution. The fuel cell testing of the system by employing S-doped Fe-N-C as the cathode displays the maximum power density 800 mW cm^{-2}. Various metal oxides are analysed for ORR and displaying excellent activities in alkaline conditions. Liang *et al*. explored the ORR activity of Co_3O_4 supported reduced graphene oxide (rGO) for ORR in 0.1 M KOH solution.[67] The synergic interaction of Co_3O_4 and rGO imparts high ORR activity and the stability. The poor stability of many metal oxides in acidic conditions limits their wide application. The transition metal sulfide (TMS) based catalysts are attracting significant attention due to their excellent stability in both acidic and alkaline environments.[68] Tang *et al*. developed highly active ORR catalyst by dispersing

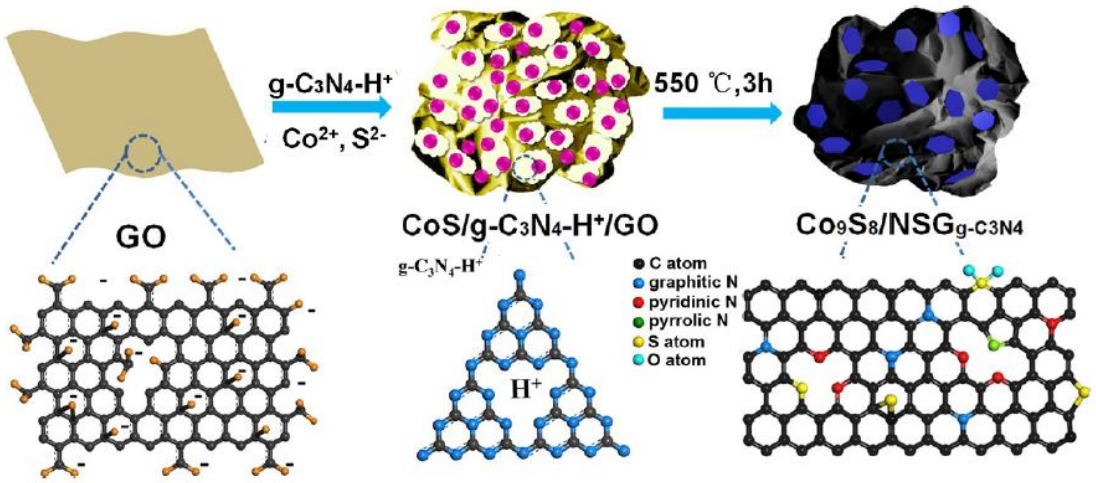

Figure 1.17*. Schematic representation of the synthesis of Co_9S_8/NSG by following the two step process.*[69] *(Reprinted with permission, Copyright © 2017,* ***American Chemical Society****).*

Co_9S_8 nanoplates on N, S-dual doped graphene support (**Figure 1.17**).[69] The dual doped graphene support provides excellent durability during ORR. Also, the interaction between Co_9S_8 nanoplates and N, S-doped graphene support provides improved activity. The study indicates that proper selection of carbon and the metal sulfide reduces the overpotential of ORR. Jakub *et al*. prepared pyrite type CoS_2 through hydrothermal route and analysed for ORR in 0.1 m $HClO_4$ solution.[70] The pyrite type CoS_2 displays good ORR activity and the number of electron transfer is nearly 4 during ORR. The durability of the catalyst is excellent in the acidic condition with nearly similar activity after 15 h stability analysis compared to the initial performance.

1.4 Water Electrolyser

The major parts of water electrolyser are anode, cathode, and membrane as separator. By applying an external power supply, the oxidation of hydroxyl ions at the anode produces O_2 from water (OER). At the same time, protons are reduced at the cathode and produce H_2 (HER). The theoretical onset potential of water electrolysis is 1.23 V in both alkaline and acidic electrolytes.[71-72] However, due to the overpotential associated with the respective electrode reactions, the potential would shift to a higher value than the theoretical potential.[27] This would reduce the efficiency of the system because an additional supply of energy is needed to facilitate the water electrolysis. Hence, the overpotential of the reactions at the respective electrodes dramatically affects the output of the system. Compared to HER, the overpotential of OER is higher. This is due to the involvement of transfer of four-electrons in OER compared to the two-electron transfer in HER. Therefore, in order to achieve better system-level efficiency, the overpotential associated with the OER catalyst should be minimal. Electrocatalysts are playing a significant role in reducing the overpotential and obtaining higher activity. Hence, the development of highly efficient, cost-effective OER catalysts is playing a crucial role in the wide commercialization of water electrolyser for H_2 generation.

1.4.1 Mechanism of Oxygen Evolution Reaction

OER is the cathodic half-cell reaction of the water electrolysis. The mechanism of OER in acidic and alkaline media is given below:

Acidic media:[73]

$$M + H_2O \longrightarrow M\text{-}OH + H^+ + e^- \quad (17)$$

$$M\text{-}OH \longrightarrow M\text{-}O + H^+ + e^- \quad (18)$$

$$M\text{-}O + H_2O \longrightarrow M\text{-}OOH + H^+ + e^- \quad (19)$$

$$M\text{-}OOH \longrightarrow M\text{-}O_2 + H^+ + e^- \quad (20)$$

$$M\text{-}O_2 \longrightarrow O_2 + M \quad (21)$$

Alkaline media:[74]

$$M + OH^- \longrightarrow M\text{-}OH + e^- \quad (22)$$

$$M\text{-}OH + OH^- \longrightarrow H_2O + M\text{-}O + e^- \quad (23)$$

$$M\text{-}O + OH^- \longrightarrow M\text{-}OOH + e^- \quad (24)$$

$$M\text{-}OOH + OH^- \longrightarrow M\text{-}O_2 + H_2O + e^- \quad (25)$$

$$M\text{-}O_2 \longrightarrow O_2 + M \quad (26)$$

where, M is the active centre.

1.4.2 Electrocatalysts for Oxygen Evolution reaction:

The RuO_2 and IrO_2 are the *state-of-the-art* catalysts for facilitating OER in the anode of the water electrolyser. The high cost along with the poor stability of these materials acts as the bottleneck for the commercial production of H_2 from water. To address these issues, developing highly efficient OER catalyst in a cost-effective method is fascinating. The following section provides the brief discussion on the development of OER catalysts for water splitting application.

1.4.2a Precious-metal based OER catalysts:

The RuO_2 and IrO_2 nanoparticles with size ~6 nm were developed by Lee *et al.* and studied for OER in both acidic and alkaline electrolytes.[75] Initially, the Ru and Ir nanoparticles were prepared in oleyalamine-mediated solution followed by heat-treatment in O_2 atmosphere. The produced rutile type RuO_2 and IrO_2 show onset potential at ~1.4 V *vs*. RHE with better stability in both acidic and alkaline conditions (**Figure 1.18a-d**). This is due to the thermodynamic stability of the developed rutile type structure of RuO_2 and IrO_2. Even though the catalyst is exhibiting improved performance, the cost of the material is high due to the use of precious metals in the system. Hence, the development of non-precious metal-based OER catalyst is highly desirable for water electrolysis application.

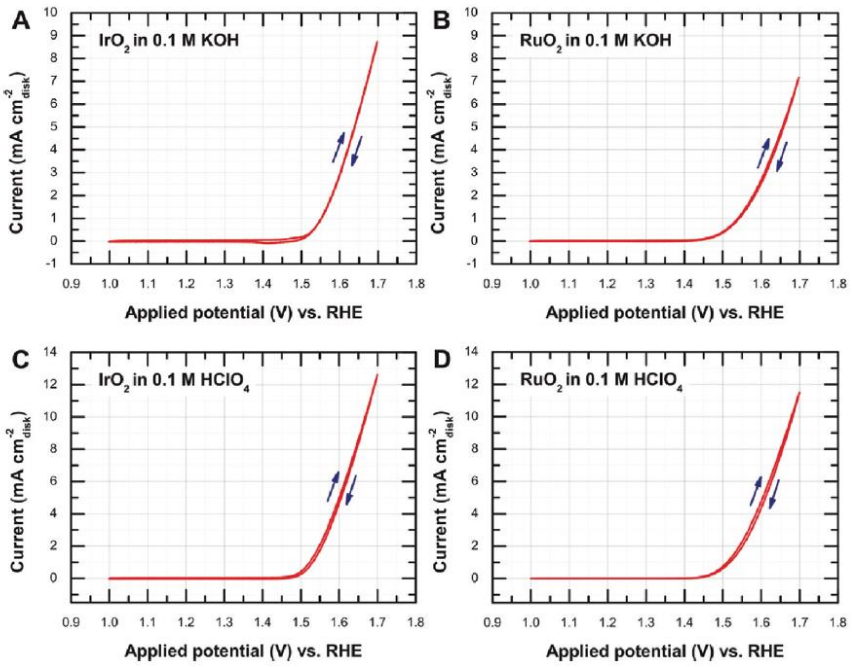

***Figure 1.18**. (a) Cyclic voltammogram (CV) of IrO_2 in 0.1 M KOH solution, (b) CV of RuO_2 in 0.1 M KOH solution (c) CV of IrO_2 in 0.1 M $HClO_4$ solution and (d) CV of RuO_2 in 0.1 M $HClO_4$ solution.[75] (Reprinted with permission, Copyright © 2012, **American Chemical Society**).*

1.4.2b Non-precious-metal based OER catalyst:

The development of cost-effective catalysts for OER and subsequent application in water electrolysis is crucial for the low-cost production of H_2 from water. Various transition metal oxides (TMOs) show enhanced OER activity in alkaline conditions. The electrical conductivity of many TMOs is poor. Hence, for obtaining a better electrochemical activity, dispersing the TMO on suitable conducting substrate is essential. The OER catalyst developed by Li *et al*. with hierarchical $CoNiO_x$/rGO by following the self-assembly followed by heat-treatment method is significant (**Figure 1.19**).[76] The material displays OER activity better than the *state-of-the-art* catalyst. The improved activity is related to the hierarchical morphology, porous structure and large surface area possessed by $CoNiO_x$/rGO. The overpotential displayed by the system is nearly 310 mV at 10 mA cm^{-2} current density in 0.1 M KOH solution. The transition metal sulfide (TMS) based catalysts are emerging as excellent materials in water splitting applications. They are mainly employed as HER catalysts and exhibit enhanced activity and stability. However, the OER activity and further the overall water splitting analysis of TMS derived catalysts have not been thoroughly investigated. Some of the interesting works in this

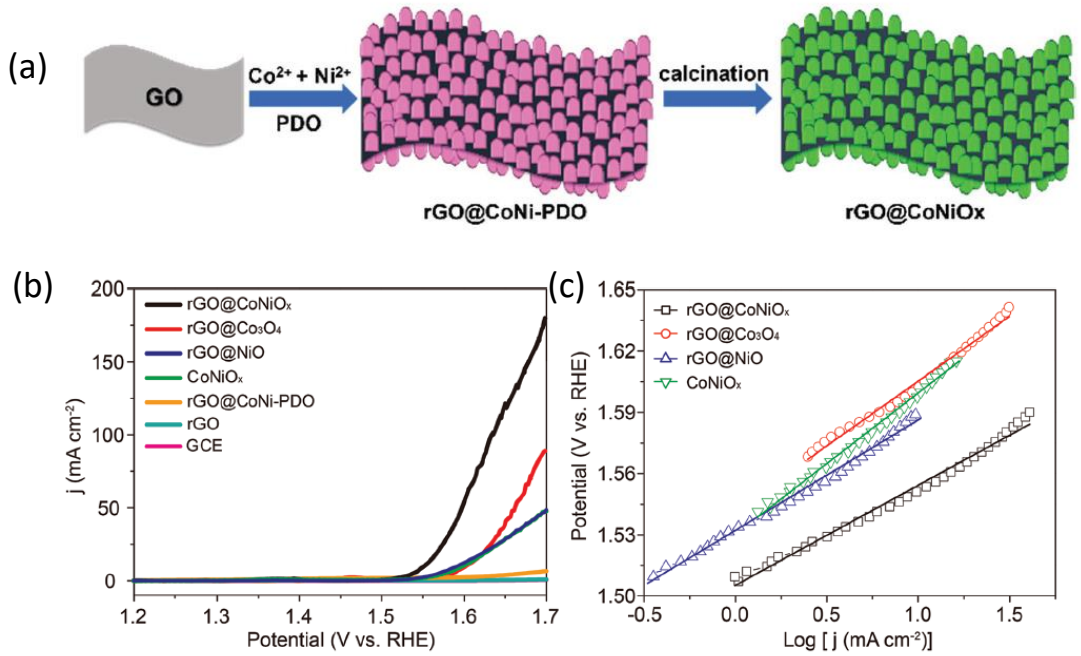

***Figure 1.19**. Schematic representation of the synthesis of $CoNi_xO$/rGO, (b) comparison of the OER activity of $CoNi_xO$/rGO with control samples in 0.1 M KOH solution and, (c) comparison of the Tafel slopes of the prepared materials.[76] (Reprinted with permission from **John Wiley and Sons; License Number: 4804661047883**).*

area are summarized here. Wang *et al*. developed the cobalt sulfide (Co-S) based catalyst for water splitting application.[77] The ZnO nanowires (NWs) were grown on the carbon paper (CP) by following the wet-chemical method. The ZnO is coated with polydopamine (PDA), and subsequently heat-treatment at high temperatures produces carbon-coated ZnO/CP. The acid washing of the material leads to the carbon tubes supported on CP (CP/CTs). Co-S is deposited through electrochemically on CP/CTs and forms the final catalysts CP/CTs/Co-S. The overall water splitting analysis displays nearly 1.74 V for achieving the current density of 10 mA cm^{-2} in CP/CTs/Co-S (**Figure 1.20**). This is around 64 mV higher than of the *state-of-the-art* catalyst-based electrolyzer. Therefore, further improvement in the activity is needed to overcome the *state-of-the-art* system. Chaiti *et al*. prepared phosphorous incorporated cobalt molybdenum sulfide on carbon cloth (P-CoMoS/CC) for water splitting application.[78] The phosphorous incorporation enhances the catalytic activity and stability. The carbon cloth acts as the substrate to decorate P-CoMoS during the hydrothermal reaction. P-CoMoS/CC requires 1.54 V to reach the current density of 10 mA cm^{-2} in 1 M KOH solution. The material displays ~90 % retention in performance after 100 h stability analysis.

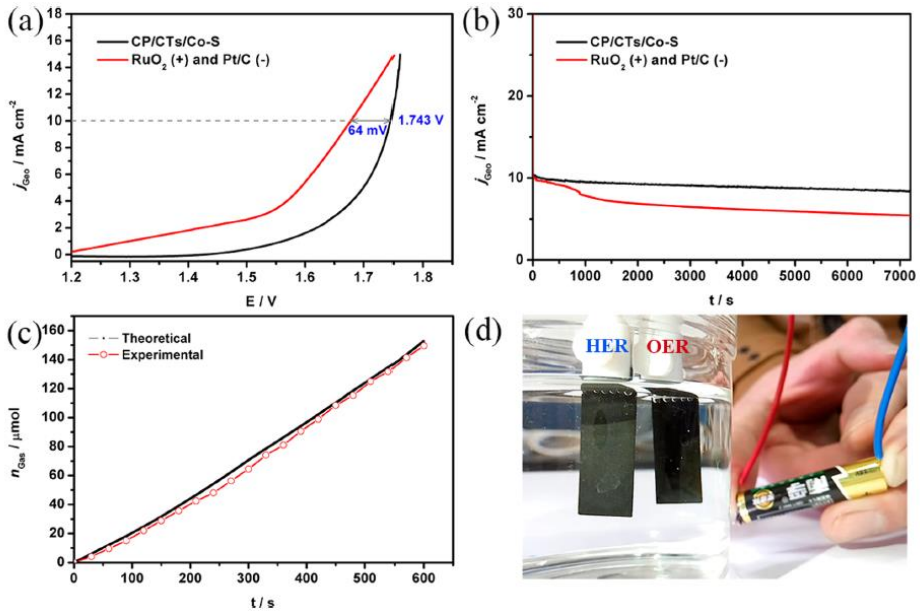

***Figure 1.20**. (a) Comparison of the overall water splitting activity of CP/CTs/Co-S with the state-of-the-art system in 1 M KOH solution, (b) stability test of the catalyst, (c) gas quantification of the evolved gases during water splitting and, (d) image corresponds to overall water splitting with a 1.5 V battery.[77] (Reprinted with permission, Copyright © 2016, **American Chemical Society**).*

1.5 Scope of the Present Research Work and Objective of the Thesis

The development of non-precious metal-based electrocatalysts is highly desirable to reduce the overpotential of ORR and OER. Such catalysts can help in further improving the efficiency of the system. The application of the noble metal-free catalysts is important in this direction due to their low cost and enhanced activity. The typical noble metal-free ORR catalysts are transition metal oxides, nitrides, phosphides, sulfides, carbides *etc*., supported on various carbon substrates. Among them, the transition metal sulfide (TMS)-based catalysts are attracting significant attention due to their excellent stability in both acidic and alkaline environments. Also, the high electronic conductivity, fascinating electrochemical activity, diverse structural types along with the cost-effective synthesis of TMS have attracted the researchers. Therefore, developing the TMS derived catalysts for ORR and OER is significant.

The key objective of the present thesis is to develop highly active and stable TMS derived catalysts for ORR and water electrolysis. Improving the active center density and simultaneously refining the activity of the catalyst can be achieved with the morphology tuning.

Modifications in the structure of the nanomaterial can bring significant enhancement in the intrinsic activity by exposing the various planes, increasing the electrochemical active surface area (ECSA), and formation of defects in the material. The role of the supporting material is also significant for accomplishing improved activity and optimum stability, since the support material provides the proper electrical conductivity and corrosion resistance to the material. Therefore, careful selection of the low-cost and highly conducting material as support material is crucial for the development of an efficient catalyst. Also, simple and scalable routes of synthesis are required for the bulk scale production of the catalyst. Many of the reported TMS-based catalysts are studied mainly in half-cell conditions. The system-level confirmation of the activity is missing in many of the recent reports. Hence, significant modulation in the activity of the TMS-derived nanomaterials is required to achieve their practical application in the devices. Also, understanding the activity parameters influencing the catalyst performance can be identified with the detailed physico-electrochemical characterizations of the developed catalysts.

The specific objectives and work components considered for the preparation of the present thesis are as follows:

1) To follow an environmentally friendly and cost-effective method for the synthesis of layer-separated distribution of MoS_2 supported on reduced graphene oxide (rGO) by the intervention of $Co(OH)_2$. Analysing the ORR activity of the prepared material in alkaline conditions. Besides, special emphasis is given to the optimisation of the catalyst by tuning the active-site density of MoS_2 by reducing the number of layers on rGO.
2) To develop a Co_9S_8 nanoparticle-based highly active and stable ORR catalyst, which is compatible with both acidic and alkaline conditions. The synthesis is optimised in such a way that a homogenous dispersion of the Co_9S_8 nanoparticles can be achieved over the nitrogen doped carbon surface. The stability improvement of the catalyst with graphitic carbon coating on the Co_9S_8 nanoparticles surface and their dispersion on the surface of nitrogen-doped carbon are also studied.
3) Synthesis of few-layer MoO_3 from MoS_2 through hydrothermal treatment and concomitantly dispersing $Ni(OH)_2$ on MoO_3. Transforming $Ni(OH)_2$ into NiO by heat-treatment to achieve better OER activity is attempted. The electrical conductivity could be maintained by judicious combination of Vulcan carbon (VC) and MoO_3 in the system. Finally, a highly efficient catalyst for OER is obtained, and it is further explored in water electrolysis application.

4) To develop a carbon-free catalyst for water splitting application. Exploring the advantages of nickel foam (NF) as both the substrate and precursor for nanomaterial. Preparation of hierarchical structure of Co_9S_8-Ni_3S_2 on NF and to explore the same as the self-standing and binder-free electrode for water electrolysis application.
5) System-level validation of the developed catalysts for PEMFC and water electrolysis applications.

1.6 References

[1] G. Fu, J.-M. Lee, *J. Mater. Chem. A* **2019**, *7*, 9386-9405.

[2] X. Zou, Y. Zhang, *Chem. Soc. Rev.* **2015**, *44*, 5148-5180.

[3] Y. Nie, L. Li, Z. Wei, *Chem. Soc. Rev.* **2015**, *44*, 2168-2201.

[4] W. Li, D. Xiong, X. Gao, L. Liu, *Chem. Commun.* **2019**, *55*, 8744-8763.

[5] W. Kong, X. Luan, H. Du, L. Xia, F. Qu, *Chem. Commun.* **2019**, *55*, 2469-2472.

[6] H. Guan, S. Zhang, X. Cai, Q. Gao, X. Yu, X. Zhou, F. Peng, Y. Fang, S. Yang, *J. Mater. Chem. A* **2019**, *7*, 2560-2574.

[7] L. Najafi, S. Bellani, R. Oropesa-Nuñez, M. Prato, B. Martín-García, R. Brescia, F. Bonaccorso, *ACS Nano* **2019**, *13*, 3162-3176.

[8] X. Zhang, Z. Du, X. Luo, A. Sun, Z. Wu, D. Wang, *Appl. Surf. Sci.* **2018**, *433*, 723-729.

[9] C. Wang, B. Tian, M. Wu, J. Wang, *ACS Appl. Mater. Interfaces* **2017**, *9*, 7084-7090.

[10] J.-T. Ren, Z.-Y. Yuan, *ACS Sustainable Chem. Eng.* **2017**, *5*, 7203-7210.

[11] K. Liang, L. Guo, K. Marcus, S. Zhang, Z. Yang, D. E. Perea, L. Zhou, Y. Du, Y. Yang, *ACS Catal.* **2017**, *7*, 8406-8412.

[12] K. Xiong, L. Li, l. zhang, W. Ding, l. peng, Y. Wang, S. Chen, S. Tan, Z. Wei, *J. Mater. Chem. A* **2014**.

[13] M. A. Khan, H. Zhao, W. Zou, Z. Chen, W. Cao, J. Fang, J. Xu, L. Zhang, J. Zhang, *Electrochemical Energy Reviews* **2018**.

[14] A.-L. Wang, H. Xu, G.-R. Li, *ACS Energy Lett.* **2016**, *1*, 445-453.

[15] M. Shao, Q. Chang, J.-P. Dodelet, R. Chenitz, *Chem. Rev.* **2016**, *116*, 3594-3657.

[16] J.-Y. Choi, R. S. Hsu, Z. Chen, *J. Phys.Chem. C* **2010**, *114*, 8048-8053.

[17] Y.-J. Wang, N. Zhao, B. Fang, H. Li, X. T. Bi, H. Wang, *Chem. Rev.* **2015**.

[18] C. Meng, O. Z. Gall, P. P. Irazoqui, *Biomedical Microdevices* **2013**, *15*, 973-983.

[19] C. Cui, L. Gan, H.-H. Li, S.-H. Yu, M. Heggen, P. Strasser, *Nano Lett.* **2012**, *12*, 5885-5889.

[20] V. R. Stamenkovic, B. Fowler, B. S. Mun, G. Wang, P. N. Ross, C. A. Lucas, N. M. Marković, *Science* **2007**, *315*, 493-497.

[21] L. Lin, Q. Zhu, A.-W. Xu, *J. Am. Chem. Soc.* **2014**, *136*, 11027-11033.

[22] R. E. Rosli, A. B. Sulong, W. R. W. Daud, M. A. Zulkifley, T. Husaini, M. I. Rosli, E. H. Majlan, M. A. Haque, *Int. J. Hydrog. Energy* **2017**, *42*, 9293-9314.

[23] H.-C. Huang, I. Shown, S.-T. Chang, H.-C. Hsu, H.-Y. Du, M.-C. Kuo, K.-T. Wong, S.-F. Wang, C.-H. Wang, L.-C. Chen, K.-H. Chen, *Adv. Funct. Mater.* **2012**, *22*, 3500-3508.

[24] R. Bashyam, P. Zelenay, *Nature* **2006**, *443*, 63-66.

[25] Z. Sun, Y. Wang, L. Lin, M. Yuan, H. Jiang, R. Long, S. Ge, C. Nan, H. Li, G. Sun, X. Yang, *Chem. Commun.* **2019**, *55*, 1334-1337.

[26] K. Karthick, S. Anantharaj, S. R. Ede, S. Kundu, *Inorg. Chem.* **2019**, *58*, 1895-1904.

[27] W. Chen, Y. Liu, Y. Li, J. Sun, Y. Qiu, C. Liu, G. Zhou, Y. Cui, *Nano Lett.* **2016**, *16*, 7588-7596.

[28] T. Reier, Z. Pawolek, S. Cherevko, M. Bruns, T. Jones, D. Teschner, S. Selve, A. Bergmann, H. N. Nong, R. Schlögl, K. J. J. Mayrhofer, P. Strasser, *J. Am. Chem. Soc.* **2015**, *137*, 13031-13040.

[29] S. Chen, J. Duan, J. Ran, M. Jaroniec, S. Z. Qiao, *Energy Environ. Sci.* **2013**, *6*, 3693-3699.

[30] D. Dong, Z. Wu, J. Wang, G. Fu, Y. Tang, *J. Mater. Chem. A* **2019**, *7*, 16068-16088.

[31] S. Mangel, E. Aronovitch, A. N. Enyashin, L. Houben, M. Bar-Sadan, *J. Am. Chem. Soc.* **2014**, *136*, 12564-12567.

[32] A. Morozan, B. Jousselme, S. Palacin, *Energy Environ. Sci.* **2011**, *4*, 1238-1254.

[33] B. Cao, J. C. Neuefeind, R. R. Adzic, P. G. Khalifah, *Inorg. Chem.* **2015**, *54*, 2128-2136.

[34] T. Wang, J. Zhuo, Y. Chen, K. Du, P. Papakonstantinou, Z. Zhu, Y. Shao, M. Li, *ChemCatChem* **2014**, *6*, 1877-1881.

[35] R. Huo, W.-J. Jiang, S. Xu, F. Zhang, J.-S. Hu, *Nanoscale* **2014**, *6*, 203-206.

[36] S. G. Peera, A. Arunchander, A. K. Sahu, *Nanoscale* **2016**, *8*, 14650-14664.

[37] B. P. Vinayan, T. Diemant, R. J. Behm, S. Ramaprabhu, *RSC Adv.* **2015**, *5*, 66494-66501.

[38] X. Zheng, J. Xu, K. Yan, H. Wang, Z. Wang, S. Yang, *Chem. Mater.* **2014**, *26*, 2344-2353.

[39] R. Ganatra, Q. Zhang, *ACS Nano* **2014**, *8*, 4074-4099.

[40] X. Xie, Z. Ao, D. Su, J. Zhang, G. Wang, *Adv. Funct. Mater.* **2015**, n/a-n/a.

[41] Y. Jing, E. O. Ortiz-Quiles, C. R. Cabrera, Z. Chen, Z. Zhou, *Electrochim. Acta* **2014**, *147*, 392-400.

[42] S. Wan, Y. Liu, G.-D. Li, X. Li, D. Wang, X. Zou, *Catal. Sci. Technol.* **2016**, *6*, 4545-4553.

[43] Z. Wang, J.-X. Zhao, Q. Cai, F. Li, *J. Mater. Chem. A* **2017**.

[44] J. Du, R. Wang, Y.-R. Lv, Y.-L. Wei, S.-Q. Zang, *Chem. Commun.* **2019**, *55*, 3203-3206.

[45] A. Arunchander, S. G. Peera, A. K. Sahu, *J. Power Sources* **2017**, *353*, 104-114.

[46] N. Seselj, C. Engelbrekt, J. Zhang, *Science Bulletin* **2015**, *60*, 864-876.

[47] S. Guo, S. Zhang, S. Sun, *Angew. Chem., Int. Ed.* **2013**, *52*, 8526-8544.

[48] A. de Frank Bruijn, G. J. M. Janssen, in *Fuel Cells: Selected Entries from the Encyclopedia of Sustainability Science and Technology* (Ed.: K.-D. Kreuer), Springer New York, New York, NY, **2013**, pp. 249-303.

[49] A. A. Gewirth, M. S. Thorum, *Inorg. Chem.* **2010**, *49*, 3557-3566.

[50] J. R. Varcoe, R. C. T. Slade, *Fuel Cells* **2005**, *5*, 187-200.

[51] S. Lazarou, E. Pyrgioti, A. T. Alexandridis, *J. Power Sources* **2009**, *190*, 380-386.

[52] F. Mack, T. Morawietz, R. Hiesgen, D. Kramer, V. Gogel, R. Zeis, *Int. J. Hydrog. Energy* **2016**, *41*, 7475-7483.

[53] L. Fukuhara, N. Kado, K. Kosugi, P. Suksawad, Y. Yamamoto, H. Ishii, S. Kawahara, *Solid State Ionics* **2014**, *268*, 191-197.

[54] M. A. Abbas, J. H. Bang, *Chem. Mater.* **2015**, *27*, 7218-7235.

[55] J. K. Nørskov, J. Rossmeisl, A. Logadottir, L. Lindqvist, J. R. Kitchin, T. Bligaard, H. Jónsson, *J. Phys. Chem. B* **2004**, *108*, 17886-17892.

[56] S.-P. Lin, K.-W. Wang, C.-W. Liu, H.-S. Chen, J.-H. Wang, *J. Phys.Chem. C* **2015**, *119*, 15224-15231.

[57] V. R. Stamenkovic, B. S. Mun, M. Arenz, K. J. J. Mayrhofer, C. A. Lucas, G. Wang, P. N. Ross, N. M. Markovic, *Nature Materials* **2007**, *6*, 241-247.

[58] C. Chen, Y. Kang, Z. Huo, Z. Zhu, W. Huang, H. L. Xin, J. D. Snyder, D. Li, J. A. Herron, M. Mavrikakis, M. Chi, K. L. More, Y. Li, N. M. Markovic, G. A. Somorjai, P. Yang, V. R. Stamenkovic, *Science* **2014**, *343*, 1339-1343.

[59] M. Oezaslan, F. Hasché, P. Strasser, *J. Phys. Chem. Lett.* **2013**, *4*, 3273-3291.

[60] K. A. Kuttiyiel, K. Sasaki, Y. Choi, D. Su, P. Liu, R. R. Adzic, *Nano Lett.* **2012**, *12*, 6266-6271.

[61] J.-S. Lee, G. S. Park, S. T. Kim, M. Liu, J. Cho, *Angew. Chem., Int. Ed.* **2013**, *52*, 1026-1030.

[62] Z. Chen, D. Higgins, A. Yu, L. Zhang, J. Zhang, *Energy Environ. Sci.* **2011**, *4*, 3167-3192.

[63] T. Corrales-Sánchez, J. Ampurdanés, A. Urakawa, *Int. J. Hydrog. Energy* **2014**, *39*, 20837-20843.

[64] M.-R. Gao, Y.-F. Xu, J. Jiang, Y.-R. Zheng, S.-H. Yu, *J. Am. Chem. Soc.* **2012**, *134*, 2930-2933.

[65] M.-Q. Wang, W.-H. Yang, H.-H. Wang, C. Chen, Z.-Y. Zhou, S.-G. Sun, *ACS Catal.* **2014**, *4*, 3928-3936.

[66] Y.-J. Wu, Y.-C. Wang, R.-X. Wang, P.-F. Zhang, X.-D. Yang, H.-J. Yang, J.-T. Li, Y. Zhou, Z.-Y. Zhou, S.-G. Sun, *ACS Appl. Mater. Interfaces* **2018**, *10*, 14602-14613.

[67] Y. Liang, Y. Li, H. Wang, J. Zhou, J. Wang, T. Regier, H. Dai, *Nature Materials* **2011**, *10*, 780-786.

[68] Y. Liu, Y. Li, H. Kang, T. Jin, L. Jiao, *Mater. Horiz.* **2016**, *3*, 402-421.

[69] Y. Tang, F. Jing, Z. Xu, F. Zhang, Y. Mai, D. Wu, *ACS Appl. Mater. Interfaces* **2017**, *9*, 12340-12347.

[70] J. S. Jirkovský, A. Björling, E. Ahlberg, *J. Phys.Chem. C* **2012**, *116*, 24436-24444.

[71] T. Liu, X. Sun, A. M. Asiri, Y. He, *Int. J. Hydrog. Energy* **2016**, *41*, 7264-7269.

[72] W. Fang, D. Liu, Q. Lu, X. Sun, A. M. Asiri, *Electrochem. Commun.* **2016**, *63*, 60-64.

[73] N.-T. Suen, S.-F. Hung, Q. Quan, N. Zhang, Y.-J. Xu, H. M. Chen, *Chem. Soc. Rev.* **2017**, *46*, 337-365.

[74] T. Reier, H. N. Nong, D. Teschner, R. Schlögl, P. Strasser, *Adv. Energy Mater.* **2017**, *7*, 1601275.

[75] Y. Lee, J. Suntivich, K. J. May, E. E. Perry, Y. Shao-Horn, *J. Phys. Chem. Lett.* **2012**, *3*, 399-404.

[76] L. Ping, Z. H. Chun, *Adv. Funct. Mater.* **2017**, *27*, 1606325.

[77] J. Wang, H.-x. Zhong, Z.-l. Wang, F.-l. Meng, X.-b. Zhang, *ACS Nano* **2016**, *10*, 2342-2348.

[78] C. Ray, S. C. Lee, K. V. Sankar, B. Jin, J. Lee, J. H. Park, S. C. Jun, *ACS Appl. Mater. Interfaces* **2017**, *9*, 37739-37749.

Chapter-2

Layer-separated MoS_2 Bearing Reduced Graphene Oxide Mediated by $Co(OH)_2$ as a Pt-free Electrocatalyst for Oxygen Reduction Reaction

A significant improvement in the electrochemical oxygen reduction reaction (ORR) activity of molybdenum sulfide (MoS_2) could be accomplished by its layer separated dispersion on reduced graphene oxide mediated by cobalt hydroxide ($Co(OH)_2$) through a hydrothermal process ($Co(OH)_2$-MoS_2/rGO). The activity makeover in this case is found to be originated from a controlled interplay of the favourable modulations achieved in terms of electrical conductivity, more exposure of the edge planes of MoS_2 and promotional role played by the coexistence of $Co(OH)_2$ in the proximity of MoS_2. The $Co(OH)_2$-MoS_2/rGO displays an oxygen reduction onset potential of 0.86 V and a half-wave potential ($E_{1/2}$) of 0.74 V *vs*. RHE in 0.1 M KOH solution, which are much higher than that of the corresponding values (0.71 and 0.35 V, respectively) displayed by the as-synthesized pristine MoS_2 (P-MoS_2) under the identical experimental conditions. The Tafel slope corresponding to oxygen reduction for $Co(OH)_2$-MoS_2/rGO is estimated to be 63 mV/decade compared to 68 mV/decade displayed by the *state-of-the-art* Pt/C catalyst. The calculated number of electron transfer during oxygen reduction for $Co(OH)_2$-MoS_2/rGO is in the range of 3.2-3.4 in the potential range of 0.70 V to 0.10 V, which again stands out as a valid evidence on the much favourable mode of oxygen reduction accomplished by the system compared to its pristine counterpart. Overall, the present study demonstrates a viable strategy of tackling the inherent limitations, such as low electrical conductivity and limited access to the active sites, faced by the layered structures like MoS_2 to position them among the group of potential Pt-free electrocatalysts for oxygen reduction.

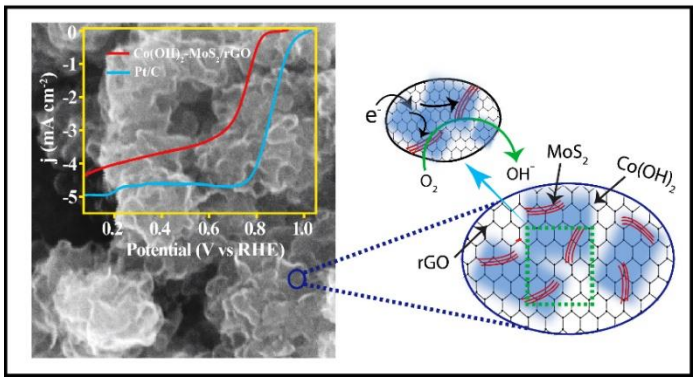

Content of this chapter is published in the following article:

Nanoscale, 2015, 7, 16729–16736.

(https://pubs.rsc.org/en/content/articlelanding/2015/NR/C5NR04415D#!divAbstract)

2.1 Introduction

The low temperature fuel cells, mainly, polymer electrolyte membrane fuel cells (PEMFCs), presently use Pt based electrocatalysts for tackling the kinetically sluggish oxygen reduction reaction (ORR).[1] As potential alternatives to the expensive Pt, electrocatalysts based on different carbon morphologies and early transition metals are being explored.[2, 3] Some of such catalysts are reported to be having close-matching ORR characteristics as that of the Pt based materials, even though a system level exploration of such materials is still in the infancy stage. As the efforts on developing the cost-effective ORR catalysts picked up substantial momentum recently, heteroatom doping on carbon morphologies has been recognized as one of the most prospective strategies to pitch for the target.[4, 5] However, most of the heteroatom doped carbonaceous materials require high annealing temperatures and, subsequently, this leads to higher energy consumption for the material synthesis.[6] Similarly, the bulk scale production of the heteroatom doped carbon by high temperature annealing in the furnace is challenging.[7] Such limitations of the processes overshadow the expected benefits of having them for various large scale applications.

Recently, layered inorganic materials, such as WS_2 [8, 9], $MoSe_2$ [10], MoS_2 [11, 12] *etc*., prepared through simple hydrothermal methods, have attained substantial research interest as many of such systems are found to be displaying interesting electrochemical activity characteristics towards oxygen evolution reaction (OER) and hydrogen evolution reaction (HER).[10, 13-15] Even though the preparation methods involved in the hydrothermal processes are simple, unfortunately, due to the unsolved issues related to conductivity and layer stacking, these layered inorganic materials so far could not attract much space in the ongoing efforts to develop cost-effective alternatives to the *state-of-the-art* Pt based electrocatalysts for ORR.[16, 17] However, considering the promising activity of MoS_2 towards HER, perhaps MoS_2 has paved a great attention among all the aforementioned layered inorganic materials.[18, 19] The synthesis of MoS_2/rGO is getting wide attention in recent years because rGO plays a vital role in reducing the stacking of MoS_2 in the composite and it also helps the system to facilitate better electrocatalytic activities.[14, 20-23]

Recent studies have revealed that the ORR activity of MoS_2 is significantly poor compared to the Pt based or even to the heteroatom doped systems.[24] There are reports on tuning the ORR activity of MoS_2 by controlling the size and also by supporting MoS_2

on gold.[24-26] These studies indicate that edge exposed synthesis of MoS_2 leads to better ORR activity compared to their growth patterns in the form of stacked sheets. Also, a recent theoretical study shows that the presence of cobalt in the MoS_2 layers can improve the ORR activity of MoS_2.[27] However, synthesis of such a combined system is not explored and hence a direct experimental validation on the modulation of the ORR properties is missing at present. In our present study, we report a method to significantly improve the ORR activity of MoS_2 by $Co(OH)_2$ intervention and by confining its growth along the surface of rGO sheets. It has been observed that when the MoS_2 formation is facilitated in the presence of graphene oxide (GO), a surface spread-out growth pattern of MoS_2 could be achieved with significantly reduced the number of the MoS_2 layers in their sheet-like growth pattern. The presence of the Co moiety is also found to be contributing in dictating the growth pattern on MoS_2, but the role of this small amount of the Co entity in reducing the overpotential for ORR is more significant.

2.2 Experimental Section

2.2.1 Materials

Ammonium molybdate tetrahydrate ($(NH_4)_6Mo_7O_{24}.\ 4H_2O$), elemental sulfur powder, graphite, potassium permanganate ($KMnO_4$), cobalt nitrate hexahydrate ($Co(NO_3)_2.\ 6H_2O$), hydrazine hydrate ($N_2H_4.\ H_2O$) were purchased from Sigma-Aldrich Chemicals. Sulphuric acid (H_2SO_4), phosphoric acid (H_3PO_4), hydrogen peroxide (H_2O_2) and hydrochloric acid (HCl) were procured from Thomas Baker. All the chemicals were used without any further purification.

2.2.2 Graphene Oxide (GO) Synthesis

GO was synthesised using the modified Hummer's method.[28] Briefly, graphite powder and $KMnO_4$ were mixed well and slowly added to a 9:1 mixture of H_2SO_4 and H_3PO_4. The solution was then kept for refluxing at 60 °C overnight. The resulting mixture was slowly added to ice containing 5 mL of 30% H_2O_2. The mixture was washed subsequently with conc. HCl, water, ethanol and diethyl ether in sequence. The obtained viscous solution was kept for drying at 50 °C in a vacuum oven for overnight.

2.2.3 Synthesis of MoS_2-P

Pristine MoS_2 (hereafter called as MoS_2-P) was synthesised with a slight modification of a reported work.[29] 0.08 mmol ammonium molybdate tetrahydrate ($(NH_4)_6Mo_7O_{24}.\ 4H_2O$),

1.1 mmol elemental sulfur powder and 1 mL hydrazine hydrate (N_2H_4. H_2O) were dispersed in 35 mL of DI water by sonication for 1 h and the mixture was transferred into a 50 mL Teflon-lined autoclave. Subsequently, hydrothermal treatment was carried out at 180 °C for 12 h and the temperature was allowed to cool down to room temperature. The resulting mixture was filtered and washed with ethanol and water. The wet cake was dried in an oven at 60 °C for 5 h. The obtained material is called as MoS_2-P.

2.2.4 Synthesis of $Co(OH)_2$-MoS_2/rGO

The overall synthesis was performed by using a simple hydrothermal method. The hydrothermal method involves the reaction of ammonium molybdate tetrahydrate ($(NH_4)_6Mo_7O_{24}$. $4H_2O$, 0.08 mmol), sulfur powder (1.1 mmol), graphene oxide (GO, 1.5 mg/ml) and cobalt nitrate ($Co(NO_3)_2$. $6H_2O$, 0.05 mmol) with hydrazine hydrate (N_2H_4. H_2O, 1 mL) as the reducing agent at 180°C for 12 h. The resulting mixture was filtered and washed with ethanol and water. The wet cake was dried in an oven at 60 °C for 5 h. Under the experimental conditions, GO is found to be undergoing partial reduction, and the corresponding entity in the final product is termed as rGO, instead of GO. Thus obtained sample is designated as $Co(OH)_2$-MoS_2/rGO.

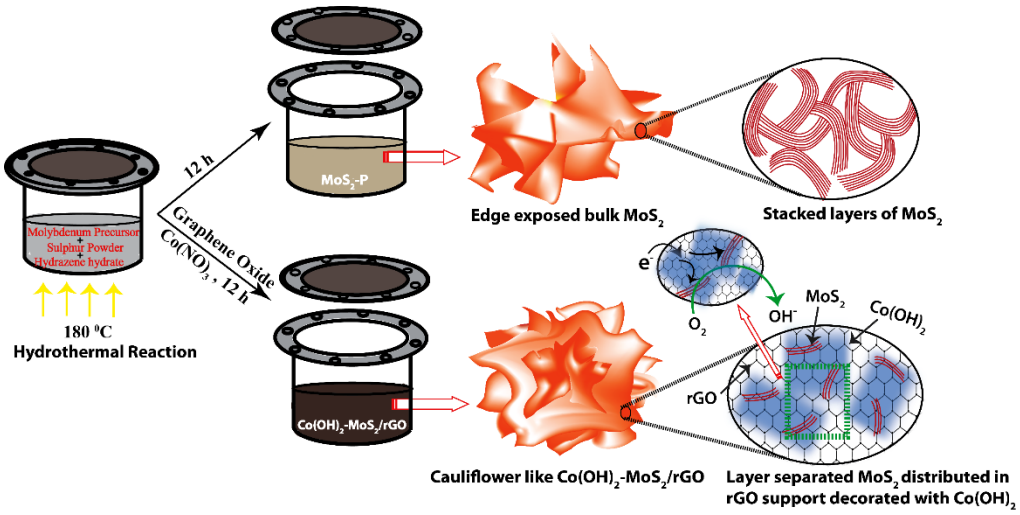

Figure 2.1. *Schematic representation of the synthesis of MoS_2-P and $Co(OH)_2$-MoS_2/rGO through the hydrothermal method. MoS_2-P leads to stacked layers of MoS_2, whereas these layers could be simultaneously separated into bundles of smaller numbers of layers and dispersed on the surface of rGO in the case of $Co(OH)_2$-MoS_2/rGO.*

2.2.5 Synthesis of MoS_2/rGO and $Co(OH)_2$/rGO

MoS_2 was also synthesized in the presence of GO but without using $Co(NO_3)_2$, which is designated as MoS_2/rGO. Synthesis of MoS_2/rGO was carried out by following the hydrothermal method as explained above without the addition of cobalt nitrate hexahydrate into it. For the synthesis of $Co(OH)_2$/rGO, the hydrothermal treatment as explained before was carried out with GO, cobalt nitrate hexahydrate and hydrazine hydrate.

2.2.6 Characterization

For performing the scanning electron microscopic (SEM) analysis, a Quanta 200 3D FEI instrument was used. FEI Technai G2 T20 instrument operated at 200 keV was used to record the transmission electron microscopic images of the samples. In the case of Raman analysis, a LabRam spectrometer (HJY, France) operating with a laser wavelength of 632.1 nm was employed. Using Cu Kα (1.5418 A°) radiation, X-ray diffraction (XRD) was done in a PANalytical X'pert pro instrument. Nitrogen adsorption-desorption experiments were conducted at 77 K using Quantachrome Quadrasorb automatic volumetric instrument using ultra-pure N_2. The X-ray photon emission spectroscopic (XPS) analysis of the samples was carried out by using VGMicrotech Multilab ESCA 3000 spectrometer.

The ORR measurements were carried out in a Bio-Logic (SP-300) instrument using a three-electrode setup. The catalyst ink for ORR study was made by the following procedure. 5 mg of the catalyst was sonicated with 1 mL of DI water-isopropyl alcohol mixture (3:1) and 40 µL of 5 wt. % Nafion for 1 h using a bath sonicator. About 20 µL of this catalyst slurry was transferred on the surface of a glassy carbon working electrode (0.196 cm^2) by maintaining a catalyst loading of 0.51 mg cm^{-2}. ORR activity was evaluated in 0.1 M KOH solution using Hg/HgO as the reference electrode and graphite rod as the counter electrode. For a comparative study, 40 wt. % Pt/C (from Johnson Matthey) was also analysed under identical conditions by keeping a Pt loading of 100 µg cm^{-2}. Cyclic voltammetry was performed in 0.1 M KOH solution with a scan rate of 50 mV s^{-1} in both nitrogen and oxygen saturated atmosphere using Hg/HgO as the reference electrode and graphite rod as the counter electrode. All the potentials were converted into RHE by calibrating Hg/HgO in the H_2 saturated 0.1 M KOH solution. [19] Linear sweep voltammetry (LSV) was carried out by recording the voltammograms at a scan rate of 5 mV s^{-1}.

The Koutecky-Levich (K-L) equation was used to obtain the kinetics of the reaction and is given as below:

$$\frac{1}{j} = \frac{1}{j_L} + \frac{1}{j_k}$$

$$\frac{1}{j} = \frac{1}{B\omega^{1/2}} + \frac{1}{j_k}$$

where, j is the measured current density, j_k is the kinetic current density, j_L is the diffusion-limited current density and ω is the angular velocity of the electrode (ω = 2πf/60, f is the rotation speed).

$$B = 0.62nFC_0^* D_0^{2/3} \nu^{-1/6}$$

$$j_k = nFKC_0^*$$

where, n is the number of electrons transferred during the reaction, F is the Faradays constant (96485 C mol^{-1}), 'C_0^*' is the bulk concentration of O_2 (1.22 x 10^{-6} mol cm^{-3}), 'D_0' is the diffusion coefficient of O_2 (1.9 x 10^{-5} cm^2 s^{-1}), 'ν' is the kinematic viscosity of the electrolyte (0.01 cm^2 s^{-1}) and 'k' is the electron transfer rate constant. A plot of 1/j against $\omega^{-1/2}$ leads to a straight line and the slope corresponds to 1/B.

The number of electron transfer (n) and percentage of hydrogen peroxide production (% H_2O_2) during ORR were calculated from rotating ring disc electrode (RRDE) analysis by using the following equations:

$$n = \frac{4\, I_d}{(I_d + I_r/N)}$$

$$\%\, H_2O_2 = \frac{200 * I_r/N}{(I_d + I_r/N)}$$

where, Ir, Id, and N are the ring current, disc current and collection efficiency (0.37), respectively.

The durability analysis of both $Co(OH)_2$-MoS_2/rGO and Pt/C was carried out by the accelerated durability test (ADT). For this, CV was performed for 5000 cycles at a scan rate of 100 mV sec^{-1} in the potential window of 1.0 to 0.60 V. The LSV was recorded before and after the 5000 cycle ADT at a scan rate of 5 mV s^{-1} and at 1600 r. p. m of the working electrode. The electrochemical impedance (EIS) study was carried out in a frequency range of 10^6 kHz to 0.1 Hz with an AC amplitude of 10 mV at 0.7 V. The electrical conductivity was measured by placing the sample pellets on a non-conducting surface and the measurement was done by the four-probe method.

2.3 Result and Discussion

2.3.1 SEM Analysis

The hydrothermally synthesized MoS_2-P shows a high density of exposed edges as evident from the SEM images presented in **Figure 2.2a** and **b**. However, the flakes look like adhered strongly, leaving an interconnected structure with protruded edges at distinct locations. The SEM-EDX elemental mapping of MoS_2-P provided in **Figure 2.2c-e** indicates the presence of molybdenum and sulfur in the system. **Figure 2.3** illustrates the SEM images of MoS_2/rGO and the presence of rGO during the growth of MoS_2 is found to be improvising the growth pattern of the system, where a flower like structure has been observed. This indicates an influential role played by rGO in dictating the growth of the MoS_2 layers.[13a]

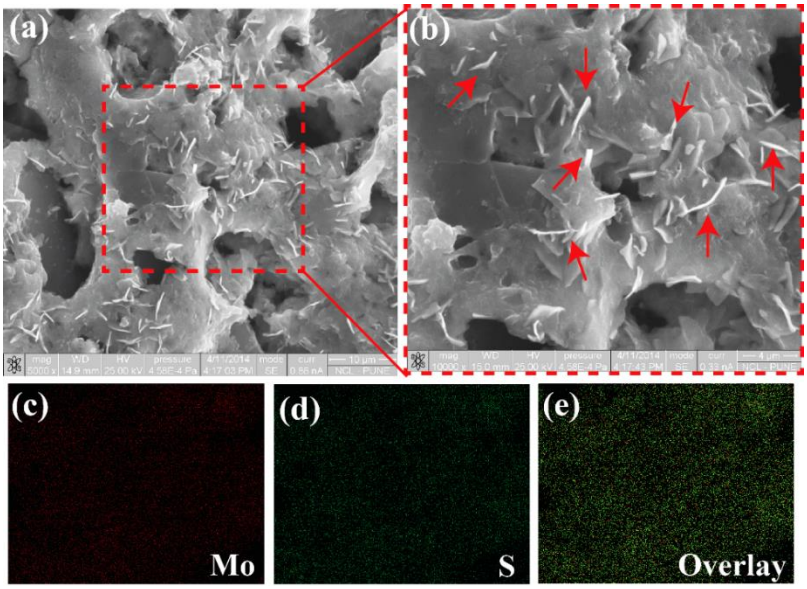

Figure 2.2. *SEM images of (a) MoS_2-P, (b) magnified portion of MoS_2-P marked in the red square (red arrows indicate the exposed edges in MoS_2-P) and (c-e) SEM-EDX elemental mapping of MoS_2-P clearly indicating the uniform distribution of Mo and S in the material.*

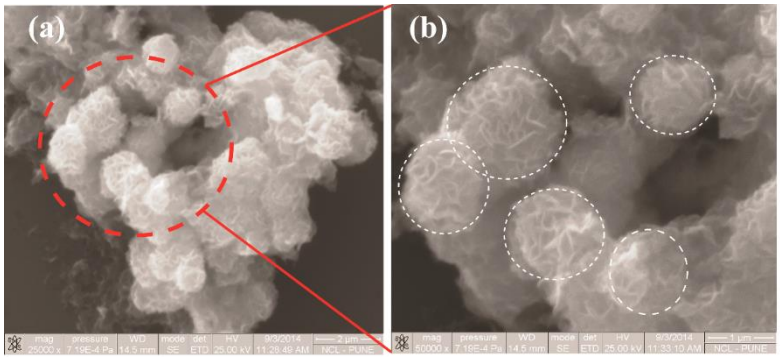

Figure 2.3. *(a-b) SEM images of MoS_2/rGO.*

Interestingly, after the intervention of $Co(OH)_2$ (*i.e.*, $Co(OH)_2$-MoS_2/rGO), a prominent change in the morphology of MoS_2/rGO has been observed (**Figure 2.4a** and **b**). Well defined cauliflower-like growth pattern with a substantially increased density of the exposed edge planes is the main characteristics of $Co(OH)_2$-MoS_2/rGO compared to the previous two systems.

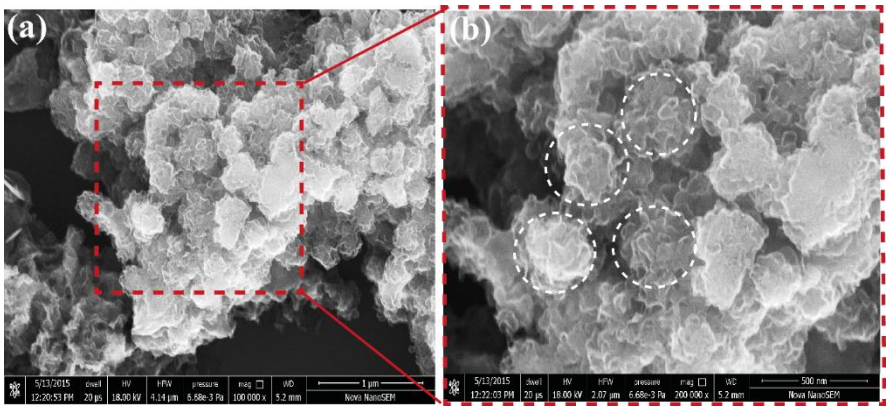

Figure 2.4. *(a) SEM images of $Co(OH)_2$-MoS_2/rGO and (b) magnified portion of the red square in image b.*

In order to check the distribution of elements in $Co(OH)_2$-MoS_2/rGO, the SEM-EDX elemental mapping was carried out and the images are presented in **Figure 2.5**. From **Figure 2.5a-f** it is confirmed that carbon, molybdenum, sulfur, cobalt and oxygen are distributed uniformly in the system. Hence, the SEM analysis concludes that the edge exposed MoS_2 is achieved if the reaction proceeds in the presence of GO. The detailed information on the edge exposed nature of the formed MoS_2 in $Co(OH)_2$-MoS_2/rGO is explained in the following section.

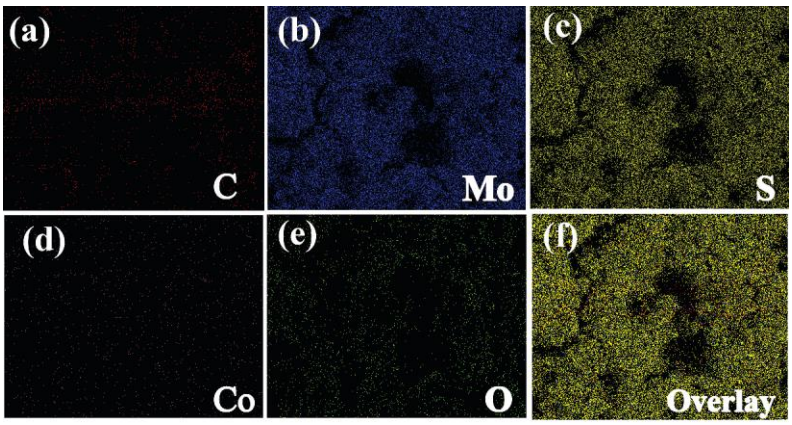

Figure 2.5. *SEM-EDX elemental mapping of $Co(OH)_2$-MoS_2/rGO; (a) carbon, (b) molybdenum, (c) sulfur, (d) cobalt, (e) oxygen and (f) overlay.*

2.3.2 TEM Analysis

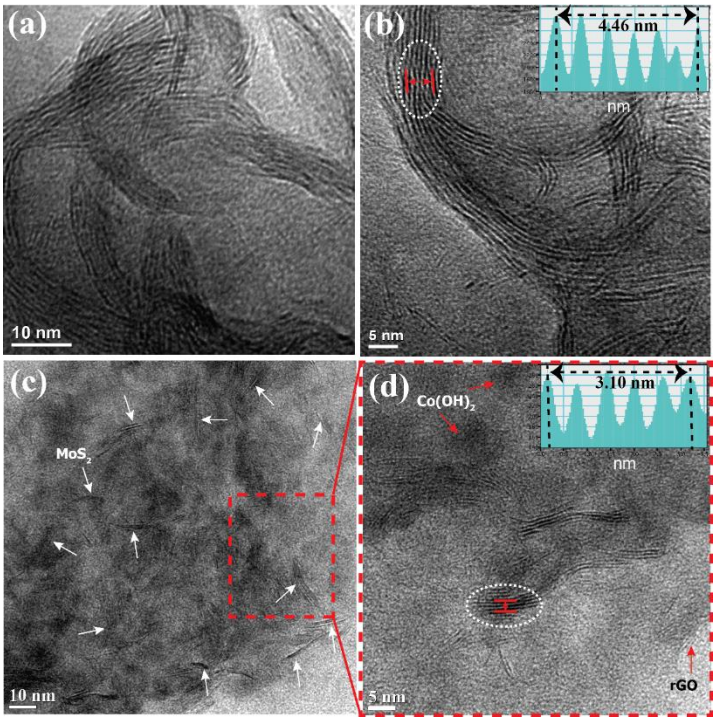

Figure 2.6. *(a) TEM image of pristine MoS_2 (MoS_2-P), (b) magnified image of MoS_2-P (inset shows the lattice fringe profile of MoS_2 marked in the white circle), (c) TEM image of $Co(OH)_2$-MoS_2/rGO (white arrows indicate the MoS_2 layers), (d) magnified image of $Co(OH)_2$-MoS_2/rGO marked in the red dotted square in image c (inset shows the lattice fringe profile of MoS_2 marked in the white circle).*

More insightful information on the growth pattern of the MoS_2 phase could be obtained from the TEM analysis. **Figures 2.6a** to **d** show the TEM images of MoS_2-P and $Co(OH)_2$-MoS_2/rGO. MoS_2-P (**Figure 2.6a** and **b**) displays an assembly consisting of the stacking of many layers together, with an estimated d-spacing of 0.65 to 0.74 nm. These are corresponding to the (002) planes of MoS_2.[20] On the other hand, in the case of $Co(OH)_2$-MoS_2/rGO, the number of layers in the MoS_2 stacking is found to be significantly reduced (**Figure 2.6c** and **d**). Also, the MoS_2 phase is found to have attained its growth along the surface of rGO in a distributed fashion. The estimated d-spacing value of MoS_2 in this case is found to be approximately 0.62 nm. On the other hand, MoS_2/rGO is also found to have attained some level of dispersion of MoS_2 on rGO, but the quality and homogeneity of the dispersion in this case is found to be inferior to that of $Co(OH)_2$-MoS_2/rGO (**Figure 2.7**). Also, the measured d-spacing value is found to be slightly higher (0.65 nm) in the case of MoS_2/rGO compared to $Co(OH)_2$-

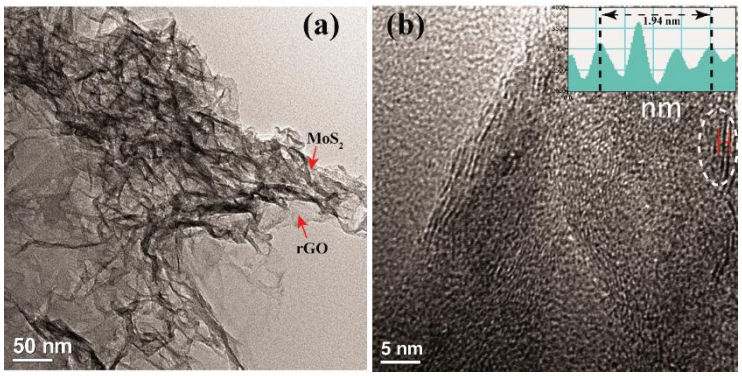

Figure 2.7. *(a-b) TEM images of MoS_2/rGO*

MoS_2/rGO. The decrease in the d-spacing after the $Co(OH)_2$ incorporation could be due to the decrease in the number of MoS_2 layers in $Co(OH)_2$-MoS_2/rGO, and this type of d-spacing reduction due to the reduction in the number of the MoS_2 layers after exfoliation is already reported in the literature.[21] From the aforementioned discussion on the analysis of the growth pattern of the MoS_2 phase in the different cases, it can be readily seen that rGO acts as an influential substrate in the system by effectively reducing the number of the stacked MoS_2 layers in its growth pattern. $Co(OH)_2$ is also found to be playing a vital role in maintaining a proper dispersion of MoS_2 on the rGO surface, all the while keeping the number of the stacked layers of MoS_2 significantly low. Also, when rGO accommodates the growth of MoS_2 on its surface, the MoS_2 phase attains a spread-out nature. This provides better accessibility of its surface, which has an influential role in modulating the catalytic activity of the system.

2.3.3 XRD Analysis

The XRD pattern corresponding to MoS_2-P as presented in **Figure 2.8** depicts the presence of the (002), (100), (102), (105) and (110) planes of MoS_2 at the 2θ values of 14.1°, 32.4°, 35.4°, 49.6° and 57.2°, respectively. These values are matching well with the reported values of the corresponding planes of the material in the literature.[12a] The peak position corresponding to the (002) plane of MoS_2 in MoS_2/rGO is found to be at 14.2° whereas that of $Co(OH)_2$-MoS_2/rGO is appeared at 14.3°, suggesting a decrease in the interplanar distance of MoS_2 from MoS_2/rGO to $Co(OH)_2$-MoS_2/rGO. This observation is in accordance with the d-spacing values deduced from the lattice fringes of MoS_2 in the TEM images of the samples. The presence of the peak at 24.1° for MoS_2/rGO and 24.8° for $Co(OH)_2$-MoS_2/rGO indicates the presence of the (002) plane for the graphitic carbon in the samples. However, there is a prominent difference in the

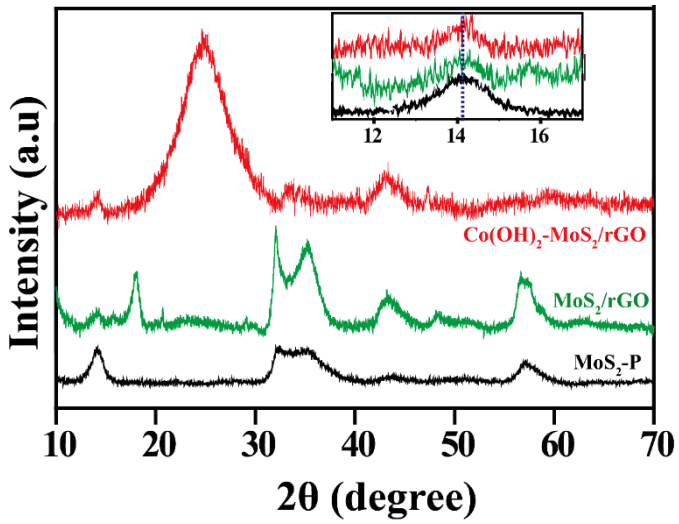

Figure 2.8. *(a) Comparison of the XRD profiles of MoS_2-P, MoS_2/rGO and $Co(OH)_2$-MoS_2/rGO (inset shows the shift in the (002) peak of MoS_2 for the respective samples)*

intensities of this peak in these two samples. This might be due to the intervention by $Co(OH)_2$ on MoS_2 in $Co(OH)_2$-MoS_2/rGO, which creates more structural deformation compared to MoS_2/rGO as evident from the SEM images (**Figure 2.3**). The XRD peaks for $Co(OH)_2$ in $Co(OH)_2$-MoS_2/rGO are observed at 13.7°, 33.6°, 40.4°, and 59.6°, which are attributed to the (003), (012), (015) and (110) planes of $Co(OH)_2$, respectively.[22]

2.3.4 Raman Analysis

The Raman spectra of the samples are presented in **Figure 2.9**. The spectra display the characteristic peaks at 380 and 407 cm^{-1} for MoS_2-P and 380 and 406 cm^{-1} for MoS_2/rGO, which indicate the E_{2g} and A_{1g} vibration modes of MoS_2 in the samples respectively.[23] The corresponding peaks of MoS_2 in the case of $Co(OH)_2$-MoS_2/rGO are found to be appearing at 378 and 401 cm^{-1}, respectively. The separation distance of the A_{1g} and E_{2g} peaks is directly related to the number of the layers of MoS_2 in its growth pattern.[23] Considering this relation, the lower value of the peak separation in the case of $Co(OH)_2$-MoS_2/rGO (23 cm^{-1}) compared to MoS_2/rGO (26 cm^{-1}) and MoS_2-P (27 cm^{-1}) stands out as a valid evidence on the reduced number of the layers occupied by MoS_2 in the former case. Indeed, rGO as a support is playing a crucial role in attaining the lower number of the sheets in MoS_2. However, since the A_{1g}-E_{2g} peak distance in the case of $Co(OH)_2$-MoS_2/rGO is found to be lower than that of MoS_2/rGO, the promoter $Co(OH)_2$ is also found to be playing a decisive supporting role in reducing the

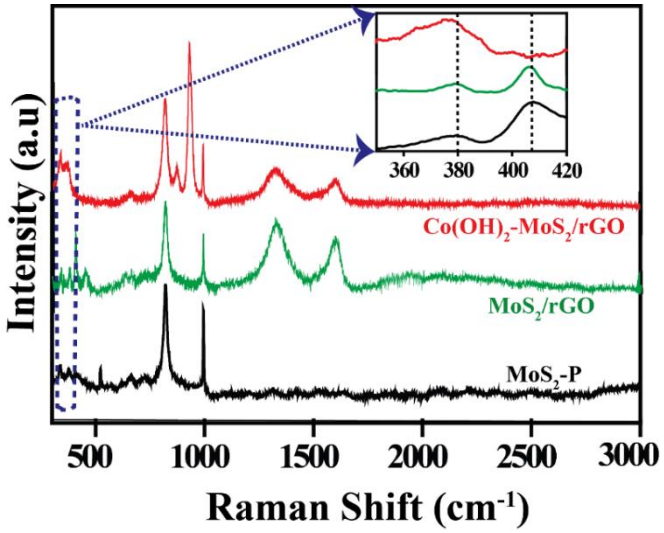

Figure 2.9. *Raman spectra of MoS_2-P, MoS_2/rGO and $Co(OH)_2$-MoS_2/rGO (inset shows the magnified region of the peaks for MoS_2 of all the three samples).*

number of the layers of MoS_2 in its growth pattern. This reduction in the number of the layers indicates more spread-out growth of MoS_2 on rGO, which is expected to lead to exposure of more edge active sites and thereby promote dioxygen adsorption and its reduction.

In addition to the peaks for MoS_2, the Raman spectra also display the D and G band of graphene in the case of the both rGO based samples. The corresponding peaks positioned for MoS_2/rGO are appearing at 1326 and 1603 cm^{-1}, whereas a redshift is observed for these peak positions (1318 and 1597 cm^{-1}, respectively) in the case of $Co(OH)_2$-MoS_2/rGO. This indicates higher strain induced on the graphene sheet in the latter case, which can be accounted by the more spread-out dispersion of the MoS_2 phase on rGO by the intervention of $Co(OH)_2$. The redshift in the Raman spectra of $Co(OH)_2$-MoS_2/rGO could also be attributed to the charge transfer from $Co(OH)_2$ to rGO. The respective I_D/I_G ratios for MoS_2/rGO and $Co(OH)_2$-MoS_2/rGO are 1.30 and 1.33, which indicate the more number of defective sites present on $Co(OH)_2$-MoS_2/rGO. The peaks that appeared at 820 and 994 cm^{-1}, as shown inside the dotted line of **Figure 2.9**, are attributed to the stretching vibration mode of the terminal Mo=O group. This indicates the presence of the oxides of molybdenum in the composite, feasibly formed during the sample preparation.[24]

2.3.5 Surface Area and Pore-size Distribution Analysis

The BET surface area (**Figure 2.10a**) of MoS_2-P is found to be 32 m^2 g^{-1}. With the dispersion of MoS_2 on rGO (*i.e.*, MoS_2/rGO), the surface area has been increased to 43.1

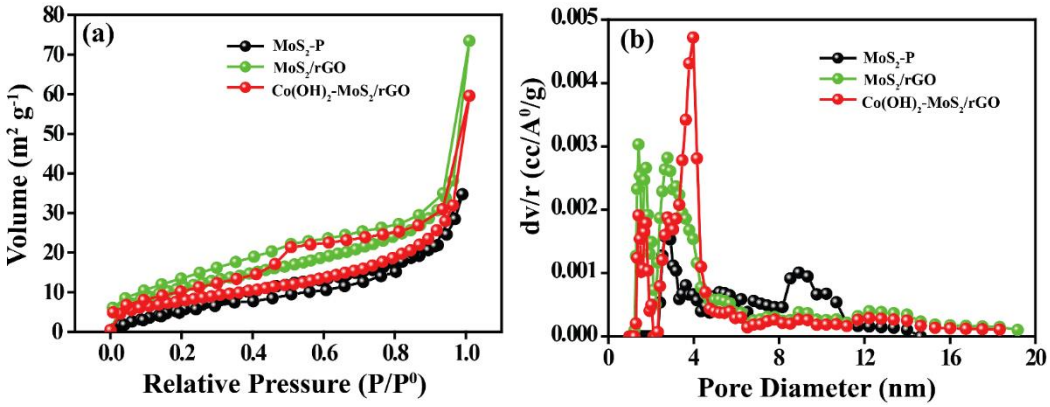

Figure 2.10. *(a) N_2 adsorption-desorption isotherm profiles of MoS_2-P, MoS_2/rGO and $Co(OH)_2$-MoS_2/rGO and (b) pore size distribution profiles of MoS_2-P, MoS_2/rGO and $Co(OH)_2$-MoS2/rGO.*

m^2 g^{-1}, which is in accordance with the recent literature reports.[10b, 13a] However, even though $Co(OH)_2$ is found to be promoting layer separated dispersion of MoS_2 on rGO, the surface area of $Co(OH)_2$-MoS_2/rGO is found to be only 29.3 m^2 g^{-1}. This slight reduction in the surface area compared to MoS_2-P and MoS_2/rGO further confirms the interaction of the layers of MoS_2 by $Co(OH)_2$ along with the surface aligned growth of $Co(OH)_2$ as a thin layer on the rGO surface. Also, there are literature reports showing lower surface area values for pure $Co(OH)_2$.[25] Interestingly, the pore size distribution of the samples (**Figure 2.10b**) shows mesoporous nature and the pore size and pore volume in the range of 3-5 nm is found to be increased from MoS_2-P to $Co(OH)_2$-MoS_2/rGO. This modulation in pore distribution characteristics is expected to make the active sites more accessible for dioxygen reduction reaction in the case of $Co(OH)_2$-MoS_2/rGO by facilitating improved mass transport.

2.3.6 XPS Analysis

The X-ray photoelectron spectra (XPS) of $Co(OH)_2$-MoS_2/rGO are shown in **Figure 2.11**. The survey spectrum of $Co(OH)_2$-MoS_2/rGO shown in **Figure 2.11a** indicates the prominent peaks for carbon, sulfur, molybdenum, oxygen and cobalt in the material. The carbon spectra (**Figure 2.11b**) show the peaks corresponding to the graphitic carbon at 284.6 eV, the C-O group at 286.2 eV and the C=O group at 287.5 eV, respectively.[26] The molybdenum spectra (**Figure 2.11c**) show peaks at 228.6 and 231.6 eV of the $3d_{5/2}$ and $3d_{3/2}$ states of molybdenum respectively, of MoS_2 [27]. The sulfur XPS spectra (**Figure 2.11d**) show the $2p_{3/2}$ and $2p_{1/2}$ states of the sulfide ions at 161.8

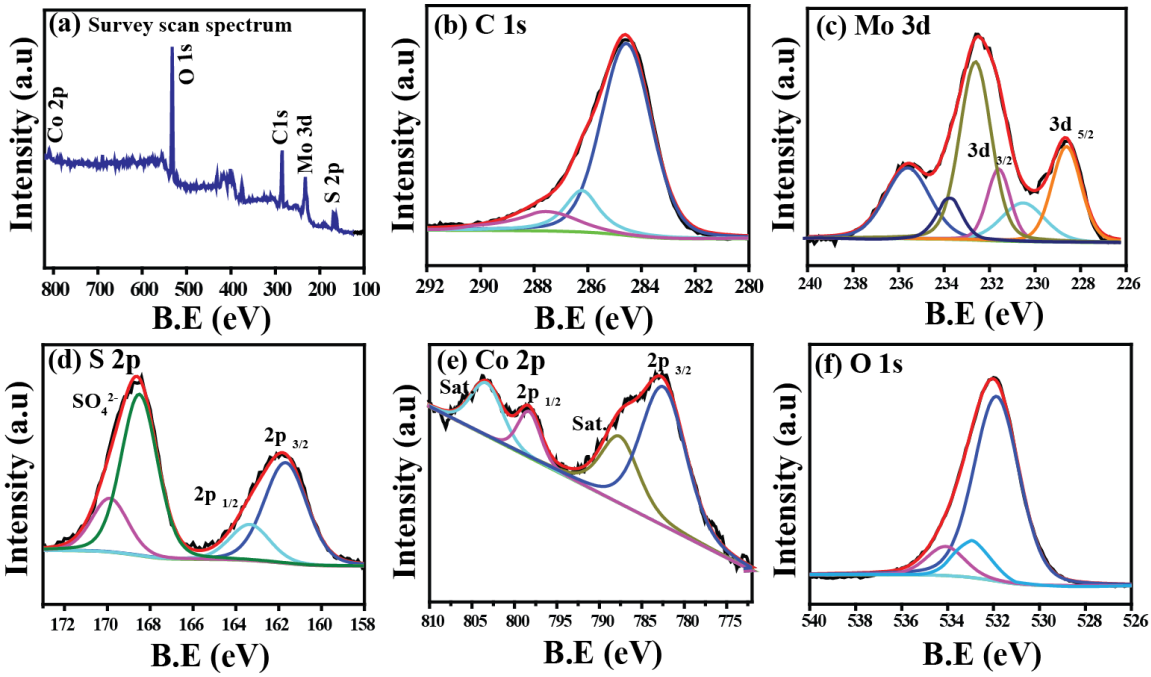

Figure 2.11. *Deconvoluted XPS of (a) survey spectra, (b) carbon, (c) molybdenum, (d) sulfur (e) cobalt and (f) oxygen in $Co(OH)_2$-MoS_2/rGO. The black curve corresponds to the raw data and the red curve represents the fitted data.*

and 163.3 eV, respectively.[28] These two spectral characteristics substantiate the presence of the MoS_2 phase in the composite. In addition to the peaks for MoS_2, the Mo spectra also show the peaks for oxidized molybdenum at higher binding energies (230.5, 232.6, 233.7 and 235.6 eV). This could be due to the formation of some percentage of oxides of molybdenum with the adsorbed oxygen molecules.[29] However, the bulk characterization technique XRD was not showing any peaks corresponding to the MoO_3 phase. XRD analysis of MoS_2-P was giving the characteristics peaks corresponding to the MoS_2 only (**Figure 2.8**). Hence, it can be concluded that the trace amount of the molybdenum oxide formed in the samples might be due to the adsorbed oxygen molecules. The deconvoluted sulfur spectra (**Figure 2.11d**) show peaks at 168.5 and 169.8 eV, which are attributed to the presence of sulfite and sulfate, respectively. The deconvoluted XPS spectra of cobalt in **Figure 2.11e** depict the peaks at 782.6 and 798.5 eV with a peak separation of 15.9 eV. These two peaks represent the $2p_{3/2}$ and $2p_{1/2}$ states of $Co(OH)_2$, respectively. The oxygen XPS spectra (**Figure 2.11f**) display a peak at 531.9 eV for the oxygen bonded with carbon and that could be originated from rGO.[30] Another peak present at 532.9 eV indicates the COOH group [31], which is an indication of the presence of a trace amount of unreduced graphene oxide in the system.

A peak appeared at 534.1 eV can be ascribed to the signature corresponding to the chemisorbed oxygen moiety in the system.[32 33]

2.3.7 Electrochemical Analysis

The electrocatalytic activity of the synthesized materials towards ORR was studied with a rotating disk electrode (RDE) having a geometrical area of 0.196 cm^2. The experiments were carried out in 0.1 M KOH solution saturated with nitrogen and oxygen depending on the requirement of oxygen-free and oxygen rich conditions. The measurements were carried out by using Hg/HgO as the reference electrode and a graphite rod as the counter electrode. The cyclic voltammograms of $Co(OH)_2$-MoS_2/rGO with N_2 and O_2 saturated 0.1 M KOH solution with a rotation speed of 900 rpm are given in **Figure 2.12a**. The increase in the cathodic current with O_2 purging in the system indicates that the material has active sites which can reduce the incoming oxygen molecules.

The comparative LSVs recorded at an electrode rotation rate of 1600 rpm and a scan rate of 5 mV s^{-1} of all the catalysts are given in **Figure 2.12b**. The ORR activity of the as synthesized MoS_2-P is found to be insignificant, displaying an onset potential of 0.71 V and a half-wave potential ($E_{1/2}$) of 0.35 V. Also, the nature of the LSV indicates highly resistive nature of the catalyst with an inferior limiting current compared to the rest of the systems. A significant improvement in the ORR activity could be observed when MoS_2/rGO was employed as the electrocatalyst. Here, the LSV gives an onset potential at 0.81 V and an $E_{1/2}$ of 0.65 V. The 100 mV positive shift in the onset as well as the 300 mV positive shift in the $E_{1/2}$ compared to MoS_2-P indicates the favourable activity modulation accomplished by the composite system. Also, the nature of the voltammogram indicates a major recovery from the ohmic overpotential faced by MoS_2-P. The improved activity is attributed to the reduced stacking of MoS_2 by rGO when the former is allowed to grow along the surface of rGO, which in turn helps to expose more active reaction centres on MoS_2. Moreover, rGO as a support improves the electrical conductivity to the system.[34] The electrical conductivity measurement of MoS_2-P, MoS_2/rGO and $Co(OH)_2$-MoS_2/rGO were obtained by using the four probe method. The electrical conductivity of MoS_2-P, which is found to have a significantly low value of 0.007 S cm^{-1}, is found to be improved drastically to 0.44 and 0.61 S cm^{-1} for MoS_2/rGO and $Co(OH)_2$-MoS_2/rGO, respectively.

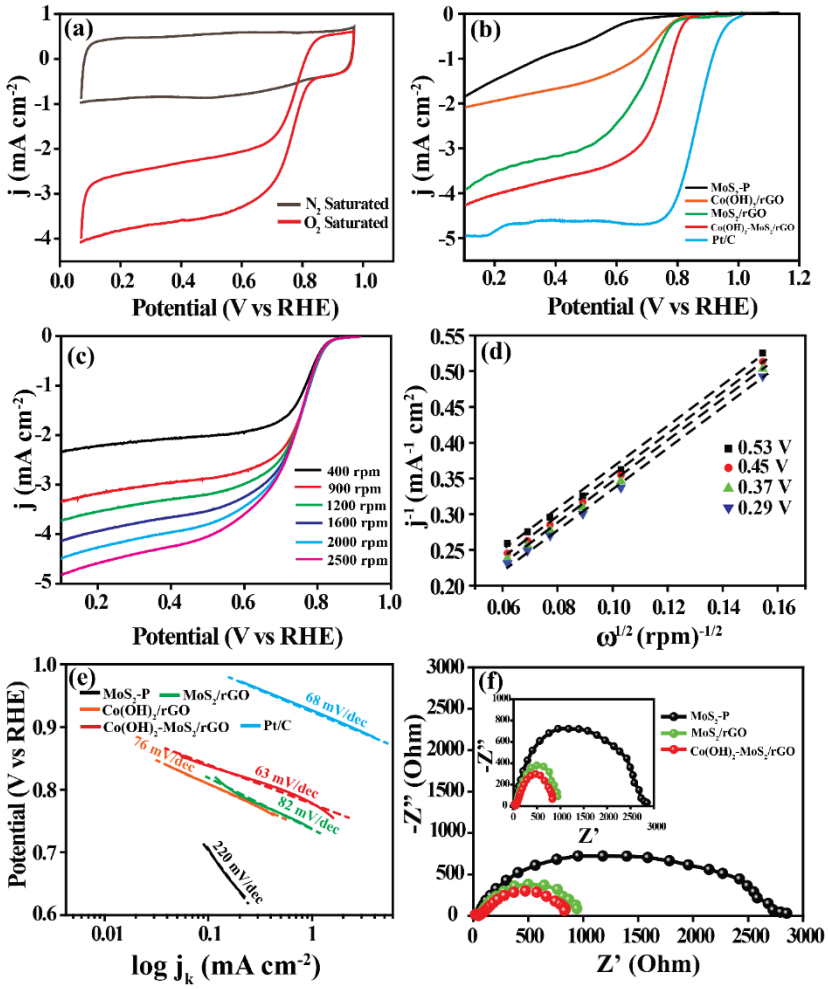

Figure 2.12. *(a) Cyclic voltammograms of $Co(OH)_2$-MoS_2/rGO in 0.1 M KOH solution with N_2 and O_2 saturation at a scan rate of 50 mV s^{-1} with an electrode rotation rate of 900 rpm, (b) comparative linear sweep voltammograms (LSVs) of the samples performed in O_2-saturated 0.1 M KOH solution at 1600 rpm of the working electrode recorded at a scan rate of 5 mV s^{-1}, (c) LSV of $Co(OH)_2$-MoS_2/rGO in O_2 saturated 0.1 M KOH solution with different rotation rates of the working electrode, (d) Koutecky–Levich (K–L)) plots of $Co(OH)_2$-MoS_2/rGO, (e) Tafel plot comparison of the samples with Pt/C, and (f) Nyquist plots of the samples recorded at 0.60 V vs. RHE.*

A much impressive performance has been displayed by $Co(OH)_2$-MoS_2/rGO compared to MoS_2/rGO, which indicates the additional benefit enjoyed by the system through the $Co(OH)_2$ interaction. The system displays an onset potential of 0.86 V and an $E_{1/2}$ of 0.74 V. The more positive $E_{1/2}$ (by 90 mV) and onset potential (by 50 mV) of $Co(OH)_2$-MoS_2/rGO compared to MoS_2/rGO indicates improved intrinsic activity and reaction centre density of the system. Since $Co(OH)_2$ supported on rGO alone shows better kinetics towards ORR (**Figure 2.12b**), the higher intrinsic activity attained by

$Co(OH)_2$-MoS_2/rGO is mainly attributed to the extra synergetic effect imparted by $Co(OH)_2$ on the edge exposed MoS_2 layers, which already has been significantly benefitted by the favourable interactions from its substrate rGO. Thus, the controlled interplay of the favourable characteristics of MoS_2, rGO and $Co(OH)_2$ has helped to acquire a composite material, where layer-separated distribution of MoS_2 on rGO, conductivity enhancement assisted by rGO and activity modulation induced by the synergistic interaction of MoS_2 with both rGO and $Co(OH)_2$ could be simultaneously maintained. With respect to the standard 40 wt. % Pt/C, the onset potential and $E_{1/2}$ of $Co(OH)_2$-MoS_2/rGO is found to be lower by 108 and 129 mV, respectively. However, the performance achieved by the present system is found to be much higher compared to the reported MoS_2 based systems in the recent literature. [24, 25]

The plots of j^{-1} *vs.* $\omega^{-1/2}$ (where 'j' and 'ω' stand for the current density and angular rotation, respectively), called the Koutecky-Levich (K-L) plots[35], as presented in **Figure 2.12d** for $Co(OH)_2$-MoS_2/rGO are found to be maintaining linear behaviour with similar slopes at different potential values. This type of behaviour in the K-L plots suggests the involvement of similar oxygen reduction kinetics in a given range of potentials.[36] Along with the analysis using the K-L plots, as another useful methodology, the Tafel slope corresponding to oxygen reduction has been calculated by plotting mass transport corrected kinetic current density against overpotential. The corresponding Tafel plots are presented in **Figure 2.12e**. The Tafel slope in the case of MoS_2-P is estimated to be 220 mV/decade and this value has been reduced to 63 mV/decade in the case of $Co(OH)_2$-MoS_2/rGO. Such a drastic change in the Tafel slope undoubtedly reveals a more facile nature of the oxygen reduction in $Co(OH)_2$-MoS_2/rGO compared to MoS_2-P.[37] The commercial Pt/C shows the Tafel slope value of 68 mV/decade.

The improved electrical conductivity of the composite also could be confirmed from the electrochemical impedance (**Figure 2.12f**). The R_s values of MoS_2-P, MoS_2/rGO and $Co(OH)_2$-MoS_2/rGO are 51.4, 48.1 and 46.6 Ω, respectively. The results show that $Co(OH)_2$-MoS_2/rGO has the lowest charge transfer resistance (R_{CT}) value as compared to MoS_2-P and MoS_2/rGO. The corresponding R_{CT} values of MoS_2-P, MoS_2/rGO and $Co(OH)_2$-MoS_2/rGO are 2805, 950 and 827 Ω, respectively. The drastic reduction in the R_{CT} value of $Co(OH)_2$-MoS_2/rGO compared to MoS_2-P indicates the improvement in the electron transfer of the system. This would improve the ORR kinetics in the system and subsequently improves the ORR activity. The electrical conductivity of MoS_2-P, MoS_2/rGO and $Co(OH)_2$-MoS_2/rGO is obtained from the four-probe method. The

electrical conductivity of MoS_2-P, which is found to be having a significantly low value of 0.007 S cm^{-1}, is appeared to be improved drastically to 0.44 and 0.61 S cm^{-1} for MoS_2/rGO and $Co(OH)_2$-MoS_2/rGO, respectively. Hence, the reduced ohmic overpotential in the case of the LSVs corresponding to MoS_2/rGO and $Co(OH)_2$-MoS_2/rGO can be directly correlated to the improvement in the electrical conductivity of the composite system. It should be noted that rGO alone also displays reasonable ORR activity, which is even substantially higher than that of the pure MoS_2-P (**Figure 2.12b**). The much improved performance of the composite of these two systems, *i.e.*, MoS_2/rGO, compared to the individual counterparts (*i.e.*, MoS_2-P and rGO separately), explicitly indicates the existence of a synergetic interaction between the participants. This interaction, fortunately turns out to be creating a favourable situation to enhance the ORR activity of the supported system.

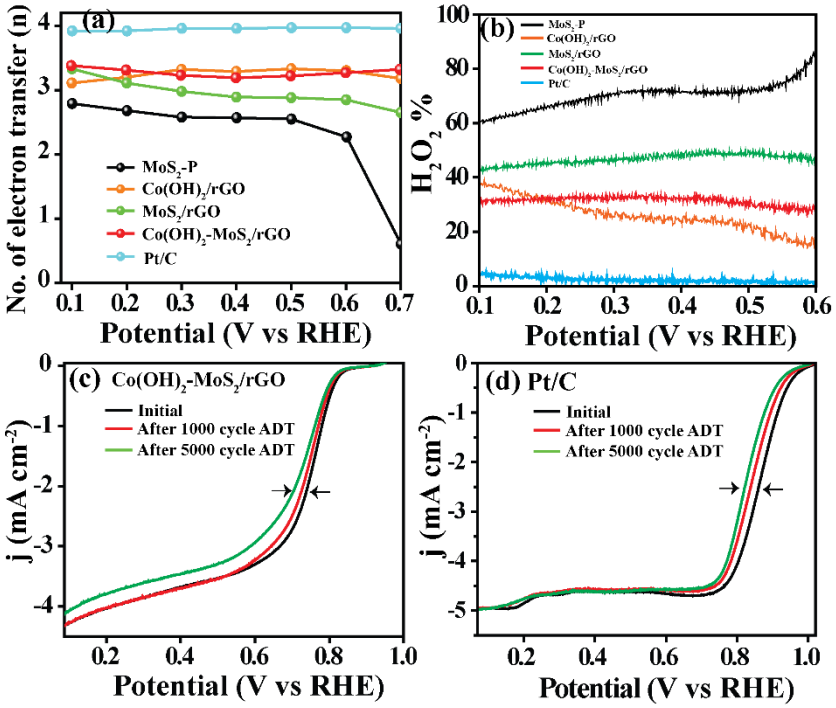

Figure 2.13. *(a) Calculated number of electron transfer (n) as a function of potential using rotating ring disc electrode (RRDE) analysis, (b) H_2O_2 % detected from the ring current during the RRDE experiment, (c-d) LSVs recorded before and after ADT of $Co(OH)_2$-MoS_2/rGO and Pt/C in O_2-saturated electrolyte at a rotation of 1600 rpm of the working electrode under a scan rate of 5 mV sec^{-1}.*

The number of electrons transferred (n) during the dioxygen reduction by $Co(OH)_2$-MoS_2/rGO has been calculated from the rotating ring disc electrode (RRDE) analysis. As given in **Figure 2.13a**, the 'n' value is found to be falling between 3.2 to 3.4 in the

potential range of 0.70 V to 0.10 V, which indicates the major contribution from the desirable 4-electron transfer. The percentage of H_2O_2 is estimated from RRDE analysis, and for $Co(OH)_2$-MoS_2/rGO it is nearly 28%, which is lower compared to the other synthesized samples (**Figure 2.13b)**. The *state-of-the-art* Pt/C shows the n value of nearly 4 and a low H_2O_2 percentage of 7%. $Co(OH)_2$-MoS_2/rGO is found to be electrochemically stable when the material was subjected to accelerated durability test (ADT) in O_2 saturated 0.1 M KOH in a potential window of 1.0 V to 0.60 V with a cycling scan rate of 100 mV s^{-1}. The LSV was taken before and after the 5000 CV cycles. The $Co(OH)_2$-MoS_2/rGO displays a 29 mV negative shift in $E_{1/2}$ after ADT without suffering a significant change in the onset potential (**Figure 2.13c**). However, Pt/C under the identical testing conditions experienced a negative shift in $E_{1/2}$ and onset potential by 39 and 15 mV, respectively (**Figure 2.13d**). This indicates that the intrinsic activity of $Co(OH)_2$-MoS_2/rGO towards ORR is not changing even after ADT compared to Pt/C, an advantage which can be credited to the layered structure of $Co(OH)_2$-MoS_2/rGO. Unlike the nanoparticles of Pt on Pt/C, the layered structure of $Co(OH)_2$-MoS_2/rGO might have acquired greater integrity with rGO, which possibly helps the system to display better resistance towards aggregation and other structural changes.

The plausible mechanism of ORR on $Co(OH)_2$-MoS_2/rGO is represented as below;

$$O_2 + * \longrightarrow O_2*$$

$$O_2* + 2H_2O + 4e^- \longrightarrow O* + 2OH^- + H_2O + 2e^-$$

$$O* + 2OH^- + H_2O + 2e^- \longrightarrow 4OH^- + *$$

The first step is the chemisorption of the O_2 molecule on the Mo surface. The charge transfer is occurring from Mo to the antibonding orbital of O_2 and leads to the elongation of the O-O bond. The next step is the coupled proton-electron transfer to O_2* and subsequently produces O* and OH- (* represents the active centre). Subsequent proton-electron transfer to O* produces OH^- and further desorbs from the catalyst surface.

2.4 Conclusions

In conclusion, a significant improvement in the electrochemical oxygen reduction reaction (ORR) activity of molybdenum sulfide (MoS_2) could be accomplished by its layer separated dispersion on reduced graphene oxide mediated by cobalt hydroxide ($Co(OH)_2$) through a hydrothermal process ($Co(OH)_2$-MoS_2/rGO). The system acquired a layer separated spread-out distribution of MoS_2 along the rGO surface, where the presence of $Co(OH)_2$ is found to be playing a vital role in maintaining a homogeneous

distribution and enhanced pore size characteristics of the dispersed layer. The composite material is showing better ORR properties in terms of the performance indices such as onset potential, half-wave potential, number of electrons involved in ORR and Tafel slope. The performance improvement in the case of $Co(OH)_2$-MoS_2/rGO can be accounted on the basis of the controlled interplay of the favourable characteristics of MoS_2, rGO and $Co(OH)_2$ in the system, where layer-separated distribution of MoS_2 on rGO, conductivity enhancement assisted by rGO and activity modulation induced by the synergistic interaction of MoS_2 with both rGO and $Co(OH)_2$ could be simultaneously maintained. Thus, overall, the present study demonstrates a viable strategy of tackling the inherent limitations, such as low electrical conductivity and limited access to the active sites faced by MoS_2 to position such layered materials among the group of potential Pt-free electrocatalysts for oxygen reduction.

2.5 References

[1] B. Lim, M. Jiang, P. H. C. Camargo, E. C. Cho, J. Tao, X. Lu, Y. Zhu, Y. Xia, *Science* **2009**, 324, 1302-1305.

[2] J.-S. Lee, G. S. Park, S. T. Kim, M. Liu, J. Cho, *Angew. Chem., Int. Ed*. **2013**, 52, 1026-1030.

[3] J. Tian, R. Ning, Q. Liu, A. M. Asiri, A. O. Al-Youbi, X. Sun, *ACS Appl. Mater. Interfaces* **2014**, 6, 1011-1017.

[4] K. Gong, F. Du, Z. Xia, M. Durstock, L. Dai, *Science* **2009**, 323, 760-764.

[5] L. Qu, Y. Liu, J.-B. Baek, L. Dai, *ACS Nano* **2010**, 4, 1321-1326.

[6] R. Zhou, S. Z. Qiao, *Chem. Commun*. **2015**, 51, 7516-7519.

[7] Z.-H. Sheng, L. Shao, J.-J. Chen, W.-J. Bao, F.-B. Wang, X.-H. Xia, *ACS Nano* **2011**, 5, 4350-4358.

[8] Y. Li, Y. Hu, S. Peng, G. Lu, S. Li, *J. Phys.Chem. C* **2009**, 113, 9352-9358.

[9] S. Cao, T. Liu, S. Hussain, W. Zeng, X. Peng, F. Pan, *Mater. Lett*. **2014**, 129, 205-208.

[10] H. Tang, K. Dou, C.-C. Kaun, Q. Kuang, S. Yang, *J. Mater. Chem. A* **2014**, 2, 360-364.

[11] W. Zhou, Z. Yin, Y. Du, X. Huang, Z. Zeng, Z. Fan, H. Liu, J. Wang, H. Zhang, *Small* **2013**, 9, 140-147.

[12] C.-B. Ma, X. Qi, B. Chen, S. Bao, Z. Yin, X.-J. Wu, Z. Luo, J. Wei, H.-L. Zhang, H. Zhang, *Nanoscale* **2014**, 6, 5624-5629.

[13] H. Liang, F. Meng, M. Cabán-Acevedo, L. Li, A. Forticaux, L. Xiu, Z. Wang, S. Jin, *Nano Lett*. **2015**, 15, 1421-1427.

[14] K. Chang, Z. Mei, T. Wang, Q. Kang, S. Ouyang, J. Ye, *ACS Nano* **2014**, 8, 7078-7087.

[15] H. Zhang, L. Lei, X. Zhang, *RSC Adv*. **2014**, 4, 54344-54348.

[16] R. Huo, W.-J. Jiang, S. Xu, F. Zhang, J.-S. Hu, *Nanoscale* **2014**, 6, 203-206.

[17] B. Cao, J. C. Neuefeind, R. R. Adzic, P. G. Khalifah, *Inorg. Chem*. **2015**, 54, 2128-2136.

[18] Y. Li, H. Wang, L. Xie, Y. Liang, G. Hong, H. Dai, *J. Am. Chem. Soc*. **2011**, 133, 7296-7299.

[19] Z. Yin, B. Chen, M. Bosman, X. Cao, J. Chen, B. Zheng, H. Zhang, *Small* **2014**, 10, 3537-3543.

[20] Z. H. Deng, L. Li, W. Ding, K. Xiong, Z. D. Wei, *Chem. Commun*. **2015**, 51, 1893-1896.

[21] F. Xiong, Z. Cai, L. Qu, P. Zhang, Z. Yuan, O. K. Asare, W. Xu, C. Lin, L. Mai, *ACS Appl. Mater. Interfaces* **2015**, 7, 12625-12630.

[22] Y.-X. Wang, S.-L. Chou, D. Wexler, H.-K. Liu, S.-X. Dou, *Chem. Eur. J*. **2014**, 20, 9607-9612.

[23] Y. Liu, L. Jiao, Q. Wu, Y. Zhao, K. Cao, H. Liu, Y. Wang, H. Yuan, *Nanoscale* **2013**, 5, 9562-9567.

[24] T. Wang, D. Gao, J. Zhuo, Z. Zhu, P. Papakonstantinou, Y. Li, M. Li, *Chem. Eur. J*. **2013**, 19, 11939-11948.

[25] T. Wang, J. Zhuo, Y. Chen, K. Du, P. Papakonstantinou, Z. Zhu, Y. Shao, M. Li, *ChemCatChem* **2014**, 6, 1877-1881.

[26] K. Zhao, W. Gu, L. Zhao, C. Zhang, W. Peng, Y. Xian, *Electrochim. Acta* **2015**, 169, 142-149.

[27] B. B. Xiao, P. Zhang, L. P. Han, Z. Wen, *Appl. Surf. Sci.* **2015**, 354, 221-228.

[28] D. C. Marcano, D. V. Kosynkin, J. M. Berlin, A. Sinitskii, Z. Sun, A. Slesarev, L. B. Alemany, W. Lu, J. M. Tour, *ACS Nano* **2010**, 4, 4806-4814.

[29] Y. Peng, Z. Meng, C. Zhong, J. Lu, W. Yu, Y. Jia, Y. Qian, *Chem. Lett*. **2001**, 30, 772-773.

[30] Y. Li, W. Zhou, H. Wang, L. Xie, Y. Liang, F. Wei, J.-C. Idrobo, S. J. Pennycook, H. Dai, *Nat Nano* **2012**, 7, 394-400.

[31] H. Hwang, H. Kim, J. Cho, *Nano Lett*. **2011**, 11, 4826-4830.

[32] V. Stengl, J. Henych, M. Slusna, P. Ecorchard, *Nanoscale Res Lett.* **2014**, 9, 167.

[33] M. Suksomboon, P. Srimuk, A. Krittayavathananon, S. Luanwuthi, M. Sawangphruk, *RSC Adv*. **2014**, 4, 56876-56882.

[34] Z. Wang, T. Chen, W. Chen, K. Chang, L. Ma, G. Huang, D. Chen, J. Y. Lee, *J. Mater. Chem. A* **2013**, 1, 2202-2210.

[35] L. Ye, W. Guo, Y. Yang, Y. Du, Y. Xie, *Chem. Mater*. **2007**, 19, 6331-6337.

[36] Z. Li, J. Wang, L. Niu, J. Sun, P. Gong, W. Hong, L. Ma, S. Yang, *J. Power Sources* **2014**, 245, 224-231.

[37] P. Xi, F. Chen, G. Xie, C. Ma, H. Liu, C. Shao, J. Wang, Z. Xu, X. Xu, Z. Zeng, *Nanoscale* **2012**, 4, 5597-5601.

[38] K. M. McCreary, A. T. Hanbicki, J. T. Robinson, E. Cobas, J. C. Culbertson, A. L. Friedman, G. G. Jernigan, B. T. Jonker, *Adv. Funct. Mater*. **2014**, 24, 6449-6454.

[39] L. Hu, Y. Ren, H. Yang, Q. Xu, *ACS Appl. Mater. Interfaces* **2014**, 6, 14644-14652.

[40] X. Zheng, J. Xu, K. Yan, H. Wang, Z. Wang, S. Yang, *Chem. Mater*. **2014**, 26, 2344-2353.

[41] K. P. Annamalai, J. Gao, L. Liu, J. Mei, W. Lau, Y. Tao, *J. Mater. Chem. A* **2015**, 3, 11740-11744.

[42] Z. Xu, Z. Li, X. Tan, C. M. B. Holt, L. Zhang, B. S. Amirkhiz, D. Mitlin, *RSC Adv.* **2012**, 2, 2753-2755.

[43] E. Desimoni, G. I. Casella, A. Morone, A. M. Salvi, *Surf. Interface Anal*. **1990**, 15, 627-634.

[44] L. Li, H. Qian, J. Ren, *Chem. Commun*. **2005**, 4083-4085.

[45] Y. Meng, *Nanomaterials* **2015**, 5, 554-564.

[46] Y. Jing, E. O. Ortiz-Quiles, C. R. Cabrera, Z. Chen, Z. Zhou, *Electrochim. Acta* **2014**, 147, 392-400.

[47] S. Dou, A. Shen, L. Tao, S. Wang, *Chem. Commun*. **2014**, 50, 10672-10675.

[48] Z.-W. Liu, F. Peng, H.-J. Wang, H. Yu, W.-X. Zheng, J. Yang, *Angew. Chem., Int. Ed*. **2011**, 123, 3315-3319.

[49] S. M. Unni, S. N. Bhange, R. Illathvalappil, N. Mutneja, K. R. Patil, S. Kurungot, *Small* **2015**, 11, 352-360.

Chapter-3

Co_9S_8 Nanoparticle-Supported Nitrogen-doped Carbon as a Robust Catalyst for Oxygen Reduction Reaction in Both Acidic and Alkaline Conditions

This chapter illustrates the synthesis of an efficient and durable catalyst for electrochemical Oxygen Reduction Reaction (ORR) which is active both in the alkaline and acidic conditions by dispersing few-layer graphitic carbon coated Co_9S_8 nanoparticles on the nitrogen-doped carbon (NVC-G) support (Co_9S_8/NVC-G). The hydrothermal route followed by heat-treatment in an inert atmosphere lead to the formation of Co_9S_8/NVC-G. The size of the Co_9S_8 nanoparticles is nearly 7-8 nm and the particles are found to be dispersed homogeneously on the NVC-G support. The few-layer graphitic carbon formed on the surface of Co_9S_8 nanoparticles is assisting to accomplish their small size and it also prevents agglomeration of the nanoparticles. The presence of Vulcan carbon, glucose, and ammonia in the reaction mixture plays a significant role in obtaining the small size and uniform distribution of the Co_9S_8 nanoparticles. The ORR activity of the obtained materials was analyzed in both 0.1 M KOH and 0.5 M H_2SO_4 solutions. Co_9S_8/NVC-G displays nearly 70 mV overpotential compared to the *state-of-the-art* Pt/C in 0.1 M KOH solution. The half-wave potential ($E_{1/2}$) difference of the present system is nearly 75 mV with the commercial Pt/C. Co_9S_8/NVC-G displays promising ORR activity in the acidic conditions as well with nearly 140 mV overpotential compared to its Pt/C counterpart. The system shows about 170 mV lower $E_{1/2}$ value with Pt/C. The system shows good stability both in acidic and basic conditions compared to the Pt/C system. The enhanced activity and stability of Co_9S_8/NVC-G could be ascribed to the reasons like homogenous dispersion of few-layer graphitic carbon coated Co_9S_8 nanoparticles on the NVC-G support and their proper anchoring with the support due to the presence of the heteroatom doped sites. Finally, testing of a single cell of a polymer electrolyte membrane fuel cell (PEMFC) was performed by employing Co_9S_8/NVC-G as the cathode catalyst and Nafion-212 as the proton exchange membrane. The system displays a maximum power density of 245 mW cm^{-2} in H_2-O_2 and 115 mW cm^{-2} in H_2-air feeding conditions, respectively. These are promising values derived from a Pt-free cathode system compared to few such reports available in the literature.

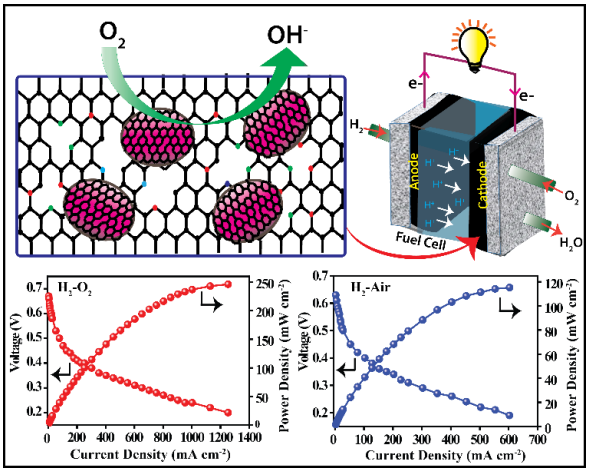

Content of this chapter is published in the following article:

ChemElectroChem 2020, 7, 3123-3134.

(https://chemistry-europe.onlinelibrary.wiley.com/doi/10.1002/celc.202000786)

3.1 Introduction

The increasing energy demand along with alarms of environmental pollution and fossil fuel depletion has forced the society to explore sustainable clean energy sources and technologies.[1, 2] The carbon emission-free power sources are receiving wide attention due to their eco-friendly and environmentally benign nature.[3] Compared to the fossil fuel based energy sources, hydrogen (H_2) is having high specific energy (142 MJ/kg) and is vital for employing as an alternate fuel owing to its carbon-neutral nature.[4] The polymer electrolyte membrane fuel cell (PEMFC) is important in this circumstance due to its high theoretical energy and power densities, high efficiency, low operating temperature and zero-emission of greenhouse gases for the conversion of H_2 into electrical energy.[5, 6] Hence, PEMFCs can be widely employed as a promising clean power technology for the stationary as well as portable applications.[7, 8] However, the sluggish kinetics of oxygen reduction reaction (ORR) on the cathode results in the energy loss and this acts as the bottleneck for accomplishing enhanced fuel cell performance.[9] Therefore, to facilitate the reactions in PEMFCs, Pt supported carbon based catalysts are being employed on the electrodes.[10] The hydrogen oxidation reaction (HOR) on the anode is faster and, therefore, it requires a relatively lower amount of Pt catalyst.[7] On the other hand, a reasonably higher amount of the Pt-based catalyst is required on the cathode for aiding ORR.[11]

Even though the Pt-based catalysts are displaying better ORR activity, the commercialization potential of PEMFCs is restricted mainly due to the issues like high cost, scarcity, low methanol tolerance and poor stability of the Pt catalysts.[6, 12] To address these issues of the Pt catalysts, various approaches have been adopted. These include the development of Pt-alloys with controlled architectures, core-shell morphologies of Pt with transition metals and, noble-metal-free ORR catalysts.[13-17] Among them, the noble-metal-free ORR catalysts are receiving substantial attention due to their low cost, improved activity, high methanol tolerance and, better stability.[18] The noble-metal-free ORR catalysts are generally comprised of metal oxide, sulfide, nitride, *etc*., supported on various carbon substrates.[19] The metal oxide-based catalysts are reported to be displaying enhanced ORR activity and stability in the alkaline conditions. However, relatively poor stability of many metal oxides in the acidic environment restricts their wide utilization for this application.[20, 21] Hence, for accomplishing the large scale commercialization of PEMFCs cost-effectively, concurrent development of the low cost, stable and efficient ORR catalysts in both acidic and alkaline conditions is

essential. In this perspective, the application of metal sulfide based catalysts is appropriate due to their noticeable ORR activity and excellent oxidative stability in the corrosive atmosphere.[22-24] Among the various metal sulfides, Co_9S_8 based catalysts are having paramount interest due to their variable oxidation states, higher catalytic activity and, stability.[23, 25-27] Though most of the reported Co_9S_8 based systems are displaying ORR activity in the alkaline medium, the performance is still lacking in the acidic conditions.[27-29] Besides, literature reports indicate that supported Co_9S_8 based systems are displaying improved catalytic activity due to the synergetic interactions and, the extended dispersion of the nanoparticles.[27, 28, 30] Therefore, rational designing of the supported Co_9S_8 based systems is certainly desirable to exhibit the ORR activity in both acidic and alkaline conditions and, for further developing the Pt-free cathodes for PEMFCs.[31, 32]

The typical carbon substrates used for supporting the nanomaterials are carbon nanotube (CNT), Vulcan carbon, heteroatom doped graphene, carbon nanofiber (CNF) *etc*.[17, 33] The carbon support plays an important role in achieving the proper dispersion of the nanomaterials and, subsequently in delivering enhanced fuel cell performance. The corrosion resistance, porosity, electrical conductivity *etc*., of the carbon greatly influence the system efficiency.[34] Due to the low cost, high surface area and better electrical conductivity, Vulcan carbon is considered as a promising substrate for anchoring the nanomaterials.[35] However, the poor stability of Vulcan carbon in the oxidative environment causes agglomeration of the supported nanoparticles during the long-term operation and this reduces the catalyst efficiency.[32, 33] It has been recognized that heteroatom doping on carbon would improve the stability of the matrix and modulates the electronic structure and adsorption energies for O_2.[36, 37] Also, heteroatom doping would assist for the uniform nucleation of nanoparticles and enhancement of the active site density.[38] Hence, for achieving the improved ORR activity and stability, supporting the nanoparticles on heteroatom-doped carbon is highly essential.

Typically, the nanoparticle deposition on Vulcan carbon can lead to the dispersion of the particles both on the surface as well as inside the micropores of carbon. The nanoparticles present in the micropores of Vulcan carbon are generally inactive towards ORR due to the ineffective formation of the “triple-phase-boundary” with the ionomer and reactant gases.[39] Hence, to improve the utilization of the nanoparticles, the extent of micropores in the Vulcan carbon has to be reduced. Literature reports are existing for the production of glucose-derived carbon through the hydrothermal carbonization

process,[34] which offers and opportunity of filling the micropores of Vulcan carbon with the glucose-derived carbon. This would eventually improve the utilization of the nanoparticles by their controlled dispersion on the carbon surface rather than in the micropores. Considering this advantage, in the present work, the Vulcan carbon-glucose combination was used in the hydrothermal system for producing the carbon support. Concurrently, nitrogen doping and nanoparticle growth occur during the hydrothermal treatment. The hydrothermal process is followed by acid washing and heat-treatment of the obtained material in an inert atmosphere to get the Co_9S_8 nanoparticle-supported nitrogen doped carbon (Co_9S_8/NVC-G) (**Figure 3.1**). The ORR activity of Co_9S_8/NVC-G was investigated in both alkaline and acidic conditions. Finally, the single cell analysis of PEMFC was performed by employing Co_9S_8/NVC-G as the cathode catalyst and Nafion-212 as the proton exchange membrane.

3.2 Experimental Section

3.2.1 Materials

Cobalt chloride hexahydrate ($CoCl_2$. $6H_2O$), glucose ($C_6H_{12}O_6$. H_2O), thiourea (CH_4N_2S) and potassium hydroxide (KOH) were procured from Sigma Aldrich Chemicals. Vulcan carbon was procured from Cabot Corporation, USA. Sulphuric acid (H_2SO_4), ammonia (NH_3), perchloric acid ($HClO_4$) and hydrogen peroxide (H_2O_2) were procured from Rankem chemicals. The Nafion-212 membrane was procured from DuPont, GmbH. 40 wt. % Pt/C was procured from Alfa Aesar. All the chemicals were used without further purification.

3.2.2 Functionalization of Vulcan carbon (fn-VC)

Dispersed about 1 g of VC in 200 mL of 30% H_2O_2 in a round bottom flask. The material was refluxed in an oil bath at 60 °C for 8 h. After reaching room temperature, filtered and washed the material with an excess quantity of DI water. The obtained black material was dried in a vacuum oven at 50 °C for 6 h. The material is hereafter called as fn-VC and used directly for further reactions.

3.2.3 Synthesis of Co_9S_8/NVC-G

For the synthesis of Co_9S_8/NVC-G, dispersed about 100 mg of fn-VC in 30 mL of DI water. To this, added 5.5 mmol of glucose ($C_6H_{12}O_6$. H_2O) and stirred for 2 h at room temperature. About 1.2 mmol of cobalt chloride hexahydrate ($CoCl_2$. $6H_2O$), 2.5 mmol of thiourea (CH_4N_2S) and 2 mL of ammonia (NH_3) were added in the above mixture

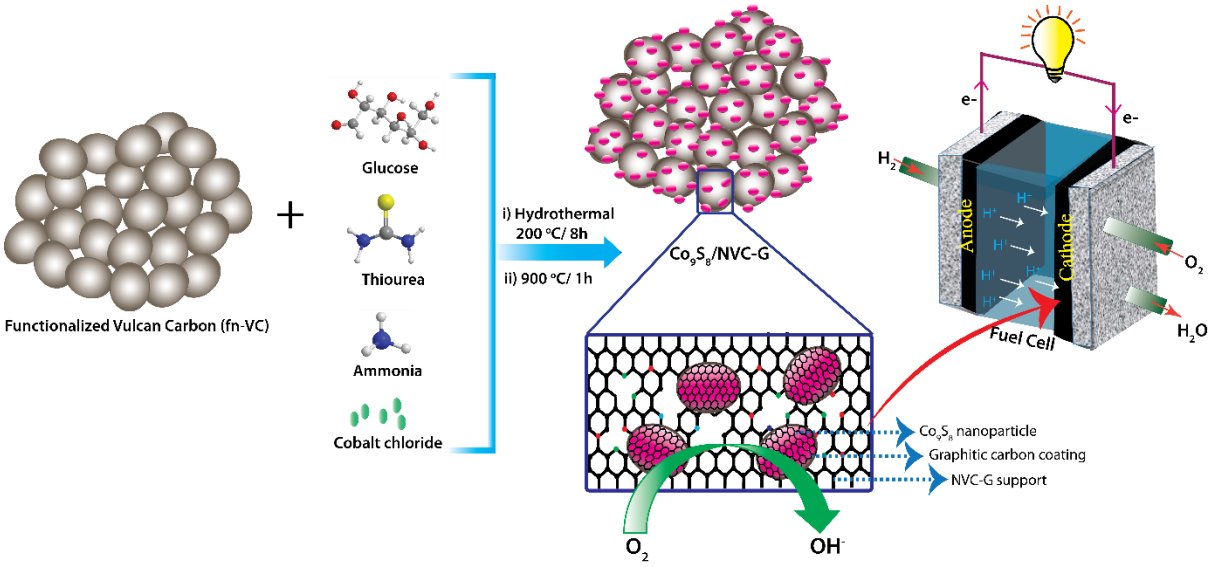

Figure 3.1. *Schematic illustration of the synthesis of Co_9S_8/NVC-G by following the two-step process; the hydrothermal route followed by heat treatment of the material at 900 °C for 1 h in an inert atmosphere lead to Co_9S_8/NVC-G. The application of the material was demonstrated by employing Co_9S_8/NVC-G as the cathode catalyst in PEMFC for facilitating ORR.*

and stirred for 1 h. Transferred the entire mixture into a Teflon lined autoclave and carried out the reaction at 200 °C for 8 h. After reaching room temperature, filtered the material with an excess quantity of DI water and dried at 60 °C in a vacuum oven for 5 h. The obtained powder material was subjected to acid washing in 0.5 M H_2SO_4 solution at 80 °C for 8 h to remove any unreacted metal precursors. The obtained material was washed with a copious amount of DI water and dried in a vacuum oven at 60 °C for 5 h. The material obtained in this step contains the mixed phases of CoS and Co_9S_8 supported on nitrogen-doped carbon. The powder material was heat-treated at 900 °C for 1 h in argon atmosphere to convert the CoS phase present in the system to the Co_9S_8 phase. The obtained material is named hereafter as Co_9S_8/NVC-G.

For comparison, materials were synthesized in the absence of fn-VC, glucose and NH_3 by keeping the other parameters identical as above and thus obtained materials are named as Co_9S_8/NC-G, Co_9S_8/NVC, and Co_9S_8/VC-G, respectively. NVC-G was prepared by treating fn-VC, glucose, and NH_3 through the hydrothermal route at 200 °C for 8 h.

3.2.4 Electrochemical Analysis

In order to analyze the electrochemical activity of the as synthesized materials, the three-

electrode set-up was used. A glassy carbon electrode (0.196 cm^2) was used as the working electrode and a graphite rod was used as the counter electrode. In the KOH electrolyte, Hg/HgO and in the H_2SO_4 electrolyte, $Hg/HgSO_4$ were used as the reference electrode, respectively. Catalyst ink for the electrochemical analysis was prepared by mixing 5 mg of the catalyst in 1 mL of DI water-isopropyl alcohol mixture (3:1) and 40 µL of 5 wt. % Nafion solution (DuPont, GmbH) by bath sonication. Drop coated an aliquot of the catalyst ink on the glassy carbon electrode and kept it for drying under an IR lamp. The catalyst loading used was 0.25 mg cm^{-2} in 0.1 M KOH solution. Since ORR kinetics is moderately slower for non-precious-metal based systems in acidic medium, the catalyst loading used in 0.5 M H_2SO_4 was 0.50 mg cm^{-2}.[18, 40] For comparison, the *state-of-the-art* 40 wt. % Pt/C was also investigated under identical conditions. For this purpose, the catalyst slurry was prepared by following the above method and about 10 µL of the aliquot was drop coated on the glassy carbon electrode. To understand the stability of the catalyst, 5000 cycles of accelerated durability test (ADT) was performed in both the alkaline and acidic conditions. For this, CV was performed in O_2-saturated electrolyte in the potential window of 0.60 to 1.0 V *vs*. RHE with a scan rate of 100 mV sec^{-1}. The LSVs were performed before and after ADT in O_2-saturated electrolyte at 1600 rpm of the working electrode and with a scan rate of 10 mV sec^{-1}.

The Koutecky-Levich (K-L) equation was used to obtain the kinetics of the reaction and the corresponding equations are given as below:

$$\frac{1}{j} = \frac{1}{j_L} + \frac{1}{j_k}$$

$$\frac{1}{j} = \frac{1}{B\omega^{1/2}} + \frac{1}{j_k}$$

where, j is the measured current density, j_k is the kinetic current density, j_L is the diffusion-limited current density and ω is the angular velocity of the electrode (ω = 2πf/60, f is the rotation speed).

$$B = 0.62nFC_0^*D_0^{2/3}\nu^{-1/6}$$

$$j_k = nFKC_0^*$$

where, n is the number of electrons transferred during the reaction, F is the Faradays constant (96485 C mol^{-1}), C_0^* is the bulk concentration of O_2 (1.22 x 10^{-6} mol cm^{-3}), D_0 is the diffusion coefficient of O_2 (1.9 x 10^{-5} cm^2 s^{-1}), ν represents the kinematic viscosity

of the electrolyte (0.01 cm^2 s^{-1}) and k is the electron transfer rate constant. By plotting 1/j against $\omega^{-1/2}$, a straight line will be generated with the slope corresponding to 1/B. The rotating ring disc electrode (RRDE) analysis was performed to find out the number of electron transfer (n) and percentage of hydrogen peroxide (% H_2O_2) produced during the reaction by using the following equations:

$$n = \frac{4\ I_d}{(I_d + I_r/N)}$$

$$\%\ H_2O_2 = \frac{200 * I_r/N}{(I_d + I_r/N)}$$

where, I_r, I_d, and N are the ring current, disc current and collection efficiency (0.37), respectively.

3.2.5 Membrane electrode assembly (MEA) preparation and single cell analysis

The membrane (Nafion-212) pre-treatment was carried out in sequential with 5% H_2O_2 and 1 M H_2SO_4, respectively. First, the membrane was treated at 80 °C for 1 h with 5% H_2O_2 to remove any organic impurities. It was then boiled at 100 °C in DI water for 1 h. In order to protonate, the membrane was treated with 1 M H_2SO_4 at 80 °C for 1 h. Subsequently, it was boiled for 1 h in DI water at 100 °C and stored at room temperature in DI water. For the fuel cell performance analysis, Co_9S_8/NVC-G was employed as the cathode catalyst, Pt/C was used as the anode catalyst and the pre-treated Nafion-212 membrane was used as the separator cum solid electrolyte. The electrodes were made by brush coating the catalyst slurry on a gas diffusion layer (GDL) with a loading of 2.5 mg cm^{-2} of the Pt-free catalyst on the cathode and 0.50 mg_{Pt} cm^{-2} of the 40 wt.% Pt/C catalyst on the anode. The membrane electrode assembly (MEA) was fabricated by sandwiching the anode-membrane-cathode combination at 0.25 ton for 1 min. at 130 °C in a hot-press (CARVER, USA). The active area of the MEA was 4 cm^2. The MEA was assembled in a standard single-cell fixture (Fuel Cell Technologies Inc., USA) with the single serpentine flow-field pattern on the graphite plates. The fuel cell performance was analyzed by using a commercial fuel cell test station (Fuel Cell Technologies Inc., USA). Current (I) – Voltage (V) polarization tests were performed in the H_2-O_2 and H_2-air feeding conditions. All the measurements were carried out at 60 °C with a relative humidity of 100%. For comparison, an MEA based on Pt/C as the cathode catalyst (0.50 mg_{Pt} cm^{-2}) was also performed under similar conditions.

3.3 Result and Discussion

3.3.1 TEM Analysis

The morphological characteristics of the synthesized materials were examined by TEM and FESEM analyses. The TEM images of Co_9S_8/NVC-G is presented in **Figure 3.2**. The dispersion of Co_9S_8 nanoparticles on the nitrogen-doped carbon surface is confirmed from **Figure 3.2a**. The high magnification image of the marked portion in **Figure 3.2a** is provided as **Figure 3.2b,** which illustrates the uniform dispersion of the Co_9S_8 nanoparticles on the NVC-G support. This could be accomplished due to the nitrogen doping on carbon, which provides the proper interaction of Co_9S_8 nanoparticles with the NVC-G support. The SAED pattern presented in the inset of **Figure 3.2b** confirms the crystalline nature of Co_9S_8/NVC-G. **Figure 3.2c** presents the high magnification image of the Co_9S_8 nanoparticles, which indicates the presence of the few-layer surface coating of the graphitic carbon on the Co_9S_8 nanoparticle. The yellow

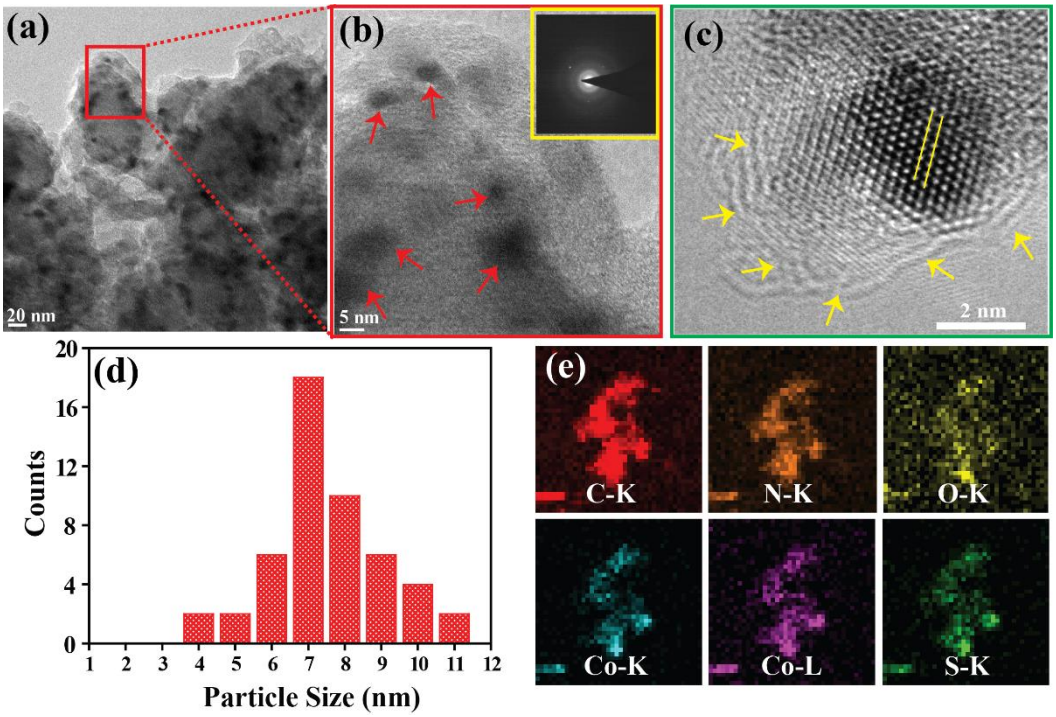

Figure 3.2. *(a) TEM image of Co_9S_8/NVC-G indicating the homogenous distribution of the Co_9S_8 nanoparticles on NVC-G, (b) high magnification image of the marked portion in image (a) and the inset represents the SAED pattern, (c) high magnification image of the Co_9S_8 nanoparticle in Co_9S_8/NVC-G with the arrow marks indicating the few-layer graphitic carbon coating on the Co_9S_8 nanoparticle surface, (d) particle size distribution analysis of Co_9S_8/NVC-G, and (e) TEM-EDX elemental mapping showing the uniform distribution of carbon, nitrogen, oxygen, cobalt, and sulfur in Co_9S_8/NVC-G.*

arrow marks in **Figure 3.2c** point towards the carbon coating formed on the surface of the Co_9S_8 nanoparticles. It can be elucidated from **Figure 3.2c** that the number of surface carbon layers on the Co_9S_8 nanoparticles is less than 10. The small size of the Co_9S_8 nanoparticle is achieved due to the formation of a thin carbon layer on the nanoparticle surface, which in turn is derived from glucose during the hydrothermal treatment. This would prevent the further growth and agglomeration of the Co_9S_8 nanoparticles. The d-spacing value of Co_9S_8 is calculated from **Figure 3.2c** and is about 0.29 nm, which is assigned to the (311) lattice plane of Co_9S_8.[24, 28] The d-spacing value of the surface coating of Co_9S_8 is calculated and is nearly 0.34 nm, corresponds to the (002) lattice plane of the graphitic carbon.[41, 42] The histogram provided in **Figure 3.2d** designates that the as-formed Co_9S_8 nanoparticles are around 7-8 nm in size in Co_9S_8/NVC-G. **Figure 3.2e** illustrates the TEM-EDX elemental mapping of Co_9S_8/NVC-G and confirms the uniform distribution of carbon, nitrogen, cobalt, and sulfur in the system.

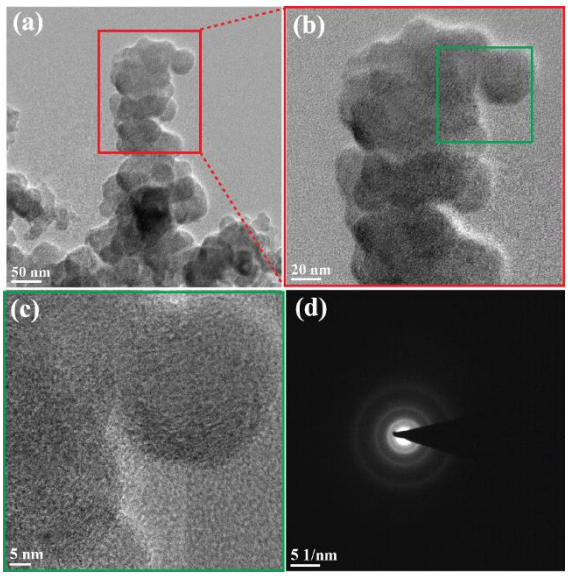

Figure 3.3. *(a-c) TEM images of NVC-G at different magnifications and (d) the corresponding SAED pattern.*

The TEM images of NVC-G is provided in **Figure 3.3**. The fused spherical morphology of NVC-G is confirmed from the TEM images (**Figure 3.3a-b**). It is clear from the figure that, there is no separate carbon sheet/agglomerate present in NVC-G. This further validates that, after the hydrothermal treatment, the glucose derived carbon is well incorporated with the Vulcan carbon and also on the surface of the Co_9S_8 nanoparticles. To understand the role played by the carbon support for obtaining the uniformly distributed Co_9S_8 nanoparticles, few control samples were prepared

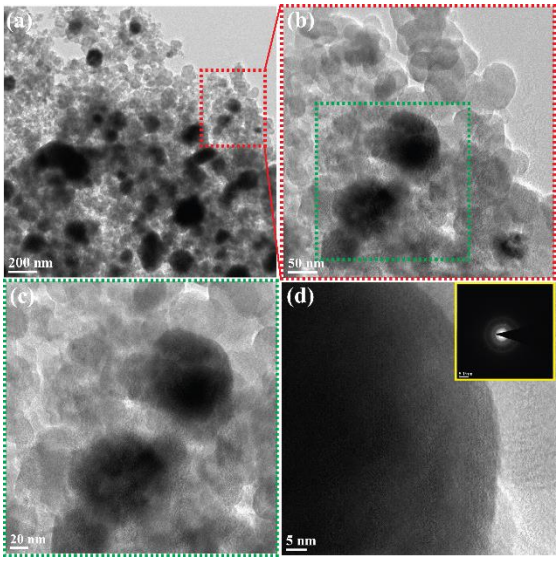

Figure 3.4. *TEM images of* Co_9S_8/NVC *(prepared in the absence of glucose) recorded at different magnifications.*

(explained in the Experimental Section). The TEM images of the material synthesized in the absence of glucose (Co_9S_8/NVC) are presented in **Figure 3.4**. It is observed from **Figure 3.4** that, in the absence of glucose during the reaction, the size of the formed Co_9S_8 nanoparticles is above 100 nm. This could be attributed that, in the absence of the glucose-derived carbon layer on the nanoparticle surface, they are undergoing coalescence with the neighbouring particles. This would result in the formation of the Co_9S_8 nanoparticles with a larger size. The material prepared in the absence of fn-VC is

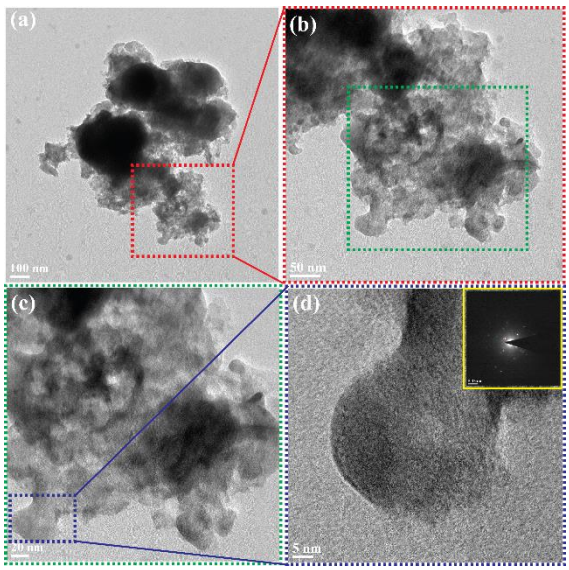

Figure 3.5. *TEM images of* Co_9S_8/NC-G *(prepared in the absence of fn-VC) recorded at different magnifications.*

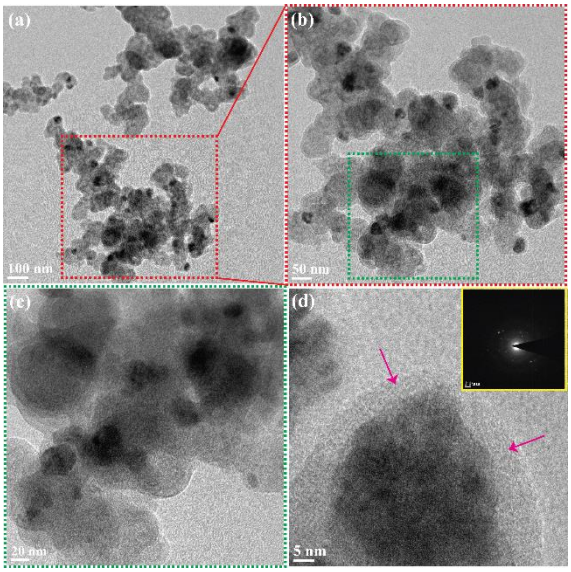

Figure 3.6. *TEM images of* Co_9S_8/VC-G *(prepared in the absence of ammonia) recorded at different magnifications.*

named as Co_9S_8/NC-G and the corresponding TEM images are provided in **Figure 3.5**. In the absence of fn-VC, the Co_9S_8 nanoparticles seem to be agglomerated as evident from **Figure 3.5a-d**. This could be ascribed to the lack of proper anchoring sites for the cobalt ions before the hydrothermal synthesis. This would result in the random growth of the nanoparticles during the hydrothermal synthesis and finally leading to the formation of agglomerated Co_9S_8 nanoparticles. The material prepared in the absence of ammonia is termed as Co_9S_8/VC-G and the corresponding TEM images are illustrated in **Figure 3.6**. It is clear from **Figure 3.6a-d** that the Co_9S_8 nanoparticles having the size in the range of 50-60 nm are formed in the absence of ammonia, and they are randomly distributed on the carbon support. **Figure 3.6d** confirms the formation of the surface carbon layer on the Co_9S_8 nanoparticles, which is indicated with the arrow marks. Even though the particle size is reduced due to the formation of the surface carbon layer on Co_9S_8, the dispersion of the Co_9S_8 nanoparticles seems to be poor. This specifies the significance of nitrogen doping in accomplishing the uniformly distributed Co_9S_8 nanoparticles on the carbon support. Further, nitrogen doping would induce the proper interaction of Co_9S_8 nanoparticles with the support and thus helps to provide enhanced stability in the system. Hence, it can be concluded that, in order to obtain the homogeneously distributed Co_9S_8 nanoparticles with smaller size on the carbon support, along with cobalt chloride and thiourea, the simultaneous presence of fn-VC, glucose, and ammonia in the reaction mixture is indeed essential.

3.3.2 FESEM Analysis

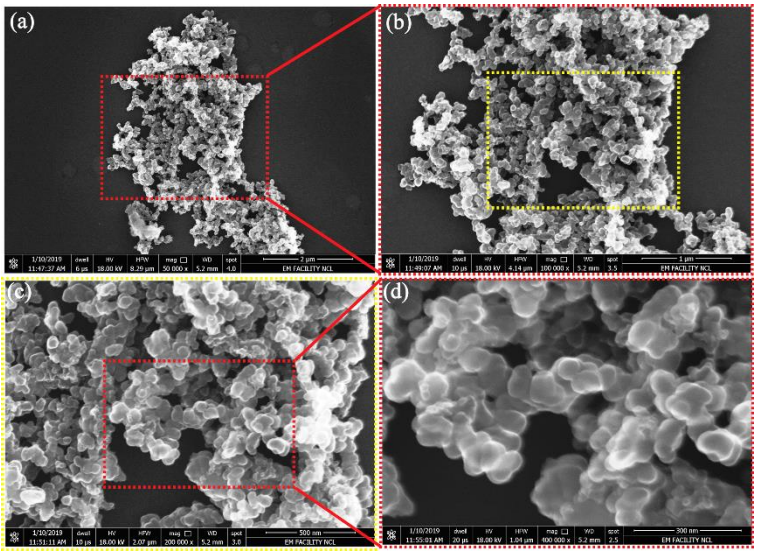

Figure 3.7. *FESEM images of NVC-G recorded at different magnifications.*

The FESEM images of NVC-G are presented in **Figure 3.7**. The images clearly specify the porous morphology of the nitrogen-doped carbon (NVC-G). From **Figure 3.7a-d**, the absence of discrete carbon sheet/agglomerate in the system confirms that the glucose-derived carbon is integrated with the Vulcan carbon. This further validates the results obtained from the TEM analysis. **Figure 3.8** shows the FESEM images of Co_9S_8/NVC-G recorded at different magnifications. **Figure 3.8d** displays the porous morphology of Co_9S_8/NVC-G and is indicated with the arrow marks. Due to the ultra-small size of Co_9S_8 nanoparticles, such particles are not evident in the FESEM images. The SEM-EDX elemental mapping of Co_9S_8/NVC-G is presented in **Figure 3.9**. The

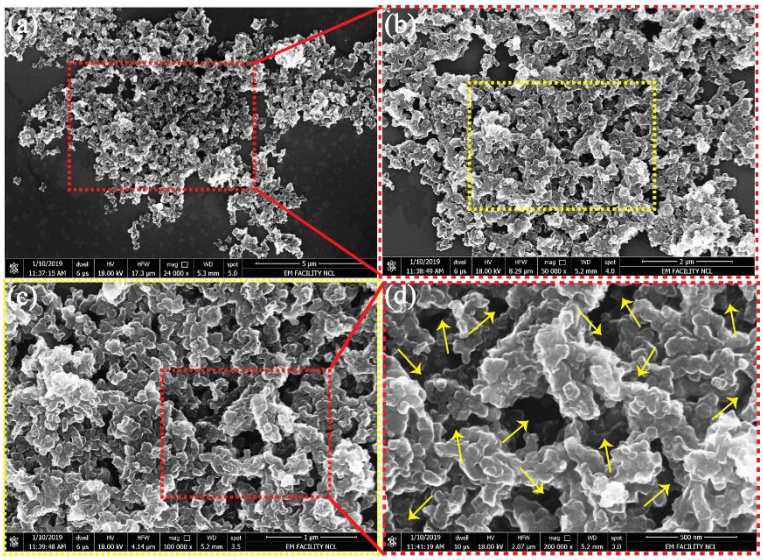

Figure 3.8. *FESEM images of Co_9S_8/NVC-G recorded at different magnifications.*

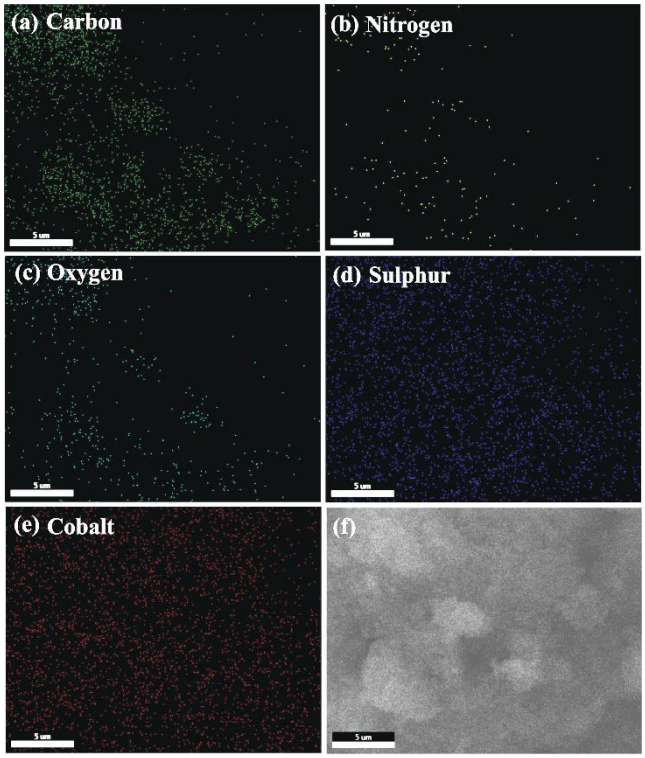

Figure 3.9. *SEM-EDX elemental mapping of Co_9S_8/NVC-G: (a) carbon, (b) nitrogen, (c) oxygen, (d) sulfur, (e) cobalt, and (f) the image corresponds to the elemental mapping.*

homogenous distribution of carbon, nitrogen, cobalt, and sulfur in Co_9S_8/NVC-G is evident from the EDX elemental mapping (**Figure 3.9)**. The minute amount of oxygen detected during the elemental mapping could be originated from the adsorbed surface oxygen during the sample preparation.

3.3.3 XRD Analysis

The composition and phase of the synthesized materials were examined by XRD. **Figure 3.10** represents the XRD profile of Co_9S_8/NVC-G in comparison with the other synthesized materials and the standard JCPDS pattern of Co_9S_8 is provided for reference. The XRD spectrum of Co_9S_8/NVC-G displays sharp peaks at 15.2°, 29.6°, 31.1°, 39.4°, 47.4°, 51.9°, and 73.2°, corresponding to the (111), (311), (222), (331), (511), (440) and (731) lattice planes of Co_9S_8, respectively.[43] This confirms the formation of the Co_9S_8 phase in Co_9S_8/NVC-G. The sharp peaks of the Co_9S_8 phase in Co_9S_8/NVC-G designate the crystalline nature of the as-formed material. The XRD spectra of Co_9S_8/VC-G, Co_9S_8/NVC and, Co_9S_8/NC-G are also exhibiting the peaks correspond to Co_9S_8. The peaks at 25.2° and 43.3° in NVC-G are corresponding to the (002) and (110) lattice planes of carbon, respectively.[44, 45] In Co_9S_8/NVC-G, after

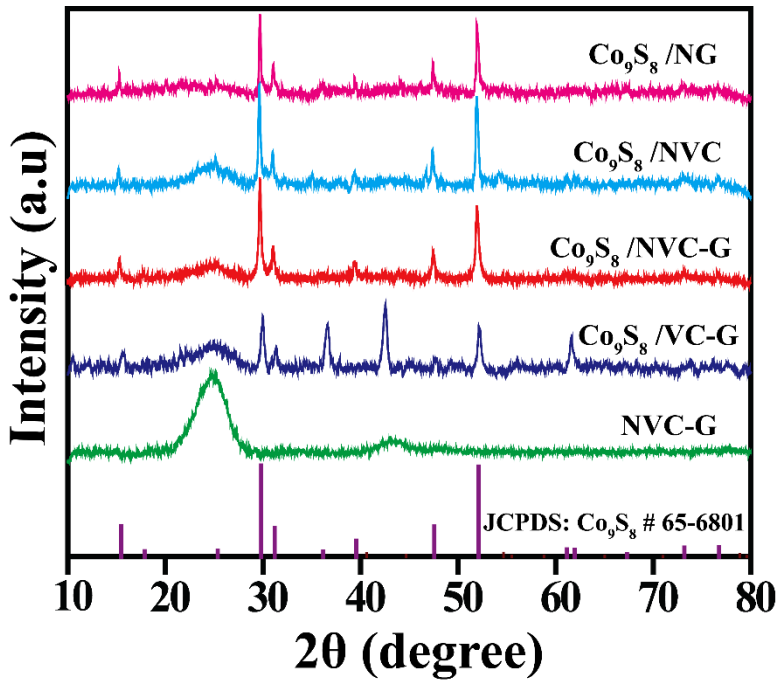

Figure 3.10. *XRD profile comparison of the synthesized materials along with the standard JCPDS pattern of* Co_9S_8.

anchoring the Co_9S_8 nanoparticles, the intensity corresponds to the (002) plane of carbon is reduced. This confirms the dispersion of Co_9S_8 nanoparticles on the nitrogen-doped carbon surface. The XRD spectra recorded before and after the heat-treatment of the material at 900 °C is provided in **Figure 3.11**. The presence of the mixed phases of CoS and Co_9S_8 on NVC-G support before heat-treatment of the system is evident from

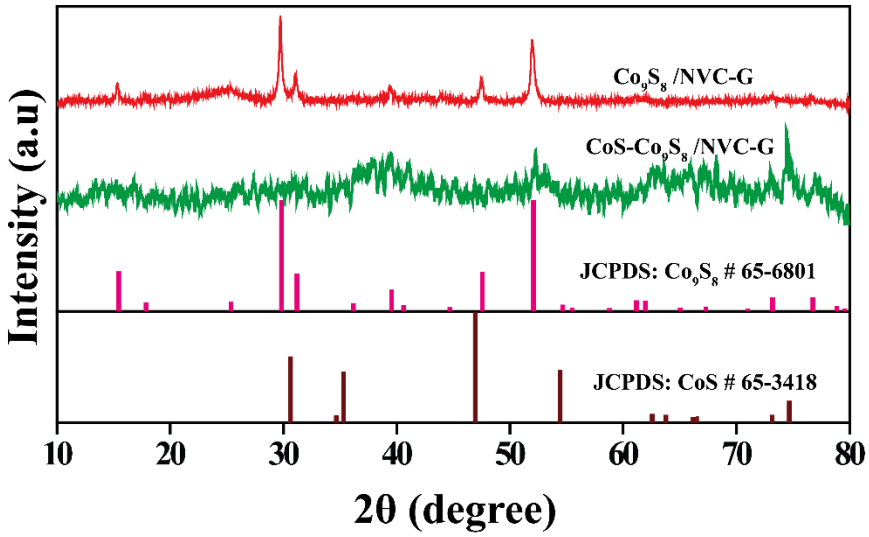

Figure 3.11. *XRD comparison of the materials obtained before and after the heat-treatment at 900 °C for 1 h in inert atmosphere.*

Figure 3.11. Also, after the heat-treatment at 900 °C in an inert atmosphere, the conversion of CoS into the Co_9S_8 phase is confirmed and leads to the formation of Co_9S_8/NVC-G. This could be ascribed that at high temperature, sulfur atoms would leave from the system and eventually the system transforms from the stoichiometric composition (CoS) to a non-stoichiometric composition (Co_9S_8).[46]

3.3.4 Thermo gravimetric Analysis

To evaluate the thermal stability and weight percentage of Co_9S_8 in Co_9S_8/NVC-G, thermogravimetric analysis (TGA) was performed in O_2 atmosphere from room temperature to 900 °C with a ramp rate of 10 °C min^{-1}. **Figure 3.12** illustrates the TGA profile of Co_9S_8/NVC-G in comparison with NVC-G. The sharp weight reduction in NVC-G at ~410 °C is due to the oxidation of carbon into CO_2. The weight loss occurred below 100 °C in Co_9S_8/NVC-G is due to the removal of the adsorbed water molecules. Co_9S_8/NVC-G shows stability up to 350 °C and a major weight loss observed after 350 °C is due to the oxidation of carbon and the conversion of Co_9S_8 into Co_3O_4.[43] The weight percentage of Co_9S_8 in Co_9S_8/NVC-G is calculated from TGA and is found to be nearly 20 %.

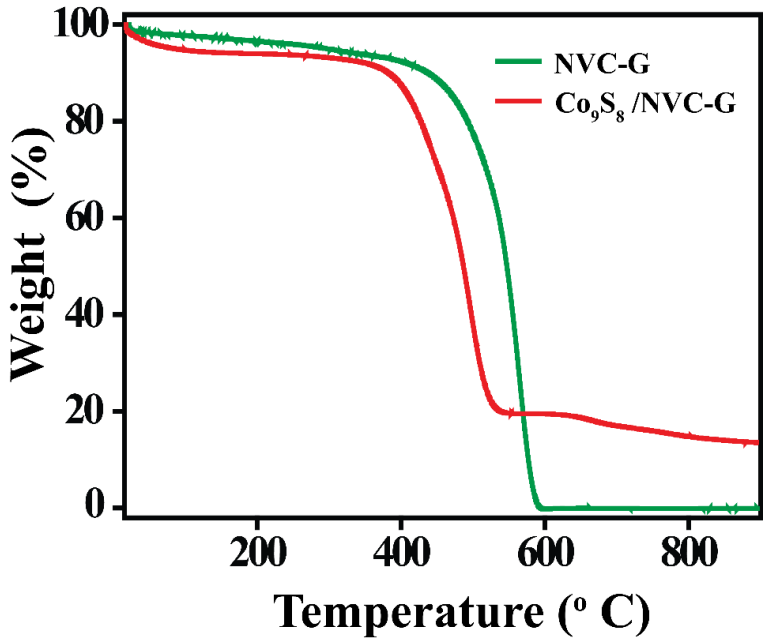

Figure 3.12. *TGA profiles of Co_9S_8/NVC-G and NVC-G performed in O_2 atmosphere from room temperature to 900 °C with a heating rate of 10 min^{-1}.*

3.3.5 Raman Analysis

Raman spectroscopy was performed to analyze the extent of defects in the carbon present in the system. **Figure 3.13** presents the comparative Raman spectra of the as synthesized materials. Co_9S_8/NVC-G displays the peaks at 463.5 and 671.1 cm^{-1} correspond to the vibrational modes of Co_9S_8, respectively.[43, 47, 48] In addition to the peaks of Co_9S_8, the synthesized materials display the D and G-band corresponding to the carbon. The D-band is arising due to the structural disorder (A_{1g}-mode) and the G-band is due to the $2E_{2g}$ vibrational mode of the carbon.[30, 49] The D and G-band of fn-VC are appeared at 1318 and 1584 cm^{-1}, respectively. However, a shift towards the higher wavenumber is observed for Co_9S_8/NVC-G and the corresponding values of D and G-band are 1338 and 1594 cm^{-1}, respectively. This is due to the inclusion of nitrogen on the carbon framework, which induces the compressive stress on the carbon in Co_9S_8/NVC-G.[50] **Figure 3.13b** illustrates the comparative I_D/I_G values of fn-VC, NVC-G, Co_9S_8/VC-G, Co_9S_8/NVC-G, Co_9S_8/NVC and, Co_9S_8/NC-G. The corresponding I_D/I_G values are 1.32, 1.19, 1.19, 1.25, 1.26 and 1.19, respectively. The lower I_D/I_G values of the synthesized materials indicate that, as compared to fn-VC, the degree of graphitization is improved in the synthesized materials. This could be attributed to the improved graphitization achieved after heat-treatment of the material at 900 °C in the inert atmosphere. This would result in the reduction of the I_D/I_G values compared to fn-VC. The slightly higher I_D/I_G value in Co_9S_8/NVC-G compared to the other synthesized

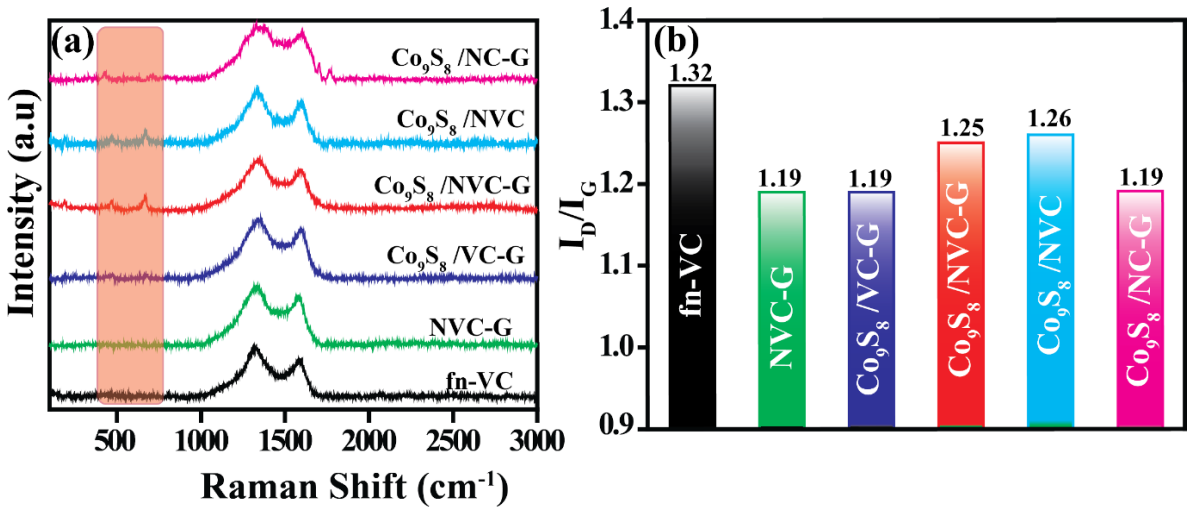

Figure 3.13. *(a) Raman spectra of the synthesized materials in comparison with fn-VC and the box indicates the characteristic peak position of Co_9S_8 and (b) bar diagram illustrating the I_D/I_G ratio of the samples calculated from the corresponding Raman spectra.*

materials designates that more amount of nitrogen is incorporated on the carbon framework in Co_9S_8/NVC-G compared to the other synthesized materials during the course of the reaction.

3.3.6 Surface Area and Pore-size Distribution Analysis

The Brunauer-Emmet-Teller (BET) method was used to analyze the surface area and pore-size distribution of the synthesized materials. The adsorption/desorption status of the gas at relative pressure on the sample surface is measured to determine the surface area of the material. From **Figure 3.14a**, it is deduced that the surface area of fn-VC is 191 $m^2\ g^{-1}$ and the corresponding value of Co_9S_8/NVC-G is 120 $m^2\ g^{-1}$. Compared to fn-VC, the drop in the surface area of Co_9S_8/NVC-G could be attributed to the presence of Co_9S_8 nanoparticles on the surface of NVC-G. The degree of micropores present in Co_9S_8/NVC-G is found to be reduced as compared to that in fn-VC (**Figure 3.14b**). This is due to the formation of glucose-derived carbon on the micropores of fn-VC during the hydrothermal treatment.

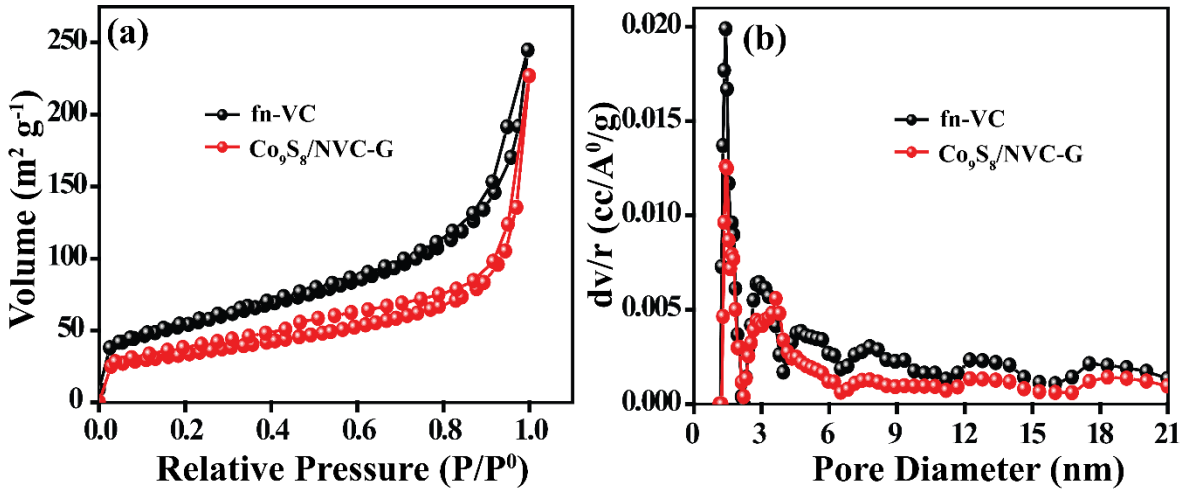

Figure 3.14. *(a) N_2 adsorption-desorption isotherms recorded for measuring the surface area of Co_9S_8/NVC-G in comparison with fn-VC and, (b) pore-size distribution comparison of Co_9S_8/NVC-G and fn-VC.*

3.3.7 XPS Analysis

The X-ray photoelectron spectroscopy (XPS) analysis was performed to understand the electronic states of the elements and the composition of the obtained material. **Figure 3.15** represents the XPS spectra of the as-prepared materials. **Figure 3.15a** illustrates the comparative survey spectra of NVC-G and Co_9S_8/NVC-G. The survey spectrum confirms the presence of carbon, nitrogen, cobalt, and sulfur in Co_9S_8/NVC-G. The

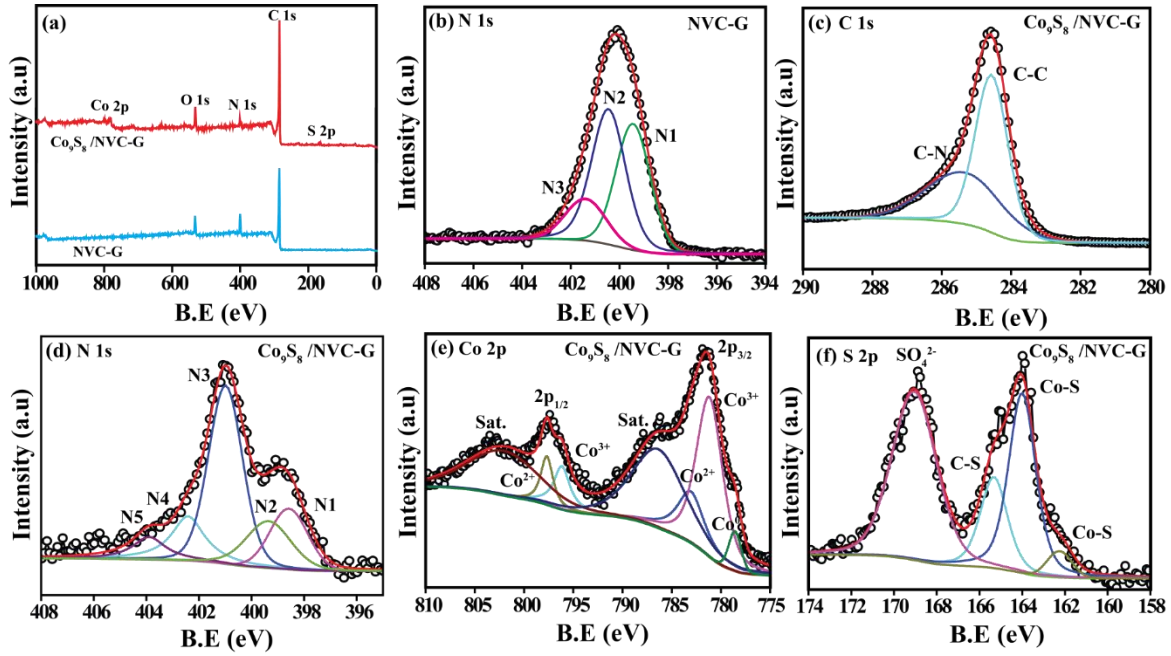

Figure 3.15. *XPS analysis of NVC-G and Co_9S_8/NVC-G: (a) comparative survey scan spectra of NVC-G and Co_9S_8/NVC-G, (b) deconvoluted N 1s spectra of NVC-G, (c) deconvoluted C 1s spectra of Co_9S_8/NVC-G, (d) deconvoluted N 1s spectra of Co_9S_8/NVC-G, (e) deconvoluted Co 2p spectra of Co_9S_8/NVC-G and (f) deconvoluted S 2p spectra of Co_9S_8/NVC-G.*

deconvoluted N 1s spectra of NVC-G is illustrated in **Figure 3.15b**. The spectra indicate the three kinds of nitrogen in NVC-G. The peaks appeared at 399.4, 400.6 and 401.4 eV correspond to the pyrrolic-N (N1), graphitic-N (N2) and quaternary-N (N3) present in NVC-G, respectively.[51] The deconvoluted C 1s spectra of Co_9S_8/NVC-G is shown in **Figure 3.15c**. The peak present at 284.5 eV corresponds to the sp^2 hybridized carbon.[52, 53] The peak appeared at 285.4 eV is characteristic of the C-N interactions in Co_9S_8/NVC-G.[43, 54] In agreement with this, the deconvoluted N 1s spectra of Co_9S_8/NVC-G display the five types of nitrogen (**Figure 3.15c**). The peaks present at 398.6, 399.4, 400.9, 402.2 and 403.7 eV correspond to the pyridinic-N (N1), pyrrolic-N (N2), graphitic-N (N3), quaternary-N (N4) and pyridinic N-oxide (N5) present in Co_9S_8/NVC-G, respectively.[51] The atomic percentage of nitrogen present in Co_9S_8/NVC-G is around 4.9 %. Out of the total nitrogen content, the occurrence of pyridinic-N and graphitic-N is nearly 27.5% and 45.6%, respectively in Co_9S_8/NVC-G. From **Figure 3.15d**, it is observed that after the heat-treatment at 900 °C, the pyrrolic-N amount in NVC-G is decreased and the amount of pyridinic-N and graphitic-N is increased. This could be attributed to the poor thermal stability of the pyrrolic-N at a

higher temperature.[55] The literature reports indicate that the pyridinic-N and graphitic-N are relatively stable at high temperatures than the pyrrolic-N.[56] Also, the pyridinic-N and graphitic-N would facilitate the adsorption of O_2 and improve the ORR activity.[9, 56] Therefore, the presence of the pyridinic and graphitic type nitrogen in Co_9S_8/NVC-G would contribute to improved ORR activity of the system. The deconvoluted cobalt XPS spectra of Co_9S_8/NVC-G indicate the peaks at 781.2 and 796.3 eV corresponding to the $2P_{3/2}$ and $2P_{1/2}$ states of Co^{+3} in Co_9S_8, respectively.[57] The peaks at 783.1 and 797.8 eV indicate the $2p_{3/2}$ and $2p_{1/2}$ states of Co^{+2} present in Co_9S_8, respectively.[57] The minute amount of cobalt in Co_9S_8/NVC-G is present in the zero oxidation state, which is designated with the peak at 778.6 eV.[58] The satellite peaks are present at 786.6 and 802.4 eV, respectively. The deconvoluted sulfur spectra display the peaks at 162.3 and 163.9 eV, which are attributed to the Co-S interaction in Co_9S_8/NVC-G, respectively.[28] The presence of C-S interaction is indicated with the peak at 165.3 eV in the deconvoluted sulfur spectra and this could be originated from the interface between the Co_9S_8 and carbon.[59] The sulfate ion is indicated with the peak at 169.1 eV, feasibly formed during the sample preparation. Hence, it is concluded from the material characterizations that the heat-treatment of the materials at 900 °C does not only provide the phase conversion of CoS into the Co_9S_8 but it also transforms the pyrollic nitrogen into the pyridinic and graphitic type nitrogen in the carbon structure.

3.3.8 Electrochemical Analysis

After the structural characterizations, the electrochemical analysis was performed in both 0.1 M KOH and 0.5 M H_2SO_4 solutions, respectively. For this, the three-electrode set-up was employed with glassy carbon as the working electrode, a graphite rod as the counter electrode and Hg/HgO (in the alkaline electrolyte) or $Hg/HgSO_4$ (in the acidic electrolyte) as the reference electrode, respectively.

3.3.8a ORR Analysis in Alkaline Condition

The examination of the material in 0.1 M KOH solution for ORR is presented in **Figure 3.16**. The cyclic voltammograms (CVs) of Co_9S_8/NVC-G in N_2 and O_2-saturated 0.1 M KOH solution performed at a scan rate of 50 mV sec^{-1} and 900 rpm of the working electrode are illustrated in **Figure 3.16a**. It is deduced from **Figure 3.16a** that Co_9S_8/NVC-G displays the sigmoid nature in the O_2-saturated condition. The sigmoid feature of CV in the O_2-saturated condition indicates the favourable reduction of O_2 in

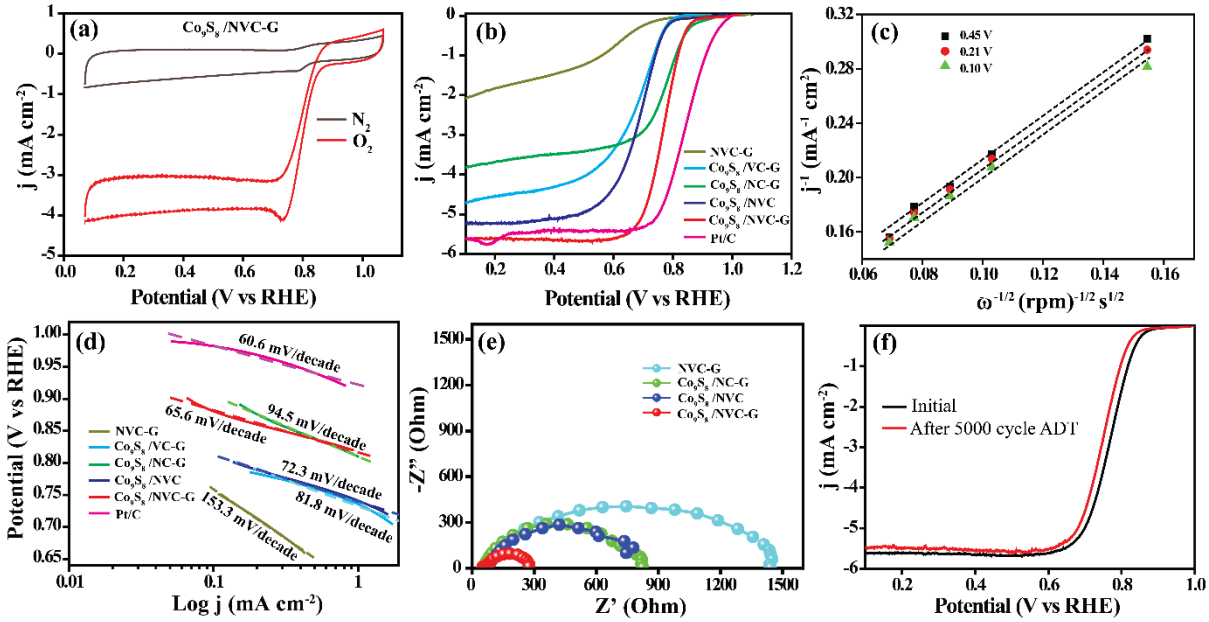

Figure 3.16. *(a) Cyclic voltammograms of Co_9S_8/NVC-G performed in N_2- and O_2-saturated 0.1 M KOH solution at a scan rate of 50 mV sec^{-1} and 900 rpm of the working electrode, (b) comparative linear sweep voltammograms (LSVs) of the samples performed in O_2-saturated 0.1 M KOH solution at 1600 rpm of the working electrode recorded at a scan rate of 10 mV sec^{-1}, (c) Koutecky-Levich plots of Co_9S_8/NVC-G, (d) Tafel plot comparison of the samples, (e) Nyquist plots of the samples recorded at 0.60 V vs. RHE, and (f) LSVs recorded before and after ADT of Co_9S_8/NVC-G in O_2-saturated 0.1 M KOH solution at 1600 rpm with a scan rate of 10 mV sec^{-1}.*

Co_9S_8/NVC-G. This demonstrates that Co_9S_8/NVC-G is facilitating the conversion of O_2 into hydroxyl ions during ORR. More insightful information about the ORR activity of the prepared materials is explained in the following section.

To acquire detailed information on the ORR activity of the prepared materials, linear sweep voltammetry (LSV) has been performed in 0.1 M KOH solution with a scan rate of 10 mV sec^{-1} and at 1600 rpm of the working electrode. The comparative LSVs of the prepared materials with *state-of-the-art* Pt/C catalyst performed in the O_2 saturated electrolyte is shown in **Figure 3.16b**. NVC-G is exhibiting low ORR activity and the corresponding onset potential and half-wave potential ($E_{1/2}$) values are 0.78 and 0.56 mV, respectively. However, the incorporation of Co_9S_8 nanoparticles on NVC-G support is enhancing the ORR activity. This is evident from the improvement in the onset potential as well as $E_{1/2}$ values of Co_9S_8/NVC-G. The system displays an onset potential of 0.93 mV and an $E_{1/2}$ value of 0.77 mV. The ohmic drop is substantially

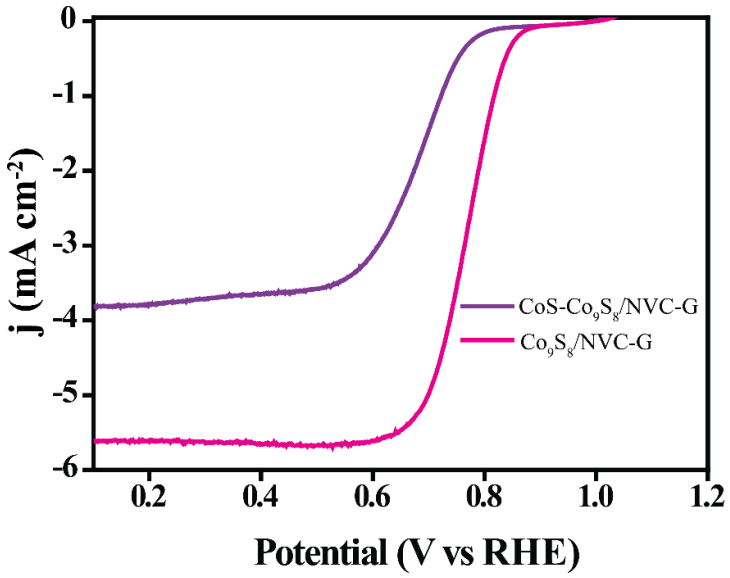

Figure 3.17. *LSV comparison of the samples prepared before and after the heat-treatment in the argon atmosphere performed in 0.1 M KOH solution at 1600 rpm of the working electrode and at 10 mV sec^{-1} scan rate.*

reduced in Co_9S_8/NVC-G. This could be attributed to the promotional role played by the NVC-G support in retaining the small size of the Co_9S_8 nanoparticles and, the possible synergetic interaction between the Co_9S_8 nanoparticles with the NVC-G support. This would improve the ORR activity and further the stability of the system. **Figure 3.17** shows the LSV comparison of the material obtained before and after the heat-treatment at 900 °C in the argon atmosphere. The corresponding samples are CoS-Co_9S_8/NVC-G and Co_9S_8/NVC-G, respectively. It is apparent from **Figure 3.17** that both the onset potential and $E_{1/2}$ values are noticeably improved in the heat-treated system (Co_9S_8/NVC-G). However, the CoS-Co_9S_8/NVC-G displays a lower onset potential value of 0.82 mV with the $E_{1/2}$ of 0.68 mV. Therefore, nearly 110 mV improvement in the onset potential and 90 mV enhancement in the $E_{1/2}$ value are achieved after the heat-treatment (Co_9S_8/NVC-G). This could be ascribed to the conversion of the CoS phase into the Co_9S_8 phase after the heat-treatment. Also, the crystallinity and graphitization of the material are improved after the heat-treatment at 900 °C. The overpotential displayed by Co_9S_8/NVC-G in comparison to *state-of-the-art* Pt/C is 70 mV in onset potential and 75 mV in $E_{1/2}$ values, respectively (**Figure 3.16b**).

The plot of $\omega^{-1/2}$ against j^{-1} is called as the Koutecky-Levich (K-L) plot, indicating the kinetics of the reaction. The K-L plot of Co_9S_8/NVC-G is provided in **Figure 3.16c**. The parallel behaviour at different potentials in the K-L plot indicates the first-order

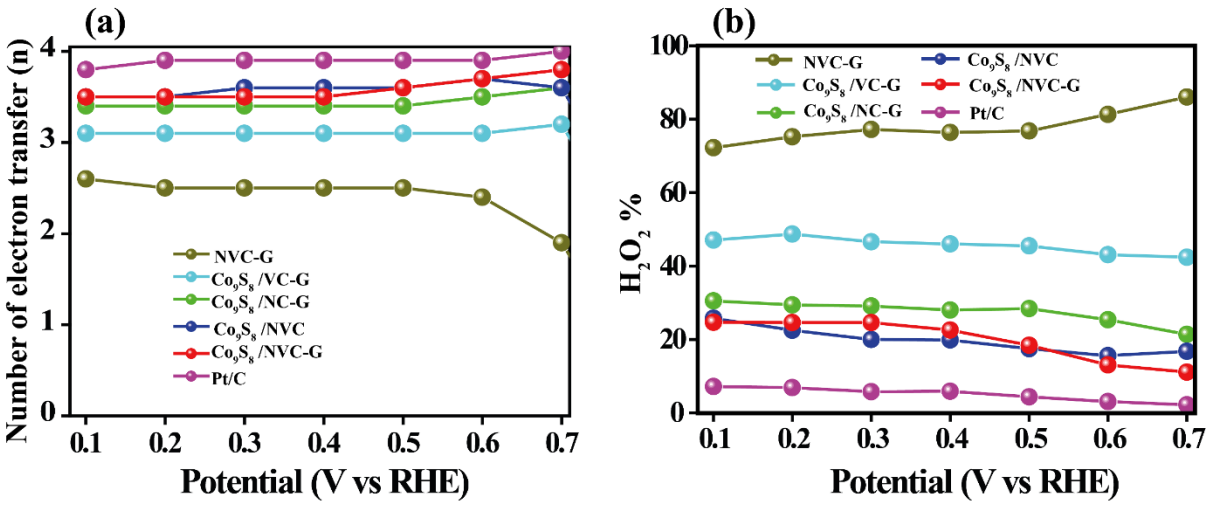

Figure 3.18. *RRDE analysis in 0.1 M KOH solution performed at a scan rate of 10 mV sec^{-1} and at 1600 rpm of the working electrode.*

kinetics of ORR in Co_9S_8/NVC-G.[60] The Tafel plot of the prepared materials is shown in **Figure 3.16d** and designates the reaction rate towards ORR. The Tafel slope of NVC-G is 153. 3 mV dec^{-1}; the slightly higher Tafel slope value indicates the relatively poor ORR kinetics in NVC-G. However, the Tafel slope is reduced to 65.6 mV dec^{-1} for Co_9S_8/NVC-G. This specifies the improved activity accomplished in Co_9S_8/NVC-G, where nearly 7-8 nm size of the Co_9S_8 nanoparticles are distributed uniformly on the NVC-G support. This would favour the adsorption of O_2 molecules and subsequently its reduction, eventually improving the ORR kinetics and resulting in the low Tafel slope value. The Tafel slope of the Pt/C catalyst is 60.6 mV dec^{-1}, which is in accordance with the literature reports.[18, 61] Hence, the lower Tafel slope values of Co_9S_8/NVC-G and Pt/C indicate the enhanced ORR activity in these systems.

The impedance analysis provides information about the resistance in the material. **Figure 3.16e** indicates the Nyquist plot of the synthesized materials in the O_2-saturated 0.1 M KOH solution at 0.60 V *vs.* RHE. Typically, the semicircle in the Nyquist plot designates the charge transfer resistance (R_{CT}) value of the material. The lower R_{CT} value is preferred for the fast ionic movement and is favourable for the improved ORR kinetics. The R_{CT} value of NVC-G is 1438 Ω and of Co_9S_8/NC-G and Co_9S_8/NVC are 744 Ω and 823 Ω, respectively. However, the R_{CT} value is drastically reduced to 278 Ω in Co_9S_8/NVC-G. This could be attributed to the presence of uniformly distributed Co_9S_8 nanoparticles on the NVC-G support, which facilitates the fast movement of electrons in the system. Also, the plausible synergetic interaction between the Co_9S_8

nanoparticle and NVC-G support promotes the electron transfer during the oxygen reduction in the system. Hence, the study further validates the interaction of Co_9S_8 nanoparticles with NVC-G support in the coexisting system and subsequently improves the ORR activity of Co_9S_8/NVC-G. The rotating ring disc electrode (RRDE) analysis was performed to analyse the number of electron transfer (n) and percentage of hydrogen peroxide (% H_2O_2) production during ORR. The comparative RRDE data of the synthesized materials and Pt/C is illustrated in **Figure 3.18**. The value of n is estimated to be close to 3.6 in Co_9S_8/NVC-G and the % H_2O_2 production is around 20%. Both of these values indicate the occurrence of favourable direct four-electron ORR pathway in Co_9S_8/NVC-G. The corresponding values of Pt/C are nearly 4 for the number of electron transfer and 5% for the % H_2O_2 production.

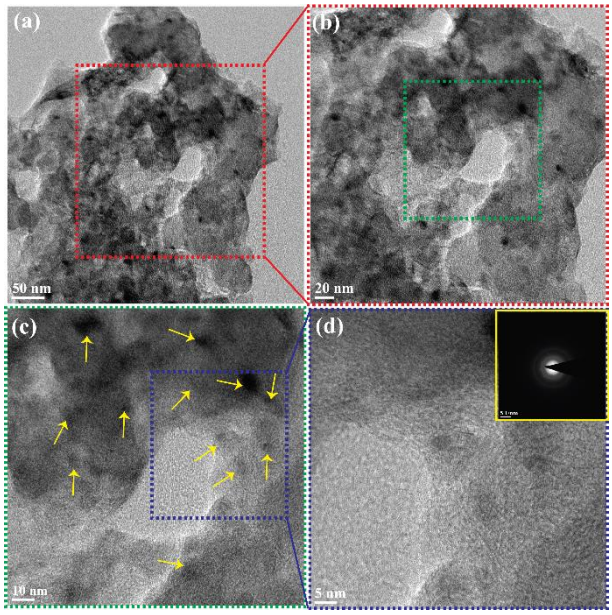

Figure 3.19. *TEM images of Co_9S_8/NVC-G recorded after 5000 ADT cycles in 0.1 M KOH solution.*

The durability of the catalyst is particularly important for providing long-term stability in the system. In order to investigate the stability, ADT was performed in the O_2-saturated 0.1 M KOH solution. The LSVs were recorded before and after the 5000 cycles of ADT. Co_9S_8/NVC-G is experiencing only an 18 mV negative shift in the $E_{1/2}$ value after the ADT analysis (**Figure 3.16f)**. Both onset potential and limiting current of Co_9S_8/NVC-G are nearly similar before and after ADT. This indicates the improved chemical stability of the system in the operating conditions. The TEM analysis of Co_9S_8/NVC-G was performed after the 5000 cycles of ADT and is provided in **Figure**

3.19. It is clear from **Figure 3.19a-d** that the small size of the Co_9S_8 nanoparticles is retained even after the durability analysis. This could be credited to the interaction of Co_9S_8 nanoparticles with the nitrogen doped carbon support and thus helps to achieve greater chemical stability in Co_9S_8/NVC-G. The presence of few-layer carbon on the surface of Co_9S_8 nanoparticles prevents agglomeration during the long-term operation which further provides improved stability. The nitrogen doping would improve the corrosion resistance of the carbon and contribute to maintaining the structural integrity

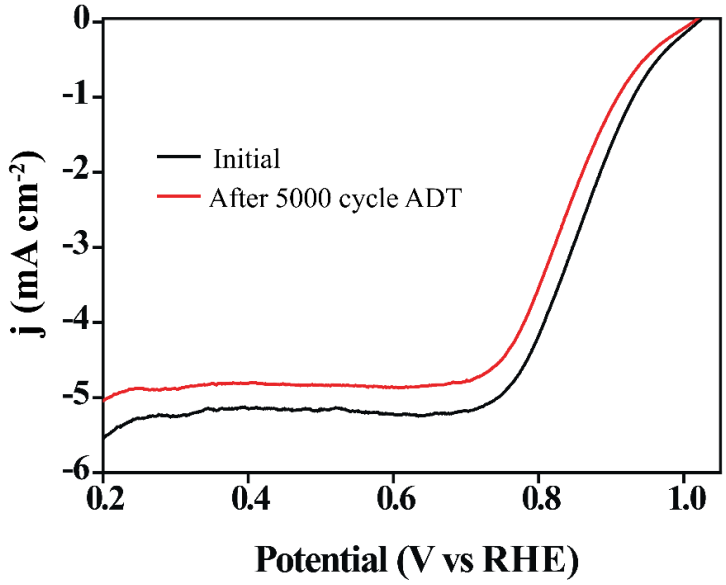

Figure 3.20. *LSVs of 40 wt. % Pt/C performed before and after the 5000 cycles of ADT in 0.1 M KOH solution with a scan rate of 10 mV* sec^{-1} *and at 1600 rpm of the working electrode.*

in the system. For comparison, ADT of the *state-of-the-art* Pt/C was performed under identical conditions. Pt/C was displaying a 35 mV negative shift in the $E_{1/2}$ value with a reduction in the limiting current after the 5000 cycles of ADT (**Figure 3.20**). This designates the poor stability of Pt/C during the long-term operation in the corrosive environment. Since, both Co_9S_8/NVC-G and Pt/C contain carbon in the system, the presence of nitrogen doped carbon in Co_9S_8/NVC-G provides structural integrity and activity maintenance in the system. However, poor stability of the carbon support in Pt/C would lead to the agglomeration of the supported Pt nanoparticles. This would eventually reduce the available active centres in Pt/C and further the activity.

The electrochemical active surface area (ECSA) of Co_9S_8/NVC-G and Pt/C was calculated from the double-layer capacitance (C_{dl}) value. For this, CV was performed in the non-Faradaic region (1.02 to 1.12 V *vs*. RHE) at different scan rates of 10, 20, 40,

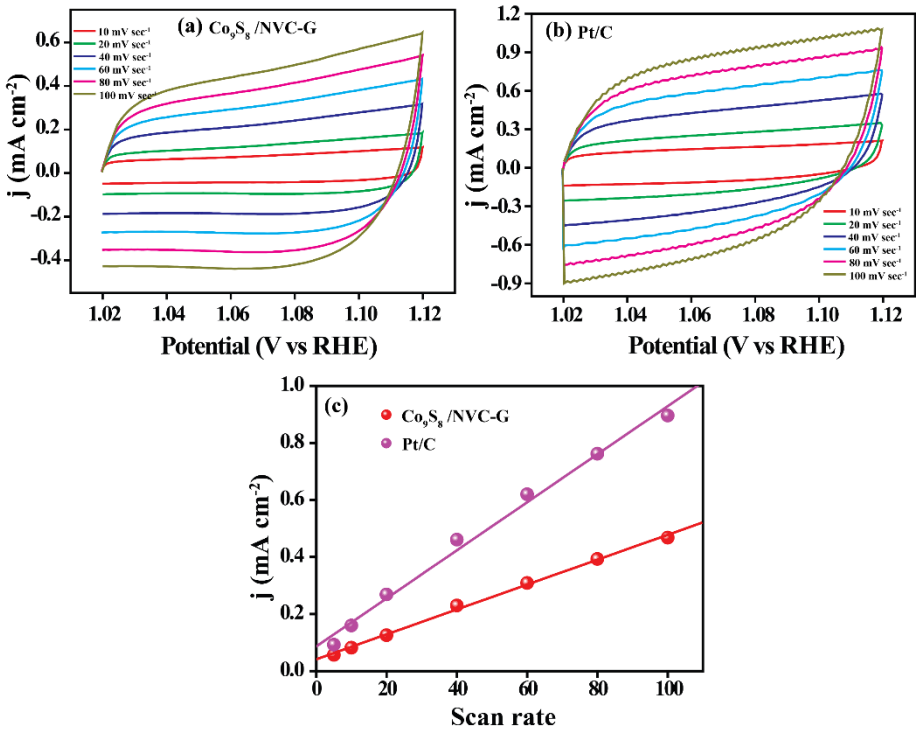

Figure 3.21. *Cyclic voltammograms recorded at different scan rates in the non-faradaic region in the N_2-saturated 1 M KOH solution; (a) Co_9S_8/NVC-G, (b) Pt/C, and (c) plots of the anodic current against scan rate in the non-faradaic region of the CVs.*

60, 80 and 100 mV sec^{-1} (**Figure 3.21a** and **b**). The peak current at 1.07 V (*vs*. RHE) is plotted against the scan rate and obtained a straight line. The slope of the line corresponds to the C_{dl} value. The ECSA is related to the C_{dl} value as expressed below:

$$ECSA = C_{dl}/C_s$$

where, C_s is the specific capacitance of the element. The C_{dl} value of Co_9S_8/NVC-G and Pt/C are 4.4 and 8.4 mF cm^{-2}, respectively (**Figure 3.21c**). The higher C_{dl} value of Pt/C could be due to the presence of more number of micropores in the supported carbon, which increases the adsorption of the ions. However, in the case of Co_9S_8/NVC-G, the number of micropores is less in the supported carbon and thereby it shows low ion adsorption capacity and consequently the low C_{dl} value.

3.3.8b ORR Analysis in Acidic Condition

Subsequent to the tests under KOH medium, the ORR activity of the prepared materials was analysed in 0.5 M H_2SO_4 solution and the corresponding data is presented in **Figure 3.22**. The LSV profiles of the samples recorded in the O_2-saturated 0.5 M H_2SO_4 solution at a scan rate of 10 mV sec^{-1} and 1600 rpm of the working electrode are presented in **Figure 3.22a**. The ORR activity of NVC-G in the acidic conditions is

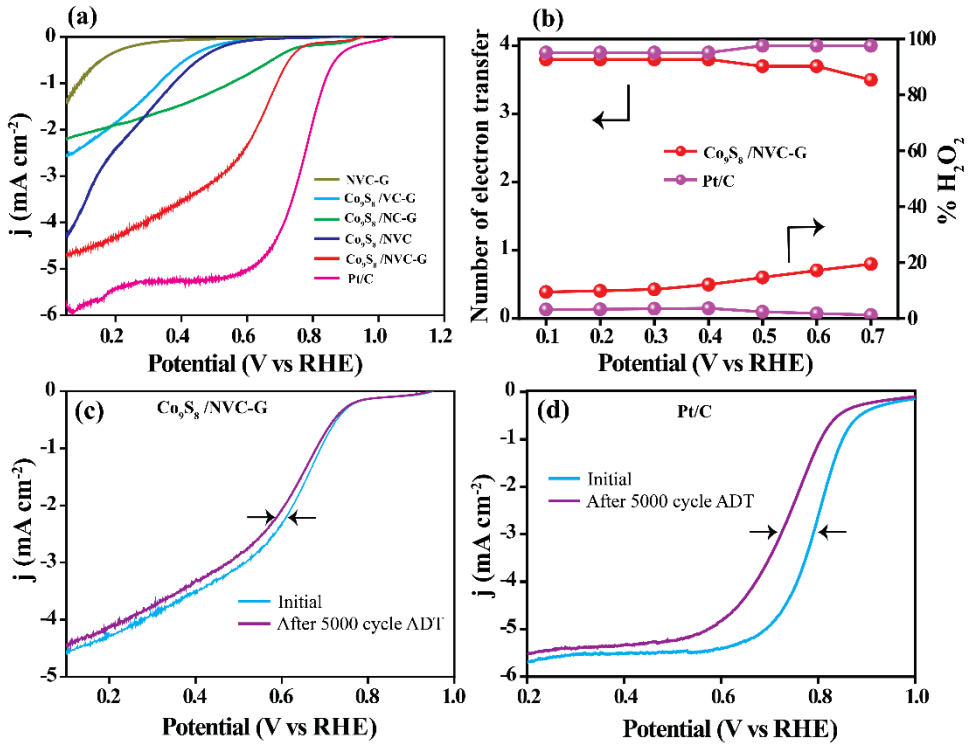

Figure 3.22. *(a) Comparative LSVs of the samples performed in O_2-saturated 0.5 M H_2SO_4 solution at 1600 rpm of the working electrode with a scan rate of 10 mV sec^{-1}, (b) comparative rotating ring disc electrode (RRDE) analysis of Co_9S_8/NVC-G and Pt/C, (c-d) LSVs recorded before and after ADT of Co_9S_8/NVC-G and Pt/C in O_2-saturated electrolyte at a rotation of 1600 rpm of the working electrode under a scan rate of 10 mV sec^{-1}.*

insignificant with an onset potential of 0.31 V. However, the ORR activity is substantially improved in Co_9S_8/NVC-G. The onset potential and $E_{1/2}$ value of Co_9S_8/NVC-G are 0.82 V and 0.60 V, respectively. These are nearly 140 mV and 170 mV lower as compared to the *state-of-the-art* Pt/C catalyst. The RRDE analysis was employed in 0.5 M H_2SO_4 solution to calculate the value of 'n' and '% H_2O_2' and the corresponding results are presented in **Figure 3.22b**. The peroxide yield was calculated from the RRDE analysis, which is estimated to be around 12 % at 0.40 V with an electron transfer number (n) of 3.8 on Co_9S_8/NVC-G. The percentage of H_2O_2 production obtained here is comparable with many of the non-precious metal based ORR catalysts reported in the literature.[62] The Pt/C shows a nearly four-electron transfer and a very low H_2O_2 production (5%) in the RRDE analysis. Hence, the low H_2O_2 yield and close matching of the number of electron transfer near to four indicates the favourable reduction of O_2 during ORR in both Co_9S_8/NVC-G and Pt/C.

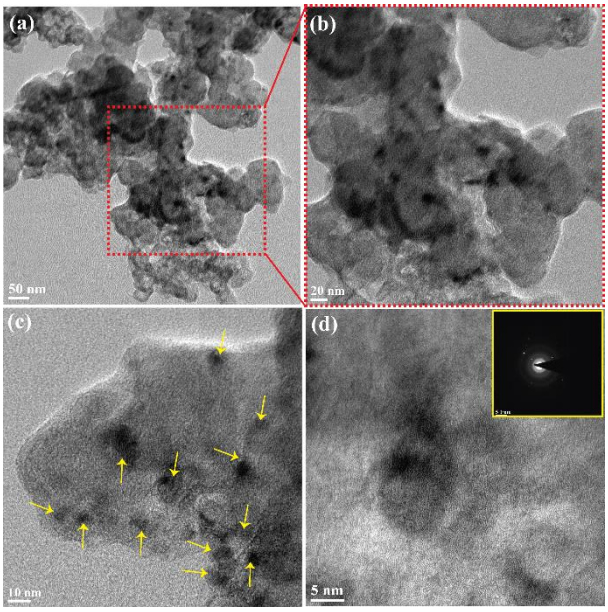

Figure 3.23. *TEM images of Co_9S_8/NVC-G recorded after the 5000 ADT cycles in 0.5 M H_2SO_4 solution.*

To check the stability of Co_9S_8/NVC-G and Pt/C in the acidic conditions, ADT was performed for 5000 cycles in the potential window of 0.60 to 1.0 V (*vs*. RHE). The LSVs were recorded before and after ADT. Co_9S_8/NVC-G displays a negligible shift of nearly 21 mV in the $E_{1/2}$ value without affecting the onset potential after the 5000 cycles of ADT (**Figure 3.22c**). This confirms the outstanding stability of Co_9S_8/NVC-G in acidic conditions. However, Pt/C is experiencing a severe loss in the performance after the stability test and this could be attributed to the agglomeration of the Pt nanoparticles due to the carbon corrosion. The Pt/C displays a 63 mV negative shift in the $E_{1/2}$ value along with a 30 mV negative shift in the onset potential (**Figure 3.22d**). The TEM images of Co_9S_8/NVC-G recorded after ADT are presented in **Figure 3.23**. The structural integrity of Co_9S_8/NVC-G after ADT is confirmed from **Figure 3.23a-d**. The nitrogen doped carbon support along with the graphitic carbon layer on the Co_9S_8 nanoparticles can help the system to withstand the harsh environment, giving improved stability of Co_9S_8/NVC-G in the acidic conditions. This further validates the significance of anchoring the Co_9S_8 nanoparticles on the nitrogen doped carbon support. Thus, the half-cell studies in both the alkaline and acidic electrolytes indicate that the ORR activity of Co_9S_8/NVC-G is better as compared to many of the metal sulfide based systems reported in both the conditions.[28, 29]

Finally, testing of a single cell of a PEMFC was performed by employing Co_9S_8/NVC-

G as the cathode catalyst, Pt/C as the anode catalyst and Nafion-212 as the membrane. The polarization analysis was performed at 60 °C and 100 % RH in the H_2-O_2 and H_2-air feed conditions and the corresponding current (I) – voltage (V) polarization plots are presented in **Figure 3.24**. Co_9S_8/NVC-G exhibits maximum power densities of 245 mW cm^{-2} and 115 mW cm^{-2} in H_2-O_2 and H_2-air feed conditions, respectively. For comparison, an MEA with Pt/C based cathode was also analysed in similar operating conditions in the single cell mode. The maximum power densities obtained for this system are 650 mW cm^{-2} and 445 mW cm^{-2} in the H_2-O_2 and H_2-air feed conditions, respectively (**Figure 3.25**). Even though the single-cell performance of Co_9S_8/NVC-G based system is lower compared to its counterpart based on Pt/C catalyst, in terms of the system cost and catalyst level durability, the obtained results are promising for a

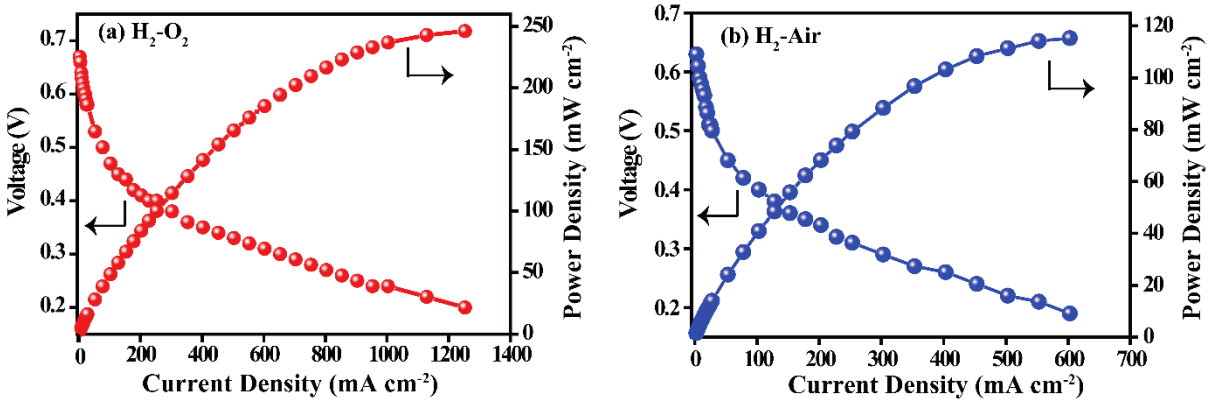

Figure 3.24. *Single cell performance evaluation of a PEMFC based on Co_9S_8/NVC-G cathode using Nafion-212 membrane at 60 °C and 100 % RH; (a) in H_2-O_2 and (b) H_2-air feed conditions.*

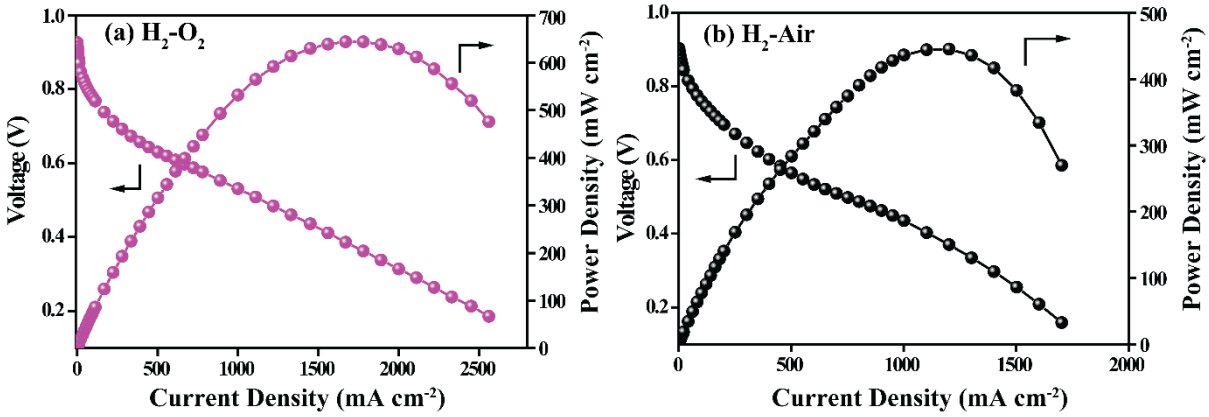

Figure 3.25. *Single cell performance evaluation of a PEMFC based on Pt/C cathode using Nafion-212 membrane at 60 °C and 100 % RH; (a) in H_2-O_2 and (b) H_2-air feed conditions.*

noble metal-free system. Hence, the PEMFC single cell performance analysis validates the promising aspect of Co_9S_8/NVC-G based ORR catalysts as a potential Pt-free cathode system for PEMFC applications.

3.4 Conclusions

The chapter deals with a highly efficient and durable ORR catalyst which could be prepared by supporting the graphitic carbon enfolded Co_9S_8 nanoparticles on nitrogen-doped carbon (Co_9S_8/NVC-G). The size of the Co_9S_8 nanoparticles is nearly 7-8 nm and the particles are found to be distributed uniformly on the NVC-G support. The present catalyst is exhibiting ORR activity in both acidic and alkaline conditions. The ORR analysis of Co_9S_8/NVC-G in 0.1 M KOH solution displays only 70 mV negative shift in the onset potential compared to the *state-of-the-art* Pt/C system. The $E_{1/2}$ difference between the present system and Pt/C is nearly 75 mV. The accelerated durability test (ADT) shows only a 19 mV negative shift in the $E_{1/2}$ value of Co_9S_8/NVC-G compared to the 35 mV negative shift incurred by Pt/C. The ORR activity investigation in 0.5 M H_2SO_4 solution also displayes promising performance for Co_9S_8/NVC-G towards ORR. The differences in the onset potential and $E_{1/2}$ values of the present system with that of Pt/C are 140 and 170 mV, respectively in the acidic electrolyte condition. The system displays a minor $E_{1/2}$ shift of 21 mV towards the lower potential after the 5000 cycles of ADT. On the other hand, Pt/C is severely affected by the stability analysis under acidic conditions. The ADT leads to nearly 63 mV negative shift in the $E_{1/2}$ value along with a 30 mV negative shift in the onset potential for Pt/C. The low H_2O_2 production of 12% and the number of electron transfer value of 3.8, which is close to the theoretical value of 4, suggest the promising aspects of Co_9S_8/NVC-G as a potential ORR catalyst. This performance advantage of Co_9S_8/NVC-G could be ascribed to the small size of Co_9S_8 nanoparticles with few-layer graphitic carbon coating and homogenous dispersion of the nanoparticles on the NVC-G support. This would favour the adsorption of oxygen and subsequently its conversion into hydroxide ions during ORR. Co_9S_8/NVC-G when employed as the cathode catalyst in an MEA of PEMFC delivered a maximum power density of 245 mW cm^{-2} in the H_2-O_2 atmosphere in its single cell mode of operation. Under H_2-air feeding condition, the same system delivered a maximum power density of 115 mW cm^{-2}. These values obtained on a single cell level is promising due to its prospect to realize a noble metal-free PEMFC system for futuristic applications.

3.5 References

[1] C. Galeano, J. C. Meier, M. Soorholtz, H. Bongard, C. Baldizzone, K. J. J. Mayrhofer, F. Schüth, ACS Catal. 2014, 4, 3856-3868.

[2] G. Hu, F. Nitze, E. Gracia-Espino, J. Ma, H. R. Barzegar, T. Sharifi, X. Jia, A. Shchukarev, L. Lu, C. Ma, G. Yang, T. Wågberg, Nat Commun 2014, 5.

[3] X. Zou, Y. Zhang, Chem. Soc. Rev. 2015, 44, 5148-5180.

[4] J. Wang, F. Xu, H. Jin, Y. Chen, Y. Wang, Adv. Mater. 2017.

[5] Y.-J. Wang, J. Qiao, R. Baker, J. Zhang, Chem. Soc. Rev. 2013, 42, 5768-5787.

[6] S. Guo, S. Zhang, S. Sun, Angew. Chem., Int. Ed. 2013, 52, 8526-8544.

[7] M. Oezaslan, F. Hasché, P. Strasser, J. Phys. Chem. Lett. 2013, 4, 3273-3291.

[8] J. Zhang, H. Yang, J. Fang, S. Zou, Nano Lett. 2010, 10, 638-644.

[9] L. Lin, Q. Zhu, A.-W. Xu, J. Am. Chem. Soc. 2014, 136, 11027-11033.

[10] A. Rabis, P. Rodriguez, T. J. Schmidt, ACS Catal. 2012, 2, 864-890.

[11] X. Ning, Y. Li, J. Ming, Q. Wang, H. Wang, Y. Cao, F. Peng, Y. Yang, H. Yu, Chem. Sci. 2019, 10, 1589-1596.

[12] B.-C. Hu, Z.-Y. Wu, S.-Q. Chu, H.-W. Zhu, H.-W. Liang, J. Zhang, S.-H. Yu, Energy Environ. Sci. 2018, 11, 2208-2215.

[13] R. Illathvalappil, V. M. Dhavale, S. N. Bhange, S. Kurungot, Nanoscale 2017, 9, 9009-9017.

[14] Y. Jiao, Y. Zheng, M. Jaroniec, S. Z. Qiao, Chem. Soc. Rev. 2015, 44, 2060-2086.

[15] Y. Nie, L. Li, Z. Wei, Chem. Soc. Rev. 2015, 44, 2168-2201.

[16] Y.-J. Wu, Y.-C. Wang, R.-X. Wang, P.-F. Zhang, X.-D. Yang, H.-J. Yang, J.-T. Li, Y. Zhou, Z.-Y. Zhou, S.-G. Sun, ACS Appl. Mater. Interfaces 2018, 10, 14602-14613.

[17] Y.-J. Wang, N. Zhao, B. Fang, H. Li, X. T. Bi, H. Wang, Chem. Rev. 2015.

[18] Z. Hu, Z. Guo, Z. Zhang, M. Dou, F. Wang, ACS Appl. Mater. Interfaces 2018, 10, 12651-12658.

[19] T. Sun, Y. Jiang, Q. Wu, L. Du, Z. Zhang, L. Yang, X. Wang, Z. Hu, Catal. Sci. Technol. 2017, 7, 51-55.

[20] A. Morozan, B. Jousselme, S. Palacin, Energy Environ. Sci. 2011, 4, 1238-1254.

[21] H. Liu, Z. Shi, J. Zhang, L. Zhang, J. Zhang, J. Mater. Chem. 2009, 19, 468-470.

[22] W. Li, D. Xiong, X. Gao, L. Liu, Chem. Commun. 2019, 55, 8744-8763.

[23] D. Dong, Z. Wu, J. Wang, G. Fu, Y. Tang, J. Mater. Chem. A 2019, 7, 16068-16088.

[24] H. Lin, S. Zhang, T. Zhang, S. Cao, H. Ye, Q. Yao, G. W. Zheng, J. Y. Lee, ACS Nano 2019, 13, 7073-7082.

[25] L.-L. Feng, M. Fan, Y. Wu, Y. Liu, G.-D. Li, H. Chen, W. Chen, D. Wang, X. Zou, J. Mater. Chem. A 2016, 4, 6860-6867.

[26] Y. Ji, X. Liu, W. Liu, Y. Wang, H. Zhang, M. Yang, X. Wang, X. Zhao, S. Feng, RSC Adv. 2014, 4, 50220-50225.

[27] Y. Tang, F. Jing, Z. Xu, F. Zhang, Y. Mai, D. Wu, ACS Appl. Mater. Interfaces 2017, 9, 12340-12347.

[28] S. Dou, L. Tao, J. Huo, S. Wang, L. Dai, Energy Environ. Sci. 2016, 9, 1320-1326.

[29] Y. Liu, H. Shen, H. Jiang, W. Li, J. Li, Y. Li, Y. Guo, Int. J. Hydrog. Energy 2017, 42, 12978-12988.

[30] J. Mujtaba, H. Sun, G. Huang, Y. Zhao, H. Arandiyan, G. Sun, S. Xu, J. Zhu, RSC Adv. 2016, 6, 31775-31781.

[31] Y. Feng, T. He, N. Alonso-Vante, Chem. Mater. 2008, 20, 26-28.

[32] Y. Feng, A. Gago, L. Timperman, N. Alonso-Vante, Electrochim. Acta 2011, 56, 1009-1022.

[33] A. Marinoiu, M. Andrulevicius, A. Tamuleviciene, T. Tamulevicius, E. Carcadea, M. Raceanu, M. Varlam, Int. J. Hydrog. Energy 2019.

[34] D. Gu, R. Ma, Y. Zhou, F. Wang, K. Yan, Q. Liu, J. Wang, ACS Sustainable Chem. Eng. 2017, 5, 11105-11116.

[35] Y. Ma, H. Wang, S. Ji, J. Goh, H. Feng, R. Wang, Electrochim. Acta 2014, 133, 391-398.

[36] J. P. Paraknowitsch, A. Thomas, Energy Environ. Sci. 2013, 6, 2839-2855.

[37] S. Kabir, K. Artyushkova, A. Serov, P. Atanassov, ACS Appl. Mater. Interfaces 2018, 10, 11623-11632.

[38] S. Fu, C. Zhu, J. Song, S. Feng, D. Du, M. H. Engelhard, D. Xiao, D. Li, Y. Lin, ACS Appl. Mater. Interfaces 2017, 9, 36755-36761.

[39] M. Uchida, Y.-C. Park, K. Kakinuma, H. Yano, D. A. Tryk, T. Kamino, H. Uchida, M. Watanabe, Phys. Chem. Chem. Phys. 2013, 15, 11236-11247.

[40] X. Ge, A. Sumboja, D. Wuu, T. An, B. Li, F. W. T. Goh, T. S. A. Hor, Y. Zong, Z. Liu, ACS Catal. 2015, 4643-4667.

[41] O. V. Kharissova, B. I. Kharisov, RSC Adv. 2014, 4, 30807-30815.

[42] J. Wu, P. Wang, F. Wang, Y. Fang, Nanomaterials 2018, 8, 864.

[43] L.-L. Feng, G.-D. Li, Y. Liu, Y. Wu, H. Chen, Y. Wang, Y.-C. Zou, D. Wang, X.

Zou, ACS Appl. Mater. Interfaces 2015, 7, 980-988.

[44] X. Zheng, J. Xu, K. Yan, H. Wang, Z. Wang, S. Yang, Chem. Mater. 2014, 26, 2344-2353.

[45] J.-F. Lin, O. Pitkänen, J. Mäklin, R. Puskas, A. Kukovecz, A. Dombovari, G. Toth, K. Kordas, J. Mater. Chem. A 2015, 3, 14609-14616.

[46] B. Li, Y. Hu, J. Li, M. Liu, L. Kong, Y. Hu, L. Kang, Metals 2016, 6, 142.

[47] J. Huang, X. Tang, Z. Li, K. Liu, J. Colloid Interface Sci. 2018, 532, 407-415.

[48] C. Guan, X. Liu, A. M. Elshahawy, H. Zhang, H. Wu, S. J. Pennycook, J. Wang, Nanoscale Horiz. 2017, 2, 342-348.

[49] Y. Chen, J. Hu, H. Diao, W. Luo, Y.-F. Song, Chem. Eur. J. 2017, 23, 4010-4016.

[50] N. P. D. Ngidi, M. A. Ollengo, V. O. Nyamori, Materials (Basel) 2019, 12, 3376.

[51] T. Palaniselvam, M. O. Valappil, R. Illathvalappil, S. Kurungot, Energy Environ. Sci. 2014, 7, 1059-1067.

[52] S. Zhang, D. Li, S. Chen, X. Yang, X. Zhao, Q. Zhao, S. Komarneni, D. Yang, J. Mater. Chem. A 2017, 5, 12453-12461.

[53] Y. Jiao, Y. Zheng, M. Jaroniec, S. Z. Qiao, J. Am. Chem. Soc. 2014, 136, 4394-4403.

[54] Y. Xu, P. Deng, G. Chen, J. Chen, Y. Yan, K. Qi, H. Liu, B. Y. Xia, Adv. Funct. Mater. 2020, 30, 1906081.

[55] S. W. Han, J. Bang, S. H. Ko, R. Ryoo, J. Mater. Chem. A 2019, 7, 8353-8360.

[56] X. Ge, A. Sumboja, D. Wuu, T. An, B. Li, F. W. T. Goh, T. S. A. Hor, Y. Zong, Z. Liu, ACS Catal. 2015, 5, 4643-4667.

[57] J. Du, R. Wang, Y.-R. Lv, Y.-L. Wei, S.-Q. Zang, Chem. Commun. 2019, 55, 3203-3206.

[58] T. N. Pham, T. Sharifi, R. Sandström, W. Siljebo, A. Shchukarev, K. Kordas, T. Wågberg, J.-P. Mikkola, Sci. Rep. 2017, 7, 6112.

[59] R. Liu, H. Zhang, X. Zhang, T. Wu, H. Zhao, G. Wang, RSC Adv. 2017, 7, 19181-19188.

[60] K. Y. Cho, Y. S. Yeom, H. Y. Seo, A. S. Lee, X. Huy Do, J. P. Hong, H.-K. Jeong, K.-Y. Baek, H. G. Yoon, Electrochim. Acta 2017, 257, 412-422.

[61] C. Xu, Y. Zhang, L. Wang, L. Xu, X. Bian, H. Ma, Y. Ding, Chem. Mater. 2009, 21, 3110-3116.

[62] Y. Yang, R. Zeng, Y. Xiong, F. J. DiSalvo, H. D. Abruña, J. Am. Chem. Soc. 2019.

Chapter-4

Coexisting Few-Layer Assemblies of NiO and MoO_3 Deposited on Vulcan Carbon as an Efficient and Durable Electrocatalyst for Water Oxidation

An efficient electrocatalyst for oxygen evolution reaction (OER) has been prepared by adopting a strategy wherein layered assembly of NiO and MoO_3 could be dispersed on Vulcan carbon support to simultaneously maintain exposure of the synergistically activated sites and electrical conductivity of the matrix. The assembly involves growth of layers of NiO on the surface of few-layer MoO_3 which in turn is dispersed on Vulcan carbon (NiO@MoO_3/VC) through a sequential hydrothermal process. The hydrothermal process played a key role in establishing the coexisting few-layer assembly of NiO and MoO_3 on Vulcan carbon, which involved conversion of preformed MoS_2 sheets to MoO_3 and concomitant growth of $Ni(OH)_2$ layer prior to its conversion to NiO during the subsequent heat treatment process. The NiO sheets have exposed edges and they are instrumental in enhancing the OER activity of NiO@MoO_3/VC. The higher activity is also credited to the lower charge transfer resistance (R_{CT}) value possessed by NiO@MoO_3/VC, which arises from the optimum combination of MoO_3 and Vulcan carbon in the system. The presence of surface nickel molybdate ($NiMoO_4$) prevents the dissolution of MoO_3 in the alkaline environment and provides excellent stability to the NiO@MoO_3/VC in 1 M KOH solution. The overpotential of NiO@MoO_3/VC for achieving the 10 mA cm^{-2} current density is 280 mV, which is an improved value over 292 mV obtained in the case of the *state-of-the-art* RuO_2 catalyst. NiO@MoO_3/VC also demonstrates an outstanding stability for 15 h in 1 M KOH solution at 1.51 V. Finally, the overall water splitting was performed in 1 M KOH solution by employing NiO@MoO_3/VC-NF as the anode catalyst and Pt/C-NF as the cathode catalyst. The system requires a potential of 1.59 V to reach the current density of 10 mA cm^{-2}, replaces the RuO_2 from the anode of the electrolyser with the home-made catalyst.

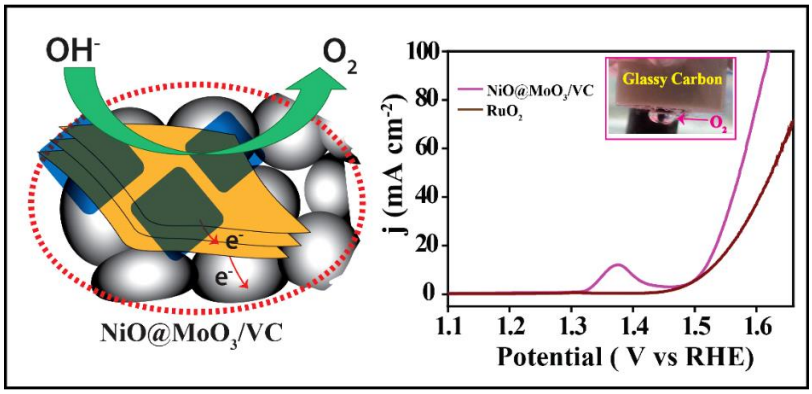

Content of this chapter is published in the following article:
ACS Appl. Energy Mater., 2019, 2, 4987−4998.
(https://pubs.acs.org/doi/abs/10.1021/acsaem.9b00665)

4.1 Introduction

Hydrogen production from water with minimum inputs is a challenging task that awaits in the near future. Technologies based on electrochemical conversions can produce hydrogen from water, and electrocatalysts play a major role in these.[1-2] Electrolysis of water produces hydrogen which is a pollution-free energy carrier of the future.[3-5] As compared to the cathodic reaction in water splitting, *i.e.*, the hydrogen evolution reaction (HER), the anodic oxygen evolution reaction (OER) is more sluggish and needs higher overpotential to accelerate the reaction.[6-7] This is because OER involves the transfer of four electrons for the evolution of an O_2 molecule rather than the two-electron transfer reaction that occurs in HER. Thus, the OER eventually becomes the rate-determining step of the overall water splitting process and its sluggishness acts as the barrier for the large-scale commercial production of H_2 from water.[8] The conversion between H_2O and O_2, known as the oxygen electrochemistry, thus plays an important role in the technology for making renewable energy from water.[9] There are numerous materials such as RuO_2 and IrO_2 that have been explored as catalysts for aiding OER. However, the limiting factors like high cost, short durability, and insufficiency in the availability of these materials form the bottleneck for the large scale production of a cost-effective and long-lasting OER catalyst.[10, 49, 56] To develop an economical and durable catalyst for OER, researchers have focused on carbon-supported, non-noble metal based alternate catalysts.[11, 45, 50, 57, 58, 60] The presence of carbon enhances electrical conductivity of the system and, additionally, it acts as a substrate to anchor the metal nanoparticles.

The agglomeration of the metal nanoparticles/sheets during long-term operation would reduce the efficiency of the system. In order to deliver efficient and stable performance, the stability of the material should be tuned by incorporating corrosion-resistant materials.[12] It has been reported that the presence of oxide and sulfide of molybdenum would reduce the agglomeration of the nanoparticles during long-term operation.[13-15, 59] There have been several reports on non-noble metal based OER catalysts and, among them, the nickel-based catalysts have showed excellent activity in the water-oxidation reaction.[16-17, 51-54, 61] The wide availability, low cost, and higher theoretical activity of nickel in OER make it an appropriate candidate for facilitating the production of oxygen from water (OER).[16] As mentioned earlier, the agglomeration of nanoparticles/sheets due to deterioration of the support material during long-term operation in the corrosive environment would reduce the activity and the overall

efficiency of the catalyst. Anchoring of the NiO nanosheets on conducting substrates like Vulcan carbon would improve the distribution of the material. However, the positive operating potential of OER is greatly favourable for carbon corrosion,[18] and for a long period of operation, this would ultimately reduce the activity of the system. The integration of materials like metal sulfides, selenides, oxides or nitrides that can withstand the harsh environment could resolve the stability issue.[19-20, 46-47] At a higher working potential and corrosive conditions, the sulfide, selenide and oxides of molybdenum display outstanding operational stability in long-term operation.[15, 21-22, 48] Hence, the incorporation of a material like MoO_3 would help to overcome the durability limitations. The anchoring of NiO nanosheets on sulfide, oxides or nitrides of molybdenum could reduce the agglomeration during the long-term operation and would provide an excellent solution to overcome the limitations of stability. However, in order to enhance the electrochemical process, the relatively low electrical conductivity associated with MoO_3 needs to be addressed.[23] The appropriate variation of the composition of MoO_3 and Vulcan carbon content in the system would resolve both the issues of agglomeration and the low electrical conductivity.[10]

A survey of previously published literature indicates that the few-layer MoS_2 possesses more active sites than the bulk MoS_2 and it has been used in optoelectronics and nanoelectronics.[24-25, 55] There are several methods for the synthesis of few-layer MoS_2 including mechanical exfoliation and chemical exfoliation. However, the size of the MoS_2 layers obtained through these methods ranges to several micrometers. This would, ultimately, reduce the overall availability of the active sites in the MoS_2 sheets. Hence, in the present work, by using the hydrothermal route, we have synthesized few-layer MoS_2 sheets of nanometer-size on the Vulcan carbon support (MoS_2/VC). The MoO_3 is then derived from the as formed few-layer MoS_2 sheets during the second step of the hydrothermal treatment in the presence of $NiCl_2$ and small amount of hydrazine hydrate as the reducing agent.[26] Conversion of MoS_2 to MoO_3 is concomitantly associated with the formation and deposition of $Ni(OH)_2$ nanosheets on the surface of MoO_3 ($Ni(OH)_2$@MoO_3/VC). The presence of the reducing agent is found to be helping the system to retain a small amount of reduced form of Ni in the major phase of $Ni(OH)_2$, which also assists the system in its performance as an electrocatalyst. Subsequent heat treatment of the as-produced material at 300 °C in an inert atmosphere converts $Ni(OH)_2$ in the composite in to NiO, leading to the final catalyst designated as NiO@MoO_3/VC (**Figure 4.1**). The OER activity of NiO@MoO_3/VC has been analysed in 1 M KOH

solution. For comparison, two control systems based on the $Ni(OH)_2$ nanosheets anchored directly on Vulcan carbon (*i.e.*, $Ni(OH)_2$/VC) and MoO_3 (*i.e.*, $Ni(OH)_2/MoO_3$) were also prepared and analysed under the same conditions. The obtained results are compared with the performance of the *state-of-the-art* RuO_2 catalyst.

4.2 Experimental Section

4.2.1 Materials

Ammonium molybdate tetrahydrate ($(NH_4)_6Mo_7O_{24}.\ 4H_2O$), thiourea ($CH_4N_2S$), hydrazine hydrate ($N_2H_4.\ H_2O$), potassium hydroxide (KOH), ruthenium (IV) oxide (RuO_2) were purchased from Sigma-Aldrich Chemicals. Hydrogen peroxide (H_2O_2) was procured from Thomas Baker. Nickel chloride hexahydrate ($NiCl_2.\ 6H_2O$) was procured from Rankem Chemicals. Vulcan carbon was procured from CABOT Corporation, USA. Vulcan carbon was functionalized by using hydrogen peroxide and taken for further use. All the chemicals were used without any further purification.

4.2.2 Synthesis of MoS_2/VC

For the synthesis of MoS_2/VC, about 100 mg of the functionalized Vulcan carbon (fn-VC) was dispersed well in 35 mL of de-ionized water using bath sonication for 2 h. After that, the dispersed fn-VC was transferred into a 50 mL Teflon lined tube, and 0.08 mmol ammonium heptamolybdate tetrahydrate ($(NH_4)_6Mo_7O_{24}.\ 4H_2O$) and 1.12 mmol of thiourea (CH_4N_2S) were added to it. The whole mixture was bath sonicated for at least 1 h for proper dispersion and hydrothermal treatment was carried out at 200 °C for 18 h with the aid of an autoclave. It was allowed to cool to room temperature and the resulting product was subsequently washed with DI water and ethanol. The obtained product was dried at 60 °C in an oven for 6 h and used for further reactions. The material obtained in this step was termed as MoS_2/VC.

4.2.3 Synthesis of $Ni(OH)_2@MoO_3$/VC

The incorporation of $Ni(OH)_2$ was carried out by the hydrothermal method. For this, about 50 mg of the MoS_2/VC synthesized through the previous step was dispersed in 35 mL of DI water. To this, 0.04 mmol of nickel chloride hexahydrate ($NiCl_2.\ 6H_2O$) and 500 µL of hydrazine hydrate ($NH_2NH_2.\ H_2O$) were added and sonicated for 1 h. The resulting mixture was transferred to a Teflon lined autoclave. The hydrothermal treatment was carried out at 200 °C for 18 h, and then, was allowed to cool down to room temperature. The MoS_2 gets oxidized and forms MoO_3 during this process. The

obtained material was washed several times with copious amount of DI water and ethanol, and then dried in an oven at 60 °C for 6 h. The resulting material was called $Ni(OH)_2$@MoO_3/VC.

4.2.4 Synthesis of NiO@MoO_3/VC

The heat treatment of the above made $Ni(OH)_2$@MoO_3/VC in an inert atmosphere led to the formation of NiO@MoO_3/VC. For this, $Ni(OH)_2$@MoO_3/VC was taken in a crucible and kept at the centre of a quartz tube whose openings were subsequently closed. Then, heat treatment of the material was carried out at 300 °C for 3 h in argon atmosphere with a ramping rate of 10 °C min^{-1}. The material was allowed to cool down to room temperature and used for the analysis. The material so-obtained was named as NiO@MoO_3/VC.

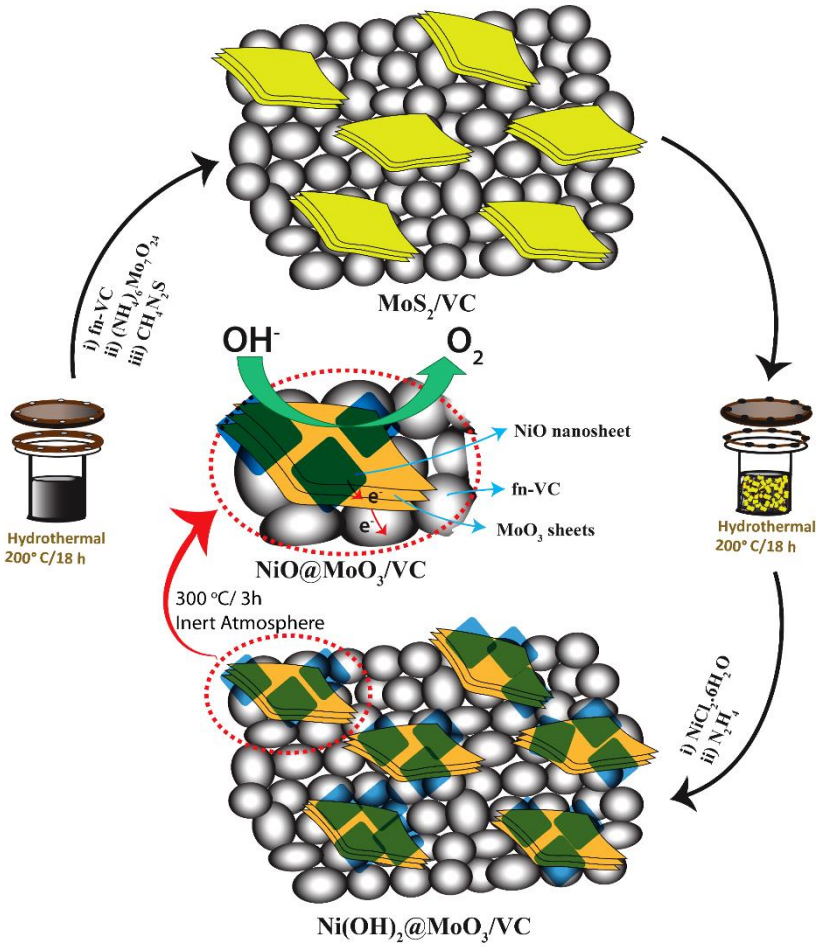

Figure 4.1. *Schematic illustration of the synthesis of MoS_2/VC and $Ni(OH)_2$@MoO_3/VC through the two-step hydrothermal synthesis route followed by heat treatment at 300 °C in an inert atmosphere to obtain NiO@MoO_3/VC.*

For making $Ni(OH)_2$/VC, about 100 mg of fn-VC was dispersed in DI water and about

0.04 mmol of nickel chloride hexahydrate and 500 µL of hydrazine hydrate were added. This mixture was transferred to the Teflon-lined autoclave and the hydrothermal treatment was done at 200 °C for 18 h. The obtained material was washed and dried to form $Ni(OH)_2$/VC.

4.2.5 Characterization

Field emission scanning electron microscopy (FESEM) was carried out in a Nova Nano SEM 450 instrument. Transmission electron microscopy (TEM) analysis of the samples was conducted in a FEI Technai G2 T20 instrument, operated at 200 KeV. X-ray diffraction (XRD) analysis was performed in a Rigaku instrument using Cu kα radiation (1.5418 Å). Raman analysis was conducted in a LabRam spectrometer (HJY, France); the operating laser wavelength was 632.1 nm. Using a Quantachrome Quadrasorb automatic volumetric instrument, the nitrogen adsorption-desorption analysis of the samples was conducted by using ultra-pure N_2. Thermo gravimetric analysis (TGA) of the materials was carried out in a PerkinElmer STA 600 analyser in air atmosphere by ramping from room temperature to 900 °C with a heating rate of 10 °C min^{-1}. The X-ray photoemission spectroscopic (XPS) analysis was conducted in a VG Microtech Multilab ECSA 3000 spectrometer.

Electrochemical analyses were carried out in a Biologic SP-300 instrument. Catalyst slurry for the electrochemical analyses was prepared by dispersing 5 mg of the catalyst in 3:1 mixture (1 mL) of DI water-iso propyl alcohol and 40 µL of 5 wt. % Nafion (DuPont) by bath sonication for 1 h. About 5 µL of the aliquot was drop coated on a glassy carbon electrode surface (3 mm diameter) and dried. Electrochemical analysis was carried out in N_2-saturated 1 M KOH solution. Hg/HgO and graphite rod were used as the reference and counter electrode, respectively. For comparative study, ruthenium (IV) oxide (Sigma-Aldrich) was analysed in the similar condition by keeping the same catalyst loading (0.35 mg cm^{-2}). All the potentials were converted in to RHE by calibrating the Hg/HgO reference electrode in H_2-saturated 1 M KOH Solution. About 65% of automatic iR compensation was applied during the LSV measurements. For this, impedance has been performed in the OCV condition and the X-intercept is taken as the resistance (R_s) value. The value of R_s is used for automatic iR compensation during the LSV analysis. The O_2 quantification analysis was carried out in a gas chromatography instrument (GC) (Agilent Technologies, 7890A) and N_2 was used as the carrier gas. For quantifying O_2, chronoamperometric analysis was conducted at 1.51 V *vs.* RHE in a gas

tight electrochemical cell having a volume of 20 mL. The evolved O_2 was collected at each 15 min interval from the electrochemical cell by using a 500 µL gastight syringe and injected in to the GC.

4.3 Results and Discussion

4.3.1 TEM Analysis

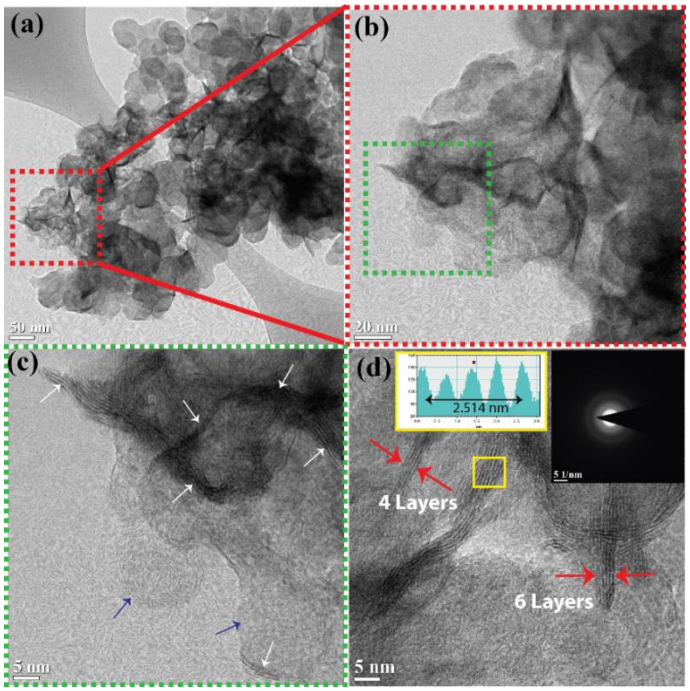

Figure 4.2. *TEM images of MoS_2/VC recorded at different magnifications: (a) growth pattern of MoS_2 layer on the functionalized Vulcan carbon (fn-VC) support; (b) magnified image of the portion marked in the red square in the panel a indicating the edge exposed growth of MoS_2; (c) higher magnification image of MoS_2 and fn-VC marked in the green square in the panel b, where the MoS_2 layers are indicated with the white arrows and the fn-VC substrate with the blue arrows; (d) higher magnification image of MoS_2 indicating its few layer structure (the inset shows the line profile of MoS_2 and the SAED pattern).*

The transmission electron microscopy (TEM) images of MoS_2/VC are presented in **Figure 4.2**. **Figure 4.2a-d** show the TEM images of MoS_2/VC recorded at different magnifications. The few-layer MoS_2 sheets are indicated by the white arrows, and the Vulcan carbon support is indicated by the blue arrows in **Figure 4.2c**. It is evident from the TEM image shown in **Figure 4.2d** that the MoS_2 sheet having 4-6 layers are distributed on the Vulcan carbon surface. The number of MoS_2 sheets varies from 4-10

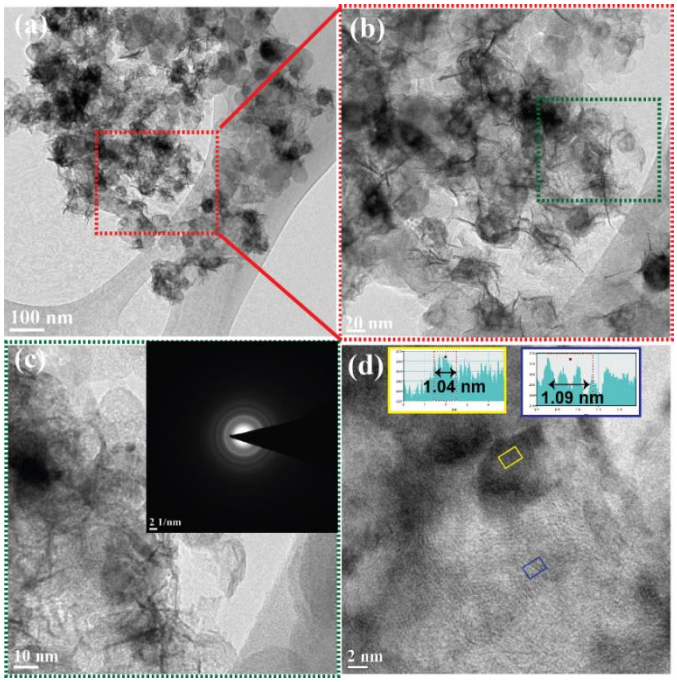

Figure 4.3. *TEM images of NiO@MoO_3/VC recorded at different magnifications: (a) the projected growth pattern of NiO-supported MoO_3 on fn-VC; (b) higher-magnification image of the portion indicated in the red square in panel a; (c) higher-magnification image of $Ni(OH)_2$, MoO_3, and fn-VC phases of the marked portion in the green square in panel b; the inset shows the SAED pattern; (d) dispersion of NiO on MoO_3, where the insets marked with the yellow and blue frames represent the NiO and MoO_3, respectively.*

layers in MoS_2/VC, and this reduction in the MoS_2 layer could increase the active sites due to the extended distribution. The inset in **Figure 4.2d** shows the line profile of MoS_2 which designates a d-spacing value of 0.63 nm and corresponds to the (002) plane of MoS_2.[27] The selected area electron diffraction (SAED) pattern shown in the inset of **Figure 4.2d** indicates the crystalline nature of the composite.

Figure 4.3 shows the TEM images of NiO@MoO_3/VC represented at different magnifications. Even though oxidation of the MoS_2 into MoO_3 is occurred during the second step of the hydrothermal treatment, it is confirmed from the TEM that the sheet structure is intact after the incorporation of the NiO nanosheets. **Figure 4.3b** is the enlarged view of the red portion as marked in **Figure 4.3a**, which indicates that the essential features of the composite remain unaltered even after the second round of the hydrothermal process. **Figure 4.3c** represents the enlarged view of the highlighted portion in **Figure 4.3b**. The SAED pattern shown in the inset of **Figure 4.3c** further

confirms the crystalline nature of the composite. The d-spacing value of NiO in NiO@MoO_3/VC is calculated from the TEM image (**Figure 4.3d**, inset in the yellow frame) and is about 0.21 nm, which corresponds to the (200) plane of NiO.[44] In **Figure 4.3d**, the inset image with blue frame shows the line profile of MoO_3 and the d-spacing value is found to be around 0.36 nm, which corresponds to the (001) plane of MoO_3.[28] The TEM images presented in **Figure 4.2** and **4.3** also reveal that the MoS_2 and MoO_3 sheets project in a sharp-edged fashion on the Vulcan carbon surface. These types of morphologies would exhibit more active sites compared to the usual stacking orientation of the bulk MoS_2 and MoO_3, where most of the active centres are buried inside the stacked layers.[25]

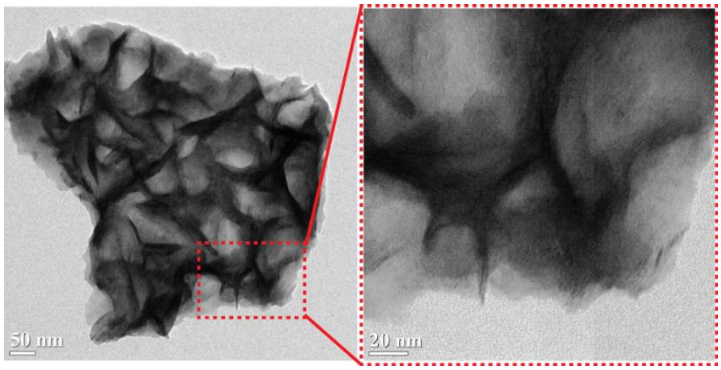

Figure 4.4. *TEM images of $Ni(OH)_2/MoO_3$ taken at different magnifications.*

The TEM images of $Ni(OH)_2/MoO_3$ (**Figure 4.4**) indicate the sheet-like morphology of MoO_3 and $Ni(OH)_2$. However, the $Ni(OH)_2$ sheets are presented in a compact form on the MoO_3 surface. This is due to the formation of large sized sheets of MoO_3 when the reaction is performed in the absence of fn-VC. In the absence of carbon, there is no suitable anchoring sites for the molybdenum ions for its uniform nucleation. This would lead to the non-uniform growth of the MoS_2 and larger sheets. The as formed large

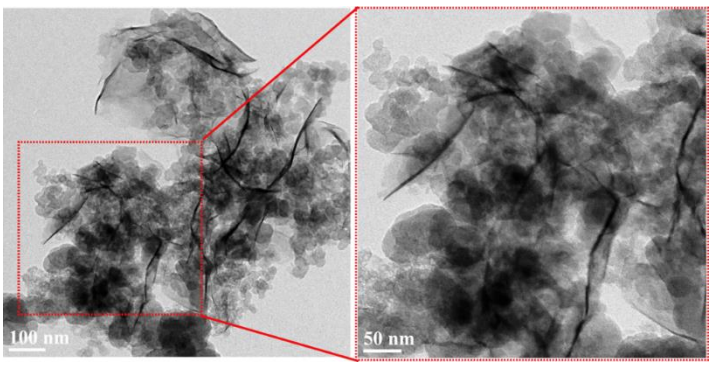

Figure 4.5. *TEM images of $Ni(OH)_2$/VC taken at different magnifications.*

scale MoS_2 sheets are used in the second hydrothermal step for carrying out the reaction. The TEM images of $Ni(OH)_2$/VC are presented in **Figure 4.5**. The layer structure of $Ni(OH)_2$ on fn-VC is confirmed from the TEM images (**Figure 4.5a-b)**.

4.3.2 FESEM Analysis

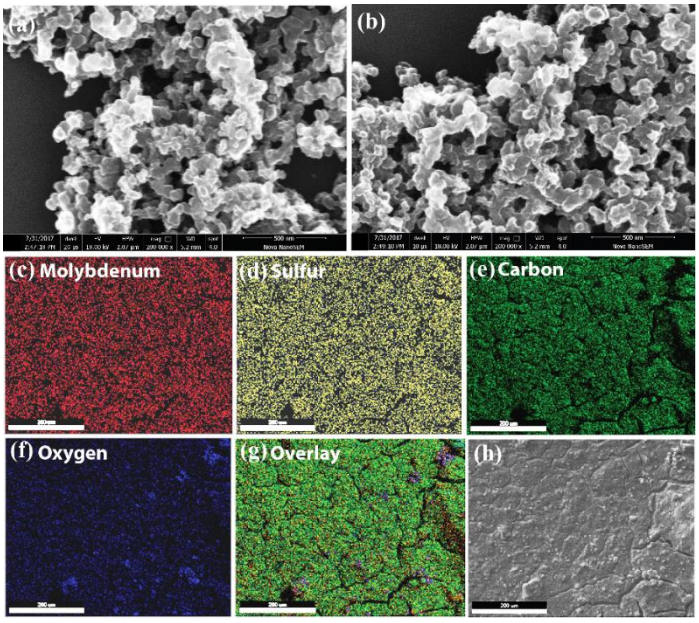

Figure 4.6. *(a-b) FESEM images of MoS_2/VC taken at different magnifications, (c-h) SEM-EDX elemental mapping of MoS_2/VC indicating the uniform distribution of molybdenum, sulfur and carbon in the system.*

The field emission scanning electron microscopy (FESEM) images of MoS_2/VC is presented in **Figure 4.6**. The mesoporous morphology of MoS_2/VC is evident from the FESEM images (**Figure 4.6a-b**). The mesoporous nature arises from the Vulcan carbon support and is retained even after the incorporation of MoS_2 on it. This is because, in the present case, the few-layer MoS_2 is present in the nanometer-sized sheets, rather than the micrometer size observed in the case of the bulk MoS_2. The SEM elemental

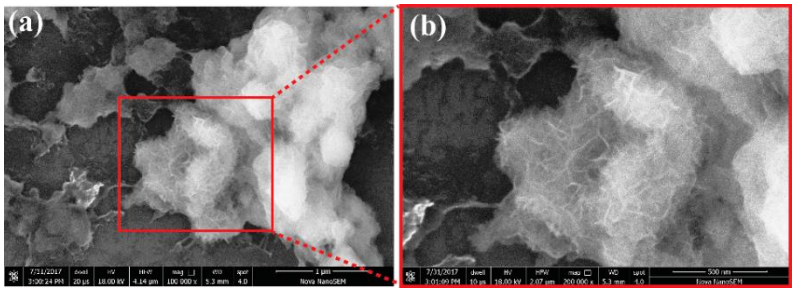

Figure 4.7. FESEM images of $Ni(OH)_2/MoO_3$ taken at different magnifications.

mapping of MoS_2/VC is illustrated in **Figure 4.6c-h**. The uniform distribution of molybdenum, sulfur and carbon is clear from the elemental mapping. The FESEM images of $Ni(OH)_2/MoO_3$ (***Figure 4.7***) show a flower-type morphology of the system.

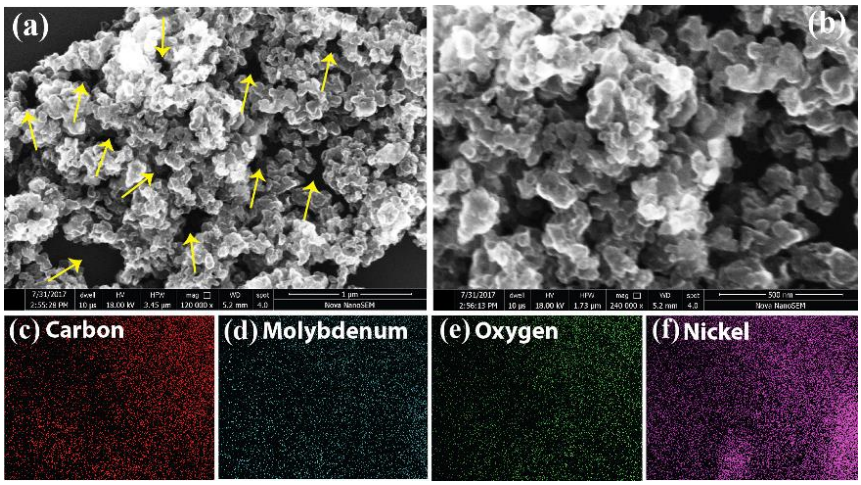

Figure 4.8. *(a-b) FESEM images of NiO@MoO_3/VC, yellow arrow marks in (a) indicate the porous structure of the material, (c-f) SEM-EDX elemental mapping of NiO@MoO_3/VC (c) carbon, (d) molybdenum, (e) oxygen and (f) nickel.*

The FESEM images of NiO@MoO_3/VC are illustrated in **Figure 4.8.** The meso- and macroporous structure of NiO@MoO_3/VC is evident in **Figure 4.8a-b**. The yellow arrow marks in **Figure 4.8a** indicate the mesoporous nature of NiO@MoO_3/VC. The SEM-EDX elemental mapping of NiO@MoO_3/VC is illustrated in **Figure 4.8c-f**. The uniform distribution of carbon, molybdenum, oxygen and nickel is clear from the elemental mapping.

4.3.3 XRD Analysis

X-ray diffraction (XRD) analysis has been carried out to find out the crystal phase of the material, and the comparative XRD spectra of the synthesized materials are presented in **Figure 4.9**. The XRD profile of fn-VC exhibits the peaks at the 2θ values of 25.1° and 43.3° corresponding to the (002) and (100) planes of carbon. The diffraction peaks in MoS_2/VC at the 2θ values of 14.3°, 32.2°, 39.5° and 58.1° are correspond to the (002), (100), (103), and (110) planes of MoS_2, respectively.[27] The slightly lower intensity of the (002) plane of MoS_2 in MoS_2/VC is because of the lower number of the MoS_2 layers in the composite.[29] The presence of $Ni(OH)_2$ in $Ni(OH)_2$@MoO_3/VC is confirmed from the diffraction peaks at the 2θ values of 19.2°,33.3°, 38.8° and 59.2°, which are corresponding to the (001), (100), (101) and (110) planes of $Ni(OH)_2$,

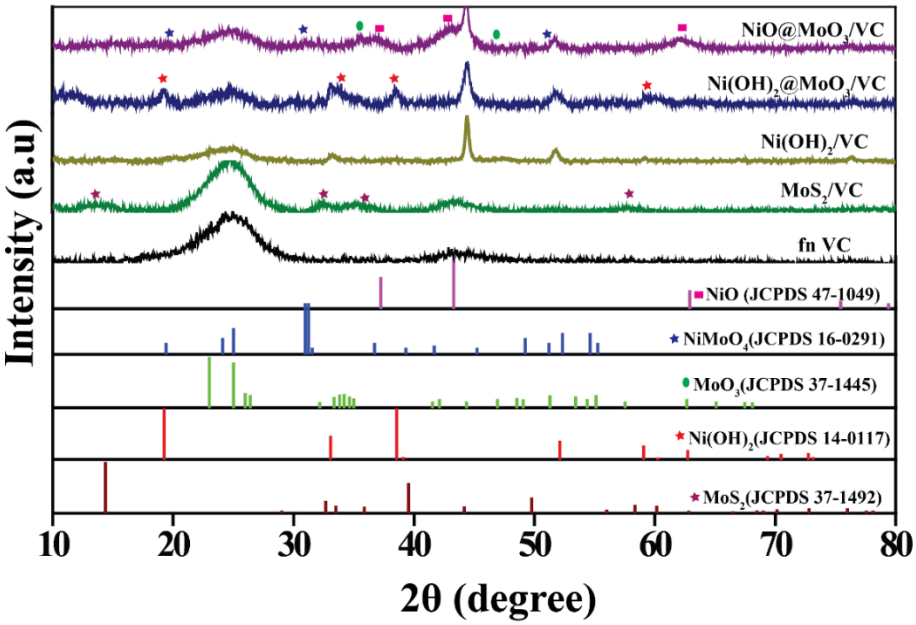

Figure 4.9. *Comparison of the XRD profiles of fn-VC, MoS_2/VC, $Ni(OH)_2$/VC, $Ni(OH)_2$@MoO_3/VC, and NiO@MoO_3/VC along with the standard XRD card numbers.*

respectively.[30-31] The peaks corresponding to the metallic nickel appeared in $Ni(OH)_2$@MoO_3/VC could be from the minute amount of Ni^0 state present in the system since we have used a reducing agent in the process. However, XPS data (explained in the following section) is not indicating any existence of Ni^0 state in the sample, suggesting deep dispersion of small amount of these moieties in the predominant $Ni(OH)_2$ phase. Upon heat treatment at 300 °C, the $Ni(OH)_2$ is converting to NiO and the peaks appeared at 2θ values of 37.1°, 42.9° and 62.2° are corresponding to the (111), (200) and (220) planes, respectively, of NiO in NiO@MoO_3/VC.[32-33] The peaks at the 2θ values of 19.5°, 30.9° and 51.9° are corresponding to the (100), (111) and (130) planes respectively of nickel molybdate ($NiMoO_4$) present in NiO@MoO_3/VC. The lower intensities of the plane corresponding to $NiMoO_4$ in NiO@MoO_3/VC indicates that nickel molybdate is present in minute amount, possibly as a surface layer. The peak at the 2θ value of 25.2° corresponds to the (002) plane of the graphitic carbon[34] whereas the peak at the 2θ values of 35.5° and 47.3° are corresponding to the (102) and (022) planes of MoO_3, respectively, in NiO@MoO_3/VC. It is clear from the XRD spectra that the peak intensity of carbon is improved in NiO@MoO_3/VC compared to the non-heat-treated counterpart ($Ni(OH)_2$@MoO_3/VC). This could be due to the improved graphitization achieved after the removal, to some extent, of amorphous carbon from the system at 300 °C in the inert atmosphere.

4.3.4 Thermogravimetric Analysis (TGA)

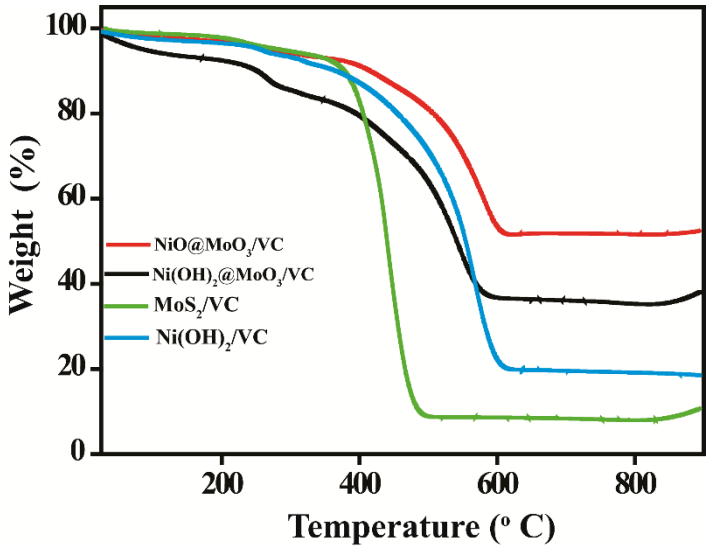

Figure 4.10. *Comparative TGA profiles of $Ni(OH)_2$/VC, MoS_2/VC, $Ni(OH)_2@MoO_3$/VC and $NiO@MoO_3$/VC recorded in air atmosphere from room temperature to 900 °C.*

The thermal stability of the material has been investigated by thermogravimetric analysis (TGA) in air atmosphere by heating the samples from room temperature to 900 °C at a heating rate of 10 °C min^{-1} as presented in **Figure 4.10**. The initial drop up to 100 °C in all the samples is because of the loss of adsorbed water molecules from the system. The $Ni(OH)_2@MoO_3$/VC displays a reduction stage at around 300 °C, which is possibly due to the removal of the amorphous carbon from the system. A quick drop after 430 °C is attributed to the conversion of carbon into CO_2.

4.3.5 Raman Analysis

Raman spectroscopy was used to study the structural defects in the samples. In detail, the bands at 1300 and 1590 cm^{-1} correspond to the D-band (A_{1g} mode) and G-band ($2E_{2g}$ mode) for the carbon, respectively[35], which demonstrate the degrees of disorder and graphitization present in the system. The comparative Raman spectra of the samples are shown in **Figure 4.11** where the D- and G-band are highlighted in the box. The positions of the D- and G-band of fn-VC are at 1314 and 1582 cm^{-1}, respectively. However, a shift towards a higher wavenumber is observed after the incorporation of MoS_2 on fn-VC (MoS_2/VC). The corresponding peak positions of D- and G- band in MoS_2/VC are at 1336 and 1597 cm^{-1}, respectively. This shift is attributed to the charge transfer between the MoS_2 layer and carbon. Compared to MoS_2/VC, the peak position of $NiO@MoO_3$/VC is shifted slightly to the lower wavenumber and the corresponding

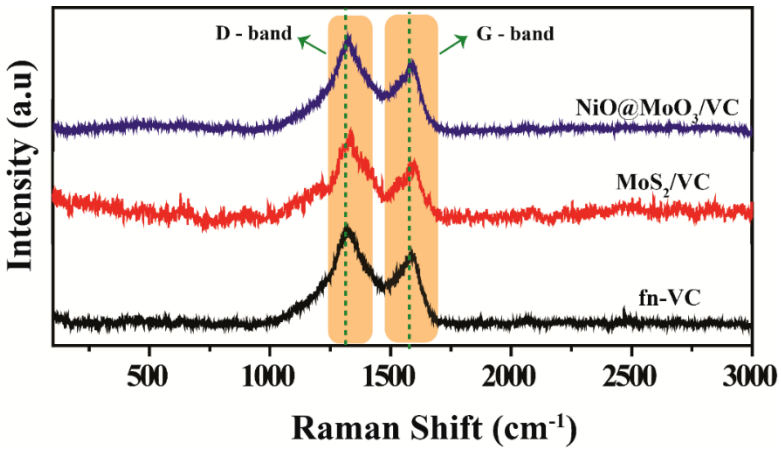

Figure 4.11. *Comparative Raman spectra of fn-VC, MoS_2/VC and NiO@MoO_3/VC.*

values are 1325 and 1592 cm^{-1}, respectively. The I_D/I_G ratio is used to analyse the structural defects present in the system and the corresponding values for fn-VC, MoS_2/VC, and NiO@MoO_3/VC are 1.32, 1.33, and 1.34, respectively. It can be observed that the I_D/I_G value has been increased after the incorporation of MoS_2 on fn-VC. This is because the disorder is increased after incorporating MoS_2 on fn-VC. A similar trend is observed after anchoring the NiO on MoO_3/VC (NiO@MoO_3/VC), where the defect has been increased, which gives rise to a higher I_D/I_G ratio among the compared samples.

4.3.6 Surface Area and Pore-size Distribution Analysis

The comparative Brunauer-Emmett-Teller (BET) data of fn-VC, MoS_2/VC, and NiO@MoO_3/VC is presented in **Figure 4.12a**. The surface area of fn-VC is found to be 191 m^2/g.[34] However, the surface area is substantially reduced after the incorporation of MoS_2 on fn-VC (MoS_2/VC) and the corresponding value is 31 m^2/g. Previously published literature too indicates lower values of surface area for the MoS_2-based systems, and this could be due to the layered structure of the material. Compared to MoS_2/VC, the nickel counterpart of the system, *i.e.*, NiO@MoO_3/VC, exhibits a slightly higher surface area of 45 m^2/g. The improvement in the surface area is because of the presence of small sized NiO nanosheets and the removal of defects during the heat treatment at 300 °C. The pore size distribution of the sample is shown in **Figure 4.12b** and fn-VC possesses both micro- and mesoporous characteristics. The mesoporous nature of the Vulcan carbon would enhance the mass diffusion of the reactants and enhance the continuous oxidation of hydroxyl ions in the system. In fact, the micro-porosity is reduced in the Mo-based systems (MoS_2/VC and NiO@MoO_3/VC) and the

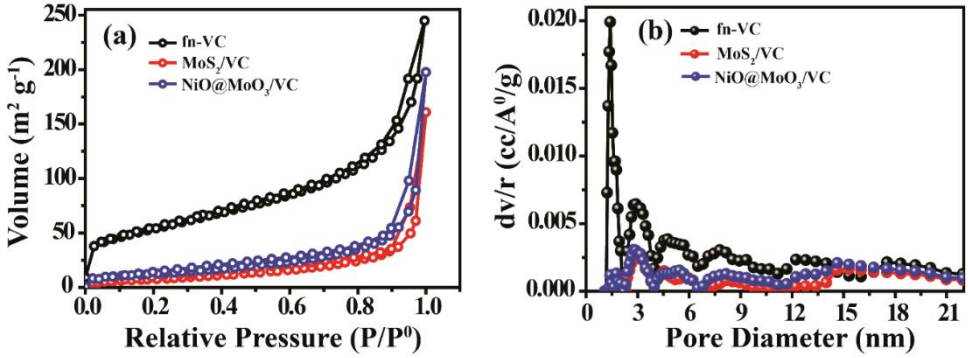

Figure 4.12. *(a) N_2 adsorption-desorption isotherm profiles of fn-VC, MoS_2/VC and NiO@MoO_3/VC and (b) pore-size distribution profiles of fn-VC, MoS_2/VC and NiO@MoO_3/VC.*

mesoporous nature is dominant. The reduction in micro-porosity is because of the dispersion of MoS_2 on fn-VC, which might block the micropores on VC. The hysteresis loop in the adsorption isotherm also reveals the mesoporous nature of the material. Because of the mesoporous nature of NiO@MoO_3/VC, the mass transfer of the hydroxyl ions would be facilitated during the water oxidation reaction.

4.3.7 MP-AES Analysis

Microwave plasma-atomic emission spectroscopy (MP-AES) analysis has been performed to find out the metal content in NiO@MoO_3/VC (**Figure 4.13**). For the MP-AES analysis, the sample was digested in aqua regia and performed the analysis to get the Ni and Mo content in NiO@MoO_3/VC. From the MP-AES data, the Ni to Mo ratio is found to be nearly 10 in NiO@MoO_3/VC. The MP-AES analysis of the electrolyte used for the electrochemical analysis is also carried out to examine the Fe impurities and found that the solution is free from Fe impurities.

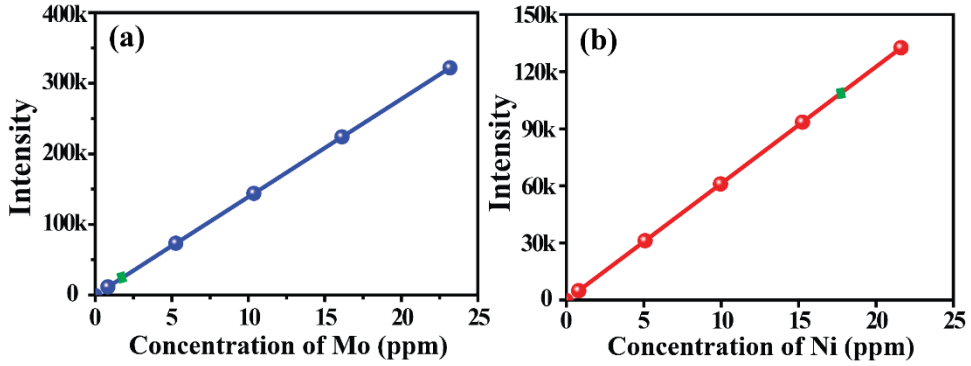

Figure 4.13. *MP-AES analysis of NiO@MoO_3/VC: (a) Mo in NiO@MoO_3/VC and (b) Ni in NiO@MoO_3/VC.*

4.3.8 XPS Analysis

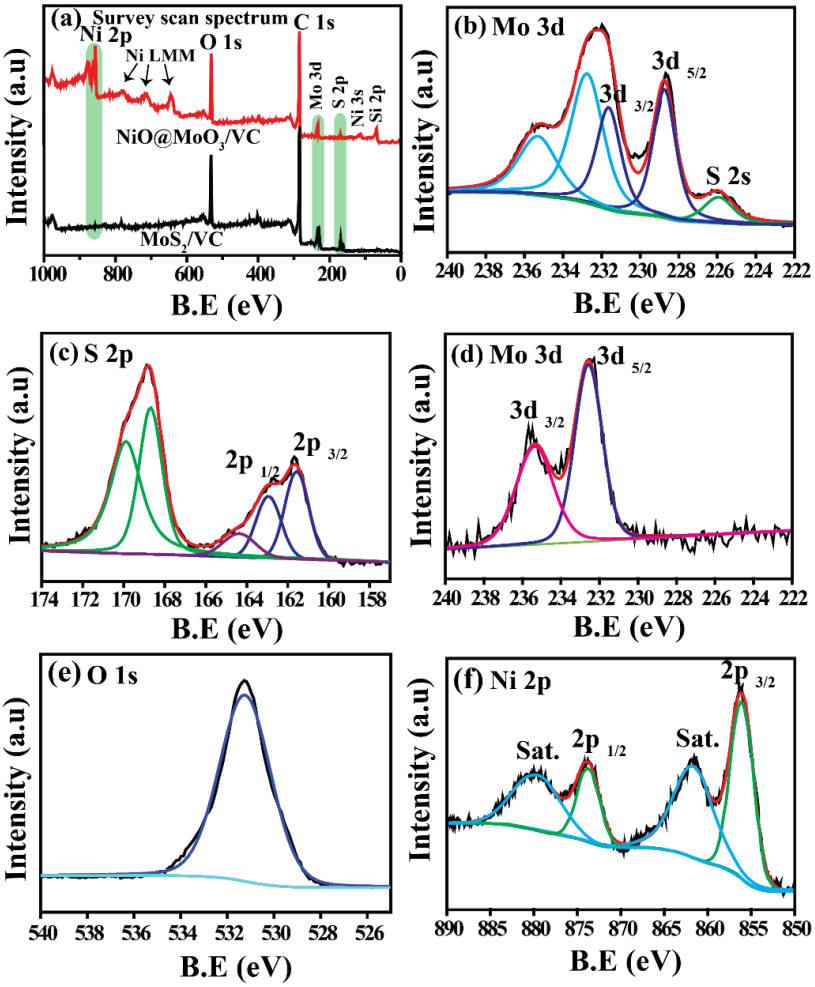

Figure 4.14. *XPS spectra of MoS_2/VC and NiO@MoO_3/VC: (a) comparative survey scan spectra of MoS_2/VC and NiO@MoO_3/VC and deconvoluted XPS of (b) molybdenum in MoS_2/VC, (c) sulfur in MoS_2/VC, (d) molybdenum in NiO@MoO_3/VC, (e) oxygen in NiO@MoO_3/VC, and (f) nickel in NiO@MoO_3/VC.*

X-ray photoelectron spectra (XPS) analysis of the material has been carried out to find out the chemical state of the elements in the composite and the data is presented in **Figure 4.14**. The survey scan spectra of MoS_2/VC and NiO@MoO_3/VC are compared in **Figure 4.14a**, which evidently indicate the presence of C, O, Ni, Mo, and S in the sample. The presence of the Ni based peak, which is absent in MoS_2/VC, is confirmed in NiO@MoO_3/VC. The oxygen peak in the survey scan spectrum is due to the metal oxides and also from the partial oxidation of the sample during the analysis. The deconvoluted molybdenum spectra of MoS_2/VC (**Figure 4.14b)** show prominent peaks at 228.7 and 231.6 eV, which correspond to the $3d_{5/2}$ and $3d_{3/2}$ of Mo^{4+} oxidation state

of MoS_2.[36] The peak at 225.9 eV is corresponding to the S 2s of MoS_2.[37] The sulfur XPS spectra of the same sample exhibits the peaks at 161.5 and 162.9 eV, corresponding to the $2p_{3/2}$ and $2p_{1/2}$ peaks of the sulfide ions of MoS_2 (**Figure 4.14c)**.[36] The peak at 164.3 eV is corresponding to the bridging disulfides S_2^{-2}.[62] The peaks at 168.7 and 169.9 eV in the S 2p spectrum correspond to the surface SO_4^{2-} species, feasibly formed by the exposure of the catalyst to air.[63-64] The deconvoluted molybdenum spectra of NiO@MoO_3/VC has its peaks at a higher binding energy (232.6 and 235.4 eV) and the peaks corresponding to Mo^{4+} is disappeared (**Figure 4.14d)**. This is due to the oxidation of MoS_2 during the second step of the hydrothermal treatment and conversion into MoO_3.[26] The Mo^{+6} oxidation state is also could be originated from the $NiMoO_4$ phase present in NiO@MoO_3/VC.[43] The O 1s spectra ((**Figure 4.14e**) of NiO@MoO_3/VC exhibits the peak at 531.3 eV, which corresponds to the Mo-O and Ni-O bond.[26, 38, 39] The Ni spectrum in NiO@MoO_3/VC shows the peaks at 856.1 and 873.6 eV, which correspond to the $2p_{3/2}$ and $2p_{1/2}$ states of Ni^{2+} (**Figure 4.14f)**.[30, 40] The satellite peaks are also visible in the deconvoluted spectra of Ni. The peaks observed at the higher binding energies of the sulfur spectra in MoS_2/VC are due to the sulfate ions.

4.3.9 Electrochemical Analysis

After the structural analysis, the electrochemical activity of the material towards OER has been investigated in an N_2-saturated 1 M KOH solution using a rotating disc electrode (RDE) set-up. Glassy carbon electrode having an active area of 0.0706 cm^2 was used as the working electrode and the catalyst loading was maintained at 0.35 mg/cm^2. Graphite rod and Hg/HgO were used as the counter and reference electrodes, respectively. The OER activity of the as-synthesized materials has been analyzed by comparing the linear sweep voltammograms (LSVs) recorded in N_2-saturated 1 M KOH solution with a scan rate of 10 mV s^{-1} and at a rotation speed of 1600 r.p.m of the working electrode. About 65% of iR compensation was applied during the LSV measurements. Prior to LSV measurements, CV has been performed in the potential window of 1.0 V to 1.6 V *vs.* RHE in N_2 saturated 1 M KOH solution with a scan rate of 50 mV sec^{-1} and at 900 r.p.m of the working electrode for at least 20 cycles. The overpotential of all the materials have been calculated from the theoretical onset potential for OER (1.23 V) and at a standard current density of 10 mA cm^{-2}, which is the current obtained at the anode of a 10% efficient solar water-splitting device under one illumination of sun light.[41] **Figure 4.15a** represents the comparative CV profiles

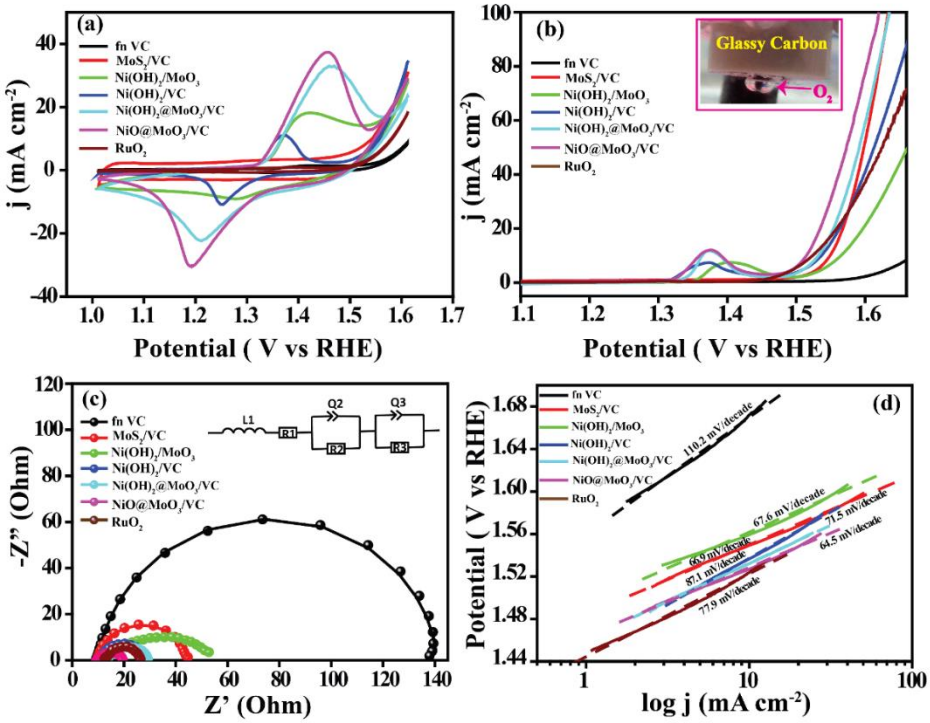

***Figure 4.15**. (a) Comparative cyclic voltammograms of the samples recorded in 1 M KOH solution with a scan rate of 50 mV s^{-1} and a rotation of 900 rpm of the working electrode; (b) comparative LSV profiles of the samples recorded in 1 M KOH solution at 1600 rpm of the working electrode and at a scan rate of 10 mV s^{-1} where the inset shows the produced O_2 gas in NiO@MoO_3/VC; (c) electrochemical impedance analysis of the samples performed at an overpotential of 350 mV in 1 M KOH solution where the inset shows the equivalent circuit used to fit the data; (d) Tafel plot comparison of the samples obtained after applying 65% iR compensation in the LSVs.*

of the samples when the analysis was carried out in 1 M KOH solution at a scan rate of 50 mV sec^{-1} with a 900-r.p.m of the working electrode. The cyclic voltammograms show the prominent redox peaks for the Ni-based samples. The oxidation peak is observed at 1.45 V for NiO@MoO_3/VC and is corresponds to the oxidation of Ni^{2+} to Ni^{3+}. The reduction peak is present at 1.19 V and is due to the conversion of Ni^{3+} into Ni^{2+} in NiO@MoO_3/VC. The corresponding oxidation and reduction peaks of $Ni(OH)_2$@MoO_3/VC is present at 1.46 and 1.21 V, respectively. Similarly, the redox peaks are present in $Ni(OH)_2$/VC at 1.37 and 1.25 V, respectively. The peak positions for the oxidation of Ni^{2+} in $Ni(OH)_2$/VC and NiO@MoO_3/VC are not similar, which indicates the interaction of NiO with MoO_3 in NiO@MoO_3/VC and shifts the oxidation at a higher potential.

In order to obtain insightful information about the OER activity of the material, LSVs have been compared and the profiles are presented in **Figure 4.15b**. An evaluation of the LSV data displays a rapid increment in current after the peak, corresponding to the oxidation of Ni^{2+}, resulting from the water oxidation. The OER activity of fn-VC, which exhibits an overpotential of 440 mV at a current density of 10 mA cm^{-2}, is insignificant. However, after the introduction of MoS_2 on fn-VC (*i.e.*, MoS_2/VC), the OER activity improves and the overpotential reduces to 318 mV at a similar current density. The trend is comparable after the incorporation of $Ni(OH)_2$ on fn-VC (*i.e.*, $Ni(OH)_2$/VC), where the overpotential at 10 mA cm^{-2} is found to be 306 mV. Even though the OER activity of fn-VC is poor, the presence of fn-VC is essential to maintain the electrical conductivity in the system. To validate this, we have synthesized $Ni(OH)_2/MoO_3$ which exhibits a higher overpotential of 334 mV at the same current density. This could be due to the lack of appropriate electrical conductivity in the system. The OER activity has been improved further in the case of $Ni(OH)_2@MoO_3$/VC, which has been formed by incorporating $Ni(OH)_2$, MoO_3, and fn-VC in the same system (explained in the synthesis part). The overpotential exhibited by this composition is 300 mV. Here, the MoO_3 is formed from the oxidation of the MoS_2 during the second step of the hydrothermal process. The heat-treatment of $Ni(OH)_2@MoO_3$/VC at 300 °C in the inert atmosphere leads to the conversion of $Ni(OH)_2$ into NiO and this transformation further improves the OER activity. Thus obtained material (*i.e.*, NiO@MoO_3/VC) exhibits an overpotential of 280 mV at 10 mA cm^{-2}, compared to the 300 mV overpotential exhibited by the non-heat-treated sample ($Ni(OH)_2@MoO_3$/VC). For comparison, the *state-of-the-art* RuO_2 catalyst has been analysed in the same condition and the overpotential found at 10 mA cm^{-2} current density is 292 mV. Thus, the OER activity of the present catalyst (NiO@MoO_3/VC) is better than that of the highly expensive commercial RuO_2 catalysts.

Impedance analysis of the materials was performed to understand the contributing resistive factors in the material which affects the OER activity. The analysis was carried out at an overpotential of 350 mV in 1 M KOH solution with an AC frequency of 200 kHz to 100 mHz and an AC amplitude of 10 mV (**Figure 4.15bc**). The impedance spectrum is fitted with an equivalent circuit of (L_1+R_1+Q_2/R_2+Q_3/R_3), where R_1, R_2, and R_3 are the resistances, Q_2 and Q_3 are the constant phase element associated with the material and L_1 is the inductance of the connecting cables. The difference between R_3 and R_1, called the charge transfer resistance (R_{CT}) value, determines the ionic transport

during the reaction. A lower R_{CT} value is preferred for better OER activity. The comparative R_{CT} values of all the synthesized samples and commercial RuO_2 catalyst are presented in **Table 4.1**. Among the synthesized samples, fn-VC exhibits a higher R_{CT} value of 129.5 Ω, which is reflected in its lower OER performance. However, after incorporating MoS_2 on fn-VC (*i.e.*, MoS_2/VC), the R_{CT} value is lowered to 35.9 Ω and concomitantly the OER activity is improved. Among the prepared samples, NiO@MoO_3/VC exhibits the lowest charge transfer resistance (R_{CT}) value of 11.3 Ω. This indicates the faster ionic transport in NiO@MoO_3/VC and hence, the improved OER activity. The lower R_{CT} value displayed by NiO@MoO_3/VC could be due to the presence of the small sized NiO nanosheets which facilitate the faster adsorption of hydroxyl ions, the better electrical conductivity and mesoporous nature of fn-VC which facilitate the electron and mass transfer during OER. Along with this, the presence of few-layered MoO_3 which effectively anchors the NiO nanosheets also contributes a determining role towards the modulated performance. Thus, a controlled interplay of all of these factors results in to a significant improvement on the performance of the system towards OER. The information about the OER kinetics is derived from the LSVs of the material by plotting log j *vs.* potential, or the Tafel Plot (**Figure 4.15d**). The Tafel slope value indicates the rate of the reaction and a lower Tafel slope correlates with faster kinetics. **Table 4.1** shows the Tafel slope comparison of the prepared materials with the *state-of-the-art* RuO_2 catalyst. The NiO@MoO_3/VC shows the lowest Tafel slope value of 64.5 mV/decade from the prepared sample, which is reflected in the improved OER performance.

Sl. No	Sample	R_{CT} (Ω)	Tafel Slope (mV/decade)	ECSA (cm^2)
1	fn-VC	129.5	110.2	16.6
2	MoS_2/VC	35.9	66.9	15.6
3	$Ni(OH)_2/MoO_3$	45.1	67.6	1.2
4	$Ni(OH)_2$/VC	22.3	87.1	8.2
5	$Ni(OH)_2$@MoO_3/VC	20.4	71.5	3.8
6	NiO@MoO_3/VC	11.3	64.5	7.2
7	RuO_2	14.1	77.9	11.5

Table 4.1: *Comparison of the R_{CT} values, Tafel slopes and ECSA of the prepared materials in comparison with the commercial RuO_2.*

In order to understand the effect of scan rate during the LSV analysis, we have performed the LSV analysis of NiO@MoO_3/VC at two different scan rates of 2 mV sec^{-1} and 10 mV sec^{-1} and presented the corresponding data as **Figure 4.16a**. The contribution from the capacitive current is decreased at lower scan rate (2 mV sec^{-1}). However, there is not much change in the overpotential value at 10 mA cm^{-2} with different scan rates. Compared to the overpotential obtained at a scan rate of 10 mV sec^{-1}, the overpotential exhibited at 2 mV sec^{-1} scan rate is about 3 mV lower. This indicates that the LSV performance is not significantly shifting with the scan rate of 2 mV sec^{-1} and 10 mV sec^{-1} in the present work. Also, we have performed the iR uncorrected LSVs of NiO@MoO_3/VC and presented the data as **Figure 4.16b**. It is deduced form **Figure 4.16b** that if the LSV is performing without any iR correction, only 7 mV higher overpotential is observed at 10 mA cm^{-2} (287 mV). The difference is noticeable only at

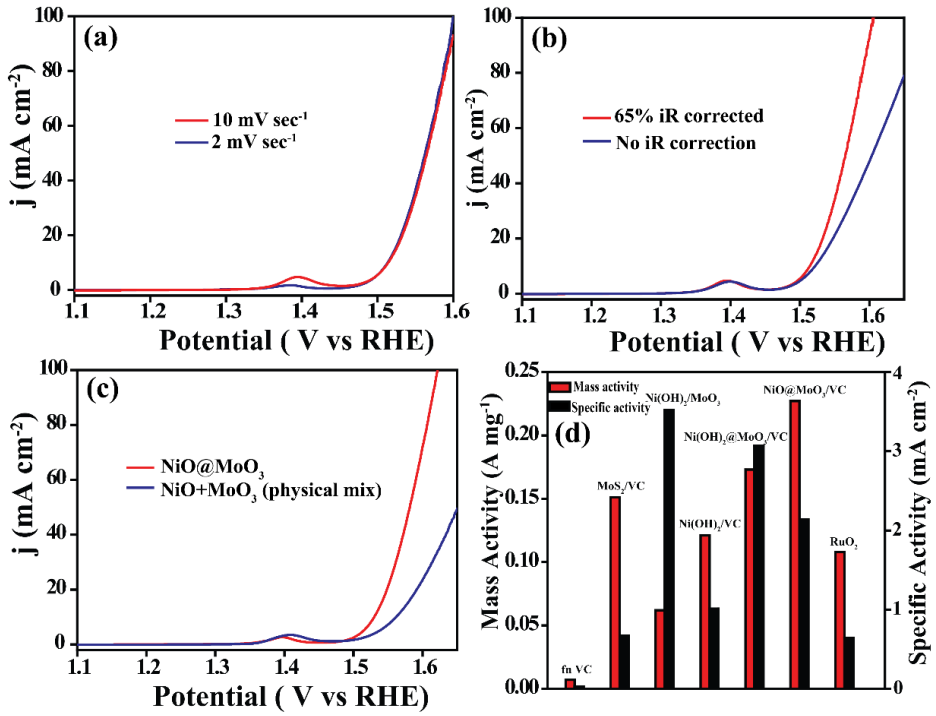

Figure 4.16. *(a) Comparative LSV profiles of NiO@MoO_3/VC recorded in 1 M KOH solution at 1600 rpm of the working electrode and at the scan rates of 2 mV sec^{-1} and 10 mV sec^{-1}, (b) comparative LSV profiles of NiO@MoO_3/VC recorded in 1 M KOH solution with and without iR correction at 1600 rpm of the working electrode and at the scan rates of 10 mV sec^{-1}, (c) comparative LSV profiles of the NiO@MoO_3 and physical mixture of NiO-MoO_3 recorded in 1 M KOH solution at 1600 rpm of the working electrode and at the scan rate of 10 mV sec^{-1} and (d) comparison of the specific and mass activities of fn-VC, MoS_2/VC, $Ni(OH)_2/MoO_3$, $Ni(OH)_2$/VC, $Ni(OH)_2$@MoO_3/VC, NiO@MoO_3/VC and RuO_2 at 1.60 V vs. RHE.*

higher current density. The lower overpotential associated with the heat-treated sample ($NiO@MoO_3/VC$) could be because of the high degree of graphitization present in the system (explained in the XRD part) which improves the electrical conductivity of the material, and the presence of the conducting substrate, mainly Vulcan carbon, could resolve the issue related to the electrical conductivity of MoO_3 in the composite. The mesoporous nature of the Vulcan carbon further facilitates OER by providing better mass transfer of the hydroxyl ions and the evolved O_2 during the water oxidation. However, the presence of MoO_3 is essential for maintaining the enhanced performance as well as the stability of the material (explained in the upcoming section) for long-term operation. We have performed the LSV analysis of the physical mixture of NiO and MoO_3 and compared with $NiO@MoO_3$ (**Figure 4.16c**). The overpotentials exhibited by $NiO@MoO_3$ and $NiO+MoO_3$ (physical mix) at 10 mA cm^{-2} current density are 300 mV and 330 mV, respectively. This indicates that the OER performance is comparatively poor if NiO and MoO_3 are present as physical mixture rather than as the composite. The improved performance possessed by $NiO@MoO_3$ could be explained because of the possible interactions occurring between NiO and MoO_3 in the composite ($NiO@MoO_3$). However, similar kind of interaction could not be expected from the physical mixture of NiO and MoO_3. This leads to the lower OER performance in the physical mixture of NiO and MoO_3. The specific and mass activities of all the samples are compared with RuO_2 and presented in **Figure 4.16d**. It is concluded from **Figure 4.16d** that both the specific and mass activities of $NiO@MoO_3/VC$ are higher than that of *state-of-the-art* RuO_2 catalyst.

The electrocatalytic active surface area (ECSA) of the samples has been found out from the electrochemical double-layer capacitance (C_{dl}) value. For this, CV has been performed in the non-Faradaic region (0.97 V to 1.07 V *vs*. RHE) at different scan rates ranging from 5 mV sec^{-1} to 60 mV sec^{-1} (**Figure 4.17**). A plot of the scan rate against the obtained current at 1.02 V would give a straight line and the slope of the line is the C_{dl} value (**Figure 4.17** and **Figure 4.18a**). The ECSA is obtained from the C_{dl} value by using the equation:

$$ECSA = C_{dl}/C_s$$

where, C_s is the specific capacitance of the metal. For $NiO@MoO_3/VC$, we have used C_s value as 40 µF, which corresponds to the composite of Ni and Mo.[42] The calculated ECSA value of $NiO@MoO_3/VC$ is 7.2 cm^2, which is in good agreement with the literature related to the Ni-based catalysts. The roughness factor (RF) of

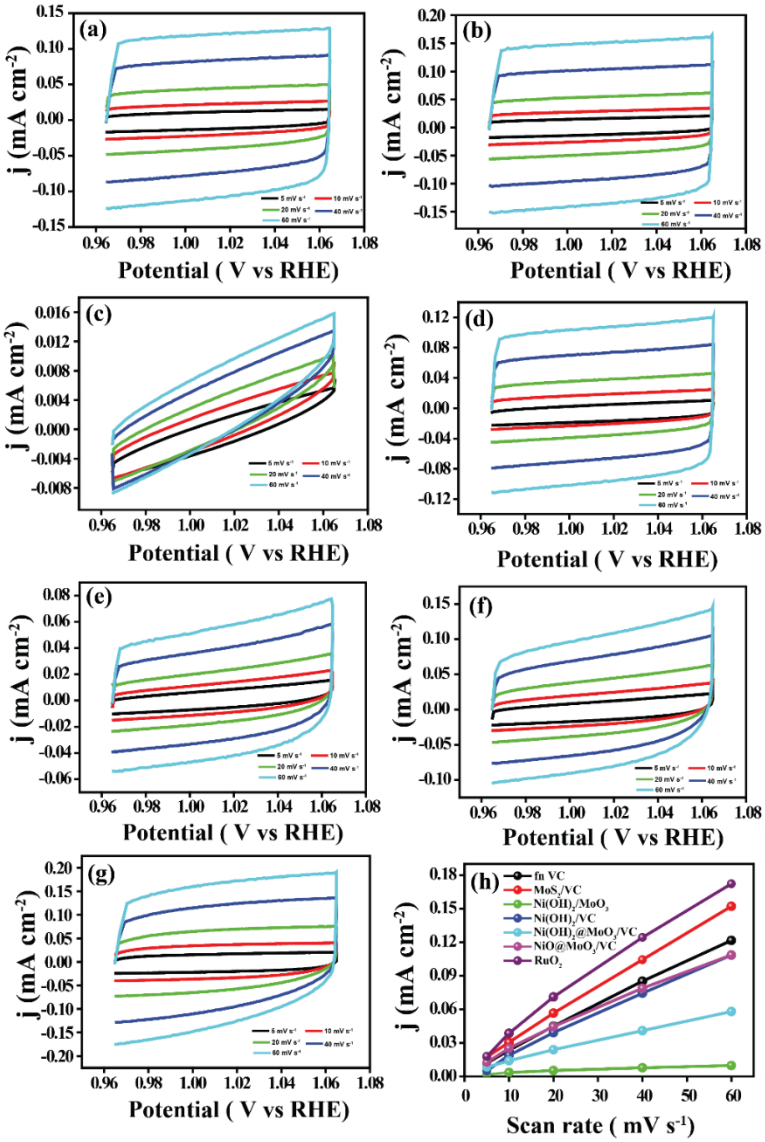

Figure 4.17. *Cyclic voltammograms of the catalyst in the non-faradaic region recorded at different scan rates in the N_2-saturated 1 M KOH solution; (a) fn-VC, (b) MoS_2/VC, (c) $Ni(OH)_2/MoO_3$, (d) $Ni(OH)_2$/VC, (e) $Ni(OH)_2@MoO_3$/VC, (f) NiO@MoO_3/VC, (g) RuO_2 and (h) plot of the anodic current against scan rate in the non-Faradaic region of the CVs.*

NiO@MoO_3/VC is calculated from the ECSA value by dividing it with the geometric area of the electrode and is around 36.8. Rotating Ring Disc Electrode (RRDE) study has been performed to find out the Faradaic Efficiency (FE) of NiO@MoO_3/VC in N_2 saturated 1 M KOH solution (**Figure 4.18b**). The main aim of the FE measurement is to confirm that the produced current is due to the oxidation of hydroxyl ions. For the RRDE analysis, a carbon disc surrounded by a platinum ring was used as the working electrode. A graphite rod as the counter electrode and Hg/HgO as the reference electrode

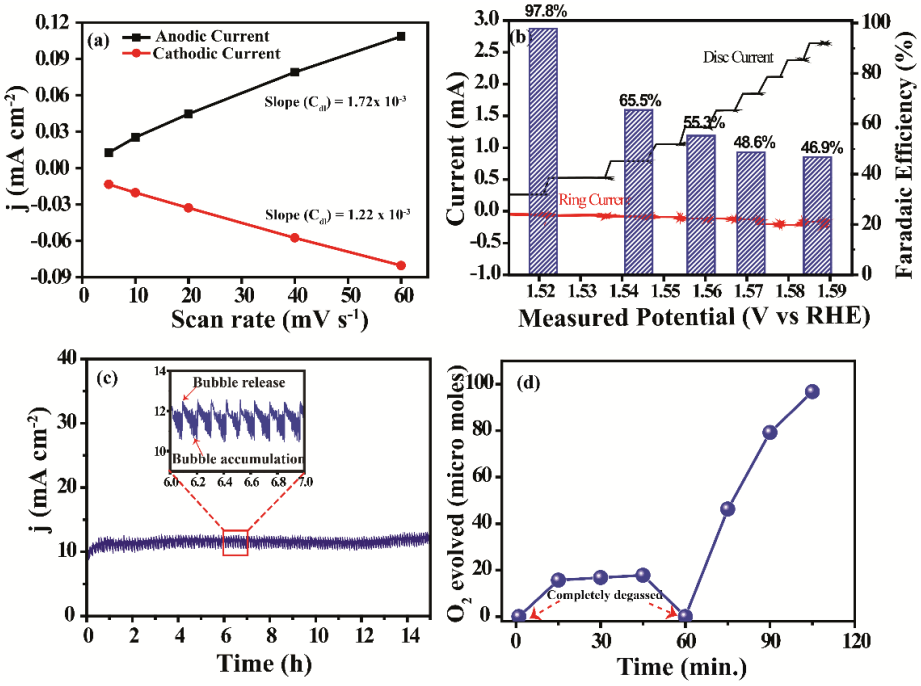

Figure 4.18. *(a) Plot of the anodic and cathodic current of NiO@MoO_3/VC against scan rate in the non-Faradaic region of the CV, (b) Faradaic efficiency analysis of NiO@MoO_3/VC using RRDE technique in the N_2-saturated 1 M KOH solution by applying different current densities on the disc electrode and at a rotation speed of 1600 rpm of the working electrode, (c) chronoamperometric response of NiO@MoO_3/VC in 1 M KOH solution for 15 h at 1.51 V, and (d) O_2 gas quantification analysis of NiO@MoO_3/VC using gas chromatography.*

were also employed. The rotation of the working electrode was maintained at 1600 r.p.m during the analysis. A range of successive current values from 1 mA cm^{-2} to 10 mA cm^{-2} were applied on the disc electrode and the subsequently generated oxygen was reduced to H_2O_2 at the platinum ring electrode, which was kept at a constant potential of 0.40 V *vs.* RHE. The Faradaic efficiency is calculated from RRDE analysis and is found to be 98% at 1 mA cm^{-2} and 47% at 10 mA cm^{-2}; this reduction in efficiency at a higher current density can be attributed to the quick evolution of O_2 gas at the disc electrode and the ring being unable to collect the entire quantity of O_2 that is being generated at the disc electrode.

The concurrent maintenance of higher activity and outstanding stability enhances the efficiency of a catalyst. Stability analysis of NiO@MoO_3/VC was carried out through chronoamperometric analysis at 1.51 V (*vs.* RHE) for 15 h in the N_2-saturated 1 M KOH solution at 1600 r.p.m of the working electrode (**Figure 4.18c**). The material shows

excellent stability at 10 mA cm^{-2} for the entire duration of the analysis without any alteration in the activity. The stability data hence confirms that the material is stable in the working condition and this could be due to the simultaneous presence of MoO_3 along with the surface dispersed $NiMoO_4$ sheets. This reduces the agglomeration of the NiO sheets and decreases carbon corrosion by providing a protecting layer on fn-VC. The presence of the surface $NiMoO_4$ layer is adequate to prevent the dissolution of MoO_3 in the alkaline environment. In order to confirm the high corrosion stability of the MoO_3 bearing $NiMoO_4$, the chronoamperometric analysis of $Ni(OH)_2$/VC was carried out under the same conditions and the data is presented in **Figure 4.19**. The stability of $Ni(OH)_2$/VC is reduced rapidly after a few hours and this could be due to the corrosion of fn-VC and the subsequent agglomeration of the $Ni(OH)_2$ nanosheets. Hence, the presence of MoO_3 appeared to be protecting fn-VC from corrosion and providing structural stability in the composite.

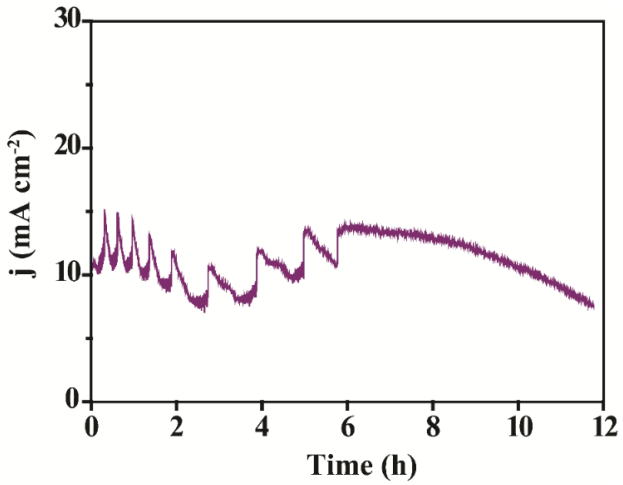

Figure 4.19. *Chronoamperometric analysis of $Ni(OH)_2$/VC in 1 M KOH solution.*

The O_2 quantification of $NiO@MoO_3$/VC has been done using gas chromatography (GC) analysis; the result of which is shown in **Figure 4.18d**. For the O_2 quantification analysis, a gas-tight electrochemical cell having a volume of 20 mL was constructed. About 10 mL of 1 M KOH solution was taken as the electrolyte. Chronoamperometric analysis of $NiO@MoO_3$/VC was performed at 1.51 V (*vs.* RHE) and the evolved O_2 was collected from the head space of the electrochemical cell using a micro syringe at 15-minute intervals and analysed using the GC instrument. Before the chronoamperometric analysis, the electrochemical cell was degassed by continuously flushing N_2 gas in the electrolyte. The quantification has been done by collecting the gas after each 15-minute

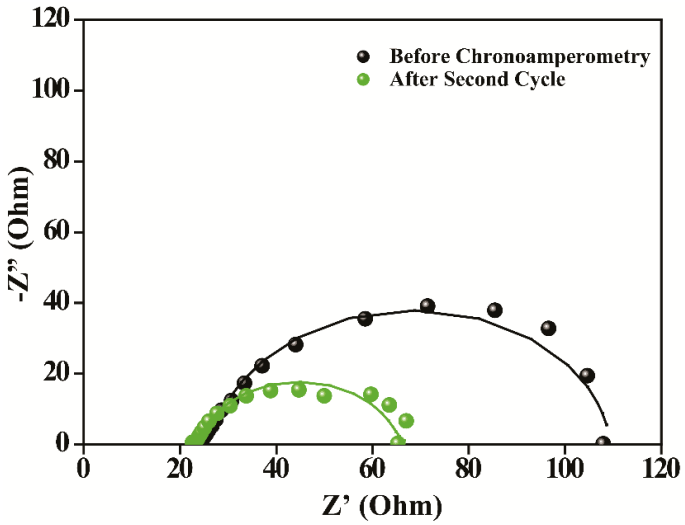

Figure 4.20. *Electrochemical impedance analysis of NiO@MoO_3/VC during O_2 quantification in 1 M KOH solution*

interval of the chronoamperometry and injecting into the GC instrument. After three sequential measurements, the electrochemical cell was degassed by purging the N_2-gas. From **Figure 4.18d**, it can be observed that in the initial quantification cycle, the amount of O_2 evolved was slightly less. However, in the second cycle, the O_2 is evolved rapidly and attains a maximum value of 100 micromoles in the third injection. The rapid increment in O_2 evolution is due to the activation of the catalyst centres in NiO@MoO_3/VC during chronoamperometry and in the second cycle, most of the catalytic centres become active. The electrochemical impedance study during the chronoamperometric analysis of NiO@MoO_3/VC (**Figure 4.20**) is confirming that the R_{CT} value is significantly reduced after the second cycle of the O_2 quantification, which indicates the activation of the catalytic centres and subsequently the faster ionic transport in the system.

Post analysis of NiO@MoO_3/VC after the chronoamperometry test is conducted to evaluate the structural stability. The TEM images of NiO@MoO_3/VC after the chronoamperometry analysis is presented in **Figure 4.21a-d**. From the TEM image, it is clear that the layer structure of MoO_3 is intact even after the 15 h of stability test and demonstrating the chemical stability of MoO_3 in the analysis conditions. The high chemical stability of MoO_3 in the present case is due to the presence of nickel molybdate ($NiMoO_4$) as the surface layer, which prevents the dissolution of MoO_3 in the alkaline condition. The d-spacing value is calculated from the TEM image (**Figure 4.21b**) and is found to be 0.21 nm, corresponding to the (200) plane of NiO. The selected area

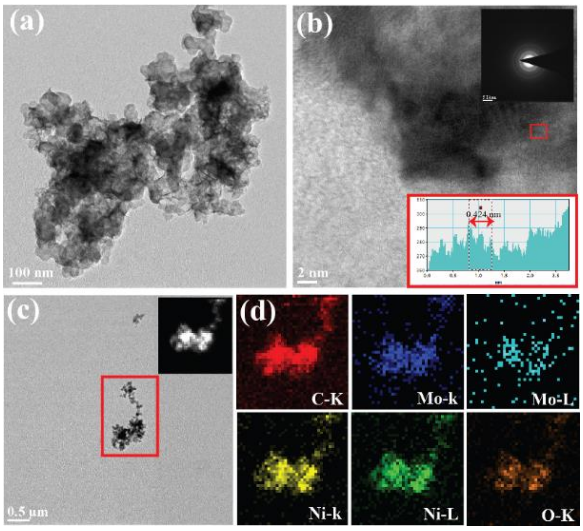

Figure 4.21. *TEM images of NiO@MoO₃/VC after 15 h chronoamperometry in 1 M KOH solution at different magnifications (a and b) and the inset in (b) represents the line profile of NiO, (c) image selected for the EDX mapping and inset shows the STM image, (d) EDX elemental mapping of NiO@MoO₃/VC represents the uniform distribution of carbon, molybdenum, nickel and oxygen in the composite.*

electron diffraction (SAED) pattern of NiO@MoO₃/VC illustrated in the inset of **Figure 4.21b** indicates the crystalline nature of the composite. The d-spacing values are calculated from the SAED pattern and are about 0.21 nm and 0.15 nm. These are corresponding to the (200) and (220) lattice planes of NiO, respectively.[44] **Figure 4.21c-d** represents the TEM-EDX elemental mapping of NiO@MoO₃/VC after the

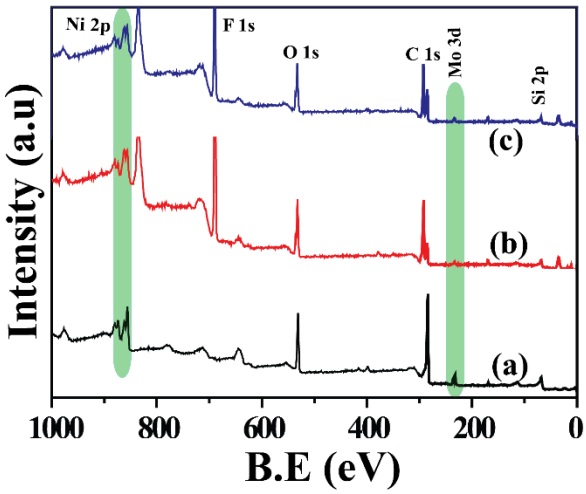

Figure 4.22. *XPS survey scan spectra comparison: (a) NiO@MoO₃/VC, (b) NiO@MoO₃/VC after 15 h chronoamperometry in 1 M KOH and (c) NiO@MoO₃/VC after 15 h aging in 1 M KOH solution without any applied potential.*

chronoamperometry analysis. **Figure 4.21c** represents the selected area for the EDX mapping and the inset shows the STEM image. **Figure 4.21d** shows the uniform distribution of nickel, molybdenum, oxygen and carbon in the composite after the chronoamperometric analysis.

XPS analysis of NiO@MoO_3/VC after the 15 h chronoamperometry analysis was carried out. For comparison, the sample obtained after the 15 h aging without any applied potential was also subjected to XPS analysis and the comparative survey spectrum is presented in **Figure 4.22**. The data shows the presence of nickel, molybdenum, oxygen and carbon after the analysis. The peak positions of the sample obtained after the chronoamperometry analysis is similar to that of the as made NiO@MoO_3/VC, which indicates the high chemical stability of NiO@MoO_3/VC in the

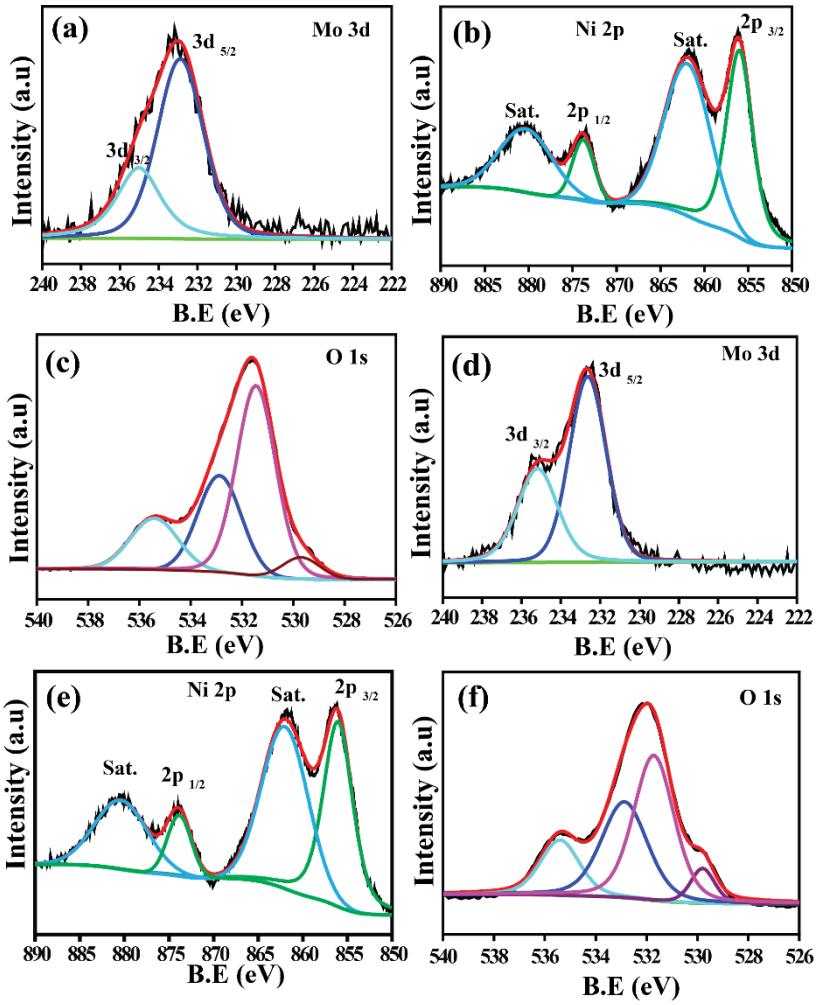

Figure 4.23. *XPS spectra of NiO@MoO_3/VC after 15 h chronoamperometry at 10 mA cm^{-2} in 1 M KOH solution (a, b and c): (a) molybdenum, (b) nickel, (c) oxygen; (d, e and f) after 15 h aging in 1 M KOH solution without any applied potential: (d) molybdenum, (e) nickel and (f) oxygen.*

long term operation. The deconvoluted XPS spectra of the samples after the analysis are shown in **Figure 4.23**. The **Figure 4.23a** shows no obvious change in the oxidation state of Mo^{+6} after the 15 h of the chronoamperometry analysis. The peaks appeared at 232.6 eV and 235.2 eV are the $3d_{5/2}$ and $3d_{3/2}$ states of Mo^{+6}, respectively. The Mo^{+6} state is originated from both $NiMoO_4$ and MoO_3 phases present in the system.

Finally, the overall water splitting was performed by employing $NiO@MoO_3$/VC coated on nickel foam (NF) as the anode catalyst and Pt/C coated on NF as the cathode catalyst. **Figure 4.24** illustrates the overall water splitting activity comparison of bare NF ||| bare NF, $NiO@MoO_3$/VC-NF ||| Pt/C-NF and RuO_2-NF ||| Pt/C-NF based electrodes.

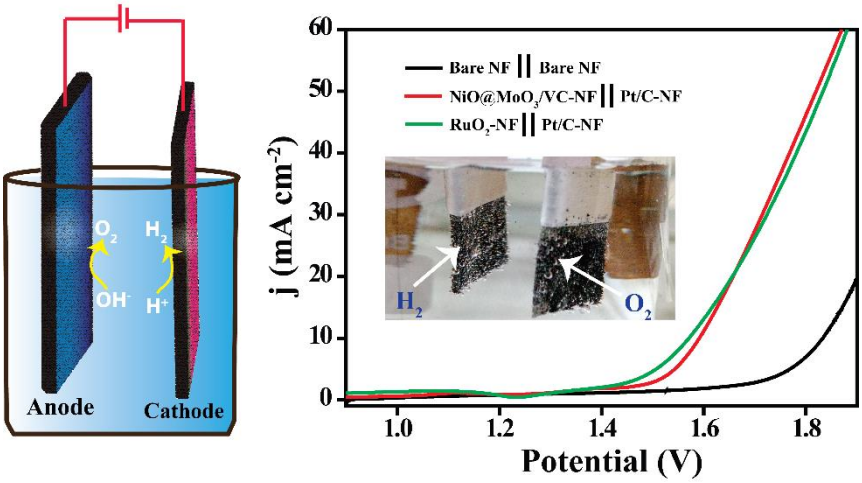

Figure 4.24. *Comparative overall water splitting activity of the catalysts in 1 M KOH solution, LSVs were performed at a scan rate of 2 mV* sec^{-1}.

The hydroxyl ions undergo oxidation at the anode and produces O_2 (OER). At the cathode, protons undergo reduction and produces H_2 (HER). The overall water splitting activity of bare NF ||| bare NF is very negligible, requires a potential of 1.83 V to achieve the current density of 10 mA cm^{-2}. However, $NiO@MoO_3$/VC-NF ||| Pt/C-NF requires only 1.59 V to reach the 10 mA cm^{-2} current density. Also, the system performing similar to the *state-of-the-art* based electrode system (RuO_2-NF ||| Pt/C-NF). The produced H_2 and O_2 are presented in the inset of **Figure 4.24** and indicated with the arrow marks. Hence, the result shows the potential application of $NiO@MoO_3$/VC as the efficient OER catalyst for the overall water splitting application.

4.4 Conclusions

A robust and highly durable water-oxidation catalyst has been synthesized by following a simple two-step hydrothermal synthesis. The produced NiO@MoO_3/VC is comprised of small sized NiO nanosheets anchored on MoO_3, which facilitates the hydroxyl ion adsorption during the water oxidation reaction. The MoO_3 is derived from the few-layer MoS_2 and this subsequently anchors the NiO nanosheets. This intimate coexistence of the phases in a directly integrated fashion increases the availability of active centres and fn-VC core in the composite improves the electrical conductivity in the system. Also, the mesoporous nature of NiO@MoO_3/VC facilitates faster transport of ions during OER. The presence of MoO_3 in the composite plays a key role in improving the stability of the system, where the presence of surface $NiMoO_4$ as a thin layer would prevent the dissolution of MoO_3 in the alkaline environment. NiO@MoO_3/VC exhibits an overpotential of 280 mV for OER at 10 mA cm^{-2} and shows good stability at 1.51 V *vs.* RHE for 15 h in 1 M KOH solution. The present catalyst is found to be exhibiting better performance compared to the *state-of-the-art* RuO_2 catalyst, which exhibits an overpotential of 292 mV at 10 mA cm^{-2} current density. Also, the performance exhibited by the present catalyst is comparable to the nickel based OER catalysts reported in the literature. The overall water splitting activity of NiO@MoO_3/VC-NF ǁ Pt/C-NF is analysed in 1 M KOH solution and the system requires nearly 1.59 V to achieve the 10 mA cm^{-2} current density. The performance is similar to the activity demonstrated by the systems based on the *state-of-the-art* catalysts (RuO_2-NF ǁ Pt/C-NF), validating the improved activity of NiO@MoO_3/VC towards OER.

4.5 References

[1] Du, C.; Yang, L.; Yang, F.; Cheng, G.; Luo, W, *ACS Catal.* **2017,** *7* (6), 4131-4137.

[2] Yoon, T.; Kim, K. S, *Adv. Funct. Mater.* **2016,** *26* (41), 7386-7393.

[3] Chen, Z.; Cummins, D.; Reinecke, B. N.; Clark, E.; Sunkara, M. K.; Jaramillo, T. F, *Nano Lett.* **2011,** *11* (10), 4168-4175.

[4] Stevens, M. B.; Enman, L. J.; Batchellor, A. S.; Cosby, M. R.; Vise, A. E.; Trang, C. D. M.; Boettcher, S. W, *Chem. Mater.* **2017,** *29* (1), 120-140.

[5] Chen, Z.; Wang, L.; Ma, Z.; Song, J.; Shao, G, *RSC Adv.* **2017,** *7* (2), 704-711.

[6] Chen, Y.; Hu, J.; Diao, H.; Luo, W.; Song, Y.-F, *Chem. Eur. J.* **2017,** *23* (16), 4010-4016.

[7] Xiao, M.; Tian, Y.; Yan, Y.; Feng, K.; Miao, Y, *Acta* **2015,** *164* (0), 196-202.

[8] Panda, C.; Menezes, P. W.; Walter, C.; Yao, S.; Miehlich, M. E.; Gutkin, V.; Meyer, K.; Driess, M, *Chem., Int. Ed.* **2017,** *56* (35), 10506-10510.

[9] Gorlin, Y.; Jaramillo, T. F, *J. Am. Chem. Soc.* **2010,** *132* (39), 13612-13614.

[10] Tan, C.; Cao, X.; Wu, X.-J.; He, Q.; Yang, J.; Zhang, X.; Chen, J.; Zhao, W.; Han, S.; Nam, G.-H.; Sindoro, M.; Zhang, H, *Chem. Rev.* **2017,** *117* (9), 6225-6331.

[11] Lee, K. J.; Shin, D. Y.; Byeon, A.; Lim, A.; Jo, Y. S.; Begley, A.; Lim, D.-H.; Sung, Y.-E.; Park, H. S.; Chae, K. H.; Nam, S. W.; Lee, K.-Y.; Kim, J. Y, *Nanoscale* **2017,** *9* (41), 15846-15855.

[12] Zhang, P.; Lu, X.; Huang, Y.; Deng, J.; Zhang, L.; Ding, F.; Su, Z.; Wei, G.; Schmidt, O. G, *J. Mater. Chem. A* **2015,** *3* (28), 14562-14566.

[13] Hao, C.; Wen, F.; Xiang, J.; Wang, L.; Hou, H.; Su, Z.; Hu, W.; Liu, Z, *Adv. Funct. Mater.* **2014,** *24* (42), 6700-6707.

[14] Liu, Y.; Liu, C.; Yu, X.; Osgood, H.; Wu, G, *Phys. Chem. Chem. Phys.* **2017,** *19* (1), 330-339.

[15] Justin, P.; Ranga Rao, G, *Int. J. Hydrog. Energy* **2011,** *36* (10), 5875-5884.

[16] Chen, S.; Duan, J.; Ran, J.; Jaroniec, M.; Qiao, S. Z, *Energy Environ. Sci.* **2013,** *6* (12), 3693-3699.

[17] He, P.; Yu, X.-Y.; Lou, X. W, *Angew. Chem., Int. Ed.* **2017,** *56* (14), 3897-3900.

[18] Amin, H. M. A.; Bondue, C. J.; Eswara, S.; Kaiser, U.; Baltruschat, H, *Electrocatalysis* **2017,** *8* (6), 540-553.

[19] Cheng, Z.; He, B.; Zhou, L, *J. Mater. Chem. A* **2015,** *3* (3), 1042-1048.

[20] Wang, Z.; Zhao, J.; Cai, Q.; Li, F, *J. Mater. Chem. A* **2017,** *5* (20), 9842-9851.

[21] Li, G.-R.; Wang, Z.-L.; Zheng, F.-L.; Ou, Y.-N.; Tong, Y.-X, *J. Mater. Chem.* **2011,** *21* (12), 4217-4221.

[22] Lai, F.; Yong, D.; Ning, X.; Pan, B.; Miao, Y.-E.; Liu, T, *Small* **2017,** *13* (7), 1602866.

[23] Ren, J.-T.; Yuan, Z.-Y, *ACS Sustainable Chem. Eng.* **2017,** *5* (8), 7203-7210.

[24] Ren, X.; Pang, L.; Zhang, Y.; Ren, X.; Fan, H.; Liu, S, *J. Mater. Chem. A* **2015,** *3* (20), 10693-10697.

[25] Ganatra, R.; Zhang, Q, *ACS Nano* **2014,** *8* (5), 4074-4099.

[26] Zhang, X.; Jia, F.; Yang, B.; Song, S, *J. Phys.Chem. C* **2017,** *121* (18), 9938-9943.

[27] Xiuqiang, X.; Zhimin, A.; Dawei, S.; Jinqiang, Z.; Guoxiu, W, *Adv. Funct. Mater.* **2015,** *25* (9), 1393-1403.

[28] Sreedhara, M. B.; Matte, H. S. S. R.; Govindaraj, A.; Rao, C. N. R, *Chem. Asian J.* **2013,** *8* (10), 2430-2435.

[29] Reddy, D. A.; Park, H.; Hong, S.; Kumar, D. P.; Kim, T. K, *J. Mater. Chem. A* **2017,** *5* (15), 6981-6991.

[30] Wu, Z.; Huang, X.-L.; Wang, Z.-L.; Xu, J.-J.; Wang, H.-G.; Zhang, X.-B, *Sci. Rep.* **2014,** *4*, 3669.

[31] Ede, S. R.; Anantharaj, S.; Kumaran, K. T.; Mishra, S.; Kundu, S, *RSC Adv.* **2017,** *7* (10), 5898-5911.

[32] Liu, W.; Lu, C.; Wang, X.; Liang, K.; Tay, B. K, *J. Mater. Chem. A* **2015,** *3* (2), 624-633.

[33] Wang, L.; Hao, Y.; Zhao, Y.; Lai, Q.; Xu, X, *J. Solid State Chem.* **2010,** *183* (11), 2576-2581.

[34] Ma, Y.; Wang, H.; Ji, S.; Goh, J.; Feng, H.; Wang, R, *Electrochim. Acta* **2014,** *133*, 391-398.

[35] Trefilov, A. M. I.; Tiliakos, A.; Serban, E. C.; Ceaus, C.; Iordache, S. M.; Voinea, S.; Balan, A, *Int. J. Hydrog. Energy* **2017,** *42* (15), 10448-10454.

[36] Huang, H.; Feng, X.; Du, C.; Song, W, *Chem. Commun.* **2015,** *51* (37), 7903-7906.

[37] Zheng, X.; Xu, J.; Yan, K.; Wang, H.; Wang, Z.; Yang, S, *Chem. Mater.* **2014,** *26* (7), 2344-2353.

[38] Zhao, D.; Qin, J.; Zheng, L.; Cao, M, *Chem. Mater.* **2016,** *28* (12), 4180-4190.

[39] Ma, J.; Yin, L.; Ge, T, *CrystEngComm* **2015,** *17* (48), 9336-9347.

[40] Li, Q.; Xing, Z.; Wang, D.; Sun, X.; Yang, X, *ACS Catal.* **2016,** *6* (5), 2797-2801.

[41] Bloor, L. G.; Solarska, R.; Bienkowski, K.; Kulesza, P. J.; Augustynski, J.; Symes, M. D.; Cronin, L, *J. Am. Chem. Soc.* **2016,** *138* (21), 6707-6710.

[42] McCrory, C. C. L.; Jung, S.; Peters, J. C.; Jaramillo, T. F, *J. Am. Chem. Soc.* **2013,** *135* (45), 16977-16987.

[43] Wang, C.; Tian, B.; Wu, M.; Wang, J, *ACS Appl. Mater. Interfaces* **2017,** *9* (8), 7084-7090.

[44] Kwon, U.; Kim, B.-G.; Nguyen, D. C.; Park, J.-H.; Ha, N. Y.; Kim, S.-J.; Ko, S. H.; Lee, S.; Lee, D.; Park, H. J, *Sci. Rep.* **2016,** *6*, 30759.

[45] Xu, J.; Li, J.; Xiong, D.; Zhang, B.; Liu, Y.; Wu, K.-H.; Amorim, I.; Li, W.; Liu, L, *Chem. Sci.* **2018,** *9* (14), 3470-3476.

[46] Li, W.; Gao, X.; Xiong, D.; Wei, F.; Song, W.-G.; Xu, J.; Liu, L, *Adv. Energy Mater.* **2017,** *7* (17), 1602579.

[47] Xiong, D.; Zhang, Q.; Thalluri, S. M.; Xu, J.; Li, W.; Fu, X.; Liu, L, *Chem. Eur. J.* **2017,** *23* (36), 8749-8755.

[48] Xiong, D.; Zhang, Q.; Li, W.; Li, J.; Fu, X.; Cerqueira, M. F.; Alpuim, P.; Liu, L,

Nanoscale **2017,** *9* (8), 2711-2717.

[49] Li, W.; Gao, X.; Xiong, D.; Xia, F.; Liu, J.; Song, W.-G.; Xu, J.; Thalluri, S. M.; Cerqueira, M. F.; Fu, X.; Liu, L, *Chem. Sci.* **2017,** *8* (4), 2952-2958.

[50] Xiong, D.; Wang, X.; Li, W.; Liu, L, *Chem. Commun.* **2016,** *52* (56), 8711-8714.

[51] Xiong, D.; Li, W.; Liu, L, *Chem. Asian J.* **2017,** *12* (5), 543-551.

[52] Wang, X.; Li, W.; Xiong, D.; Liu, L, *J. Mater. Chem. A* **2016,** *4* (15), 5639-5646.

[53] Wang, X.; Li, W.; Xiong, D.; Petrovykh, D. Y.; Liu, L, *Adv. Funct. Mater.* **2016,** *26* (23), 4067-4077.

[54] Li, W.; Gao, X.; Wang, X.; Xiong, D.; Huang, P.-P.; Song, W.-G.; Bao, X.; Liu, L, *J. Power Sources* **2016,** *330*, 156-166.

[55] Li, W.; Wang, X.; Xiong, D.; Liu, L, *Int. J. Hydrog. Energy* **2016,** *41* (22), 9344-9354.

[56] Anantharaj, S.; Ede, S. R.; Karthick, K.; Sam Sankar, S.; Sangeetha, K.; Karthik, P. E.; Kundu, S, *Energy Environ. Sci*. **2018**, 11 (4), 744-771.

[57] Sun, Z.; Wang, Y.; Lin, L.; Yuan, M.; Jiang, H.; Long, R.; Ge, S.; Nan, C.; Li, H.; Sun, G.; Yang, X, *Chem. Commun*. **2019**, 55 (9), 1334-1337.

[58] Sun, Z.; Lin, L.; Nan, C.; Li, H.; Sun, G.; Yang, X, *ACS Sustainable Chem. Eng*. **2018**, 6 (11), 14257-14263.

[59] Tariq, M.; Zaman, W. Q.; Sun, W.; Zhou, Z.; Wu, Y.; Cao, L.-m.; Yang, J, *ACS Sustainable Chem. Eng*. **2018**, 6 (4), 4854-4862.

[60] Sankar, S. S.; Ede, S. R.; Anantharaj, S.; Karthick, K.; Sangeetha, K.; Kundu, S, *Catal. Sci. Technol*. **2019**, 9 (8), 1847-1856.

[61] Karthick, K.; Anantharaj, S.; Ede, S. R.; Kundu, S, *Inorg. Chem*. **2019**, 58 (3), 1895-1904.

[62] Zhao, L.; Jia, J.; Yang, Z.; Yu, J.; Wang, A.; Sang, Y.; Zhou, W.; Liu, H, *Appl. Catal., B* **2017**, 210, 290-296.

[63] Shaofang F.; Chengzhou Z.; Junhua S.; Shuo F.; Dan D.; Mark H.; Dongdong X.; Dongsheng L.; Yuehe L.; *ACS Appl. Mater. Interfaces* **2017**, 9, 36755−36761.

[64] Xiaohu L.; Qiulan Z.; Shuo D.; Ji L.; Jiawen Z.; Xiulin D.; Yali L.; *ACS Appl. Mater. Interfaces* **2018**, 10, 22291-22302.

Chapter-5

Hierarchical Nanoflower Arrays of Co_9S_8-Ni_3S_2 on Nickel Foam: Highly Efficient Binder-free Electrocatalyst for Overall Water Splitting Application

Hydrogen production is vital for furnishing the future energy demand and managing the environmental sustainability. Electrolysis of water is considered as the suitable method for H_2 generation in a carbon-free pathway. Here, we have explored the synthesis of highly efficient Co_9S_8-Ni_3S_2 based hierarchical nanoflower arrays on nickel foam (NF) through the one-pot hydrothermal method (Co_9S_8-Ni_3S_2/NF) for overall water splitting applications. The nanoflower arrays are self-supported on the NF without any binder, possessing the required porosity and structural characteristics. The obtained Co_9S_8-Ni_3S_2/NF is displaying high hydrogen evolution reaction (HER) as well as oxygen evolution reaction (OER) activities in 1 M KOH solution. The overpotentials exhibited by this system at 25 mA cm^{-2} are nearly 277 and 102 mV for HER and OER, respectively in 1 M KOH solution. Subsequently, the overall water splitting was performed in 1 M KOH solution by employing Co_9S_8-Ni_3S_2/NF as both the anode and cathode electrodes, where the system required only 1.49, 1.60 and 1.69 V to deliver the current densities of 10, 25, and 50 mA cm^{-2}, respectively. Comparison of the activity of Co_9S_8-Ni_3S_2/NF with the *state-of-the-art* Pt/C and RuO_2 coated on NF displays an enhanced performance for Co_9S_8-Ni_3S_2/NF both in the half-cell as well as in the full cell, emphasizing the significance of the present work. The post analysis of the material after the water electrolysis confirms that the surface $Co(OH)_2$ formed during the course of the reaction serves as the favorable active sites. Overall, the activity modulation achieved in the present case is attributed to the presence of open-pore morphology of the as formed nanoflowers of Co_9S_8-Ni_3S_2 on NF and the simultaneous presence of the surface $Co(OH)_2$ along with the highly conducting Co_9S_8-Ni_3S_2 core which facilitates the adsorption of the reactants and subsequently its conversion into the gases products during water electrolysis.

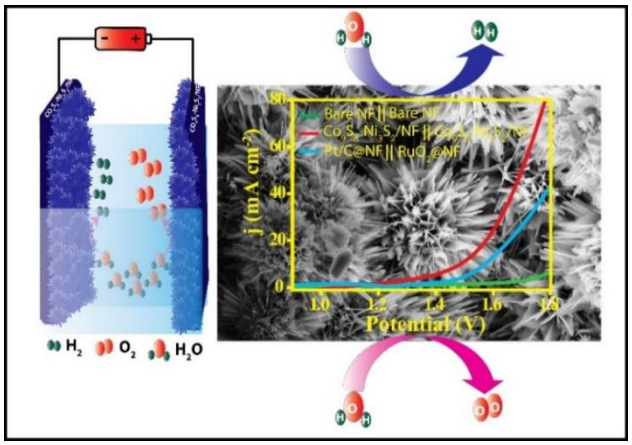

Content of this chapter is published in the following article:

Chem. Eur. J., 2020, 26, 7900-7911.

(https://chemistry-europe.onlinelibrary.wiley.com/doi/abs/10.1002/chem.202000839)

Reproduced by permission from Chem. Eur. J, License Number: 4879200388836.

5.1 Introduction

The depletion and inadequacy of non-renewable energy sources with their environmental glitches inflict the society to develop sustainable and cost-effective routes for clean energy.[1, 2] The viable carbon-free energy sources are receiving extensive attention due to their pollution-free and environmental benign nature.[3] Hydrogen is being considered as an ideal candidate for the future energy source due to its high energy density (140 MJ kg^{-1}).[4, 5] The polymer electrolyte membrane fuel cells (PEMFCs) convert the chemical energy of H_2 in to electrical energy.[6] The carbon-free nature of H_2 makes the system further elegant.[7] However, steam reforming of natural gas, coal gasification, *etc*., adopted for the hydrogen production release CO and CO_2 and, thus, are not carbon neutral in nature.[8, 9] Therefore, these methods are not feasible for the green production of H_2. Hence, a clean and efficient method should be followed for the generation of H_2. Electrolysis of water produces H_2 in a carbon-neutral way and it plays an important role in the sustainable production of H_2.[10] Electrochemical water splitting involves two reactions at the electrodes; the hydrogen evolution reaction (HER) at the cathode and oxygen evolution reaction (OER) at the anode. However, the overpotential associated with HER and OER makes the water electrolysis more challenging.[11, 12] Hence, developing highly efficient and durable catalyst for facilitating HER and OER is indeed essential for the economical H_2 generation from water.[13]

Various catalysts have been developed and investigated for reducing the overpotential associated with the water electrolysis. Among them, the noble metal based catalysts, especially Pt, Ru, and Ir are the benchmark catalysts for aiding the water electrolysis.[14, 15] However, the highly expensive and insufficient reserves of the *state-of-the-art* Pt, Ru, and Ir restrict the wide commercial application of the water electrolysis.[16, 17] In order to improve the productive and profitable H_2 generation from water electrolysis, replacing the noble metal based catalysts with low cost, highly efficient and durable materials is essential.[11, 18-20] Extensive research has been done over the past decades to develop efficient catalysts for water electrolysis. These include the application of various low-cost transition metal based catalysts for facilitating OER and HER.[21, 22] The vast availability and comparable catalytic activity of the transition metal based catalysts can eventually replace the precious-metal based catalysts. Among the various transition metal based catalysts, the metal sulfide based catalysts have been displaying remarkable HER and OER performances.[21, 23-27] This can be attributed to the high electrical conductivity and variable oxidation states possessed by the various

metal sulfides.[28] Currently, designing of the efficient bi-functional catalysts, which can facilitate both OER and HER for water electrolysis, is receiving substantial attention mainly because such systems can reduce the complications associated in designing the water electrolyzer set-up.[15, 29, 30] In addition, the application of a single material as both the anode and cathode catalyst can reduce the cost of operation of the system.[31]

The large scale system development of water electrolysis is restricted mainly due to the high overpotential and physical coating of the catalyst material on the conducting substrate using binders.[12] This would lead to undesirable contact resistance in the system and subsequently to reduced catalytic activity.[32] In-situ anchoring of the nanomaterials on a conducting substrate and subsequently developing the self-supported bi-functional electrodes for HER and OER can resolve the above mentioned issues.[33] Also, developing the catalysts with hierarchical nanostructures is receiving wide attention due to their unique properties and surface enhanced catalytic activities.[17, 26] The hierarchical nanostructures would improve the electrochemical active surface area (ECSA) and subsequently the catalytic activity.[33] In the present work, hierarchical nanoflower arrays of Co_9S_8-Ni_3S_2 is achieved on the NF substrate (Co_9S_8-Ni_3S_2/NF) through hydrothermal reaction (**Figure 5.1**). The high porosity, surface area, electrical conductivity and low cost of NF make this as an appropriate substrate for the nanomaterial's growth.[34] The self-supported Co_9S_8-Ni_3S_2/NF electrode was used as the bi-functional and binder-free electrode for water electrolysis applications. The Co_9S_8-Ni_3S_2/NF was investigated for the HER and OER applications in 1 M KOH solution. Finally, the system was applied as both the anode and cathode electrodes for aiding the water electrolysis applications in 1 M KOH solution.

5.2 Experimental Section

5.2.1 Materials

Cobalt chloride hexahydrate ($CoCl_2$. $6H_2O$), thiourea (CH_4N_2S), potassium hydroxide (KOH) and ruthenium oxide (RuO_2) were purchased from Sigma-Aldrich Chemicals. 40 wt. % Pt/C was procured from Alfa Aesar. Hydrochloric acid (HCl) was procured from Thomas Baker. All the chemicals were used without any further purification. Nickel foam (NF) was procured from Global Nanotechnology Pvt. Ltd. The thickness of NF is 1.4 mm whereas its pore size and surface density are 580 µm and 1450 g/m^2, respectively.

5.2.2 Synthesis of Co_9S_8-Ni_3S_2/NF nanoflower

Initially, NF (2.5 cm x 3.5 cm) was cleaned with 1 M HCl, DI water and ethanol sequentially by sonication followed by drying at 60 °C for 5 h in a vacuum oven. The cleaned NF was used for the further synthesis. For the synthesis of Co_9S_8-Ni_3S_2/NF, dissolved 2.5 mmol of cobalt chloride hexahydrate ($CoCl_2$. $6H_2O$) and 13.1 mmol of thiourea (CH_4N_2S) in 30 mL of distilled water. After stirring for 30 min. at room temperature, the solution was transferred into a 40 mL Teflon lined autoclave. The cleaned NF was kept vertically in this solution and the hydrothermal treatment at 200 °C for 12 h was performed. After cooling down to room temperature, the material was removed from the bath and subsequently washed several times with ethanol and distilled water. The material was dried in a vacuum oven at 60 °C for 5 h and the obtained material is called hereafter as Co_9S_8-Ni_3S_2/NF.

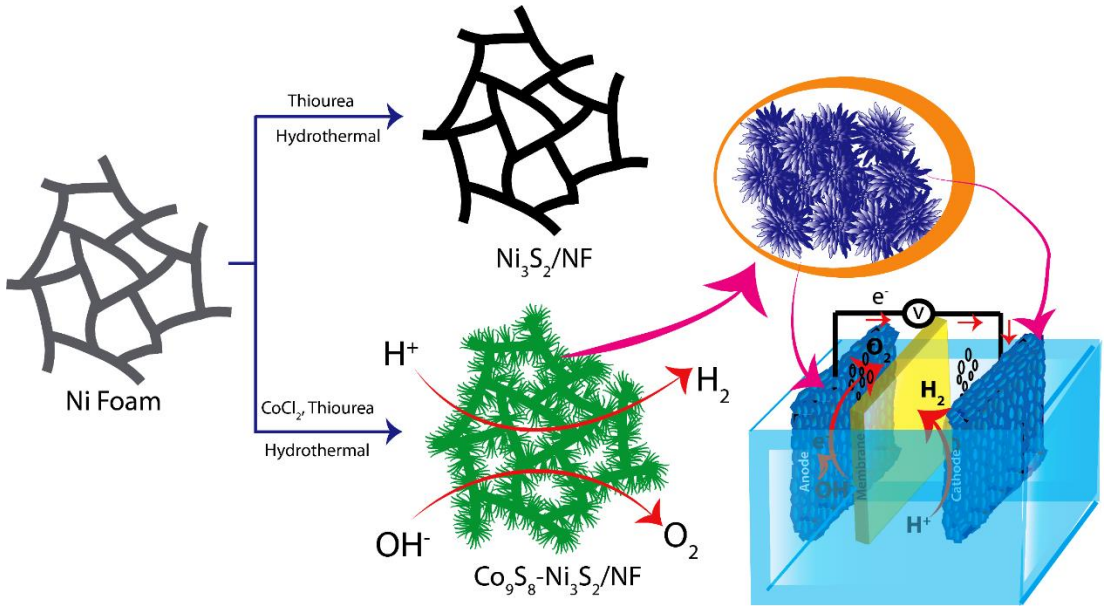

Figure 5.1. *Schematic illustration of the synthesis of Co_9S_8-Ni_3S_2/NF through the hydrothermal route and the employment of this system as the bi-functional electrode in the water electrolysis application.*

In order to understand the structural development, control samples were prepared through the same method by adding 1.2 mmol of $CoCl_2$. $6H_2O$ and 13.1 mmol of CH_4N_2S in the first case (Co_9S_8-Ni_3S_2/NF-1) and 2.5 mmol of $CoCl_2$. $6H_2O$ and 6.5 mmol of CH_4N_2S in the other case (Co_9S_8-Ni_3S_2/NF-2) and kept the remaining parameters similar as in the previous case. For comparison, Ni_3S_2 directly grown on the NF was also synthesized by adopting the similar method except the addition of cobalt

chloride during the hydrothermal treatment. The material obtained is called as Ni_3S_2/NF. The loading of the metal sulfides on Co_9S_8-Ni_3S_2/NF was calculated by weighing the material before and after the reaction, which is found to be nearly 28 ± 2 mg cm^{-2}. The digital images of bare NF, Ni_3S_2/NF and Co_9S_8-Ni_3S_2/NF are presented in **Figure 5.2**.

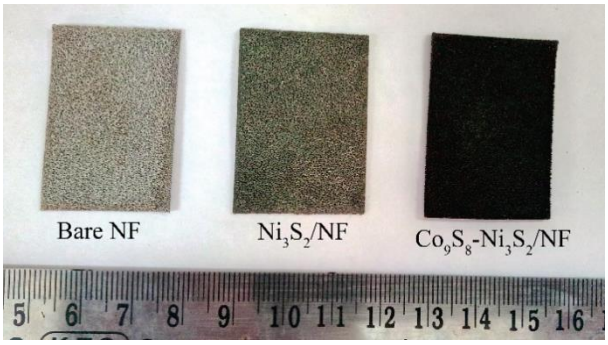

Figure 5.2. *Digital images of bare NF, Ni_3S_2/NF and Co_9S_8-Ni_3S_2/NF.*

5.2.3 Characterization

The field emission scanning electron microscopic (FESEM) images were obtained in a Nova Nano SEM 450 instrument. Using a FEI Technai G2 T20 instrument which was operated at 200 keV, the transmission electron microscopic (TEM) images of the materials were obtained. X-ray diffraction (XRD) studies were conducted using a PANalytical X′ pert pro instrument using Cu Kα (1.5418 Å) radiation. Using a VG Microtech Multilab ESCA 3000 spectrometer, X-ray photon emission spectroscopic (XPS) analysis of the samples was carried out. Non-invasive X-ray microtomography imaging was performed by using Xradia Versa 510 X-ray Microscope (Zeiss X-ray Microscopy, Pleasanton, CA, USA).

5.2.4 Electrochemical Analysis

The as developed Co_9S_8-Ni_3S_2/NF was analysed for the electrochemical water splitting applications in 1 M KOH solution. The electrochemical investigations of the materials toward OER and HER have been performed using the three electrode set-up. For this, Co_9S_8-Ni_3S_2/NF was taken as the working electrode with an active area of 1 cm^2. A graphite rod and Hg/HgO were used as the counter and reference electrodes, respectively. During the analysis, the electrolyte was continuously purged with N_2-gas. Initially, about 10 cycles of cyclic voltammogram (CV) was performed at a scan rate of 10 mV sec^{-1}. In order to find out the overpotential, linear sweep voltammetry (LSV) was performed at a scan rate of 2 mV sec^{-1}. All the LSV measurements were performed

without any iR correction. For comparison, Pt/C and RuO_2 were coated on NF (1 cm^2 active area) with a loading of 3 mg cm^{-2} and performed the analysis under similar conditions. All the potentials were converted in to RHE by calibrating the reference electrodes in the H_2-saturated electrolytes. For water electrolysis analysis, Co_9S_8-Ni_3S_2/NF was employed both as the anode and cathode electrodes by maintaining an active area of 1.0 cm^2. All the electrochemical analyses were performed at room temperature (~25° C).

The electrochemical active surface area (ECSA) of the samples was measured by performing CV in the non-Faradaic region (0.91 to 1.01 V) at different scan rates. The peak current obtained at 0.96 V is plotted against the corresponding scan rate gives a straight line, where the slope represents the double-layer capacitance (C_{dl}) value. Using the specific capacitance (C_s) of the elements, the ECSA value can be calculated from the following equation:

$$ECSA = C_{dl}/C_s$$

The alkaline water electrolyzer was constructed with Co_9S_8-Ni_3S_2/NF as both the electrodes by powering with a 1.5 V dry cell battery. The amount of gas evolved during the water electrolysis was evaluated by using gas chromatography (5700 Nucon Gas Chromatograph with Carbosphere column and Argon as carrier gas) with thermal conductivity detector. The program used in GC for all the analyses involved the detector temperature of 100 ºC and an oven temperature of 50 ºC at the time of injection. A gas phase syringe (injection volume of 500 µL) was used to inject the sample at the headspace of the reactor.

5.3 Results and Discussion

5.3.1 FESEM Analysis

The FESEM analysis has been performed to acquire the structural details of the obtained material after the hydrothermal synthesis and the corresponding images are presented in **Figure 5.3**. **Figure 5.3a** depicts the FESEM image of bare NF. The inset in the figure represents the high magnification image of the bare NF and it reveals the rough surface texture of the material. After the hydrothermal treatment of NF in presence of thiourea, Ni_3S_2 is formed on the surface of NF (Ni_3S_2/NF) as shown in the image presented in **Figure 5.3b**. The inset in **Figure 5.3b** represents the enlarged view of Ni_3S_2/NF, which indicates the vertical spike kind arrangement of Ni_3S_2 on the NF surface. **Figure 5.3c** represents the FESEM image of Co_9S_8-Ni_3S_2/NF. The hierarchical nanoflower arrays of

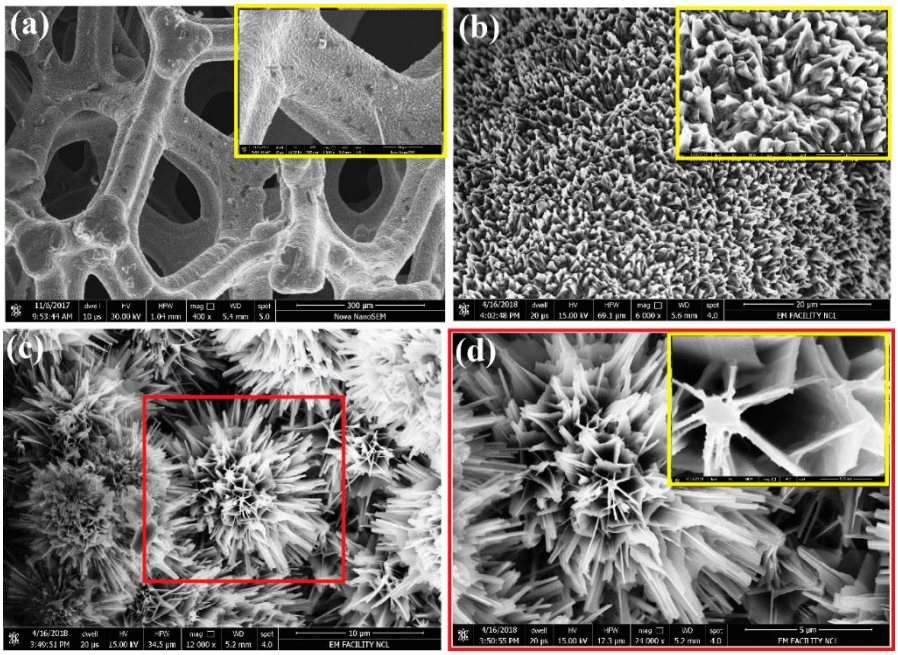

Figure 5.3. *(a) FESEM image of bare NF with the inset image shows a magnified portion, (b) FESEM image of Ni_3S_2/NF with magnified location in the inset, (c) FESEM image of Co_9S_8-Ni_3S_2/NF and (d) higher magnification image of the highlighted portion in (c) and the inset shows the porous morphology of the nanoflower.*

Co_9S_8-Ni_3S_2 on the NF surface is achieved by adding cobalt chloride during the hydrothermal treatment of thiourea with NF. It is clear from **Figure 5.3c** that, after the incorporation of cobalt ions during the synthesis, the morphology of the obtained material is changed from nanospikes to nanoflower arrays. This could be attributed to the growth of Co_9S_8 layers on the surface of Ni_3S_2, which leads to the formation of Co_9S_8-Ni_3S_2 nanoflower arrays on NF. The diameter of the nanoflowers are nearly 10 µm and they are found to be distributed uniformly on NF. **Figure 5.3d** is the high magnification image of the highlighted portion in **Figure 5.3c**; the inset in the image indicates the open-pore cavities of the as formed Co_9S_8-Ni_3S_2/NF. This would emphasis the significance of Co_9S_8 on Ni_3S_2 for obtaining the uniformly distributed and open-pore morphology of the nanoflower arrays.

It can be deduced from the FESEM image that the nanoflower morphology is formed from the thin layer assemblies of the nanopetals of Co_9S_8-Ni_3S_2. The sequential arrangement of the Co_9S_8-Ni_3S_2 nanopetals provides the open-pore cavities in the system. The porosity present in the nanoflowers of Co_9S_8-Ni_3S_2/NF is in the macro porous range and it would facilitate the diffusion of the electrolyte and the evolved gases during the water electrolysis. Thus, the porous nature of Co_9S_8-Ni_3S_2/NF is highly

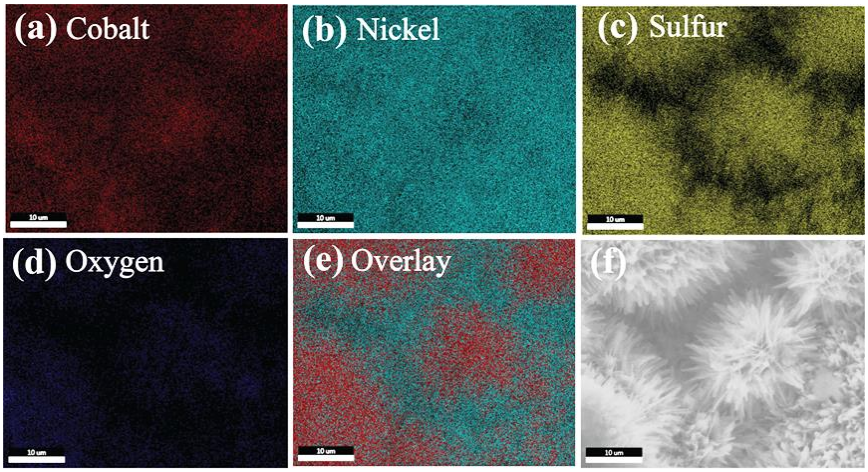

Figure 5.4. *(a-f) SEM-EDX elemental mapping of Co_9S_8-Ni_3S_2/NF indicating the uniform distribution of cobalt, nickel and sulfur.*

helpful during the water electrolysis application. To get an insight about the elemental distribution in Co_9S_8-Ni_3S_2/NF, the SEM-EDX elemental mapping was performed and this data is presented in **Figure 5.4**. From the elemental mapping, it is found that cobalt, nickel and sulfur are distributed uniformly in the system. The origin of oxygen in the elemental mapping could be from the trace amount of adsorbed oxygen on the sample. The uniform distribution of the constituent elements in the system in the elemental

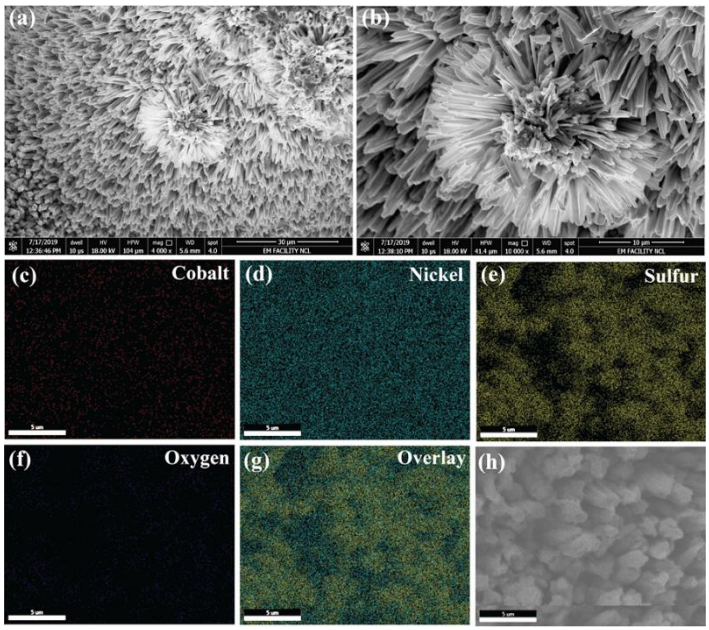

Figure 5.5. *(a-d) FESEM images of Co_9S_8-Ni_3S_2/NF-1 recorded at different magnifications. (c-h) SEM-EDX elemental mapping of Co_9S_8-Ni_3S_2/NF-1; (c) cobalt, (d) nickel, (e) sulfur, (f) oxygen, (g) overlay and (h) the image corresponding to the elemental mapping.*

mapping data points towards the uniform distribution of the Co_9S_8-Ni_3S_2 moieties on NF.

In order to understand the structural evolution, control samples were prepared by varying the amounts of cobalt chloride and thiourea during the synthesis (explained in the Experimental section). The material synthesized with lower concentration of cobalt chloride during the synthesis is found to be affecting on the formation of the nanoflower structure and, instead, it leads to the spike kind morphology (Co_9S_8-Ni_3S_2/NF-1) and the corresponding FESEM image is presented in **Figure 5.5a-b**. The SEM-EDX elemental mapping of this system as shown in **Figure 5.5c-h** illustrates the uniform distribution of Co, Ni and S in the material. Similarly, lowering the amount of thiourea leads to the formation of partially formed nanoflower morphologies on NF (Co_9S_8-Ni_3S_2/NF-2). The corresponding images are presented in **Figure 5.6a-b**. The SEM-EDX elemental mapping of this sample presented in **Figure 5.6c-h** points towards the uniform distribution of Co, Ni and S in the material.

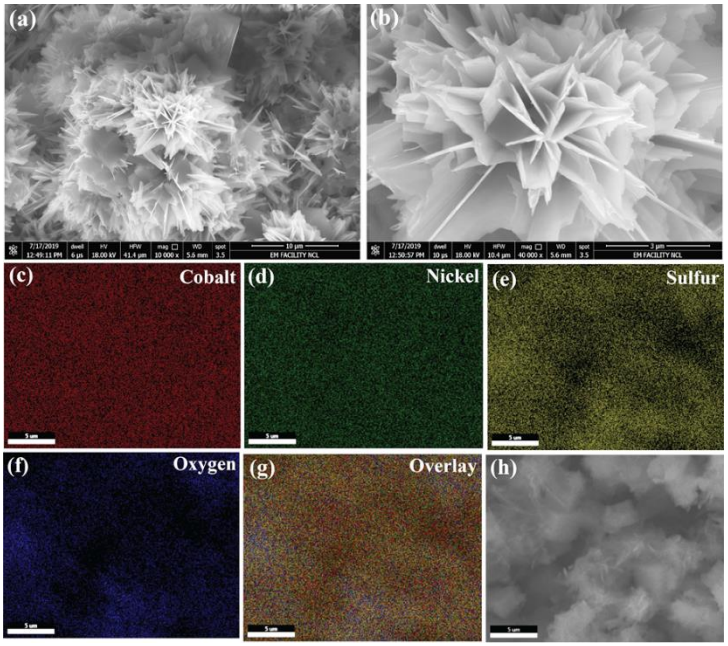

Figure 5.6. *(a-d) FESEM images of Co_9S_8-Ni_3S_2/NF-2 recorded at different magnifications. (c-h) SEM-EDX elemental mapping of Co_9S_8-Ni_3S_2/NF-2; (c) cobalt, (d) nickel, (e) sulfur, (f) oxygen, (g) overlay and (h) the image corresponding to the elemental mapping.*

5.3.2 Contact Angle Analysis

The contact angle measurement of the catalyst provides the surface wettability details

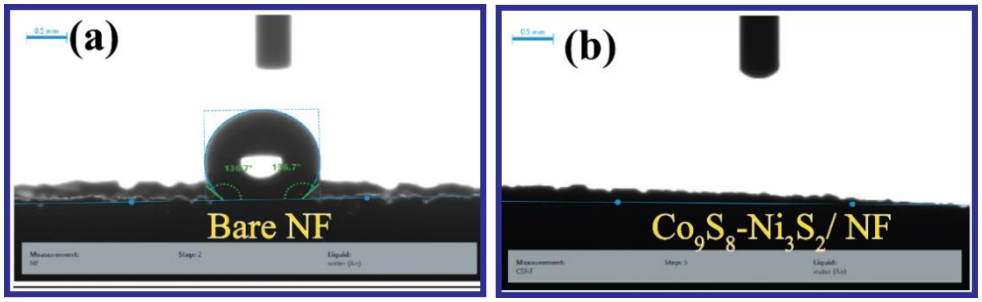

Figure 5.7. *The images corresponding to the contact angle measurement of (a) bare NF and (b) Co_9S_8-Ni_3S_2/NF.*

and this has further implications in establishing the electrode-electrolyte interface in the test systems for the electrochemical evaluations. For water electrolysis, the hydrophilicity of the system favors for the better contact of the electrolyte with the catalyst. Along with the active centers, better electrode-electrolyte interactions would subsequently improve the catalytic performance. The contact angle of bare NF with water is ~134°, which indicates the highly hydrophobic nature of the bare NF (**Figure 5.7a**).[34] However, the excellent hydrophilic nature makes fast spreading of water on the surface of Co_9S_8-Ni_3S_2/NF, making the measurement of water contact angle on the system difficult (**Figure 5.7b**). This extremely hydrophilic nature of Co_9S_8-Ni_3S_2/NF plays a critical role in establishing better electrode-electrolyte interactions and helps for the easy release of the evolved gases from the catalyst surface during water electrolysis. Thus, altogether, this characteristic of the system favorably affects the interaction of the electrolyte towards the catalyst and its subsequent conversion to H_2 and O_2.[35]

5.3.3 TEM Analysis

The TEM images of Co_9S_8-Ni_3S_2/NF are provided in **Figure 5.8**. The sheet-like morphology of the Co_9S_8-Ni_3S_2 nanopetals is evident from the TEM images (**Figure 5.8a**). It is confirmed from **Figure 5.8a** that the nanoflower morphology is formed from the interconnected arrangement of the nanopetals of Co_9S_8-Ni_3S_2. **Figure 5.8b** is the enlarged portion as marked in **Figure 5.8a**. The layer structure of Co_9S_8 is highlighted in the green square and the enlarged view is presented as **Figure 5.8c**. The d-spacing value is calculated from the TEM image (**Figure 5.8c**) and is found to be 0.25 nm, which is corresponding to the (400) lattice plane of Co_9S_8.[36] The SAED pattern provided in **Figure 5.8d** indicates the crystalline nature of Co_9S_8-Ni_3S_2/NF. The TEM EDX-elemental mapping provided in **Figure 5.8e-j** indicates the uniform distribution of cobalt, nickel and sulfur over NF. This result further validates the findings from SEM

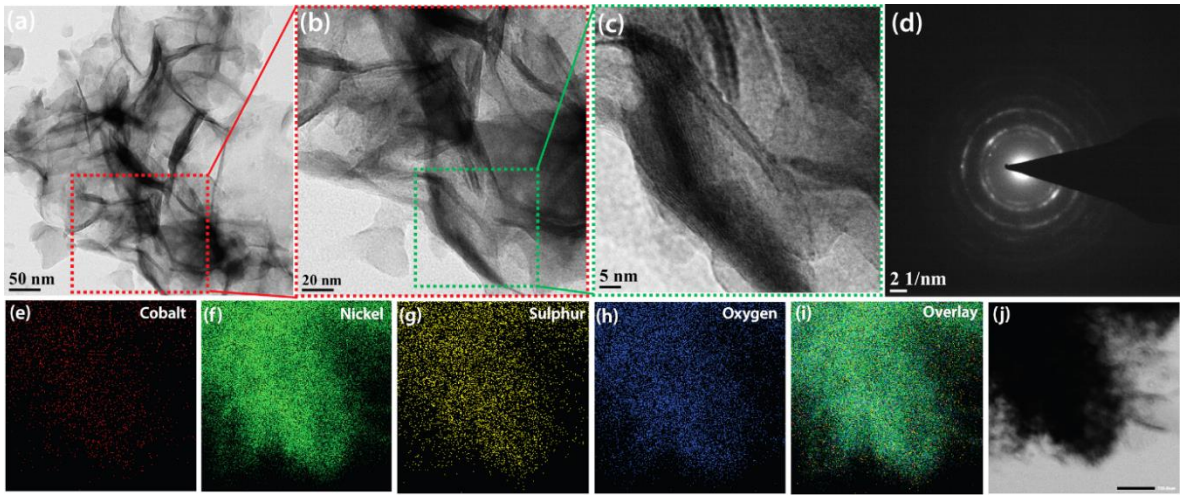

Figure 5.8. *(a-c) TEM images of Co_9S_8-Ni_3S_2/NF at different magnifications, (d) SAED pattern of Co_9S_8-Ni_3S_2/NF, and (e-j) TEM-EDX elemental mapping of Co_9S_8-Ni_3S_2/NF.*

EDX-elemental mapping of Co_9S_8-Ni_3S_2/NF. The TEM images of Ni_3S_2/NF are presented in **Figure 5.9**. The spike kind arrangement of Ni_3S_2 is clear from the TEM images (**Figure 5.9a-b**).

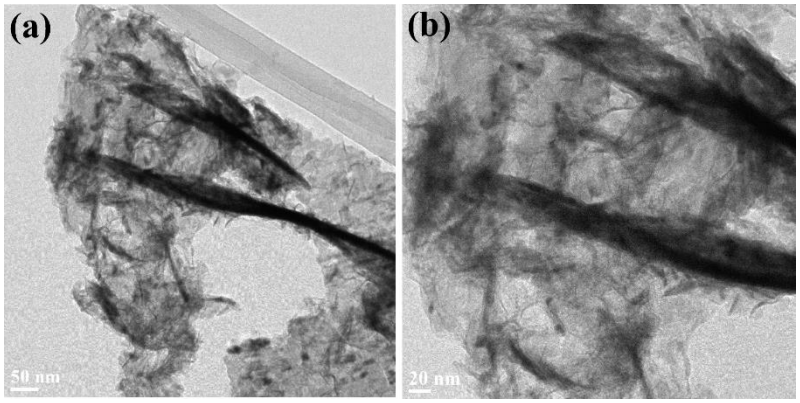

Figure 5.9. *(a-b) TEM images of Ni_3S_2/NF recorded at different magnifications.*

5.3.4 XRD Analysis

The XRD data of bare NF, Ni_3S_2/NF and Co_9S_8-Ni_3S_2/NF along with standard JCPDS pattern is represented in **Figure 5.10**. The bare NF exhibits sharp peaks at the 2θ values of 45.1°, 52.2° and 76.8° corresponding to the (111), (200) and (220) lattice planes of Ni, respectively.[34] Ni_3S_2/NF exhibits the characteristic diffraction peaks at the 2θ values of 21.9°, 31.3°, 38.1°, 50.1° and 55.5°, which are attributed to the (101), (110), (021), (211) and (122) lattice planes of Ni_3S_2, respectively. Co_9S_8-Ni_3S_2/NF displays the diffraction peaks at the 2θ values of 25.3°, 30.1°, 36.2°, 40.8°, 52.3°, 55.7°, 58.1° and

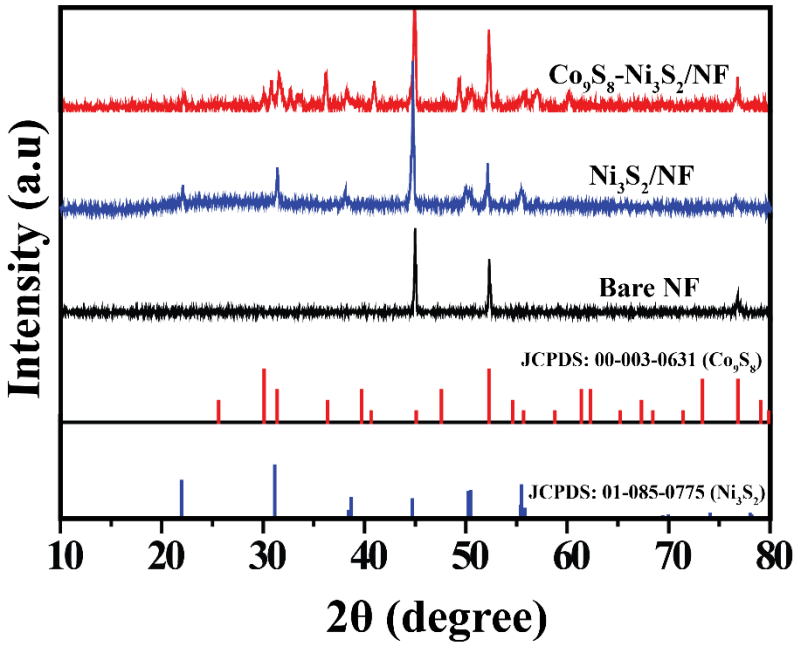

Figure 5.10. *Comparative XRD patterns of bare NF, Ni_3S_2/NF and Co_9S_8-Ni_3S_2/NF along with the standard card numbers.*

60.9° corresponding respectively to the (220), (311), (400), (420), (440), (600), (620) and (533) lattice planes of Co_9S_8. In addition, Co_9S_8-Ni_3S_2/NF also shows the characteristics peaks corresponding to Ni_3S_2 at 2θ values of 22.1°, 31.5°, 38.2°, 50.3° and 55.7°, respectively. The sharp peaks in the XRD spectrum indicates the crystalline nature of the as formed materials. Thus, XRD confirms the coexistence of the Ni_3S_2 and Co_9S_8 phases in Co_9S_8-Ni_3S_2/NF with crystalline characteristics.

5.3.5 X-ray Microtomography Analysis

The pore characteristics and surface morphology of the samples were analyzed by non-invasive X-ray microtomography imaging and the obtained images of bare NF and the Co_9S_8-Ni_3S_2/NF are presented in **Figure 5.11a-d**. The three-dimensional tomography images indicate the open-pore arrangement of the bare NF (**Figure 5.11a-b**). This is in line with the FESEM results obtained for the bare NF. The thin-layer growth pattern of Co_9S_8-Ni_3S_2 on NF is confirmed with the tomography analysis. The red color on the surface indicates the distribution of Co_9S_8-Ni_3S_2 on NF and the yellow color in the core designates the NF substrate in the tomography image (**Figure 5.11c**, **d**). From **Figure 11d**, it is confirmed that Co_9S_8-Ni_3S_2 nanflowers are distributed uniformly on the NF surface. The macro pores of the NF skeleton is intact even after the inclusion of Co_9S_8-Ni_3S_2 hierarchical nanoflower arrays. These results further validate the conclusions attained from the FESEM analysis.

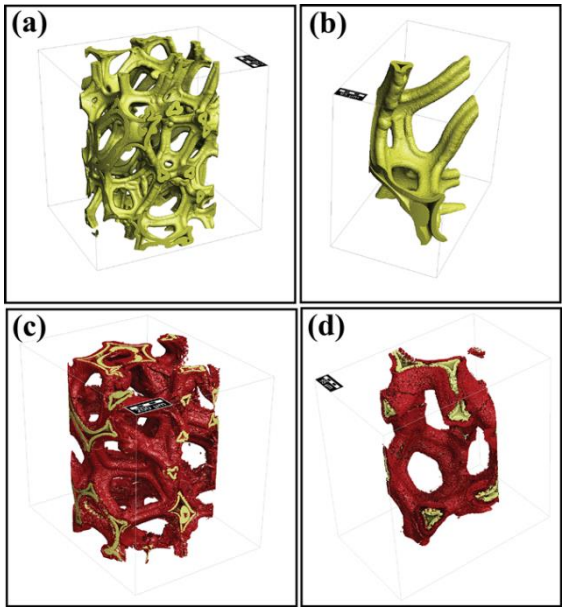

Figure 5.11. *Tomography images of (a, b) bare NF and (c, d) Co_9S_8-Ni_3S_2/NF.*

5.3.6 XPS Analysis

In order to understand the chemical compositions of Co_9S_8-Ni_3S_2/NF, surface analysis was performed by using XPS and the data is provided in **Figure 5.12**. The survey scan spectrum in **Figure 5.12a** confirms the presence of Ni, Co and S in the sample. The

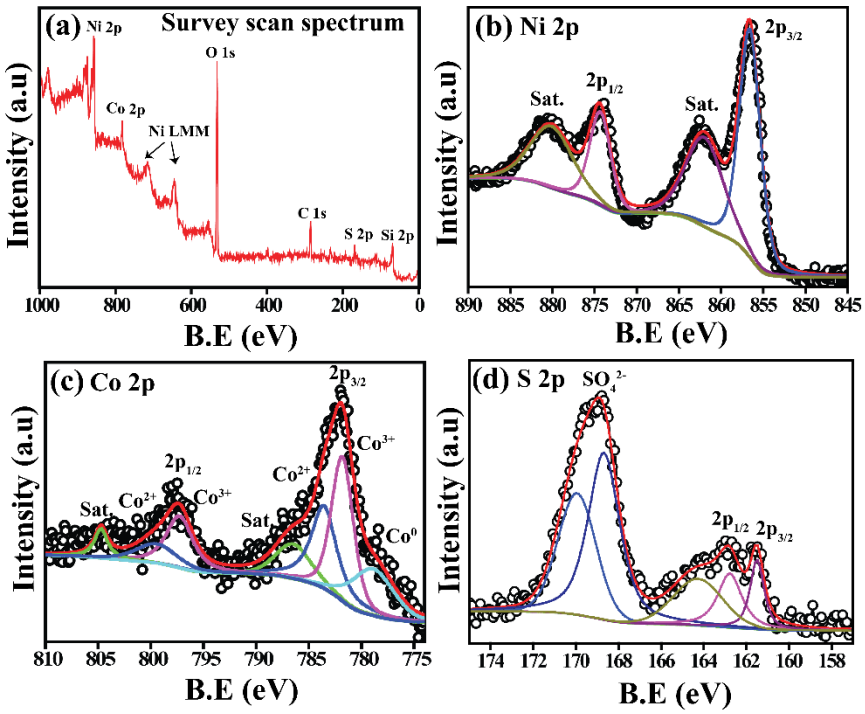

Figure 5.12. *(a) XPS survey scan spectrum of Co_9S_8-Ni_3S_2/NF, (b) deconvoluted Ni 2p spectrum of Co_9S_8-Ni_3S_2/NF, (c) deconvoluted Co 2p spectrum of Co_9S_8-Ni_3S_2/NF and (d) deconvoluted S 2p spectrum of Co_9S_8-Ni_3S_2/NF.*

presence of carbon in the survey spectrum is from the carbon-adhesive tape used for sticking the material. The presence of oxygen in the survey spectrum could be due to the adsorbed oxygen in the sample. The deconvoluted Ni 2p XPS spectra of Co_9S_8-Ni_3S_2/NF is shown in **Figure 5.12b**. The peaks at 856.7 and 874.4 eV are corresponding to the $2p_{3/2}$ and $2p_{1/2}$ peaks of Ni^{2+} in Ni_3S_2, respectively.[32, 34] The satellite peaks are present at 862.3 and 880.4 eV, respectively, in the Ni 2p spectrum. The deconvoluted Co 2p spectra presented in **Figure 5.12c** display the peaks at 781.9 and 797.3 eV, which are corresponding to the $2p_{3/2}$ and $2p_{1/2}$ peaks of Co^{3+} in Co_9S_8, respectively.[32] The peaks observed at 783.6 and 799.5 eV are corresponding to the $2p_{3/2}$ and $2p_{1/2}$ peaks of Co^{2+} in Co_9S_8, respectively.[32] The peak appeared at 778.8 eV is corresponding to the Co^0 state, indicating the presence of minute amount of the reduced cobalt ions in the material.[37] The deconvoluted sulfur 2p spectra show the peaks at 161.5 and 162.8 eV and these are assigned to the $2p_{3/2}$ and $2p_{1/2}$ peaks for the sulfide ions in Co_9S_8 and Ni_3S_2 (**Figure 5.12d**).[32, 38] The bridging disulfide S_2^{2-} is indicated with the peak at 164.3 eV.[39] The peaks at 168.7 and 169.9 eV in the S 2p spectra are corresponding to the surface SO_4^{2-} species, feasibly formed by the exposure of the catalyst in air.[21]

5.4 Electrochemical Analysis

The electrochemical activity of the as synthesized materials were investigated for OER and HER applications in 1 M KOH solution in a three-electrode set-up using a potentiostat (Bio-Logic SP-300). Working electrode was constructed by dipping about 1 cm^2 area of the synthesized material in the electrolyte and the remaining portion is masked by Teflon tape. Graphite rod was used as the counter electrode instead of Pt mesh during the electrochemical analysis. This would avoid the influence of possible deposition of Pt on the working electrode. The Hg/HgO was used as the reference electrode. The linear sweep voltammetry (LSVs) were carried out in the N_2-saturated 1 M KOH solution at a scan rate of 2 mV sec^{-1}. Prior to the LSV measurement, about 10 cycles of CV was performed in the potential window of 1.0 V to 1.5 V *vs.* RHE with a scan rate of 10 mV sec^{-1}. All the LSV measurements were performed without any iR correction. The HER analysis of the catalysts were performed and presented in **Figure 5.13**. The comparative LSVs of the as synthesized samples and *state-of-the-art* Pt/C coated NF (Pt/C@NF) in 1 M KOH solution is shown in **Figure 5.13a**. From **Figure 5.13a**, it is clear that the bare NF displays the poor HER activity and there requires nearly 469 mV overpotential to attain the current density of 25 mA cm^{-2}. The Pt/C@NF

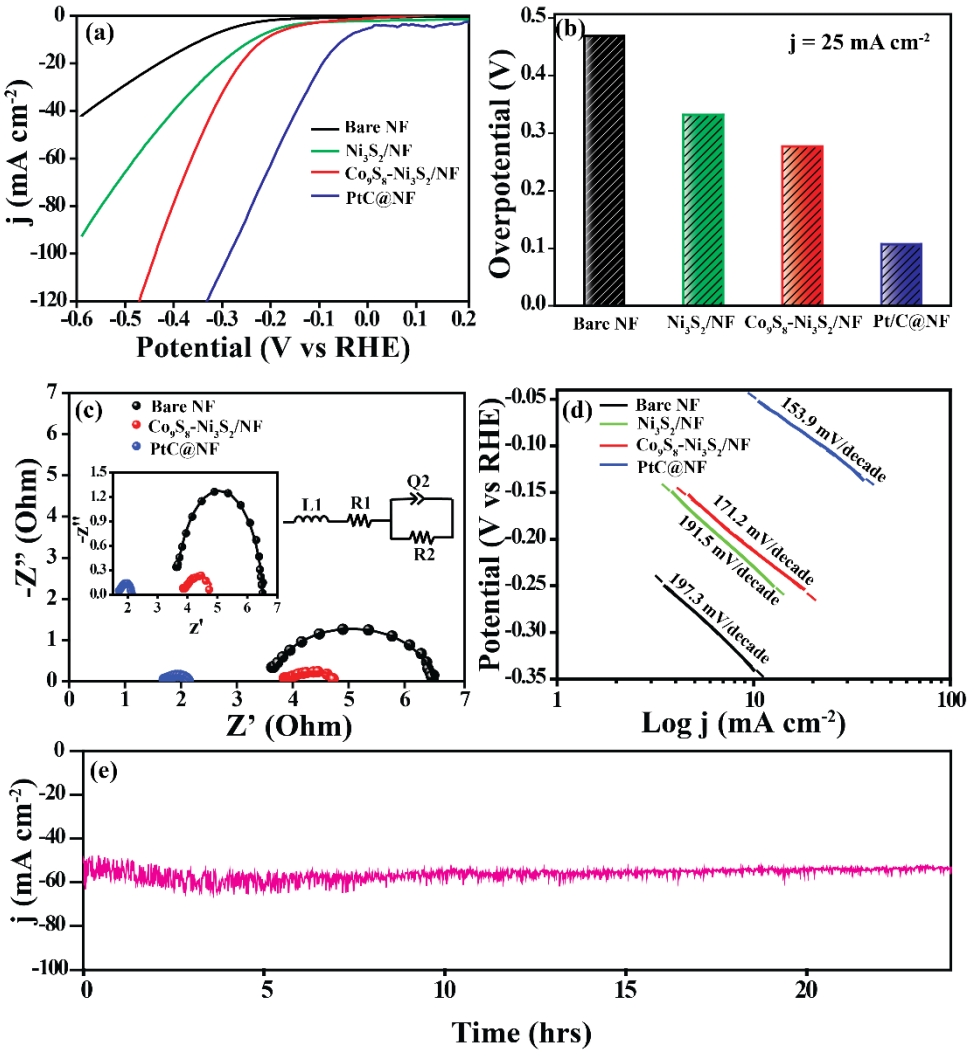

Figure 5.13. *(a) Comparative HER linear sweep voltammograms (LSVs) of the samples recorded in 1 M KOH solution recorded at a scan rate of 2 mV sec^{-1} in N_2 saturated atmosphere, (b) bar diagram indicating the HER overpotential of the samples at a current density of 25 mA cm^{-2}, (c) electrochemical impedance analysis of the samples performed at an overpotential of 300 mV in 1 M KOH solution where the inset shows the equivalent circuit used to fit the data, (d) comparison of the Tafel plot of the samples, and (e) chronoamperometric response of Co_9S_8-Ni_3S_2/NF during HER in 1 M KOH solution for 24 h at a current density of 50 mA cm^{-2}.*

requires an overpotential of 107 mV to delivering the current density of 25 mA cm^{-2}. After incorporating Ni_3S_2 on NF (Ni_3S_2/NF), the HER activity is improved significantly. The overpotential exhibited by Ni_3S_2/NF at a higher current density of 25 mA cm^{-2} is 332 mV. A further reduction in the overpotential is observed after the incorporation of Co_9S_8-Ni_3S_2 nanoflowers on NF (Co_9S_8-Ni_3S_2/NF) and the corresponding overpotential

at 25 mA cm^{-2} is 277 mV. From **Figure 5.13b**, it is clear that the HER activity of Co_9S_8-Ni_3S_2/NF is superior to bare NF and Ni_3S_2/NF and lower as compared to Pt/C@NF. The key parameters behind the improved HER activity of Co_9S_8-Ni_3S_2/NF are credited to the uniform distribution of Co_9S_8-Ni_3S_2 nanoflowers on the NF which provides the suitable active sites for the reaction. Also, the open-pore cavity nature of as formed Co_9S_8-Ni_3S_2/NF nanoflower helps for the diffusion of electrolyte and subsequently the produced gases. The better electrical conductivity possessed by the system assists for the faster kinetics during the reaction.

The electrochemical impedance spectroscopy (EIS) is an important tool to understand the ionic resistant in the material. For this, EIS has been performed and the obtained Nyquist plot is examined to understand the electrical resistance in the material. The EIS was performed in 1 M KOH solution at a potential of -0.30 V *vs.* RHE with a frequency range of 200 kHz to 100 mHz and an AC amplitude of 10 mV. The Nyquist plot is fitted with an equivalent circuit of L_1+R_1+Q_2/R_2, where L_1 is the inductance, R_1 and R_2 are the resistance and Q_2 is the constant phase element. The difference between R_2 and R_1 provides the charge transfer resistance (R_{CT}) value and is calculated from the obtained Nyquist plot (**Figure 5.13c**). The R_{CT} values of bare NF and Co_9S_8-Ni_3S_2/NF are 2.90 and 0.92 **Ω**, respectively. Hence, compared to bare NF, Co_9S_8-Ni_3S_2/NF displays a lower R_{CT} value, which is an indicative of the fast electronic transport during the gas evolution reaction. The lower R_{CT} value eventually improves the HER kinetics and subsequently the catalytic activity. The R_{CT} value exhibited by Pt/C@NF is 0.47 **Ω**, much lower as compared to the other samples. In order to understand the HER kinetics, Tafel slope of the materials has been calculated and presented as **Figure 5.13d**. The Tafel equation is $\eta = a + b \log j$, where 'η' is the overpotential, 'a' is the Tafel constant, 'b' is the Tafel slope and 'j' is the current density. Therefore, the plot of log j against the overpotential results into a straight line and the slope of the plot represents the Tafel slope value (b). The Tafel slope of bare NF is 197.3 mV/decade and for Ni_3S_2/NF it is 191.5 mV/decade. The Tafel slope is fund to be 171.2 mV/decade for Co_9S_8-Ni_3S_2/NF and 153.9 mV/decade for Pt/C@NF. The slightly higher Tafel slope in the present case for all the systems is due to the fact that the LSV measurements were performed without any iR correction. From the Tafel slope values, it can be confirmed that the HER kinetics is faster in both Pt/C@NF and Co_9S_8-Ni_3S_2/NF. Along with higher activity, the long-term stability in the corrosive conditions is an important parameter for evaluating the catalyst efficiency. Thus, chronoamperometric analysis of Co_9S_8-Ni_3S_2/NF in 1 M KOH solution

was conducted at a current density of 50 mA cm^{-2} for 24 h and the corresponding data is presented in **Figure 5.13e**. From the figure, it is confirmed that the system exhibits a stable performance in the investigated period under the high current density condition. The data thus validates the higher structural integrity of Co_9S_8-Ni_3S_2/NF for HER. In the mechanism of HER over Co_9S_8-Ni_3S_2, the first step is the adsorption of the water molecule on the catalyst surface (Volmer reaction). The next step is the combination of two H_{ads} to produce H_2 (Tafel reaction). Therefore, in Co_9S_8-Ni_3S_2/NF, the Volmer-Tafel pathway is followed for the generation of H_2. The Tafel slope value of Co_9S_8-Ni_3S_2/NF is 171 mV/decade and indicates that Volmer reaction is the rate determining step for HER.

$$H_2O(l) + e^- \longrightarrow H_{ads} + OH^-_{(aq)} \qquad \text{(Volmer reaction)}$$

$$H_{ads} + H_{ads} \longrightarrow H_{2(g)} \qquad \text{(Tafel reaction)}$$

Subsequent to the HER studies, the OER activity of the synthesized materials was investigated in 1 M KOH solution and the corresponding results are presented in **Figure 5.14**. The advantages of using similar electrolyte for OER and HER are mainly related to the opportunities for reducing the cost of the overall water splitting and simplifying the electrolyzer design. **Figure 5.14a** represents the comparative LSVs of the material towards OER. The OER activity of bare NF is negligible and the overpotential at 25 mA cm^{-2} is 397 mV. The OER activity of Ni_3S_2/NF is also not significant as its HER performance as can be reflected from the overpotential value of 365 mV at the current density of 25 mA cm^{-2}. Interestingly, Co_9S_8-Ni_3S_2/NF requires only 102 mV overpotential to reach the current density of 25 mA cm^{-2} during OER. This is an improved value compared to the *state-of-the-art* RuO_2 coated NF (RuO_2@NF), where it requires an overpotential of 383 mV at the similar current density. The significantly high OER activity of Co_9S_8-Ni_3S_2/NF is expected to be originated from the controlled interplay of the favoring factors such as hydrophilic and porous nature of the system along with the intrinsic activity of the catalytic sites. The hydrophilicity and porous architecture assist reactant mass transport, effective active site utilization and evolution of gases subsequent to the reactions. The better contact of the catalyst with the electrolyte would improve the interaction of the ions with the catalytic sites, for which the hydrophilic nature of the system plays a critical role. Similarly, the open-pore cavities would facilitate both the diffusion of the electrolyte and the evolved gases during the reaction and thus help to enable a seamless process by minimizing the

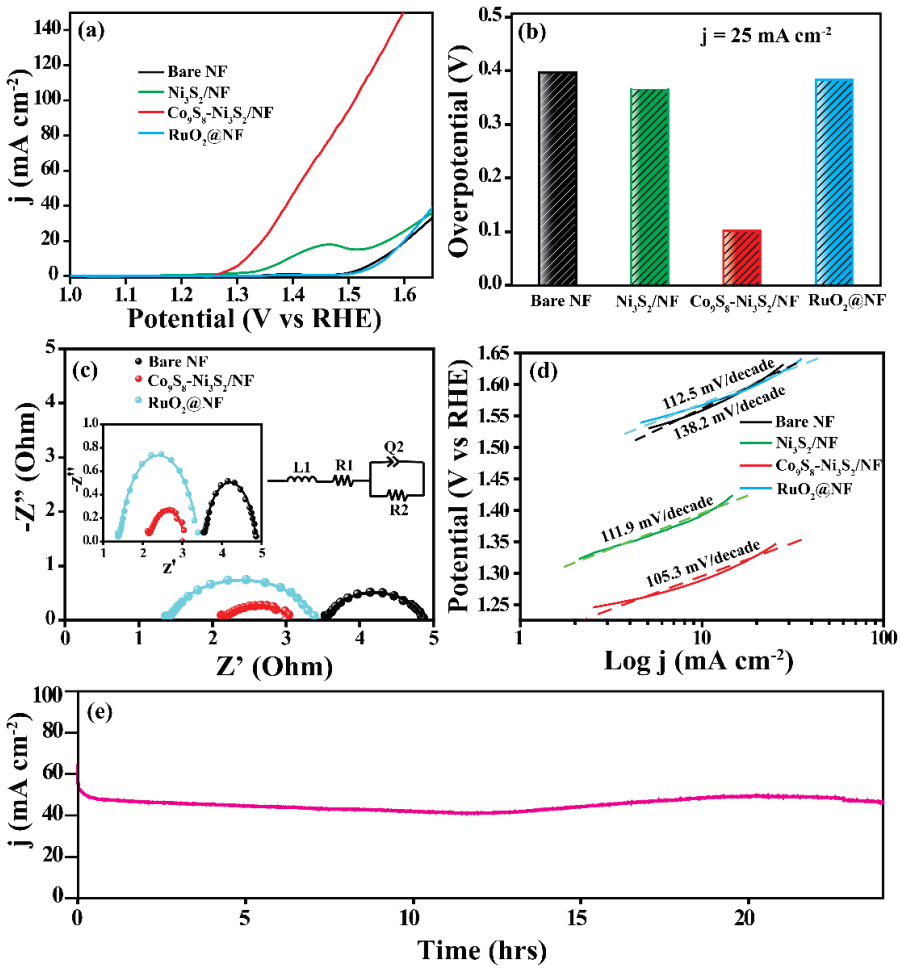

Figure 5.14. *(a) Comparative OER linear sweep voltammogram (LSVs) of the samples recorded in 1 M KOH solution with a scan rate of 2 mV sec^{-1} in N_2 saturated atmosphere, (b) bar diagram indicating the OER overpotential of the samples at 25 mA cm^{-2} current density, (c) electrochemical impedance analysis of the samples performed at an overpotential of 300 mV in 1 M KOH solution where the inset shows the equivalent circuit used to fit the data, (d) comparison of the Tafel plot of samples, and (e) chronoamperometric response of Co_9S_8-Ni_3S_2/NF during OER in 1 M KOH solution for 24 h at a current density of 50 mA cm^{-2}.*

sluggishness expected at high current density conditions. From **Figure 5.14b**, it can be deduced that the OER activity of Co_9S_8-Ni_3S_2/NF is significantly better than that of bare NF, Ni_3S_2/NF and RuO_2@NF at the set current density value of 25 mA cm^{-2}.

In order to understand the charge transfer characteristics displayed by the various systems during OER, EIS investigation was performed at 1.53 V *vs.* RHE. The corresponding Nyquist plots are presented in **Figure 5.14c**. The R_{CT} value calculated from the Nyquist plot for bare NF is 1.33 **Ω**. On the other hand, the R_{CT} value measured

for Co_9S_8-Ni_3S_2/NF is 0.87 Ω, pointing towards fast electron transport during OER on this system. However, the R_{CT} value of RuO_2@NF is found to be much higher compared to the other materials (2.01 Ω). A probable reason for this is the reduced electrical conductivity of RuO_2@NF. For attaining efficient water electrolysis, both the anode and cathode materials should exhibit lower R_{CT} values. Hence, in the present case, Co_9S_8-Ni_3S_2/NF shows the lower R_{CT} value during HER and OER. Therefore, Co_9S_8-Ni_3S_2/NF can be considered as a suitable bi-functional catalyst for water electrolysis applications. The Tafel plots of the catalysts are presented in **Figure 5.14d**, which are indicative of the intrinsic activity towards OER kinetics under the experimental conditions. The Tafel

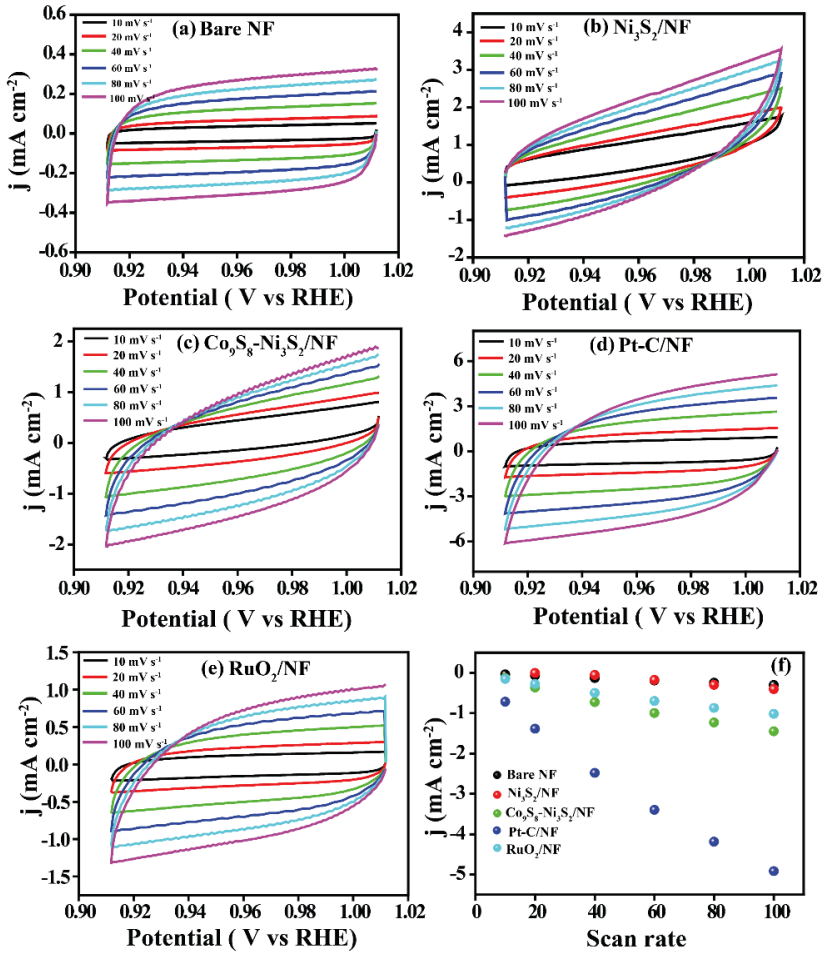

Figure 5.15. *Cyclic voltammograms recorded for the catalyst in the non-Faradaic region at different scan rates in the N_2-saturated 1 M KOH solution: (a) bare NF, (b) Ni_3S_2/NF, (c) Co_9S_8-Ni_3S_2/NF, (d) Pt/C@NF, (e) RuO_2@NF and (f) the plot of the cathodic current density against the scan rate in the non-faradaic region of the CVs.*

slope measured for bare NF is 138 mV/decade and this indicates poor OER activity of the substrate material. Ni_3S_2/NF and RuO_2@NF are having the Tafel slopes of 112 mV/decade and 113 mV/decade, respectively. However, Co_9S_8-Ni_3S_2/NF shows a

comparatively lower Tafel slope value of 105 mV/decade. This serves as a strong performance indicator pointing towards the improved kinetics achievable on Co_9S_8-Ni_3S_2/NF for OER. The proposed mechanism of OER over Co_9S_8-Ni_3S_2 as follows;

$$OH^-_{(aq)} \longrightarrow OH_{ads} + e^-$$

$$OH_{ads} + OH^-_{(aq)} \longrightarrow H_2O(l) + e^- + O_{ads}$$

$$O_{ads} + OH^-_{(aq)} \longrightarrow OOH_{ads} + e^-$$

$$OOH_{ads} + OH^-_{(aq)} \longrightarrow O_{2(g)} + H_2O_{(l)}$$

In order to obtain the further information about the improved catalytic activity of Co_9S_8-Ni_3S_2/NF, the electrochemical active surface area (ECSA) was analyzed. The catalytic activity is related to the ECSA and is proportional to the double layer capacitance (C_{dl}) value. The C_{dl} values of all the samples were measured by performing CV in the non-Faradaic region (**Figure 5.15a-e**). For this, CV was performed in the potential window of 0.91 to 1.01 V at different scan rates of 10, 20, 40, 60, 80 and 100 mV sec^{-1}. The plot of scan rate versus current density at 0.96 V results into a straight line with the slope corresponds to the C_{dl} value (**Figure 5.15f**). The C_{dl} value of bare NF is 2.8 mF cm^{-2} and for Ni_3S_2/NF it is 8.9 mF cm^{-2}. Therefore, after sulfurizing NF, a substantial improvement in the C_{dl} value is observed. Similar observation is noticed in Co_9S_8-Ni_3S_2/NF and the corresponding C_{dl} value is 10.1 mF cm^{-2}, which is about 3.6-fold higher than the bare NF. For comparison, the *state-of-the-art* catalysts coated on NF (*i.e.*, Pt/C@NF and RuO_2@NF) were performed in the same condition. The values obtained for Pt/C@NF and RuO_2@NF are 38.3 and 8.2 mF cm^{-2}, respectively. The higher C_{dl} value possessed by Pt/C@NF could be due to the presence of carbon in the catalyst. The higher C_{dl} value of Co_9S_8-Ni_3S_2/NF in comparison to bare NF indicates the higher surface roughness and further the exposed active sites in Co_9S_8-Ni_3S_2/NF. [30, 40] The improvement in the C_{dl} value could be due to the vertical orientation of the as formed nanoflowers of Co_9S_8-Ni_3S_2 on NF. The higher ECSA can improve the electrode-electrolyte interface and this further can lead to better contact of the electrolyte with the active sites of the catalyst. This would subsequently enhance the OER and HER activities of Co_9S_8-Ni_3S_2/NF.

After confirming the excellent bi-functional activity and outstanding stability of Co_9S_8-Ni_3S_2/NF in the half cell, the overall water splitting was performed in 1 M KOH

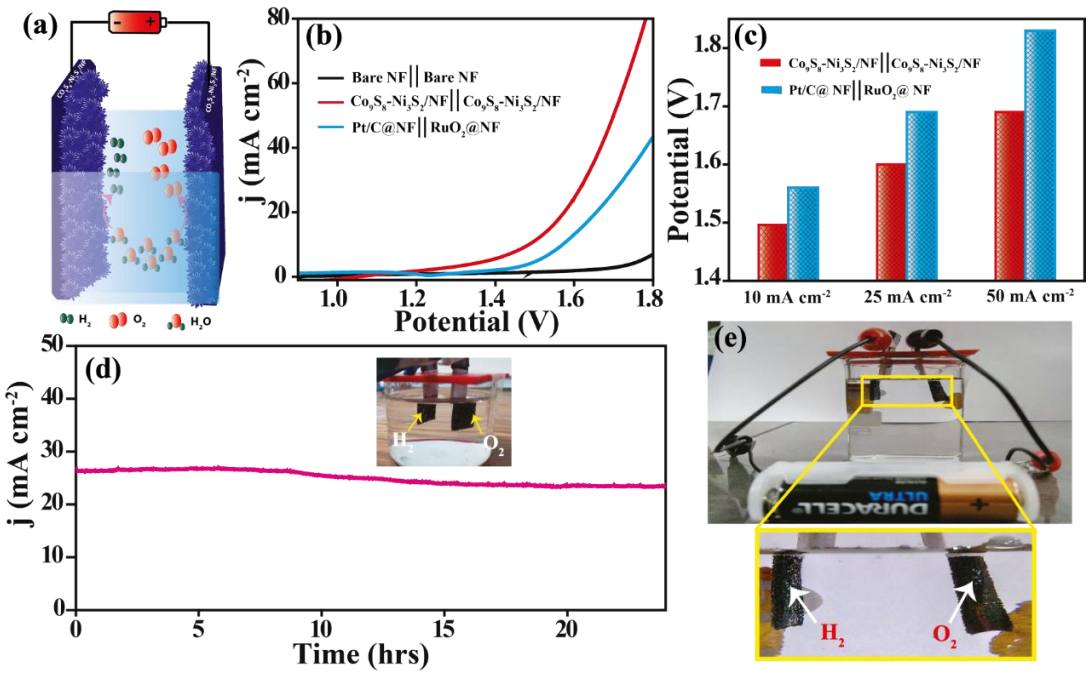

Figure 5.16. *(a) Schematic illustration of the deployment of Co_9S_8-Ni_3S_2/NF based water electrolyzer, (b) comparative LSVs recorded during the overall water splitting analysis in 1 M KOH solution at a scan rate of 2 mV sec^{-1}, (c) bar diagram indicating the water electrolysis activity comparison of Co_9S_8-Ni_3S_2/NF with the state-of-the-art catalysts at different current densities, (d) chronoamperometric response of Co_9S_8-Ni_3S_2/NF during the water electrolysis in 1 M KOH solution for 24 h at a current density of 25 mA cm^{-2} and (e) demonstration of Co_9S_8-Ni_3S_2/NF based water electrolyzer powered with a dry cell battery.*

solution and the set of data collected in this direction is presented in **Figure 5.16**. In order to perform water electrolysis, Co_9S_8-Ni_3S_2/NF was employed as both the anode and cathode in a two-electrode system (Co_9S_8-Ni_3S_2/NF ǁ Co_9S_8-Ni_3S_2/NF) with an active area of 1 cm^{-2}. For comparison, bare NF ǁ NF and Pt/C@NF ǁ RuO_2@NF systems were also performed for water electrolysis applications under similar conditions. **Figure 5.16a** illustrates the schematics of water electrolysis by employing Co_9S_8-Ni_3S_2/NF as both the anode and cathode electrodes. The hydroxyl ions undergo oxidation at the anode and produce O_2 gas. Similarly, at the cathode, the protons undergo reduction and produce the H_2 gas. **Figure 5.16b** illustrates the overall water splitting activity comparison of bare NF ǁ NF, Co_9S_8-Ni_3S_2/NF ǁ Co_9S_8-Ni_3S_2/NF and Pt/C@NF ǁ RuO_2@NF. It is clear from the figure that the water electrolyzer based on bare NF is having negligible catalytic activity, where it requires a potential of 1.83 V to deliver the

current density of 10 mA cm^{-2}. However, the electrolyzer based on Co_9S_8-Ni_3S_2/NF requires only 1.49, 1.60 and 1.69 V for delivering the current densities of 10, 25 and 50 mA cm^{-2}, respectively. Similarly, the Pt/C@NF ||| RuO_2@NF based electrolyzer requires about 1.56, 1.69 and 1.83 V for delivering the current densities of 10, 25 and 50 mA cm^{-2}, respectively. From **Figure 5.16c**, it can be deduced that the activity of the Co_9S_8-Ni_3S_2/NF based water electrolyzer is performing better compared to the *state-of-the-art* system (Pt/C@NF ||| RuO_2@NF). Also, the potential achieved to generate 10 mA cm^{-2} current density using Co_9S_8-Ni_3S_2/NF based electrolyzer is better as compared to many of the reported catalysts for the overall water splitting applications. The stability analysis of the Co_9S_8-Ni_3S_2/NF based water electrolyzer was also performed and the corresponding data collected for 24 h is presented in **Figure 5.16d**. This result indicates the suitability of using Co_9S_8-Ni_3S_2/NF based electrodes for water electrolysis applications. Finally, as a real demonstration, the alkaline water electrolyzer was constructed by Co_9S_8-Ni_3S_2/NF as both the electrodes by powering with a 1.5 V dry cell battery. The gas evolution at the electrodes is evident during the water electrolysis, which is more pronounced in the enlarged portion of **Figure 5.16e**.

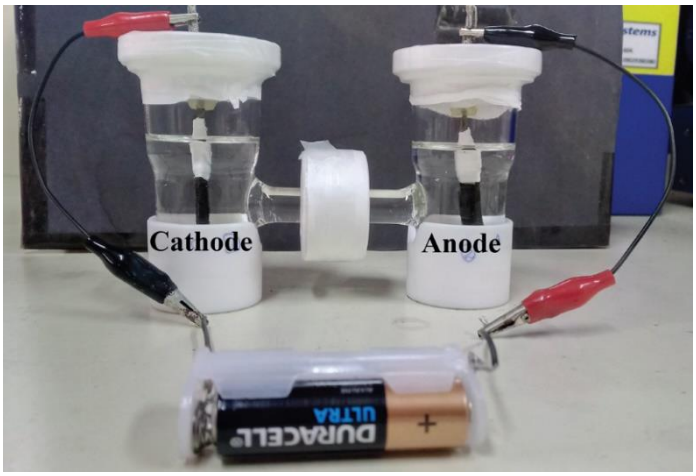

Figure 5.17. *Digital image of the alkaline water electrolyser constructed with Co_9S_8-Ni_3S_2/NF as both the electrodes powered by a 1.5 V battery.*

The gas chromatography was used to evaluate the evolved gas during the water electrolysis in 1 M KOH solution. For this, a two-compartment home-made set-up was fabricated. The compartments were separated with an anion exchange membrane (Fumatech FAA-3). Co_9S_8-Ni_3S_2/NF was used as both the electrodes which was powered by a 1.5 V dry cell battery (**Figure 5.17**). The produced gas was collected from the headspace by using a micro syringe (500 µL) and injected into the GC. **Figure 5.18**

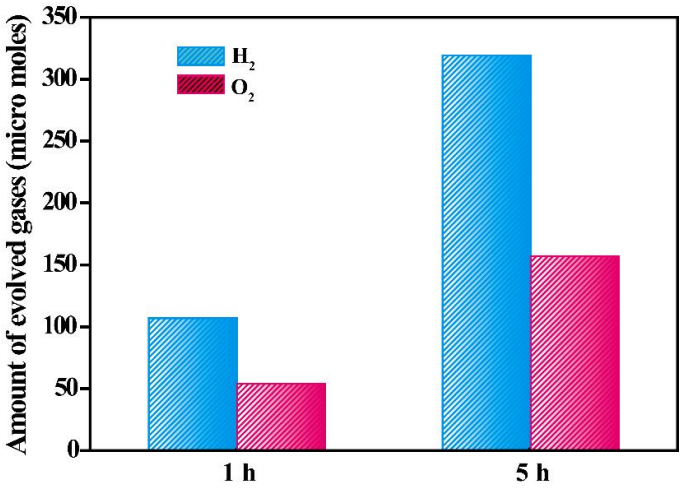

Figure 5.18. *Bar diagram indicating the amount of the evolved gases during the alkaline water electrolysis using Co_9S_8-Ni_3S_2/NF as both the electrodes powered by a 1.5 V battery.*

illustrates the quantification of gases during the water electrolysis with respect to time. From **Figure 5.18**, it is confirmed that H_2 and O_2 were produced on the respective electrodes. The amount of H_2 produced after 1 h was 107 mmol and the amount of O_2 generated in the same time interval was 54 mmol. The amount of gas quantified after 5 h was 319 mmol for H_2 and 157 mmol for O_2, respectively. The produced H_2 and O_2 are nearly in the 2:1 ratio, following closely to the theoretical value ($H_2O \longrightarrow H_2 + ½ O_2$). In short, the gas quantification analysis is obviously indicating the water splitting capability of Co_9S_8-Ni_3S_2/NF by using a 1.5 V power supply.

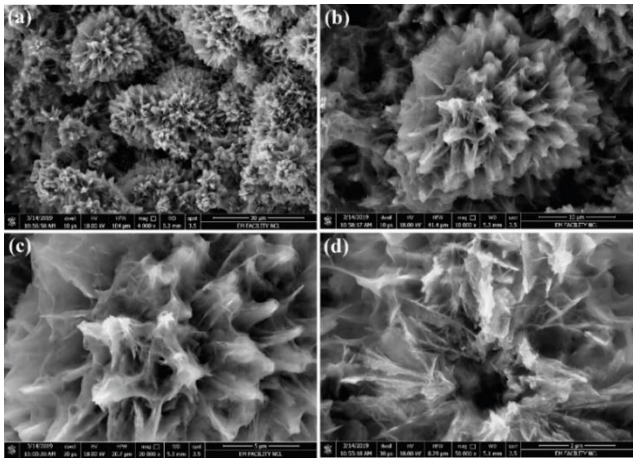

Figure 5.19. *FESEM images of Co_9S_8-Ni_3S_2/NF recorded after the 24 h overall water splitting application in 1 M KOH solution.*

Post characterization of Co_9S_8-Ni_3S_2/NF after 24 h chronoamperometry during overall water splitting was carried out to understand the possible structural and chemical

changes incurred in the material. **Figure 5.19** presents the FESEM image of Co_9S_8-Ni_3S_2/NF subsequent to the 24 h testing. The nanoflower morphology of the material is found to be retained after the stability analysis. However, the presence of surface sheet-layer morphology is observed on the nanoflowers of Co_9S_8-Ni_3S_2, which could be ascribed to the formation of $Co(OH)_2$ layers on the surface of the material during the course of the reaction.[41] Still, after the water electrolysis, the nanoflower structure is found to be intact. This further points towards the simultaneous presence of Co_9S_8-Ni_3S_2 as the core and $Co(OH)_2$ as the surface layer during the electrolysis process.

The XPS investigation of the material obtained after the water electrolysis was carried out to check the chemical modifications occurred in Co_9S_8-Ni_3S_2/NF and the corresponding spectrum is shown in **Figure 5.20**. The survey spectrum illustrated in **Figure 5.20a** indicates the presence of Co, Ni, S and O in the system after the water electrolysis. **Figure 5.20b** illustrates the deconvoluted Ni spectra, which indicates the peaks at 855.8 and 873.4 eV corresponding to the $2p_{3/2}$ and $2p_{1/2}$ states of Ni^{2+} in $Ni(OH)_2$ and NiOOH, respectively.[31] The deconvoluted Co 2p spectra presented in **Figure 5.20c** show the peaks at 780.8 and 796.5 eV, inferring to the $2p_{3/2}$ and $2p_{1/2}$ states of Co^{2+} in $Co(OH)_2$, respectively.[31, 42] The satellite peaks are observed at 784.1 and 802.8 eV, respectively. **Figure 5.20d** represents the deconvoluted S 2p spectra which

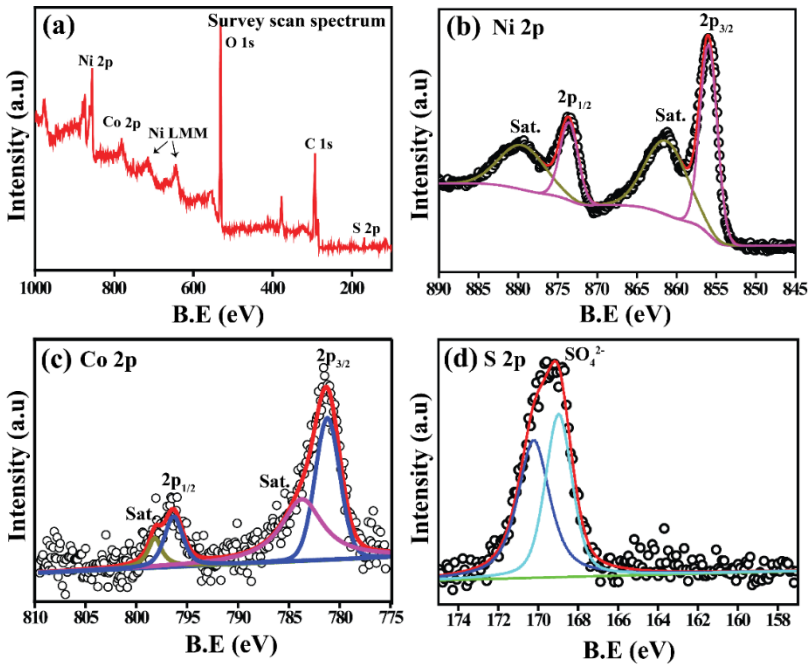

Figure 5.20. *XPS investigation of Co_9S_8-Ni_3S_2/NF after the 24 h overall water splitting application: (a) survey scan spectrum, (b) deconvoluted nickel 2p spectra, (c) deconvoluted spectra of cobalt 2p and (d) deconvoluted sulphur 2p spectra.*

indicate the peaks corresponding to the sulfate ions at 168.7 and 169.9 eV. The peaks at 161.5 and 162.8 eV corresponding to sufide ions are absent. This indicates the partial oxidation of Co_9S_8 and the formation of $Co(OH)_2$ as a surface layer in Co_9S_8-Ni_3S_2/NF during the course of water electrolysis.[31, 43] Hence, it can be concluded from the post analysis that, during the water electrolysis, $Co(OH)_2$ is formed at the surface, which provides the favorable anchoring sites for the adsorption of ions (H^+ and OH^-). Concomitantly, Co_9S_8-Ni_3S_2 core maintains electrical conductivity and electrocatalytic activity in Co_9S_8-Ni_3S_2/NF during the process, leading to accomplish HER and OER at substantially reduced overpotentials for the respective reactions.

5.5 Conclusions

We have developed a bi-functional electrocatalyst for facilitating the overall water splitting by growing Co_9S_8-Ni_3S_2 nanoflowers *in-situ* on nickel foam (NF) through a simple and environmentally friendly hydrothermal method. The nanoflower arrays which are self-supported on NF without any binder possess characteristic pore and structural morphologies which are beneficial to accomplish the electrolysis process. The obtained catalyst, which is designated as Co_9S_8-Ni_3S_2/NF, displays high HER as well as OER activities in 1 M KOH solution. The overpotentials exhibited by the system at 25 mA cm^{-2} are nearly 277 and 102 mV for HER and OER, respectively. The stability analysis of Co_9S_8-Ni_3S_2/NF during HER and OER in 1 M KOH solution performed at 50 mA cm^{-2} for 24 h points towards excellent durability and structural integrity possessed by the system. By using Co_9S_8-Ni_3S_2/NF as both the anode and cathode electrodes, the overall water splitting was successfully performed in 1 M KOH. It was found that the system requires only 1.49, 1.60 and 1.69 V for delivering the current densities of 10, 25 and 50 mA cm^{-2}, respectively. The system for the overall water electrolyzer also displays good durability in performance and structural integrity of the catalyst system. The higher activity accomplished by the Co_9S_8-Ni_3S_2/NF based system is credited to the features like higher electrical conductivity of NF, porosity and hydrophilicity possessed by the material and the lower charge transfer resistance (R_{CT}) of the composite. The $Co(OH)_2$ formed on the surface of Co_9S_8-Ni_3S_2 during the water electrolysis acts as the anchoring sites of the ions.

5.6 References

[1] L. Zhang, J. Xiao, H. Wang, M. Shao, *ACS Catal.* **2017**, *7*, 7855-7865.

[2] C. Wei, R. R. Rao, J. Peng, B. Huang, I. E. L. Stephens, M. Risch, Z. J. Xu, Y. Shao-Horn, *Adv. Mater.* **2019**, *31*, 1806296.

[3] Y. Jiao, Y. Zheng, M. Jaroniec, S. Z. Qiao, *Chem. Soc. Rev.* **2015**, *44*, 2060-2086.

[4] L. Najafi, S. Bellani, R. Oropesa-Nuñez, M. Prato, B. Martín-García, R. Brescia, F. Bonaccorso, *ACS Nano* **2019**, *13*, 3162-3176.

[5] Z. Wu, B. Fang, Z. Wang, C. Wang, Z. Liu, F. Liu, W. Wang, A. Alfantazi, D. Wang, D. P. Wilkinson, *ACS Catal.* **2013**, *3*, 2101-2107.

[6] L. Wang, A. Holewinski, C. Wang, *ACS Catal.* **2018**, *8*, 9388-9398.

[7] J. K. Nørskov, J. Rossmeisl, A. Logadottir, L. Lindqvist, J. R. Kitchin, T. Bligaard, H. Jónsson, *J. Phys. Chem. B* **2004**, *108*, 17886-17892.

[8] R. Zhang, C. Tang, R. Kong, G. Du, A. M. Asiri, L. Chen, X. Sun, *Nanoscale* **2017**, *9*, 4793-4800.

[9] J. D. Costa, J. L. Lado, E. Carbó-Argibay, E. Paz, J. Gallo, M. F. Cerqueira, C. Rodríguez-Abreu, K. Kovnir, Y. V. Kolen'ko, *J. Phys.Chem. C* **2016**, *120*, 16537-16544.

[10] X. Zou, Y. Zhang, *Chem. Soc. Rev.* **2015**, *44*, 5148-5180.

[11] X. Zhang, S. Zhang, J. Li, E. Wang, *J. Mater. Chem. A* **2017**, *5*, 22131-22136.

[12] C. Ray, S. C. Lee, K. V. Sankar, B. Jin, J. Lee, J. H. Park, S. C. Jun, *ACS Appl. Mater. Interfaces* **2017**.

[13] S. Anantharaj, S. R. Ede, K. Sakthikumar, K. Karthick, S. Mishra, S. Kundu, *ACS Catal.* **2016**, *6*, 8069-8097.

[14] T. Tang, W.-J. Jiang, S. Niu, N. Liu, H. Luo, Y.-Y. Chen, S.-F. Jin, F. Gao, L.-J. Wan, J.-S. Hu, *J. Am. Chem. Soc.* **2017**, *139*, 8320-8328.

[15] A.-L. Wang, H. Xu, G.-R. Li, *ACS Energy Lett.* **2016**, *1*, 445-453.

[16] J. Wang, H.-x. Zhong, Z.-l. Wang, F.-l. Meng, X.-b. Zhang, *ACS Nano* **2016**, *10*, 2342-2348.

[17] J.-T. Ren, Z.-Y. Yuan, *ACS Sustainable Chem. Eng.* **2017**, *5*, 7203-7210.

[18] S. Ji, T. Li, Z.-D. Gao, Y.-Y. Song, J.-J. Xu, *Chem. Commun.* **2018**, *54*, 8765-8768.

[19] T. Yoon, K. S. Kim, *Adv. Funct. Mater.* **2016**, *26*, 7386-7393.

[20] C. Panda, P. W. Menezes, C. Walter, S. Yao, M. E. Miehlich, V. Gutkin, K. Meyer, M. Driess, *Angew. Chem., Int. Ed.* **2017**, *56*, 10506-10510.

[21] C. Ouyang, X. Wang, S. Wang, *Chem. Commun.* **2015**, *51*, 14160-14163.

[22] C. Guan, X. Liu, A. M. Elshahawy, H. Zhang, H. Wu, S. J. Pennycook, J. Wang, *Nanoscale Horiz.* **2017**, *2*, 342-348.

[23] X. Zhou, X. Yang, H. Li, M. N. Hedhili, K.-W. Huang, L.-J. Li, W. Zhang, *J. Mater.*

Chem. A **2017**, *5*, 15552-15558.

[24] Y. Tong, X. Yu, G. Shi, *Phys. Chem. Chem. Phys.* **2017**, *19*, 4821-4826.

[25] L. Wang, S. Zhao, X. Wu, S. Guo, J. Liu, N. Liu, H. Huang, Y. Liu, Z. Kang, *RSC Adv.* **2016**, *6*, 66893-66899.

[26] S. Wan, Y. Liu, G.-D. Li, X. Li, D. Wang, X. Zou, *Catal. Sci. Technol.* **2016**, *6*, 4545-4553.

[27] H. Gu, Y. Huang, L. Zuo, W. Fan, T. Liu, *Inorg. Chem. Front.* **2016**, *3*, 1280-1288.

[28] Z. Ma, Q. Zhao, J. Li, B. Tang, Z. Zhang, X. Wang, *Electrochim. Acta* **2018**, *260*, 82-91.

[29] S. Hao, L. Chen, C. Yu, B. Yang, Z. Li, Y. Hou, L. Lei, X. Zhang, *ACS Energy Lett.* **2019**, *4*, 952-959.

[30] T. Liu, X. Sun, A. M. Asiri, Y. He, *Int. J. Hydrog. Energy* **2016**, *41*, 7264-7269.

[31] W. Fang, D. Liu, Q. Lu, X. Sun, A. M. Asiri, *Electrochem. Commun.* **2016**, *63*, 60-64.

[32] J. Lin, H. Wang, X. Zheng, Y. Du, C. Zhao, J. Qi, J. Cao, W. Fei, J. Feng, *J. Power Sources* **2018**, *401*, 329-335.

[33] C. Ray, S. C. Lee, K. V. Sankar, B. Jin, J. Lee, J. H. Park, S. C. Jun, *ACS Appl. Mater. Interfaces* **2017**, *9*, 37739-37749.

[34] J. Cao, J. Zhou, Y. Zhang, Y. Wang, X. Liu, *ACS Appl. Mater. Interfaces* **2018**, *10*, 1752-1760.

[35] K. Ao, D. Li, Y. Yao, P. Lv, Y. Cai, Q. Wei, *Electrochim. Acta* **2018**, *264*, 157-165.

[36] H. Wang, S. Lu, Y. Chen, L. Han, J. Zhou, X. Wu, W. Qin, *J. Mater. Chem. A* **2015**, *3*, 23677-23683.

[37] T. N. Pham, T. Sharifi, R. Sandström, W. Siljebo, A. Shchukarev, K. Kordas, T. Wågberg, J.-P. Mikkola, *Sci. Rep.* **2017**, *7*, 6112.

[38] L.-L. Feng, G.-D. Li, Y. Liu, Y. Wu, H. Chen, Y. Wang, Y.-C. Zou, D. Wang, X. Zou, *ACS Appl. Mater. Interfaces* **2015**, *7*, 980-988.

[39] L. Zhao, J. Jia, Z. Yang, J. Yu, A. Wang, Y. Sang, W. Zhou, H. Liu, *Appl. Catal., B* **2017**, *210*, 290-296.

[40] W. Kong, X. Luan, H. Du, L. Xia, F. Qu, *Chem. Commun.* **2019**, *55*, 2469-2472.

[41] S. Jin, *ACS Energy Lett.* **2017**, *2*, 1937-1938.

[42] H. Xu, C. Zhang, W. Zhou, G.-R. Li, *Nanoscale* **2015**, *7*, 16932-16942.

[43] Y. H. Deng, C. Ye, B. X. Tao, G. Chen, Q. Zhang, H. Q. Luo, N. B. Li, *J. Power Sources* **2018**, *397*, 44-51.

Chapter-6

Summary

This chapter summarizes the overall research work explained in the preceding chapters that dedicatedly focused on the development of efficient oxygen reduction reaction (ORR) and oxygen evolution reaction (OER) electrocatalysts. The wide application of the polymer electrolyte membrane fuel cells (PEMFCs) and water electrolyzers are restricted primarily due to the high cost and poor stability of the electrocatalysts. To address these problems, the development of efficient and cost-effective catalysts is essential. In this regard, the development of Transition Metal Sulfide (TMS) derived nanomaterials is playing a vital role. The high electronic conductivity, interesting electrochemical activities, better corrosion stability, diverse structural types along with the cost effectiveness in the synthesis of the TMS derived nanomaterials made these systems as the attracting candidates for ORR and OER applications. To improve the active centre density and subsequently the catalytic activity of the produced TMS derived catalysts, various strategies have been adopted during the synthesis. Systematic methodologies have been developed in each case to achieve improved activity and thereby reducing the overpotential of the synthesized materials in comparison with the *state-of-the-art* catalysts. Tuning the morphology, electrochemical active surface area and electrical conductivity of the prepared materials could be carefully performed for achieving efficient catalysts for ORR and OER. The synthesized electrocatalysts display remarkable activities for ORR and OER in terms of reduced overpotential and improved stability. The enhancement achieved in the catalytic performance is correlated with the structural modifications of the developed catalysts. A discussion on the future prospects of the thesis work in the development of PEMFCs and water electrolysers is included at the end of this chapter.

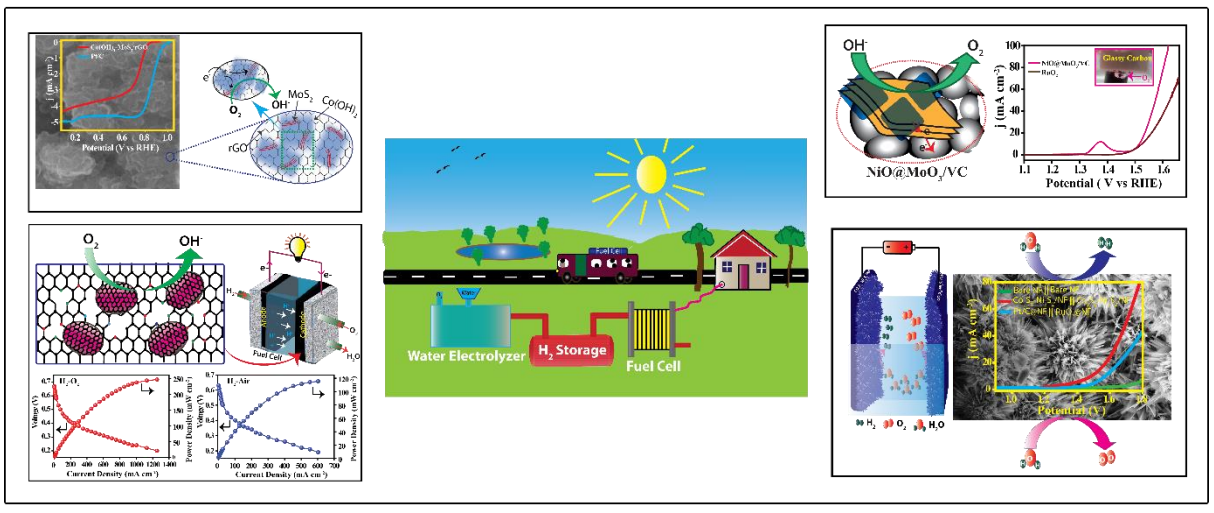

The major accomplishments of the thesis work are summarized below:

Layer-separated MoS_2 Bearing Reduced Graphene Oxide Mediated by $Co(OH)_2$ as a Pt-free Electrocatalyst for Oxygen Reduction Reaction

A significant improvement in the ORR activity of MoS_2 could be accomplished by its layer separated dispersion on reduced graphene oxide (rGO) mediated by cobalt hydroxide through a hydrothermal process ($Co(OH)_2$-MoS_2/rGO). The activity makeover in this case is found to be originated from a controlled interplay of the favourable modulations achieved in terms of electrical conductivity, more exposure of the edge planes of MoS_2 and promotional role played by the coexistence of $Co(OH)_2$ in the proximity of MoS_2. The noticeable features of the work are listed below:

- The system acquired a layer separated spread-out distribution of MoS_2 along the rGO surface, where the presence of $Co(OH)_2$ is found to be playing a vital role in maintaining a homogeneous distribution and enhanced pore-size characteristics of the dispersed layer.
- The $Co(OH)_2$-MoS_2/rGO displays an oxygen reduction onset potential of 0.86 V *vs.* RHE and a half-wave potential ($E_{1/2}$) of 0.74 V *vs.* RHE in 0.1 M KOH solution, which are much higher than that of the corresponding values (0.71 and 0.35 V, respectively) displayed by the as-synthesized pristine MoS_2 (P-MoS_2) under the identical experimental conditions.
- The calculated number of electron transfer during oxygen reduction for $Co(OH)_2$-MoS_2/rGO is in the range of 3.2-3.4 in the potential range of 0.70 V to 0.10 V, which again stands out as a valid evidence on the much favourable mode of oxygen reduction accomplished by the system compared to its pristine counterpart.
- The study demonstrates a viable strategy of tackling the inherent limitations, such as low electrical conductivity and limited access to the active sites, faced by the layered structures like MoS_2 to position them among the group of potential Pt-free electrocatalysts for oxygen reduction.

Co_9S_8 Nanoparticle-Supported Nitrogen-doped Carbon as a Robust Catalyst for Oxygen Reduction Reaction in Both Acidic and Alkaline Conditions

To accomplishing the large-scale commercialization of PEMFCs cost-effectively, concurrent development of the low cost, stable and efficient ORR catalysts in both acidic and alkaline conditions is essential. In this direction, an highly efficient and durable ORR catalyst which

could be prepared by supporting the graphitic carbon enfolded Co_9S_8 nanoparticles on nitrogen-doped carbon (Co_9S_8/NVC-G) is developed. The key aspects of the work are listed below:

- The size of the Co_9S_8 nanoparticles is nearly 7-8 nm and the particles are found to be distributed uniformly on the NVC-G support. The few-layer graphitic carbon formed on the surface of Co_9S_8 nanoparticles is assisting to accomplish their small size and it also prevents agglomeration of the nanoparticles.
- The ORR analysis of Co_9S_8/NVC-G in 0.1 M KOH solution displays only 70 mV negative shift in the onset potential compared to the *state-of-the-art* Pt/C system. The $E_{1/2}$ difference between the present system and Pt/C is nearly 75 mV. The accelerated durability test (ADT) shows only a 19 mV negative shift in the $E_{1/2}$ value of Co_9S_8/NVC-G compared to the 35 mV negative shift incurred by Pt/C.
- The ORR activity investigation in 0.5 M H_2SO_4 solution also displays promising performance for Co_9S_8/NVC-G towards ORR. The differences in the onset potential and $E_{1/2}$ values of the present system with that of Pt/C are 140 and 170 mV, respectively in the acidic electrolyte condition. The system displays a minor $E_{1/2}$ shift of 21 mV towards the lower potential after the 5000 cycles of ADT.
- Co_9S_8/NVC-G when employed as the cathode catalyst in an MEA of a PEMFC delivered a maximum power density of 245 mW cm^{-2} in the H_2-O_2 atmosphere in its single-cell mode of operation. Under H_2-air feeding condition, the same system delivered a maximum power density of 115 mW cm^{-2}. These values obtained on a single cell level is promising due to its prospect to realize a noble metal-free PEMFC system for futuristic applications.

Coexisting Few-Layer Assemblies of NiO and MoO_3 Deposited on Vulcan Carbon as an Efficient and Durable Electrocatalyst for Water Oxidation

A robust and highly durable water-oxidation (OER) catalyst was synthesized by following a simple two-step hydrothermal route followed by heat-treatment of the material. The produced NiO@MoO_3/VC is comprised of small-sized NiO nanosheets anchored on MoO_3, which facilitates the hydroxyl ion adsorption during the water oxidation reaction. The MoO_3 is derived from the few-layer MoS_2 and this subsequently anchors the NiO nanosheets. The salient features of the work are listed below:

- The material was prepared by adopting a strategy wherein layered assembly of NiO and MoO_3 could be dispersed on Vulcan carbon support to simultaneously maintain exposure of the synergistically activated sites and electrical conductivity of the matrix.

The assembly involves the growth of layers of NiO on the surface of few-layer MoO_3 which in turn is dispersed on Vulcan carbon (NiO@MoO_3/VC) through a sequential hydrothermal process.

- The water oxidation studies were conducted in 1 M KOH solution and NiO@MoO_3/VC is exhibiting only 280 mV overpotential at 10 mA cm^{-2} current density, which is an improved value over 292 mV obtained in the case of the *state-of-the-art* RuO_2 catalyst. The stability analysis of NiO@MoO_3/VC at 1.51 V *vs.* RHE for 15 h demonstrates the excellent tolerance of NiO@MoO_3/VC in the corrosive conditions.
- The NiO sheets have exposed edges and they are instrumental in enhancing the OER activity of NiO@MoO_3/VC. The higher activity is also credited to the lower charge transfer resistance (R_{CT}) value possessed by NiO@MoO_3/VC, which arises from the optimum combination of MoO_3 and Vulcan carbon in the system.
- The overall water splitting was performed in 1 M KOH solution by employing NiO@MoO_3/VC as the anode catalyst and Pt/C as the cathode catalyst. The system requires a potential of 1.59 V to reach the current density of 10 mA cm^{-2}, replaces the RuO_2 from the anode of the electrolyzer with the home-made catalyst.

Hierarchical Nanoflower Arrays of Co_9S_8-Ni_3S_2 on Nickel Foam: Highly Efficient Binder-free Electrocatalyst for Overall Water Splitting Application

The development of the non-precious-metal based water electrolyzer is limited mainly due to the high overpotential and physical coating of the catalyst on the conducting substrate using binders. This would lead to undesirable contact resistance in the system and subsequently to reduced catalytic activity. In-situ anchoring the nanomaterials on a conducting substrate and subsequently developing the self-supported bi-functional electrodes for HER and OER can resolve these issues. The key features of the work are listed below:

- The self-standing and binder-free electrode is prepared by growing Co_9S_8-Ni_3S_2 nanoflowers in-situ on nickel foam (NF) through a simple and environmentally friendly hydrothermal method (Co_9S_8-Ni_3S_2/NF).
- The overpotentials exhibited by Co_9S_8-Ni_3S_2/NF at 25 mA cm^{-2} are nearly 277 and 102 mV for HER and OER, respectively, in 1 M KOH solution. The material displays impressive stability during HER and OER in 1 M KOH, which was confirmed through an evaluation lasted for 24 h at 50 mA cm^{-2}.
- The overall water splitting was performed in 1 M KOH solution by employing Co_9S_8-Ni_3S_2/NF as both the anode and cathode electrodes, where the system required only

1.49, 1.60 and 1.69 V to deliver the current densities of 10, 25, and 50 mA cm^{-2}, respectively.

- The higher activity accomplished by the Co_9S_8-Ni_3S_2/NF based system is credited to the features like higher electrical conductivity of NF, porosity and hydrophilicity possessed by the material and the lower charge transfer resistance (R_{CT}) of the composite.
- As a real demonstration, the alkaline water electrolyzer was constructed by Co_9S_8-Ni_3S_2/NF as both the electrodes by powering with a 1.5 V dry cell battery and the evolved gases were quantified by using gas chromatography.

Future Prospects

The transition metal sulfide derived electrocatalysts developed in this dissertation for aiding ORR and OER are having great scope in sustainable energy production. The cost-effective synthesis and high durability possessed by the prepared materials are significant. The proton exchange membrane fuel cell (PEMFC) performance of the developed catalyst is notable in the Pt-free systems. However, compared to the Pt-based system, the performance is lower. Therefore, further studies are required to improve the ORR performance of the catalysts by developing various morphologies and tuning the kinetics by incorporating suitable materials. The anion exchange membrane fuel cells (AEMFCs) provide the feasibility of using noble metal-free catalysts for delivering higher efficiency. However, the limitation in the availability of highly hydroxyl ion-conducting and durable anion exchange membrane (AEM) becames the major challenge in the development of AEMFC and, restricts the advantages of its exploration. The available AEMs are underperforming even with commercial Pt/C in AEMFC operation. Hence, studies are required in this area to explore the advantages of ORR catalysts that are active in the alkaline conditions. The developed ORR catalysts can also be applied in the metal-air batteries. The metal-air batteries are having high theoretical energy density. However, the practical energy density is limited by the sluggish kinetics on the cathode electrode where the ORR takes place. Therefore, the developed ORR catalysts can be explored in the cathode of the metal-air batteries for obtaining the high energy density.

The OER catalysts developed in this dissertation are employed for water electrolysis in alkaline conditions. The catalysts display better stability in the corrosive conditions. The material developed on nickel foam in Chapter 5 is interesting due to the carbon-free nature because the carbon-free catalysts have the advantage of eliminating the possible carbon oxidation at high

potential during water electrolysis. To reduce the cost of the water electrolyzer and the associated complications in device fabrication, the production of H_2 in a neutral medium and seawater is essential. The large overpotential in the neutral medium due to lack of ionic conductivity can be overcome with the development of an efficient electrocatalyst. Research is required in this direction to develop efficient OER catalysts in the neutral medium and, further to commercialize the water electrolyzer with seawater for sustainable H_2 production.

List of Publications

1) Hierarchical Nanoflower Arrays of Co_9S_8-Ni_3S_2 on Nickel Foam: Highly Efficient Binder-free Electrocatalyst for Overall Water Splitting Application. **Illathvalappil, R**.; Walko, P. S.; Kanheerampockil, F.; Bhat, S. K.; Devi, R. N.; Kurungot, S., ***Chem. Eur. J*. 2020, 26, 7900-7911**.
2) Co_9S_8 Nanoparticle-Supported Nitrogen-doped Carbon as a Robust Catalyst for Oxygen Reduction Reaction in Both Acidic and Alkaline Conditions. **Illathvalappil, R**.; Kurungot, S., ***ChemElectroChem*, 2020, 7, 3123-3134.**
3) Coexisting Few-Layer Assemblies of NiO and MoO_3 Deposited on Vulcan Carbon as an Efficient and Durable Electrocatalyst for Water Oxidation. **Illathvalappil, R**.; George, L.; Kurungot, S., ***ACS Appl. Energy Mater*., 2019, 2 (7), 4987-4998**.
4) Imidazole-Linked Crystalline Two-Dimensional Polymer with Ultrahigh Proton Conductivity. Ranjeesh, K. C.; **Illathvalappil, R**.; Veer, S. D.; Peter, J.; Wakchaure, V. C.; Goudappagouda; Raj, K. V.; Kurungot, S.; Babu, S. S., ***J. Am. Chem. Soc*. 2019, 141 (38), 14950-14954**.
5) Fe^{3+} Stabilized 3D Cross-Linked Glycine-melamine Formaldehyde Networks as Precursor for Highly Efficient Oxygen Reduction Catalyst in Alkaline Media. Kottarathil, S.; **Illathvalappil, R**.; S, N.; G.S, S.; A, P. M.; N. Nair, B.; Anilkumar, G. M.; Kurungot, S.; Yamaguchi, T.; Hareesh, U. S., ***Mater. Lett*., 2020, 264, 127365**.
6) Studies on Nano Composites of SPEEK/Ethylene glycol/Cellulose Nanocrystals as Promising Proton Exchange Membranes. Bano, S.; Negi, Y. S.; **Illathvalappil, R**.; Kurungot, S.; Ramya, K., ***Electrochim. Acta*, 2019, 293, 260-272**.
7) Carbon Derived from Soft Pyrolysis of a Covalent Organic Framework as a Support for Small-Sized RuO_2 Showing Exceptionally Low Overpotential for Oxygen Evolution Reaction. Chakraborty, D.; Nandi, S.; **Illathvalappil, R**.; Mullangi, D.; Maity, R.; Singh, S. K.; Haldar, S.; Vinod, C. P.; Kurungot, S.; Vaidhyanathan, R., ***ACS Omega, 2019, 4 (8), 13465-13473***.
8) A Copper (II)-Coordination Polymer Based on a Sulfonic-Carboxylic Ligand Exhibits High Water-Facilitated Proton Conductivity. Tayade, S. B.; **Illathvalappil, R**.; Lapalikar, V.; Markad, D.; Kurungot, S.; Pujari, B.; Kumbhar, A. S., ***Dalton Trans., 2019, 48 (29), 11034-11044***.

9) $NiCo_2O_4$ nanoarray on CNT Sponge: a Bi-functional Oxygen Electrode Material for Rechargeable Zn-air Batteries. Gangadharan, P. K.; Bhange, S. N.; Kabeer, N.; **Illathvalappil, R**.; Kurungot, S., ***Nanoscale Advances, 2019, 1 (8), 3243-3251***.
10) Morphological Ensembles of N-Doped Porous Carbon Derived from ZIF-8/Fe-Graphene Nanocomposites: Processing and Electrocatalytic Studies. Thomas, M.; **Illathvalappil, R**.; Kurungot, S.; Nair, B. N.; Mohamed, A. P.; Anilkumar, G. M.; Yamaguchi, T.; Hareesh, U. S., ***ChemistrySelect, 2018, 3 (30), 8688-8697***.
11) Layered TiO_2 Nanosheet-Supported $NiCo_2O_4$ Nanoparticles as Bi-functional Electrocatalyst for Overall Water Splitting. Vadakkekara, R.; **Illathvalappil, R**.; Kurungot, S., ***ChemElectroChem, 2018, 5 (24), 4000-4007***.
12) Preparation and Investigations of ABPBI Membrane for HT-PEMFC by Immersion Precipitation Method. Chaudhari, H. D.; **Illathvalappil, R**.; Kurungot, S.; Kharul, U. K., ***J Membrane Sci., 2018, 564, 211-217***.
13) Metalloporphyrin Two-Dimensional Polymers via Metal-Catalyst-Free C–C Bond Formation for Efficient Catalytic Hydrogen Evolution. Chandran Ranjeesh, K.; **Illathvalappil, R**.; Chandrakant Wakchaure, V.; Goudappagouda; Kurungot, S.; Babu, S. S., ***ACS Appl. Energy Mater., 2018, 1 (11), 6442-6450.***
14) Morphological Ensembles of N-Doped Porous Carbon Derived from ZIF-8/Fe-Graphene Nanocomposites: Processing and Electrocatalytic Studies. Thomas, M.; **Illathvalappil, R**.; Kurungot, S.; Nair, B. N.; Mohamed, A. P.; Anilkumar, G. M.; Yamaguchi, T.; Hareesh, U. S., ***ChemistrySelect, 2018, 3 (30), 8688-8697***.
15) Water Mediated Proton Conductance in a Hydrogen-bonded Ni(ii)-Bipyridine-Glycoluril Chloride Self-assembled Framework. Tayade, S. B.; Bhat, S. S.; **Illathvalappil, R**.; Dhavale, V. M.; Kawade, V. A.; Kumbhar, A. S.; Kurungot, S.; Näther, C., ***CrystEngComm., 2018, 20 (8), 1094-1100***.
16) Melamine Formaldehyde-Metal Organic Gel Interpenetrating Polymer Network Derived Intrinsic Fe-N-doped Porous Graphitic Carbon Electrocatalysts for Oxygen Reduction Reaction. Kottarathil, S.; **Illathvalappil, R**.; Sumitha, N. S.; Sailaja, G. S.; Kurungot, S.; Nair, B. N.; Peer Mohamed, A.; Anilkumar, G. M.; Yamaguchi, T.; Hareesh, U. S., ***New J Chem., 2018, 42 (23), 18690-18701***.
17) Nitrogen-doped Graphene Anchored with Mixed Growth Patterns of CuPt Alloy Nano-particles as a Highly Efficient and Durable Electrocatalyst for the Oxygen Reduction Reaction in an Alkaline Medium. **Illathvalappil, R**.; Dhavale, V. M.; Bhange, S. N.; Kurungot, S., ***Nanoscale, 2017, 9 (26), 9009-9017.***

18) Ultrahigh Ionic Conduction in Water-Stable Close-Packed Metal-Carbonate Frameworks. Manna, B.; Desai, A. V.; **Illathvalappil, R**.; Gupta, K.; Sen, A.; Kurungot, S.; Ghosh, S. K., ***Inorg. Chem., 2017, 56 (16), 9710-9715***.

19) Chitosan Intercalated Metal Organic Gel as a Green Precursor of Fe Entrenched and Fe Distributed N-Doped Mesoporous Graphitic Carbon for Oxygen Reduction Reaction. Kottarathil, S.; **Illathvalappil, R**.; Kurungot, S.; Nair, B. N.; Mohamed, A. P.; Yamaguchi, T.; Anilkumar, G. M.; Hareesh, U. S.; Sailaja, G. S. ***ChemistrySelect, 2017, 2 (28), 8762-8770***.

20) Hydrogen-Bonded Organic Frameworks (HOFs): A New Class of Porous Crystalline Proton-Conducting Materials. Karmakar, A.; **Illathvalappil, R**.; Anothumakkool, B.; Sen, A.; Samanta, P.; Desai, A. V.; Kurungot, S.; Ghosh, S. K., ***Angew. Chem. Int. Ed., 2016, 55 (36), 10667-10671***.

21) Conjugated porous polymers as precursors for electrocatalysts and storage electrode materials. Bhosale, M. E.; **Illathvalappil, R.**; Kurungot, S.; Krishnamoorthy, K., ***Chem. Commun., 2016, 52 (2), 316-318***.

22) Understanding the Electron Transfer Process in ZnO-Naphthol Azobenzoic Acid Composites from Photophysical Characterisation. George, L.; Kunhikannan, A. K.; **Illathvalappil, R**.; Ottoor, D.; Kurungot, S.; Devi, R. N., ***Phys. Chem. Chem. Phys., 2016, 18 (32), 22179-22187***.

23) Graphene Oxide Sheathed ZIF-8 Microcrystals: Engineered Precursors of Nitrogen-Doped Porous Carbon for Efficient Oxygen Reduction Reaction (ORR) Electrocatalysis. Thomas, M.; **Illathvalappil, R**.; Kurungot, S.; Nair, B. N.; Mohamed, A. A. P.; Anilkumar, G. M.; Yamaguchi, T.; Hareesh, U. S., ***ACS Appl. Mater. Interfaces, 2016, 8 (43), 29373-29382***.

24) Low Band Gap Benzimidazole COF Supported Ni_3N as Highly Active OER Catalyst. Nandi, S.; Singh, S. K.; Mullangi, D.; **Illathvalappil, R**.; George, L.; Vinod, C. P.; Kurungot, S.; Vaidhyanathan, R., ***Adv. Energy Mater., 2016, 6 (24), 1601189***.

25) Layer-separated MoS_2 Bearing Reduced Graphene Oxide Formed by an In-situ Intercalation-cum-anchoring Route Mediated by $Co(OH)_2$ as a Pt-free Electrocatalyst for Oxygen Reduction. **Illathvalappil, R**.; Unni, S. M.; Kurungot, S., ***Nanoscale, 2015, 7 (40), 16729-16736***.

26) Carbon Nanohorn-Derived Graphene Nanotubes as a Platinum-Free Fuel Cell Cathode. Unni, S. M.; **Illathvalappil, R**.; Bhange, S. N.; Puthenpediakkal, H.; Kurungot, S., ***ACS Appl. Mater. Interfaces, 2015, 7 (43), 24256-24264***.

27) Surface-modified Single Wall Carbon Nanohorn as an Effective Electrocatalyst for Platinum-free Fuel Cell Cathodes. Unni, S. M.; Ramadas, S.; **Illathvalappil, R**.; Bhange, S. N.; Kurungot, S., ***J. Mater. Chem. A, 2015, 3 (8), 4361-4367***.

28) Nitrogen-Induced Surface Area and Conductivity Modulation of Carbon Nanohorn and Its Function as an Efficient Metal-Free Oxygen Reduction Electrocatalyst for Anion-Exchange Membrane Fuel Cells. Unni, S. M.; Bhange, S. N.; **Illathvalappil, R**.; Mutneja, N.; Patil, K. R.; Kurungot, S., ***Small, 2015, 11 (3), 352-360***.

29) Nanoporous Graphene by Quantum Dots Removal from Graphene and its Conversion to a Potential Oxygen Reduction Electrocatalyst via Nitrogen Doping. Palaniselvam, T.; Valappil, M. O.; **Illathvalappil, R**.; Kurungot, S., ***Energy Environ. Sci., 2014, 7 (3), 1059-1067***.

30) Layer-separated Distribution of Nitrogen Doped Graphene by Wrapping on Carbon Nitride Tetrapods for Enhanced Oxygen Reduction Reactions in Acidic Medium. Unni, S. M.; **Illathvalappil, R**.; Gangadharan, P. K.; Bhange, S. N.; Kurungot, S., ***Chem. Commun., 2014, 50 (89), 13769-13772***.

31) New Approach of Blending Polymeric Ionic Liquid with Polybenzimidazole (PBI) for Enhancing Physical and Electrochemical Properties. Rewar, A. S.; Chaudhari, H. D.; **Illathvalappil, R**.; Sreekumar, K.; Kharul, U. K., ***J. Mater. Chem. A, 2014, 2 (35), 14449-14458***.

Patents

1) A process for the preparation of PBI based membrane electrode assembly (MEA) with improved fuel cell performance and stability. Kurungot, S.; **Illathvalappil, R**.; Bhange, S. N.; Unni, S. M., ***US 2016/0315343 A1***.

2) CuPt alloy with mixed dispersion on nitrogen doped grapheme as a highly efficient and durable electrocatalyst for alkaline fuel cell application. Kurungot, S.; **Illathvalappil, R**.; Dhavale, V. M., ***Application No. 2016-NF-0156***.

Erratum